CASE WESTERN RESERVE UNIVERSITY
Case School of Engineering

CASE WESTERN RESERVE UNIVERSITY

EMAE 356: Aerospace Design

Preliminary Design of a Crewed Mission to Deimos

Team Alpha Final Report

Authors:

Ethan Cogdill[1]

Joshua Berman Nathaniel Berntson

Owen Braun Abigail Burianek Alexander Dudowski

Tyler Griffith Nathan Kralik Katelyn Lamm

Paul Racanelli Jocelyn Schechter

Joseph Schlager Alex Schreiter Preston Yen

May 8, 2025

[1]Systems Engineer

Abstract

Given a 20-year period beginning in 2025, a crewed mission to Deimos, one of Mars' moons, is designed for the purpose of tele-operating Mars surface assets and studying the origins of Deimos. The mission, departing no later than October 19, 2041 carries four crew members to Deimos' orbit. In two rotations lasting 135 days, two crew members descend to the surface of Deimos while the other two crew trail Deimos in orbit around Mars. The estimated cost for this mission is $329 billion, which includes the infrastructure update cost, technology research and development, and design and testing funding. The entire mission will take 972 days: approximately 258 days of travel to Mars, 454 days in Mars orbit, and 258 days of travel back to Earth for return on July 17, 2044. The mission utilizes 6 launches of an extended, 150-mT class of Space Launch System (SLS) heavy lift vehicle to launch all payloads into a 400km Low Earth Orbit (LEO) staging orbit. The mission architecture utilizes a high performance solid core nuclear thermal propulsion system, bimodal power generation, next generation lightweight hybrid composite LH_2 tanks, as well as compact fission micro-reactors in order to maximize the mass efficiency of the architecture. Through development of these next generation technologies, this crewed mission to Deimos allows for the possibility of future crewed Mars exploration missions.

Contents

Nomenclature

Symbols: Section 8, Structural Design

t_b	MMOD Bumper Thickness (m)
t_w	MMOD Rear Wall Thickness (m)
α	Angle between Vertical and Frustum Surface
α_{th}	Thermal Expansion Coefficient
α_{wind}	Helical Winding Angle
γ	Empirical Factor for Critical Stresses
λ	Eigenvalue Diagonal Matrix
ν	Poisson's Ratio
ω_f	Forcing Frequency
$\omega_{n_{axial}}$	Payload Cantilevered Axial Natural Frequency
$\omega_{n_{lat}}$	Payload Cantilevered Lateral Natural Frequency
ω_n	Natural Frequency
$\phi_{payload}$	Payload Adapter Radius-to-Thickness Parameter
ρ_o	Knockdown Factor for Frustum
$\sigma_{allowable}$	Allowable Stress
σ_{axial}	Axial Loading Stress
$\sigma_{cr,b}$	Critical Bending Stress
$\sigma_{cr,c}$	Critical Compression Stress

$\sigma_{current}$	Current Loading Stress
$\sigma_{lateral}$	Lateral Loading Stress
A_{cs_n}	Payload Element Beam Cross Sectional Area
A_{member}	Cross-Sectional Area of member
b_{rib}	Isogrid Rib Thickness
d	Isogrid Cell Height
D_b	Base Diameter
D_i	Inner Diameter
D_o	Outer Diameter of Member
D_t	Top Diameter
D_{out}	Outer Diameter
E	Modulus of Elasticity
E^*	Transformed Young's Modulus
F_ϕ	Lateral Force
F_θ	Axial Force
F_a	Axial Force
$F_{critical}$	Critical Force
h_n	Height of Component
I_{member}	Moment Area of Inertia per member
K	Ellipsoid Diameter to Height Coefficient

K_a	Axial Stiffness Matrix
K_l	Lateral Stiffness Matrix
k_n	Individual Payload Element Stiffness
k_p	Payload Adapter Stiffness
L	Lagrangian
L_{member}	Length of member
LF_ϕ	Axial Load Factor
LF_θ	Lateral Loading
M	Mass Matrix
M_b	Bending Moment
m_n	Mass of Arbitrary Component
m_p	Payload Adapter Mass
n	Thickness-to-Outer Radius Ratio
N_{cells}	Isogrid Number of Cells
$N_{cr(1)}$	General Instability
$N_{cr(2)}$	Skin Buckling
$N_{cr(3)}$	Rib Crippling
p_{allow}	Allowable Pressure
p_{burst}	Burst Pressure
R_i	Inner Radius of Member

R_o	Outer Radius of Member
T	Kinetic Energy
t^*	Equivalent Monocoque Thickness
t_{eff}	Effective Weight Thickness
t_{equiv}	Equivalent Weight Thickness
t_{member}	Thickness of Member
t_{skin}	Isogrid Skin Thickness
V	Potential Energy
v	Poisson's Ratio
$V.F.$	Composite Volume Factor
X_{fl}	Longitudinal Failure Strength
X_{ft}	Transverse Failure Strength
X_{tu}	Ultimate Tensile Strength
X_{ty}	Yield Tensile Strength

Symbols: Section 9, Propulsion

α	Pressure Margin
α	Nozzle angle (°)
α (rad)	Nozzle angle
ΔP	Pressure Loss Through Pipe
$\dot{m}$	Propellant Mass Flow Rate

$\dot{m}_{\text{fuel}}$	Fuel mass flow rate
$\dot{m}_{\text{GG}}$	Gas generator mass flow rate
$\dot{m}_{\text{oxi}}$	Oxidizer mass flow rate
$\dot{m}_{\text{tot}}$	Total mass flow rate
$\dot{m}_{propellant}$	Propellant Mass Flow Rate
$\dot{m}_{ullage}$	Ullage Mass Flow Rate
$\dot{V}_{propellant}$	Propellant Volumetric Flow Rate
$\dot{V}_{ullage}$	Ullage Volumetric Flow Rate
η_{GG}	Gas generator efficiency
η_{nozzle}	Nozzle efficiency
η_{pump}	Pump efficiency
η_{turbine}	Turbine efficiency
γ	Ratio of Specific Heats
γ_{GG}	Specific heat ratio for gas generator
ω	Angular Velocity
ρ	Density
ρ_{gas}	Gas density
$\rho_{propellant}$	Propellant Density
ρ_{ullage}	Ullage Density
σ	Thoma Factor

ϵ	Nozzle expansion ratio
Isp	Specific impulse
A/A^*	Area Ratio
A^*	Nozzle throat area
A_e	Nozzle exit area
a_{launch}	Loading Factor
C_F	Thrust coefficient
C_p	Specific heat
D	Diameter
D_c	Chamber diameter
d_throat	Throat diameter
D_t	Throat diameter
$D_{propellant}$	Propellant Piping Diameter
d_s	Specific Diameter
D_{ullage}	Ullage Piping Diameter
E	Quality Factor
f	Darcy Friction Factor
F_T	Thrust
F_{axial}	Axial Force on Launch
h	Enthalpy

h	height
H_f	Head Loss
L	Length
$L_{propellant}$	Propellant Pipe Length
L_{ullage}	Ullage Pipe Length
M	Mach Number
M_{exit}	Exit Mach number
m_{fuel}	Fuel mass
m_{oxi}	Oxidizer mass
m_{prop}	Propellant mass
m_{piping}	Total Piping Mass
m_{ullage}	Total Ullage Mass
n_{s_p}	Pump Specific Speed
O/F	Fuel to oxidizer ratio
P_0	Stagnation Pressure in The Reactor
P_p	NTP Pump Power
P_t	NTP Turbine Power
P_v	Vaporization Pressure
P_{nozzle}	Pressure at the nozzle exit
$P_{\text{tank,ox}}$	Pressure in the oxidizer tank

P_{tank}	Pressure in the fuel tank
$P_{\text{ti}}/P_{\text{te}}$	Turbine pressure ratio
$P_{propellant}$	Propellant Piping Internal Pressure
P_{ullage}	Ullage Piping Internal Pressure
R	Radius
R_{t}	Throat radius
S	Allowable Stress
s	Entropy
t	Piping Thickness
T_0	Stagnation Temperature in The Reactor
T_s	Limiting Reactor Temperature
T_t	Fluid Temperature Through the Reactor
T_w	Wall Temperature
T_{ti}	Turbine inlet temperature
$U_{propellant}$	Propellant Velocity
U_{ullage}	Ullage Velocity
v	Velocity
V_{tank}	Tank Volume
W	Weld Joint Reduction Factor
Y	Material Coefficient

Symbols: Section 16, Trajectory Analysis

α_f	Flight Path Angle
τ	Dimensionless Time
θ	True Anomaly
a_{bo}	Dimensionless Burn Out Acceleration
a_{po}	Dimensionless Power On Acceleration
I	Specific Impulse
$r(\tau)$	Dimensionless Radius
R_{ref}	Planet Radius
$v(\tau)$	Dimensionless Velocity
v_{infty}^2	Dimensionless Characteristic Energy
v_j	Dimensionless Exhaust Velocity
$V_{c,ref}$	Circular Orbit Velocity
$\Delta V_{Capture}$	Change in Velocity for Mars Capture
$\Delta V_{Departure}$	Change in Velocity for Earth Departure
$\Delta V_{Hohmann}$	Hohmann Total Change in Velocity
ΔV_{simul}	Simultaneous Plane Change Delta-V
a_0	Initial Acceleration
d_0	Initial Position/Distance
e	Orbital Eccentricity

m_0	Total Initial Mass
m_f	Final Unfueled Mass on Return
$t_{transfer}$	Single Leg Transfer Time
V_0	Initial Velocity
V_∞	Hyperbolic Escape Velocity
V_e	Engine Exit Velocity
V_{Earth}	Earth Orbit Velocity about Sun
V_{eq}	Engine Equivalent Velocity
V_{LEO}	Low Earth Orbit Velocity
V_{Mars}	Mars Orbit Velocity about Sun
V_{MPO}	Mars Parking Orbit Velocity
V_{normal}	Velocity in Normal Direction
$V_{tangent}$	Velocity in Tangential Direction
a	Orbital radius

Symbols: Section 11, Power

α	Total Capture CS / Fission CS
$\dot{m}$	Mass Flow Rate
$\dot{V}$	Volumetric Flow Rate
η	Isentropic Efficiency
η_s	Operational Time

η_c	Compressor Isentropic Efficiency
$\eta_{thermal}$	Thermal Efficiency
η_t	Turbine Isentropic Efficiency
γ_{mix}	Ratio of Specific Heats)
ω_s	Specific Speed
ε_r	Regenerator Effectiveness
$AllowableBurnup$	Fraction Fissioned
C_{pHe}	He Specific Heat (Pressure)
C_{pmix}	Mixture Specific Heat (Pressure)
C_{pXe}	Xe Specific Heat (Pressure)
C_{vHe}	He Specific Heat (Constant Volume)
C_{vmix}	Mixture Specific Heat (Constant Volume)
C_{vXe}	Xe Specific Heat (Constant Volume)
C_{min}	Minimum Specific Heat
D_P	Pipe Diameter
D_r	Reactor Diameter
D_s	Specific Diameter
D_{hs}	Hydraulic Diameter
f	Friction Factor
f_a	Alternator Frequency

F_R	Fission Rate
M_{He}	He Molar Mass
M_{Xe}	Xe Molar Mass
N	Alternator Rotation Speed
N_p	Number of Pipes
N_u	Numbers of Atoms per Unit Volume
NTU	Number fo Transfer Units
P	Number of Poles
P_e	Power
P_t	Total Reactor Power
r_i	Tie Tube Inner Radius
r_o	Tie Tube Outer Radius
T_c	Core Temperature
T_{lm}	Log Mean Temperature
V_c	Cell Voltage
V_m	Moderator Volume
V_r	Reactor Volume (no pipes)
V_{fuel}	Fuel Volume
v_p	Fluid Velocity in Pipe
W	Adiabatic Head

X_{He}	He Mole Fraction
X_{Xe}	Xe Mole Fraction
A	Solar Panel Area
S	Solar Irradiance
t	Operational Time
Wh	Storage Capacity

Symbols: Section 14, Mars Assets

α	Thermal Diffusivity
β	Inverse of Density Scale Height
$\dot{q}_{conv}$	Convective Heat Flux
$\dot{Q}_{cw}$	Cold Wall Heat Flux
$\dot{Q}_{hw}$	Hot Wall Heat Flux
$\dot{q}_{rad}$	Radiative Heat Flux
$\dot{s}$	Recession Rate
ϵ	Emissivity
ρ_o	Density at Sea Level
σ	Stefan-Boltzmann Constant
θ_e	Entry Angle
A	Cross-Sectional Area
C_D	Drag Coefficient

c_p	Specific Heat
h	Altitude
H_r	Recovery Enthalpy
H_w	Wall Enthalpy
k	Thermal Conductivity
m	Mass
Q^*	Heat of Ablation
R_B	Body Radius
R_C	Corner Radius
R_N	Nose Radius
R_{eff}	Effective Nose Radius
t	Time
T_{surr}	Surrounding Temperature
T_w	Equilibrium Wall Temperature
V_e	Entry Velocity
x	Heat Shield Thickness

Symbols: Section 10, Thermal Control

$\dot{Q_W}$	Waste Habitat Electrical Heat
α	Thermal Diffusivity
$\dot{m}_{He-Xe}$	Mass flow rate of Helium-Xenon Gas Mixture

ν	Kinematic Viscosity
$\overline{N}$	Layer Density
ρ	Fluid Density
a_b	Albedo
A_s	Solar Exposed Surface Area
A_t	Total Surface Area
A_{c-s}	Total cross-sectional area of He-Xe
BOR	Boil-Off Rate
D_s	Specific Diameter
G_S	Solar Flux
H_v	Enthalpy of Vaporization
Ka	Solar Altitude Factor
M_{LH2}	Mass of Liquid Hydrogen Propellant in a Tank
N_s	Specific Speed
N_t	Total Number of tubes within the Heat Exchanger
Pr_s	Average Temperature Prandtl Number
q_1	Energy Flux at Earth Surface
Re	Reynolds Number
V	Velocity
α	Thermal Diffusivity

$\bar{T}_w$	Average Pipe Outside Wall Temperature
Δx	Small Approximately Diffential Element in x-direction
Δy	Small Approximately Diffential Element in y-direction
$\dot{Q}$	Rate of Heat Transfer
$\dot{Q}_{cond}$	Rate of Heat Transfer for Conduction
$\dot{Q}_{conv}$	Rate of Heat Transfer for Convection
$\dot{Q}_{rad}$	Rate of Heat Transfer for Radiation
ϵ	Emissivity
η_p	Pump Pressure Efficiency
Nu	Nusselt Number
Pe	Péclet number
Pr	Prandtl number
Re	Reynolds number
ν	Kinematic Viscosity
ρ	Density
A	Total Area of a Radiator
A_c	Cross Sectional Area of Radiator Fin
A_{surf}	Surface Area of Radiator Fin
c_p	Specific Heat Capacity at Constant Pressure
D_i	Internal Tube Diameter

D_o	Outer Tube Diameter
h	Heat Transfer Coefficient
k	Thermal Conductivity
k_{wall}	Heat Exchanger Wall Thermal Conductivity
L	Length of a Radiator Fin
m	Mass of a Radiator
N	Number of Tube-fin Radiator Sections in a Radiator
N_{rpm}	Rotational Speed
t	Thickness of Radiator Fin
T_m	Mean Fluid Temperature
T_s	Temperature of Space
T_w	Pipe Outside Wall Temperature
T_y	Temperature of Radiator in y-direction
T_{fin}	Temperature at End of Radiator Fin
t_{wall}	Tube Wall Thickness
V	Fluid Velocity
w	Width of a Radiator Fin
w_{tot}	Total Width of a Radiator

Constants

μ_{Earth}	Earth Gravitational Parameter	$3.986 \times 10^{14}\ m^3 s^{-2}$

μ_{Mars}	Mars Gravitational Parameter	$4.283 \times 10^{13}\ m^3 s^{-2}$
σ	Stefan-Boltzmann Constant	$5.67 \times 10^{-8}\ W/(m^2 K^4)$
a_{Earth}	Distance Earth to Sun	$1.496 \times 10^{8}\ km$
a_{Mars}	Distance Mars to Sun	$2.224 \times 10^{8}\ km$
G	Universal Gravitational Constant	$6.668 \times 10^{-11}\ m^3 kg^{-1} s^{-2}$
g_0	Earth Gravitational Constant	$9.8067\ ms^{-1}$
M_{Mars}	Mass of Mars	$64.169 \times 10^{22}\ kg$
R_{LEO}	Earth Parking Orbit Radius	$6780\ km$
R_{MPO}	Mars Parking Orbit Radius	$23\,458\ km$
T_{Earth}	Earth Orbital Period	$365.25\ days$
T_{Mars}	Mars Orbital Period	$687\ days$

Acronyms

ATCS Active Thermal Control System

ATS Atmospheric Temperature Sensor

CAD Computer Aided Design

CoDR Conceptual Design Review

CWRU Case Western Reserve University

DEV Deimos Excursion Vehicle

ECLSS Environmental Control and Life Support Systems

ECT Earth Capture Tank

EDT Earth Departure Tank

ESM European Service Module

EVA Extravehicular Activity

FMECA Failure Mode, Effects, and Criticality Analysis

FTIR Fourier Transform Infrared Spectroscopy

GPR Ground Penetrating Radar

HFE Human Factors Engineering

HS Humidity Sensor

HSI Human Systems Integration

IPV Inter-Planetary Vehicle

ISS International Space Station

JSC Johnson Space Center

LEO Low Earth Orbit

LiDAR Light Detection and Ranging

MCT Mars Capture Tank

MDE Multi-Layer Insulation

MDT Mars Departure Tank

MEDA Mars Environmental Dynamics Analyzer

MEPAG Mars Exploration Program Analysis Group

MLI Multi-Layer Insulation

MMH Mono-methyl Hydrazine

MMOD Micro-meteoroid and Orbital Debris

MMRTG Multi Mission Radio Isotope Thermoelectric Generator

MPO Mars Parking Orbit

NASA National Aeronautics and Space Administration

NHV Net Habitable Volume

NTP Nuclear Thermal Propulsion

OGA Oxygen Generation Assembly

OMS Orbital Maneuvering System

OMT Orbital Maneuvering System Tanks

PDR Preliminary Design Review

PICA Phenolic Impregnated Carbon Ablator

PS Pressure Sensor

SE&I Systems Engineering and Integration

SLS Space Launch System

SRR System Requirements Review

SSME Space Shuttle Main Engine

TL Subteam Lead Position

TMSA Tele-operating Mars Surface Asset

TRL Technological Readiness Level

WBS Work Breakdown Structure

WRS Water Recycling System

WS Wind Sensor

List of Figures

List of Tables

1 Introduction

1.1 Project Purpose

One of the primary purposes of this manned mission to the surface of Deimos is to enable efficient control of the tele-operated Mars surface assets. The crew will be able to seamlessly communicate with the assets on Mars, allowing for more efficient experimentation and data collection, along with a higher volume of collected data. Additionally, the crew will be able to perform experiments on the surface of Deimos, by collecting and analyzing surface samples, and conducting tests in the near-zero gravity environment. This mission also benefits space exploration on a large scale. New technologies developed for this mission will be the groundwork for manned space travel to Mars, and the crew of this mission will be the first humans to step foot on a celestial body other than Earth and its moon. In short, this mission will directly align with NASA's mission statement: "NASA explores the unknown in air and space, innovates for the benefit of humanity, and inspires the world through discovery."

1.2 Project Background

This mission has been preceded by many other manned and unmanned missions to other celestial bodies. From 1962 to 1972, NASA launched 11 total crewed Apollo missions, 6 of which completed a lunar landing [23]. These missions were crucial in the development of manned space travel, and led to some of the most groundbreaking scientific advancements in recent history. This mission to Deimos functions as the next step in manned space travel, and takes heavy inspiration from the Apollo missions of the late 19th century. This mission presents its own complications, however, namely the vastly increased distance between Earth and Mars compared to the Moon. Therefore, inspiration was also taken from the existing unmanned missions to the surface of Mars. There have been 5 total NASA rovers sent to the surface of Mars: Sojourner in 1997, Spirit and Op-

portunity in 2004, Curiosity in 2012, and Perseverance in 2021 [24]. Although unmanned, these missions nonetheless successfully transported their payloads from Earth to Mars. However, the manned aspect of this mission also needs consideration. Therefore, the International Space Station was also used as a template for survival in space for longer periods of time. In 2023, astronaut Frank Rubio set the record for longest mission in space, staying on the ISS for 371 days [25]. Although this planned mission involves survival in space for significantly longer than this, the ISS is still the only existing example of long-term habitation in space, and thus was instrumental in this mission design. Although a mission of this scale is unprecedented, previous missions were able to lay a foundation that heavily supported this design. Combining elements from past missions and expanding them to fit this scale allowed for the creation of this mission design.

2 Mission Overview

2.1 Mission Statement

Given a 20-year time span starting in 2025 derive an architecture that delivers a crew of four to the surface of Deimos. Lay out a series of Mars moon surface excursions driven by science, technology demonstration, and possible future human exploration site reconnaissance on Mars. The architecture must also include tele-operating Mars surface assets (i.e., rovers, ISRU production plants, infrastructure cameras, small Mars fliers, deployment of power and support systems, etc.) while the astronauts are not conducting Extravehicular Activities (EVAs).

The challenge is to develop an architecture for a crewed mission to the surface of Deimos and return to Earth that utilizes an extended 150-mT class Space Launch System (SLS) launch vehicle to come up with a viable system design. Innovative technologies and systems include: in situ resource utilization, efficient orbital transfer propulsion systems (re-usability is an option), advanced habitation and life support systems, among many

others [26].

2.2 Concept of Operations

The concept of operations of the mission is illustrated in Figure 2.1.

Phase 1 of the mission entails 6 launches from Kennedy Space Center (KSC) to Low Each Orbit (LEO) where the assembly of the mission vehicle is accomplished.

Phase 2 is the Hohmann transfer transit to Mars neighborhood initiated by the Earth departure burn and terminated by the Mars capture burn for a total ΔV of 6.3 km/s and transit time of 8.5 months. A conceptual representation of the interplanetary transfer orbits is illustrated in Figure 2.2. After each major burn, emptied propellant tanks will be jettisoned. Soon after the Earth departure burn, the Tele-operating Mars Surface Assets (TMSA) vehicle will detach from the Inter-Planetary Vehicle (IPV) and perform the minuscule maneuvering (to then be corrected over time) required to set it on trajectory to encounter Mars atmosphere as opposed to a Deimos altitude orbit.

Phases 3a and 3b occur in parallel with one another after entering a Deimos altitude orbit around Mars. The interplanetary vehicle will maintain a 100 km trailing orbit behind Deimos for the full 15 month stay in the Mars neighborhood while two of the four astronauts pilot the Deimos Excursion Vehicle (DEV) to the surface of the moon in two 4.5 month shifts. During this time, the tele-operation of the TMSA and the science goals on Deimos surface will be conducted.

After a full sidereal period of 15 months, the IPV and four astronauts enter Phase 4: a return Hohmann transfer trajectory to Low Earth Orbit (LEO). Similar to Phase 2, this operation constitutes 2 burns (this time Mars escape and Earth capture) and lasts a duration of 8.5 months, with a reduced total ΔV of 5.8 km/s.

Finally, the crew and what remains of the mission vehicle, return to LEO on June 17, 2044.

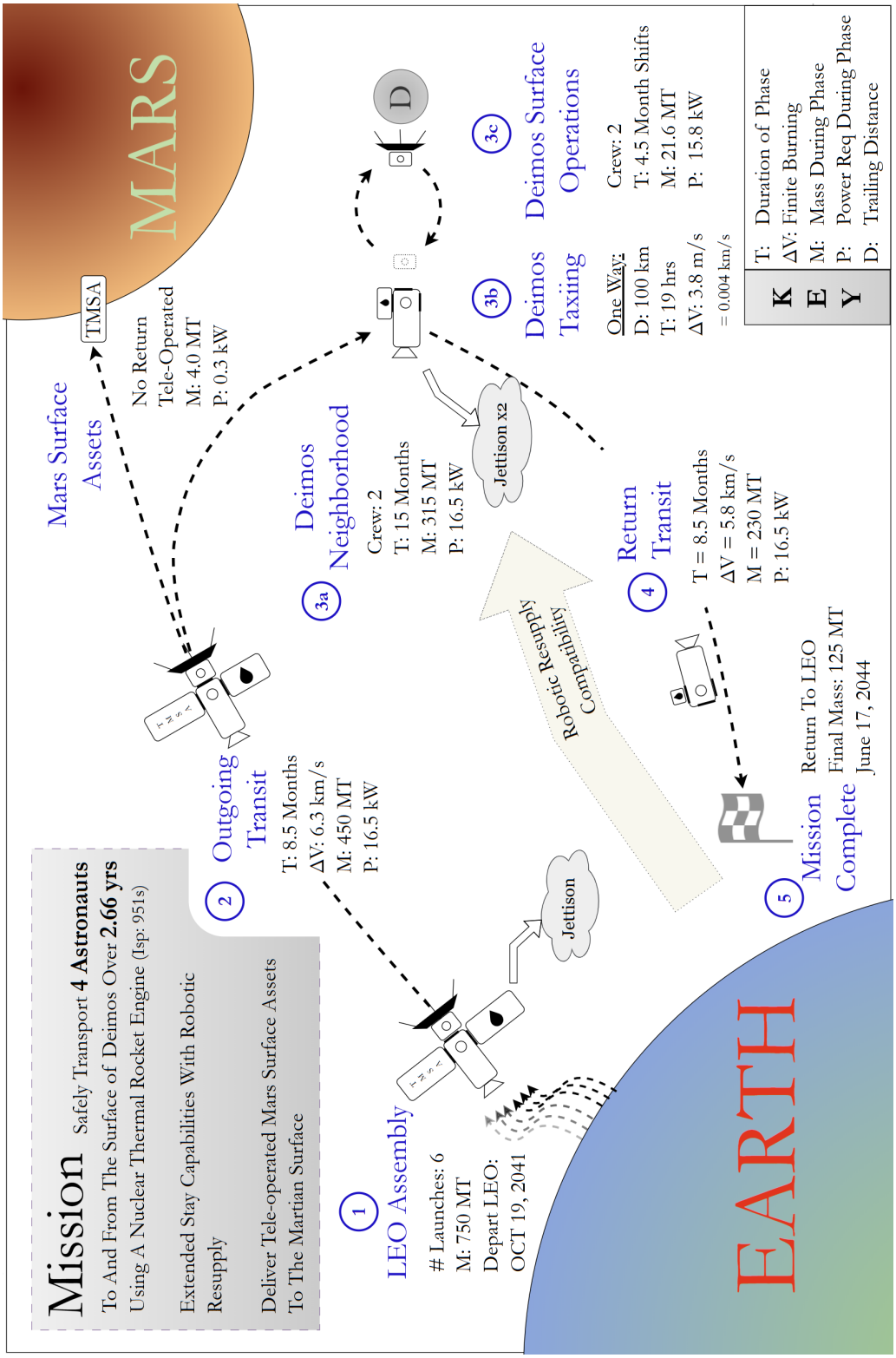

Figure 2.1: Concept of Operations

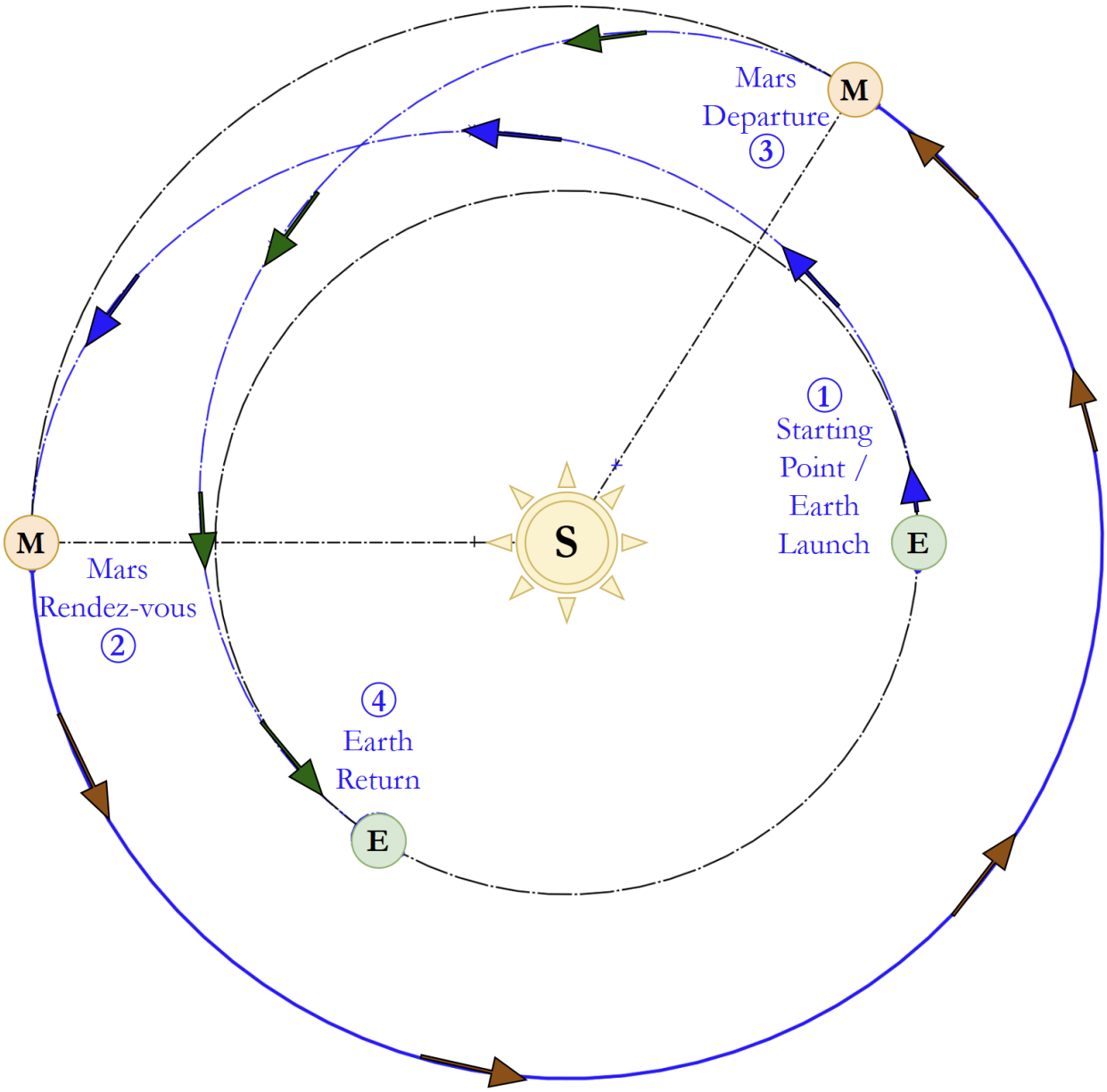

Figure 2.2: Conceptual Trajectories

2.3 Requirements

During the Systems Requirements Review (SRR) phase, numerical mission requirements were developed from reading technical reports, creating preliminary trade studies, as well as team discussion to reach a consensus on major mission operational decisions. Table 2.1 below summarizes the mission requirements and constraints as seen in the mission statement, while Table 2.2 contains the most important derived requirements that drive the overall mission architecture and design of the vehicle. The overall Functional Block Diagram(FBD) for the IPV and DEV were developed in parallel with the requirements. A full list of all requirements organized by FBD number is in Appendix H.1.

Mission Objectives/Constraints
Mission completion within 20 year, 2025-2045 window
Mission crew of 4, minimum
All crew must participate in Deimos surface stay of 270 days
Robotic resupply capability for mission extended duration
Deliver tele-operating Mars surface assets
Use of extended 150-mT class Space Launch System launch vehicle
Designs consistent with Reference [27]

Table 2.1: Mission Objectives and Constraints

Table 2.2: Major Derived Requirements

X.	X.X	Requirement Description	Requirement(s)	Rationale
0	0.1	Launch Date	The mission shall launch no later than October 2041. The optimal launch window is October 19 2041. The mission shall return no later than December 31, 2044	Ref [28]
0	0.2	Mission Duration	The total mission duration shall be maximum 972 days.	Trade Study
0	0.3	Wet Mass	The assembled interplanetary vehicle shall have a maximum fully fueled mass of 750mT	Trade Study
I-0	0	Dry Mass	The assembled vehicle shall have a maximum dry mass of 241 mT before LEO departure	Trade Study
I-2	2.2	Water Mass	The interplanetary vehicle must carry 9.23 mT of consumable water.	75% recycling efficiency; see Trade Study
I-2	2.3	Food	The interplanetary vehicle must carry 6.22mT of food.	Trade Study
I-2	2.1	O2 / N2	The interplanetary vehicle must carry 1.77mT of N2, 6.92mT of O2.	Trade Study
I-3	3.1	IPV Power Peak	The interplanetary vehicle must have a power supply capable of producing a minimum peak of 25.1 kWe	Trade Study
I-3	3.2	IPV Power Nominal	The interplanetary vehicle must have a power supply capable of producing a minimum nominal power of 16.1 kWe	Trade Study
I-6	6.1	Mission Total	The interplanetary vehicle should have a minimum total deltaV of 11.84 km/s	Delta-V Trade Study
I-4	4.3.1	Micrometeoroid Impacts	Spacecraft shall be able to withstand all potential unavoidable obstacles during space travel, including micrometeorites traveling up to 10.5 km/s.	Ref [29]
I-4	4.2.1	Career Radiation Dose	An individual astronaut's total effective radiation dose due to space flight radiation exposure shall be less than 1.3mSv/day across the entire mission	Ref [30]
I-5	5.0	Structural FoS	All designed structures shall have an FoS of 1.5.	Ref [31]
I-6	6.3.4	IPV Engine Isp	The interplanetary vehicle shall use a propulsion system with minimum 850s and maximum 950s	Trade Study
I-6	6.3.3	IPV Engine Thrust	The IPV Engines shall have a thrust level of 351kN per Nuclear Thermal engine.	Trade Study
D-3	3.1	DEV Power Peak	The DEV must have a power supply capable of producing a minimum of 20.1 kWe (Peak)	Trade Study
D-3	3.2	DEV Power Nominal	The DEV must have a power supply capable of producing a minimum of 15.8 kWe (nominal)	Trade Study
D	D-0	Lander Mass	The Deimos lander (without systems or supplies) shall be a maximum of 15 mT.	Trade Study
M-1	M-1.1	Mass Budget for TMSAs	The total mass of all Tele-operating Mars Surface Assets (TMSAs) shall not exceed a maximum of 4 MT	Trade Study
M-2	M-2.1	Power Budget for TMSAs	The total continuous power usage of all Tele-operating Mars Surface Assets (TMSAs) shall not exceed 3 kWe	Trade Study

3 System Overview

3.1 Functional Block Diagram

The engineering requirements seen in Section 2.3 are developed concurrently with the Functional Block Diagrams. The Functional Block Diagrams act to illustrate the logical flow of the engineering requirements guiding the CoDR and PDR phase of system design and are seen in Figures 3.1 and 3.2. It should be noted that these FBDs develop represent the state of the requirements as of the CoDR phase of the project.

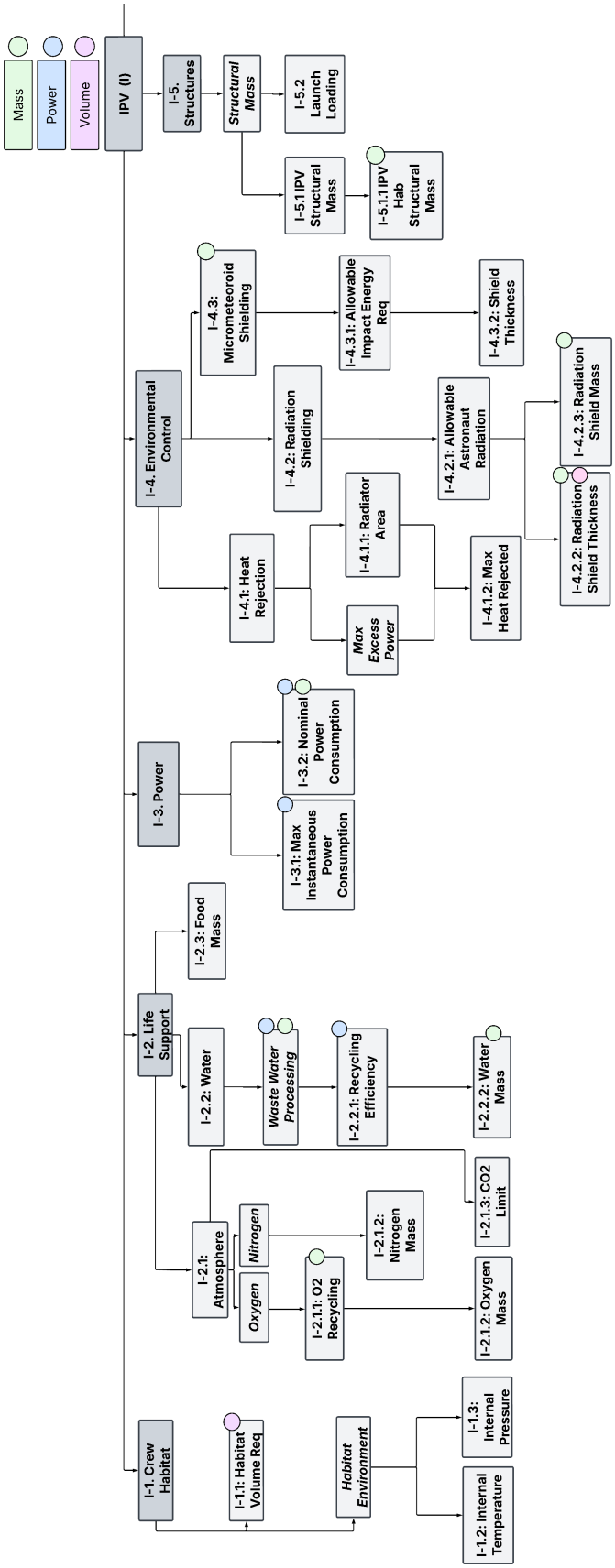

Figure 3.1: IPV Requirements Functional Block Diagram 1

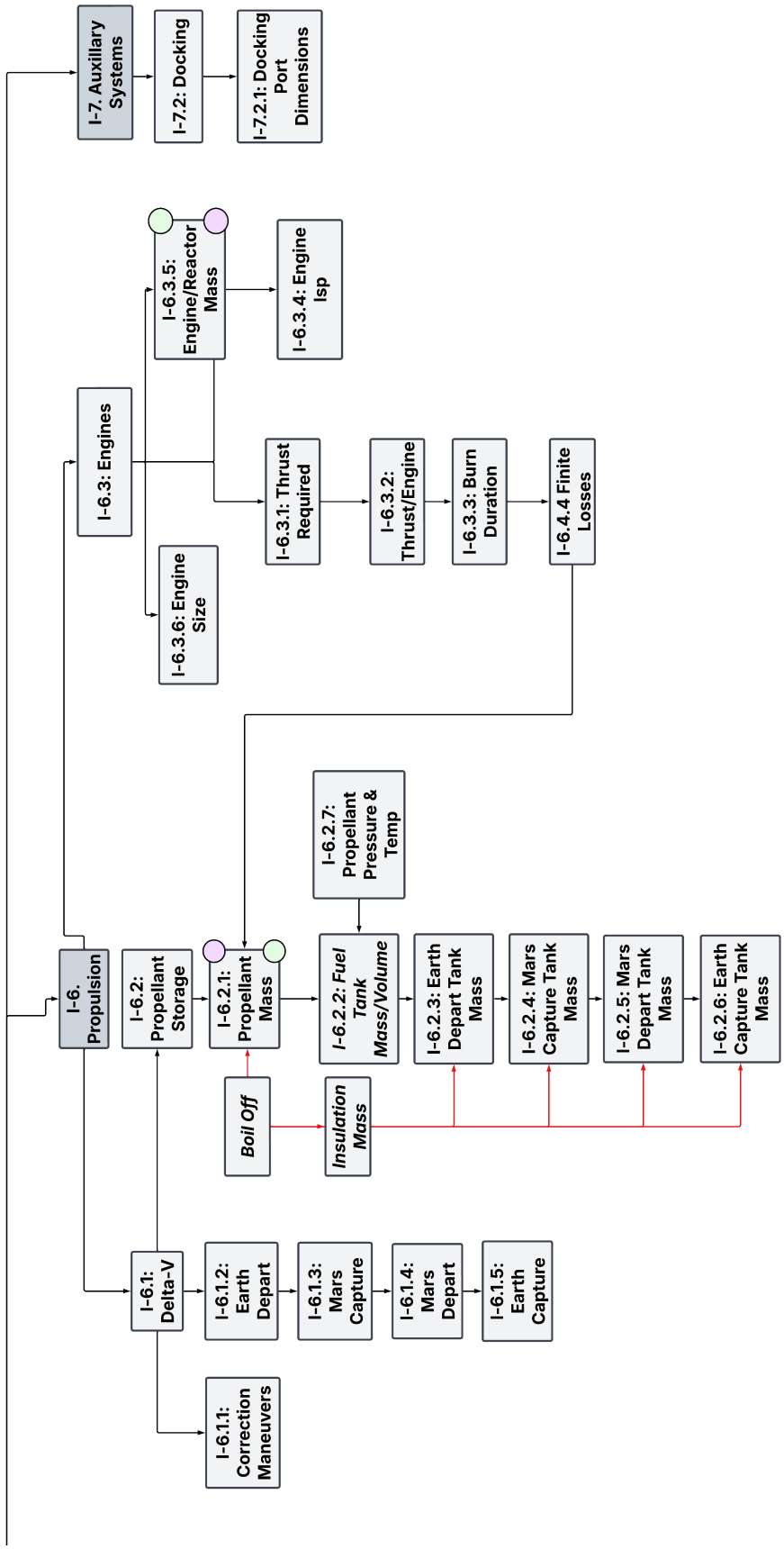

Figure 3.2: IPV Requirements Functional Block Diagram 2

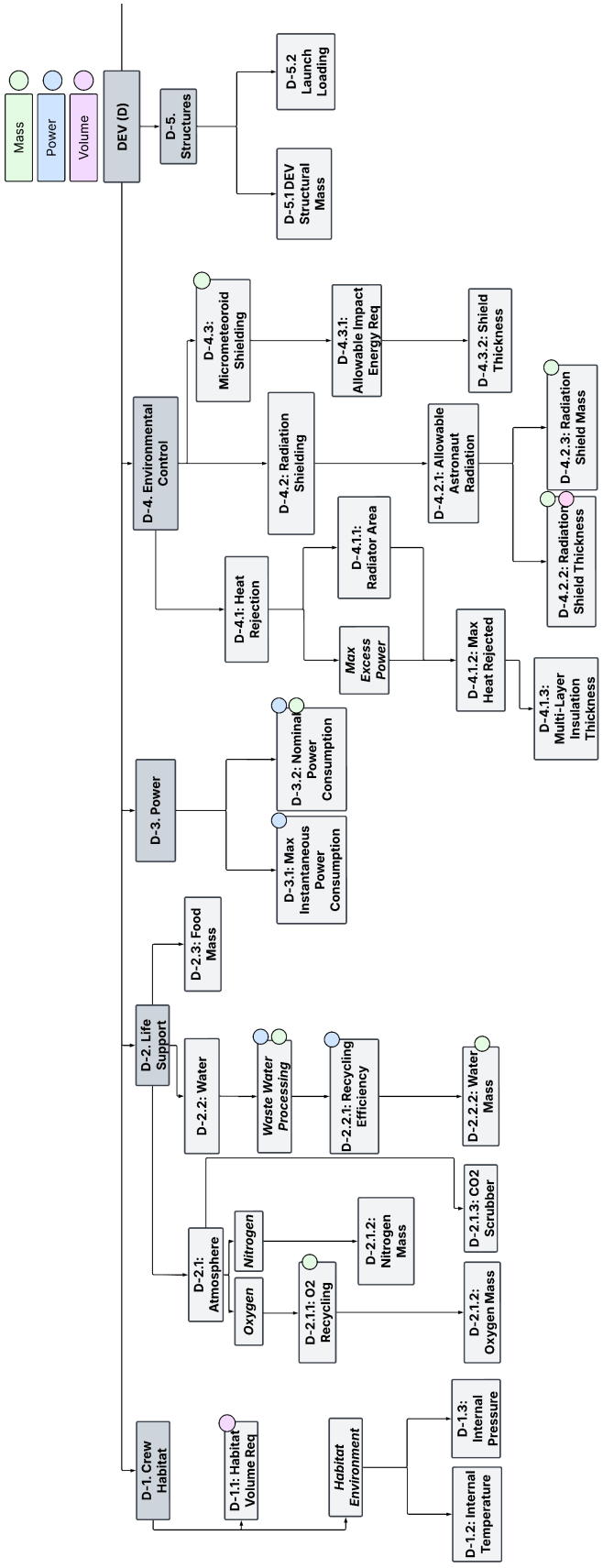

Figure 3.3: DEV Requirements Functional Block Diagram 1

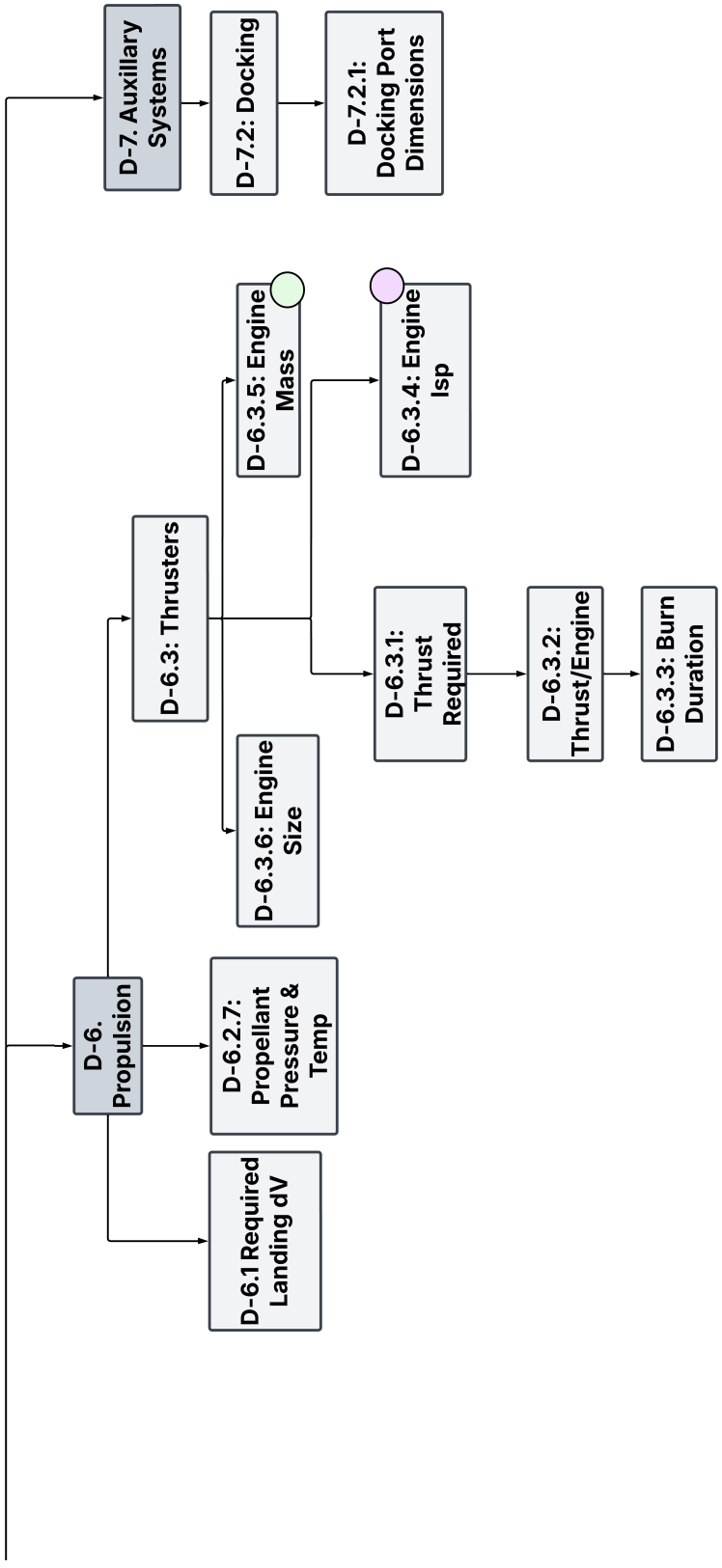

Figure 3.4: DEV Requirements Functional Block Diagram 2

4 System Modeling

4.1 Major Design Drivers

There are several key factors that influence the design decisions for this mission. The primary focus for the design is mass: since the IPV needs to be launched in a reasonable amount of SLS launches, every component needs to be as light as possible. Therefore, mass affects every aspect of the design, such as structural considerations, life support systems, power generation, and propulsion systems. Another key factor is volume. Not only must the components be light enough to launch, they must also fit inside a conventional fairing. Therefore, designs which allow for a simpler packaging configurations are in many ways superior to designs that require more complex packaging. These first two factors can be easily defined numerically, either by the total system mass or dimensions of individual components, however another important factor to consider is the simplicity of the design architecture. Ease of assembly is critical for a mission of this scale, where components must be assembled in space within a rigid timeline. Although this cannot be defined with a value, overall complexity is nonetheless a critical design driver in the development of this mission.

4.2 Key Technological Readiness Levels

4.2.1 Nuclear Thermal Propulsion

A nuclear thermal rocket engine is selected due to the mass savings that accompany an engine with higher Isp. A TRL of 7 is assigned to the designed *Harmonia* nuclear thermal propulsion engine. NTP systems have been tested and fired in a vacuum on Earth but no flight ready systems have ever been flown. The NERVA prototypes have significantly more structural and shielding mass than Harmonia is expected to have. These prototypes were able to sustain a burn for around 60 minutes with an Isp of around 875 [32]. The largest

improvements that need to be made are in Zirconium Carbide coatings on the fuel rods to prevent corrosion and degradation of fuel elements [33]. Harmonia's reactor temperature is not expected to greatly exceed those of the NERVA A# engines and therefore would not have a great effect on the TRL evaluation. The turbomachinery used in the reactor expander cycle is assigned a TRL of 9. Turbopumps and turbines that have a much larger mass flow rate have been utilized for cryogenic hydrogen systems in space [34].

4.2.2 Hybrid Composite Tanks

A hybrid composite tank design is selected for primary structure mass savings across all propellant tank structures and is assigned a TRL of 6. Due to the mass constrained nature of the mission, the integration of the composite tank technology is vital to the success of the mission architecture. A previous testing campaign from Boeing and NASA [35] has demonstrated that large scale composite tanks are possible to manufacture and can withstand flight-like loading conditions. Boeing constructed two test tanks, with diameters of 2.4m and 5.5m, but tank walls were designed to carry the line loads predicted for a 10m diameter tank. The tanks manufactured by Boeing underwent mechanical testing, including burst and leak tests to validate their structural performance and compatibility with cryogenic propellants such as LH2. It is important to note that these tanks were linerless and constructed of a mixture of thin and thick composite plies for reduced permeability. The tanks outlined in Section 8.4.3 are composed of several composite ply layers in addition to a internal metallic liner to prevent hydrogen permeation. The use of the metallic liner is necessary due to the long duration cryogenic LH_2 storage that these tanks must support. However, the introduction of a metallic internal liner introduces the risk of induced thermal stresses due to the coefficient of thermal expansion mismatch between the composite and the metallic liner. The thermal expansion issue is discussed in more depth in Section 8.4.2. This is an area that requires more research in order to investigate possible solutions to this issue.

4.2.3 Bimodal and DEV Reactor

Brayton cycles are commonly found on jet turbines and air breathing engines as a means of power generation [36]. Moreover, Brayton cycles are proven methods of power generation as opposed to Stirling engines. As such, a Brayton cycle is used for both bimodal and DEV reactors. However, the Brayton cycles for the DEV and bimodal utilize a Xenon and Helium mixture as the working fluid as opposed to air. XeHe Brayton cycles have been tested in space-like environments and fission reactors were actually flown in the past and are therefore at a TRL of 6 [37][38][39].

5 Vehicle Design

5.1 IPV Assembly Vehicle Design

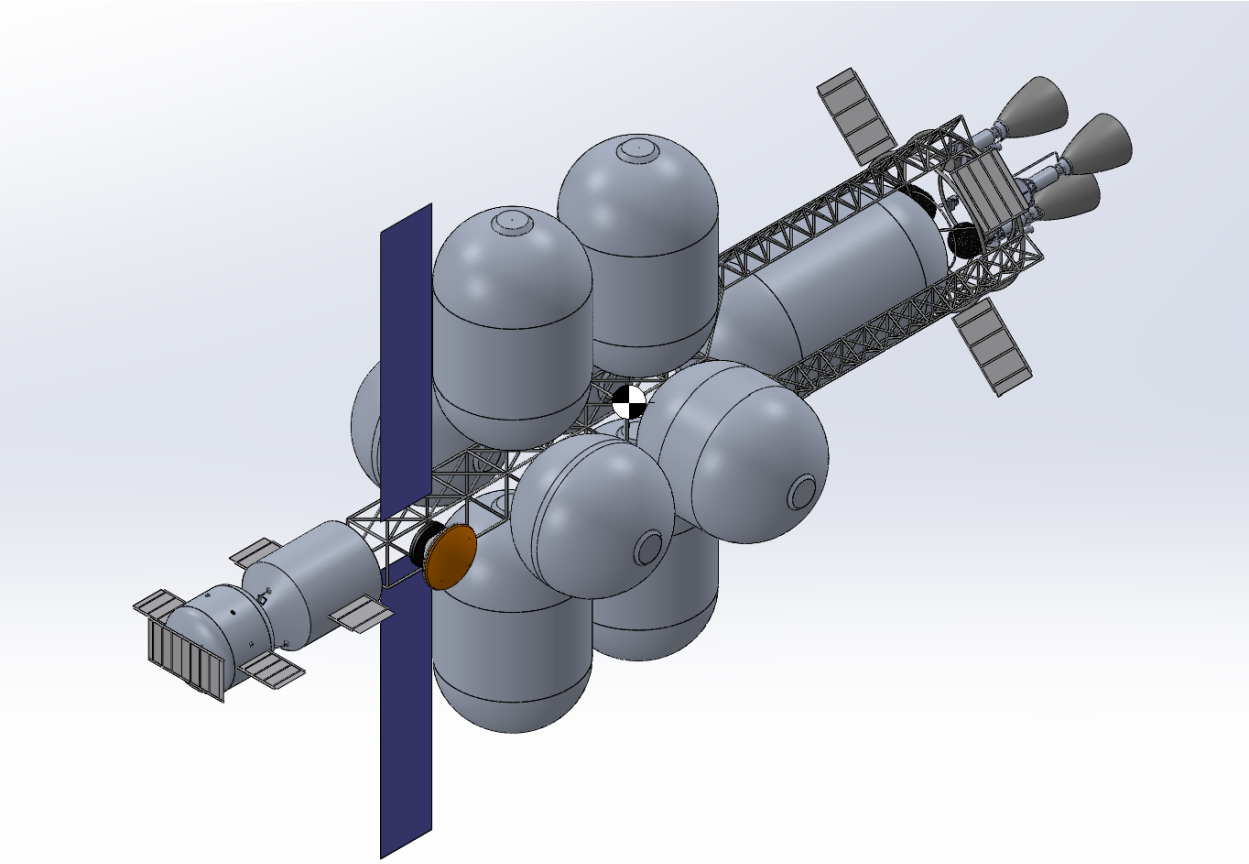

Figure 5.1: Isometric View of Fully Assembled IPV

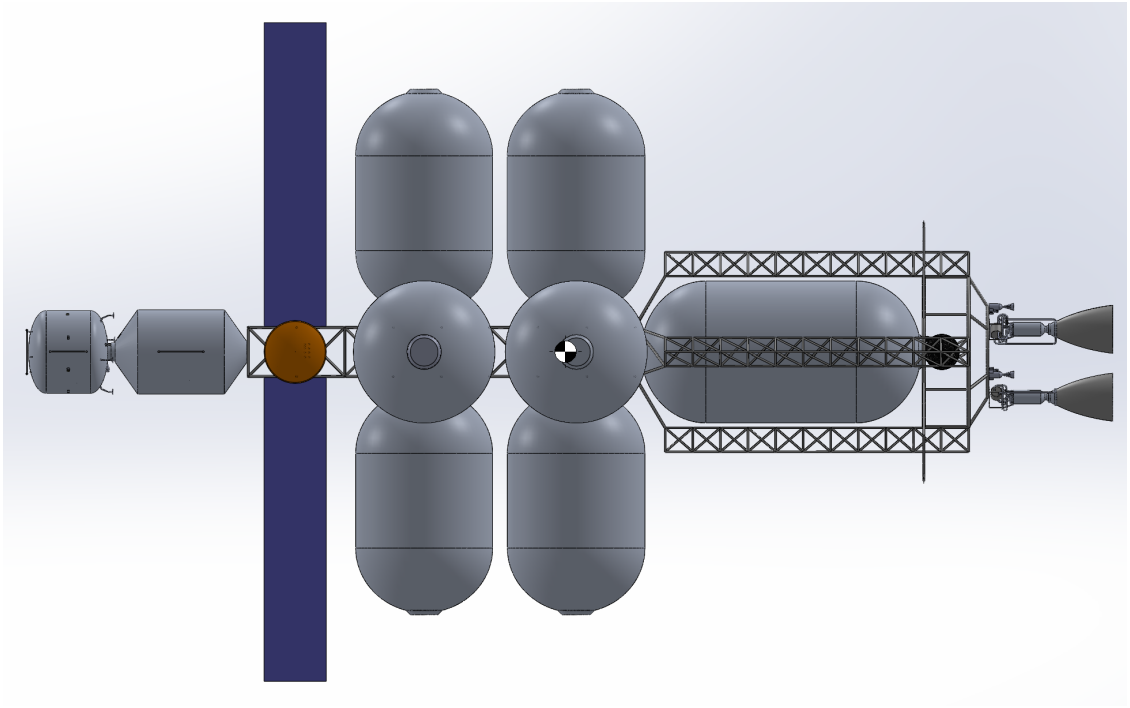

Figure 5.2: Side View of Fully Assembled IPV

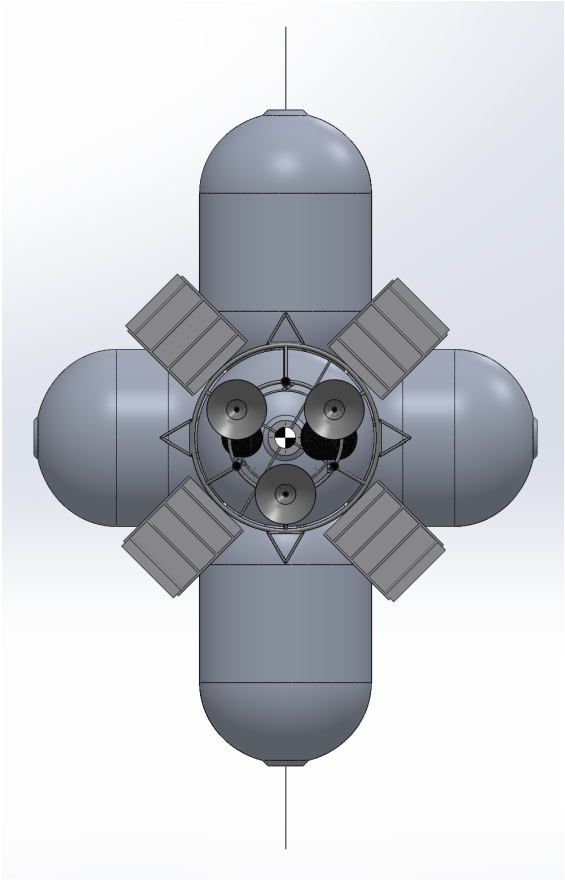

Figure 5.3: Back View of Fully Assembled IPV

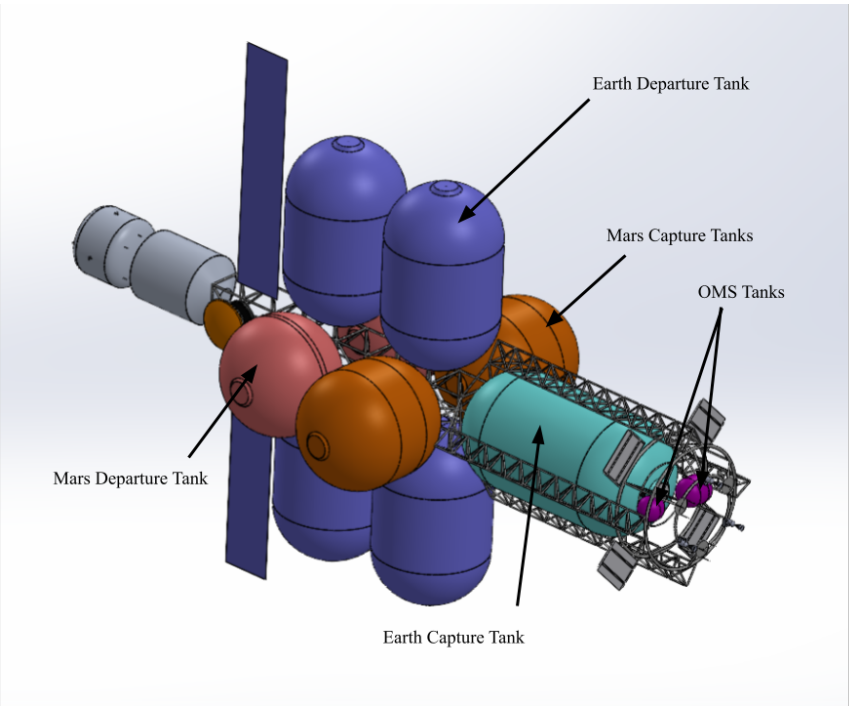

Figure 5.4: Propellant Tank Layout Diagram

5.1.1 IPV Propellant Tank Subassembly

Figure 5.4 shows the placement of the 5 major propellant tank configurations on the IPV. The EDT, MCT, MDT, ECT, and OMST, which are specified based on color in the figure, are assembled onto the IPV structure in a radial configuration. The mass breakdown of each tank configuration is detailed in 5.5, and detailed tank structure sizing analyses are provided in Section 8.4.2. The geometry and quantity of each tank is constrained by the volume and mass constraints of the SLS launcher. The mass restriction drives the IPV to utilize multiple identical tanks. In the final design configuration of the IPV, there are 4 EDT, 2 MCT, 2 MDT, and 1 ECT. The transverse attachment of the IPV LH_2 tanks shortens the necessary main truss structural mass and simultaneously decreases the solar heated cross-sectional surface area of the IPV.

5.1.2 IPV Structures Subassembly

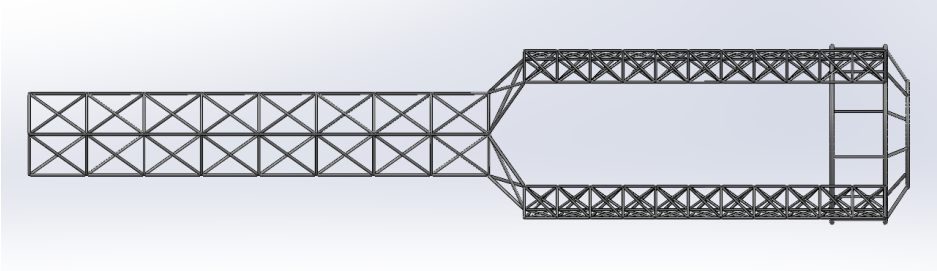

Figure 5.5: Truss Structure Subassembly

Figure 5.5 shows the subassembly of the truss structures for the Inter-Planetary Vehicle. From left to right, the truss sections are the following: the main truss, the connection truss, the triangular trusses, and the engine thrust structure.

To connect the truss sections together and to the rest of the vehicle, the main truss section has connections at the left side to join the Habitat, and has 8 sections on its sides where the EDT, MCT, and MDT will connect to. There is be 4 connections at the right side of the main truss for the connection trusses to attach to. The connection truss has 8 connections to the near side of each of the triangular trusses. Finally, the triangular trusses connect to both of the large ring trusses on the engine thrust structure.

To assemble these trusses in orbit, the method that is chosen is ultrasonic spot welding. Each truss joint is fused via the ultrasonic spot welder on the assembly vehicle. For more details on the assembly methods and sizing for the truss sections, refer to the Assembly and Structural Design Sections (Section 6.3).

The engine thrust structure is not assembled in orbit, and will be assembled with the Harmonia Nuclear Thermal Rocket Engines and the Orbital Maneuvering System Engines on the surface of the Earth. This is detailed in Launch 6 of the Launch Packaging Section.

5.1.3 IPV Power System Subassembly

The IPV has the capability to generate power via two methods: solar arrays and a bi-modal Brayton cycle. The solar panels are located (colored yellow) in front of the pro-

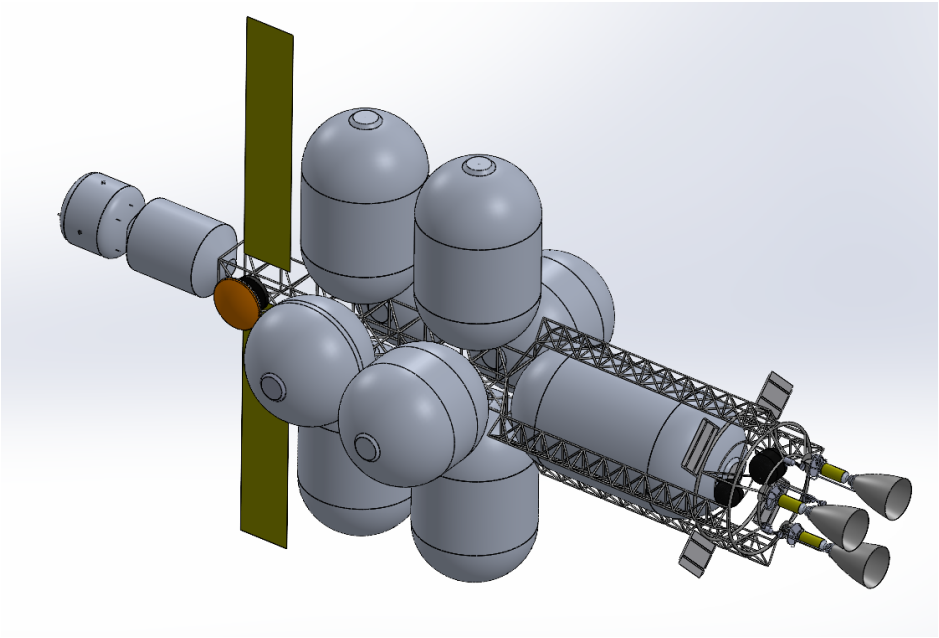

Figure 5.6: IPV Power Generation

pellant tanks with a total 198 m^2 with the capability to produce more than 35 kWe. The solar panels are meant to serve as backup power generation in case of total engine failure. The main power generation technique aboard the IPV is a bimodal Brayton cycle. A XeHe mixture is run through the reactor within the engines (as a part of a Brayton cycle) located at the aft of the ship to produce 25.16 kWe. Both power generation techniques and a full power management and distribution diagram are located in Section 11.

5.1.4 Thermal Control Subassembly

Throughout the mission, heat is produced by many of the operational systems within the IPV and from the crew, which requires continuous dissipation in order to prevent excessive temperature rise within both the habitable zones in the IPV and critical high-temperature locations prone to melting. In order to prevent this catastrophic build-up, thermal energy must be transferred away and then dissipated. A collection of active thermal control systems (ATCS) is required to ensure that critical components in the IPV and the crew remain at acceptable operational temperatures. The thermal control systems use

fluids mechanically pumped along closed loops in order to collect, transport, and reject heat generated throughout the IPV. Analysis of the resulting ATCS and the respective subcomponents is presented in Section 10.

Radiator Placement

A series of radiators are required for heat rejection of power cycles and habitat volumes. These include radiators for the bimodal power cycle on the IPV, as well as for the DEV's power cycles. The DEV has two separate reactors used for power generation, which therefore requires two separate radiators. In addition, radiators are required for habitat volumes to regulate solar irradiation, which would heat these volumes without ceasing if their are no radiators to cool these spaces. All of these radiators can be seen in Fig. 5.7 with appropriate labels. The number in parentheses next to these labels shows how many of the given radiator is shown deployed in this figure.

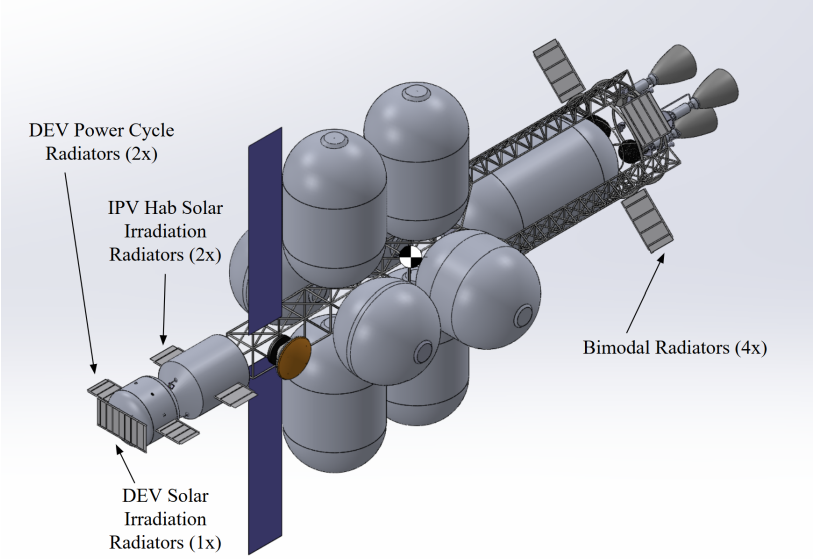

Figure 5.7: Placement and Labeling of All Radiators

A key factor when considering radiator placement are the radiators' view factors. These include view factors between the radiators themselves, as well as view factors with the propellant tanks. If there are view factors between radiators, then these radiators radi-

ate into each other, decreasing their effectiveness in rejecting heat. Given this, all radiators on the IPV are designed to have no view factors with each other, which is made possible using insulation on some radiators. In Fig. 5.8, radiators are shown in a side-view of the IPV, with yellow lines representing insulated regions, and red arrows representing the normal direction of radiation from a given radiator.

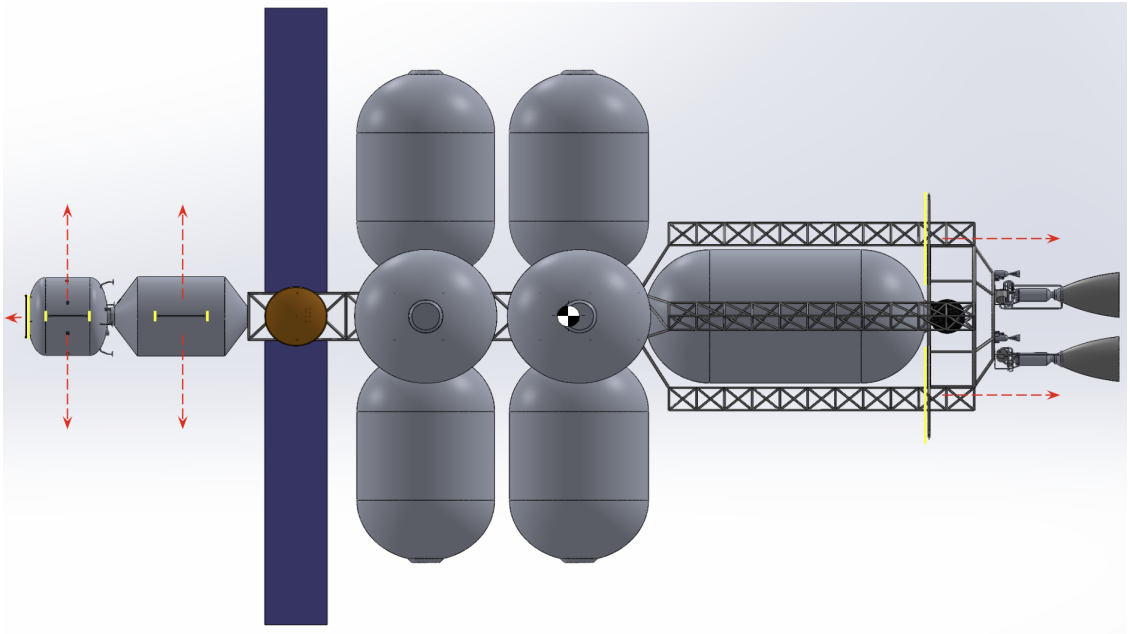

Figure 5.8: Location of Insulation on Radiators

As shown in this diagram, radiators do not have a view factor with each other, which is optimal for maximizing the effectiveness of radiative heat transfer. However, insulation is needed to prevent view factors with tanks. This is required as if radiation heats up these tanks, boil-off effects will become much worse, which would significantly increase the mass of the tanks given they would need more propellant to counter this effect. As such, a high-temperature MLI is used to insulate the sides and faces of radiators so that they do not radiate into tanks. This is especially important for the bimodal radiators, which operate at high temperature, and face backward toward the tanks. Without the use of this high-temperature MLI, there would be significant boil-off consequences.

For the IPV Hab solar irradiation radiators and DEV power cycle radiators, insulation

is placed on the sides of the radiators to prevent radiation from these radiators hitting tanks. This is visualized in Fig. 5.9, which shows that radiation coming from the radiator does not hit propellant tanks, as indicated with the dashed green lines.

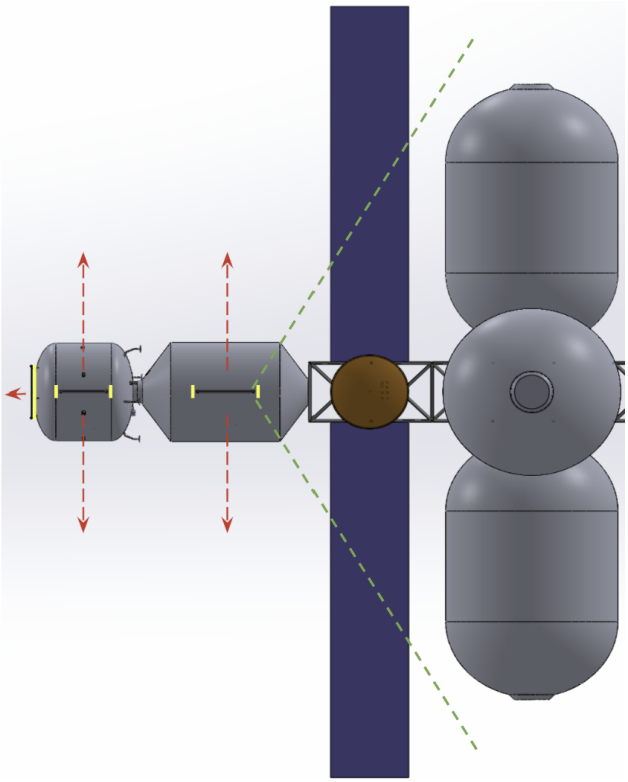

Figure 5.9: Close-Up of IPV Habitat Radiators and Their View Factors

All radiators are positioned such that they do not face the sun during transit between Earth and Mars. This is critical to ensure that the radiators are only rejecting heat from the system they connect to, and not from the sun as well, to maximize their efficiency. This can be seen in Fig. 5.8, where the solar panels (blue rectangles in figure) point towards the sun, as they must in order to generate power, whereas the radiators do not. Given this placement, only the very top edge of the radiator is exposed to solar irradiation, which is negligible.

It is important to note that the DEV power cycle radiators are arranged in such a way that they will be effective in Earth-Mars transit, as well as when landing on Deimos. This is because they will not be pointing towards the sun in transit, nor when landed on Deimos,

and do not interfere with landing legs.

Additional information on radiators and their analysis can be found in Section 10.4.

Multilayered Insulation

While not directly part of the ATCS, another key component that is further analyzed in section 10 below in the report is the Multi-layered Insulation (MLI) surrounding the DEV, HAB and cryogenic tanks. Solar thermal radiation absorbed by the IPV during transit comprises the majority of thermal energy required to be dissipated in order to store the cryogenic propellant and keep the resulting crew alive for the length of the mission. As a result, MLI shielding is a crucial component for mission success as it significantly minimizes the amount of thermal energy imparted to the IPV. This section of shielding is comprised of many thin alternating layers of a highly reflective, low absorptive material and a highly insulating mesh, as shown in Figure 5.10, and results in a significant decrease in the solar thermal radiation absorbed by the IPV.

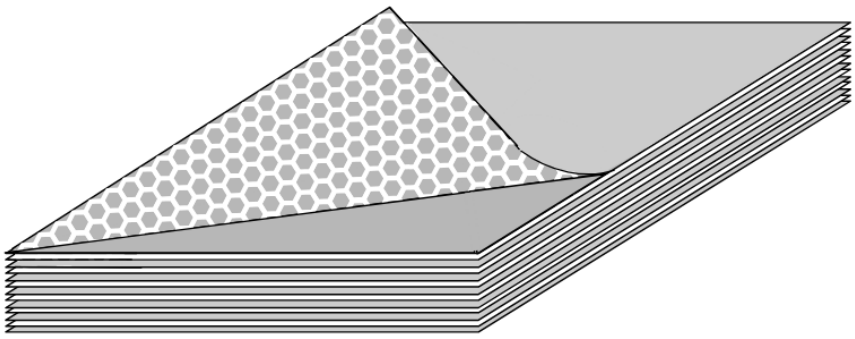

Figure 5.10: MLI Diagram

Radiation Shielding

The radiation shielding provides the crew of the IPV protection from the harmful radiation environment in deep space. The radiation shielding consists of a water wall solution with polyethylene bags held in place via a semi-rigid grid structure. This shielding signif-

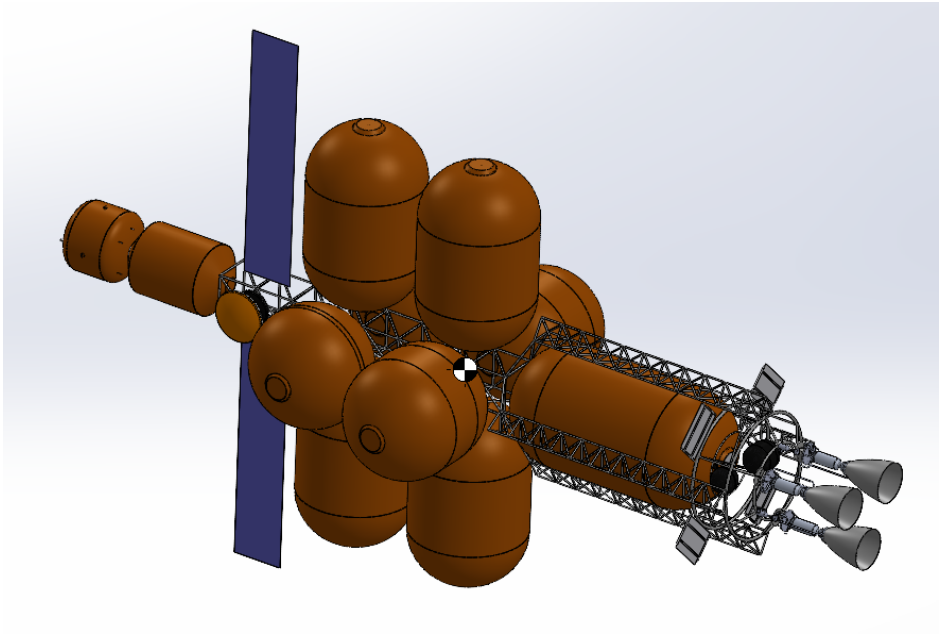

Figure 5.11: Enter Caption

icantly limits the radiation dosage absorbed by all electronics and crew members inside of the IPV and DEV during mission operation. The locations for the habitable volumes of the IPV habitable space and the DEV are highlighted in green in Figure 5.12

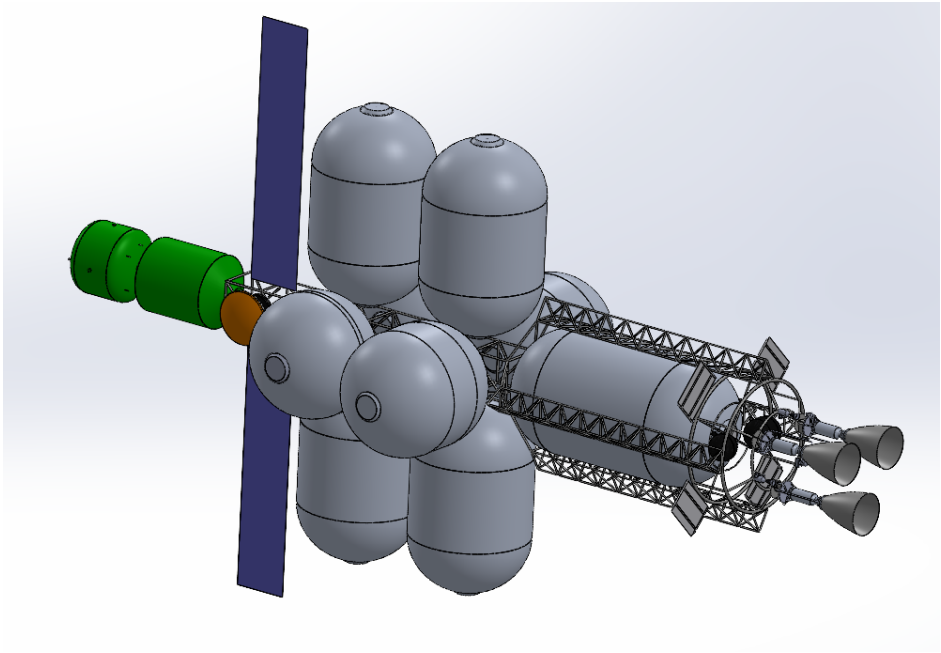

Figure 5.12: Radiation Shielding: Highlighted in Green

5.2 Critical Dependencies

The flow diagram (Figure 5.13) depicts the critical dependencies that have been identified for the mission architecture.

As human safety is paramount during the mission, the dependency diagram is centered around the nominal operation of the DEV and IPV Hab, which require both power and adequate heat rejection to maintain crew safety. The key critical path identified is the bimodal propulsion subsystem, as it must provide the primary source of power to mission-critical systems for the entire duration of the mission. On a systems level, nominal function of the Active Thermal Control Systems (ACTSs), life support recycling systems, and avionics is directly dependent on the functioning of the power generation subsystems. Therefore, it is essential that the mission architecture incorporate reliable, failure-tolerant, and redundant power generation systems.

5.3 Habitable Spaces

The habitable space for the DEV and the IPV are connected during interplanetary travel via an airlock. Both habitable volumes have three types of shielding: radiation, MLI, and MMOD, shown with dimensions in Appendix A.4. Radiation shielding is discussed in Section 12.4. MLI is discussed in Section 5.1.4. MMOD shielding is discussed in Section 8.8.

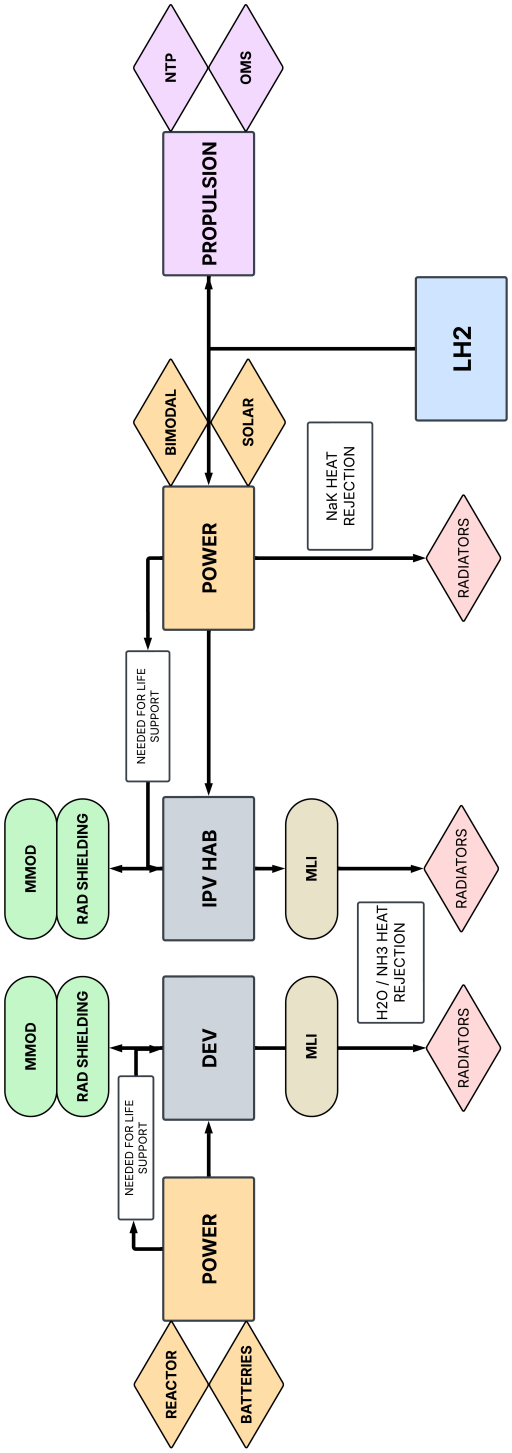

Figure 5.13: Critical Dependencies Diagram

Combined Functional Space	Minimum volume - 2 crew	Minimum volume - 4 crew
Exercise-1 (cycle ergometer)	–	6.12
Exercise-2 (treadmill)	3.38	3.38
Exercise-3 (resistive device)	2.8	3.92
Group social-1 (open area) / mission planning-3 (training)	9.1	18.2
Group social-2 (Table) / Meal consumption / mission planning-1 (Table)	5.05	10.09
Human waster-1 (waste collection)	1.18	2.36
Human waster-2 (cleansing) / hygiene-1 (cleansing)	2.18	4.35
Logisitcs-2 (temporary stowage)	–	6
Maintenance-1 (computer)	3.4	3.4
Maintenance-2 (work surface) / logistic-1 (work surface)	2.41	4.82
Meal preparation - 1 (food prep)	2.18	4.35
Meal preparation - 2 (work surface)	3	3.3
Medical - 1 (computer)	1.2	1.2
Medical - 3 (medical care)	2.7	5.8
Mission planning-2 (computer/command) / spacecraft monitoring	3.42	3.42
Private habitation-1 (work surface) / medical-2 (ambulatory care)	8.7	17.4
Private habitation-2 (sleep & relaxation) / hygiene-2 (non-cleansing)	6.98	13.96
Waste management	3.2	3.76
Total minimum NHV	60.87	115.83
Minimum NHV per crew	30.44	28.96

Table 5.1: Habitable volume breakdown

5.3.1 DEV

The DEV is designed to deliver 2 of the astronauts from the IPV in Mars Parking Orbit to the surface of Deimos, and provide them with a habitat for the 135 day surface stay. The design provides proper living conditions, allow the astronauts to conduct research, and be able to transport through space using a propulsion system. There are several vehicle design concepts that are considered for the DEV. Figure's 5.14 and 5.15 show some of options that are contemplated.

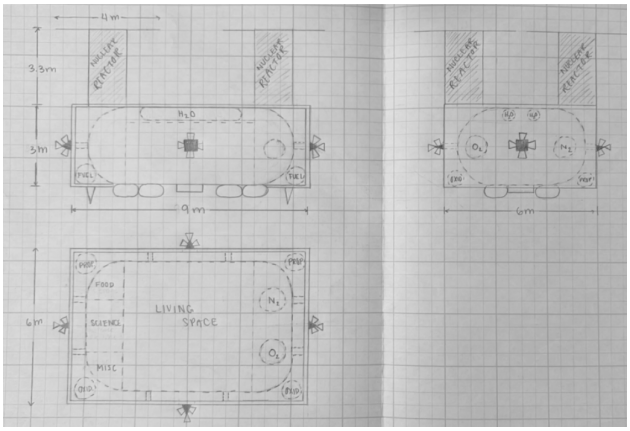

Figure 5.14: Option not chosen for DEV design

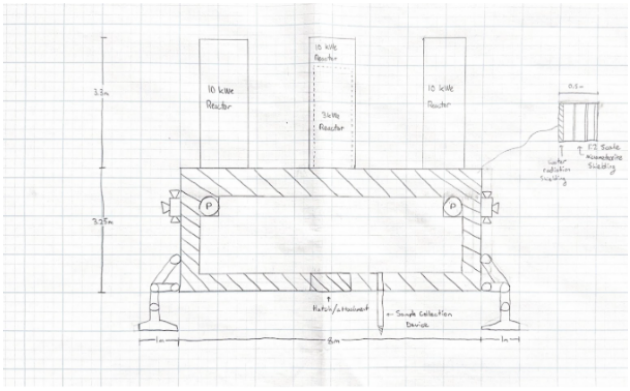

Figure 5.15: Option chosen for DEV design

The DEV needs to easily maneuver and rotate, thus a relatively simple design without any unusual shapes is chosen. For this reason, the design must be symmetrical about the central axis. Additionally, it must be possible to easily pressurize the volume for habitability. Therefore, a cylindrical shape is chosen for the vessel structure. The moments of inertia around the y axis and the x axis tend to be identical for cylinders as seen in Figure 5.16.

Space vehicles follow the 3-1-3 Euler angle sequence. Having a symmetrical shape such as a cylinder allows for simpler attitude control and calculations. Although a simple cylinder would work theoretically, the shape needs to be capable of being pressurized. This means that if it remains only a cylinder, the sharp edges of a cylinder will become stress concentrations,resulting in the vessel possibly fracturing. In order to prevent this

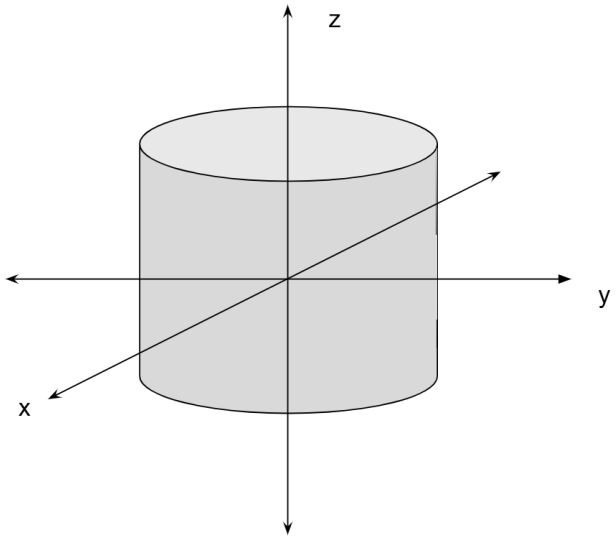

Figure 5.16: Option not chosen for DEV design

from happening, elliptical caps replace the flat sides of the cylinder as seen in Figure 5.17.

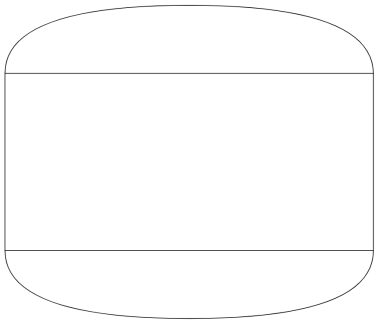

Figure 5.17: DEV habitat shape

Once pressure vessel's shape is been decided upon, the dimensions of the DEV can be determined.

The biggest focus for sizing the DEV is finding the habitable and storage/systems volumes needed for the crew's mission. Since this trip will be long term, an appropriate habitable volume is needed for the crew to live and work. Using the study for habitable volume on long duration missions done by researchers at NASA JSC, a minimum habitable volume of 28.96m^3 is needed per person for a mission of 4 crew members [40]. Using this information, the minimum required volume for two crew members is derived to be

about 30.44m^3 per crew member totaling to a minimum of 62.17m^3 for the DEV's habitable volume. This is determined using the data used in the study for 4 and 6 crew mates. The goal is to minimize the volume as much as possible while still providing the proper livable volumes for the crew. The break down of the habitable volume is seen in Table 5.1.

For the mission of 2 crew members, two functional spaces in the the study are determined to be unnecessary. The first is Exercise - 1 (cycle ergonometric). Although in most cases it is recommended to have a some type of device specific to support ergonometric exercise, the other two exercise devices can provide the same benefits. A treadmill will provide the astronauts with aerobic exercise while also providing the astronaut with bone loading and sensorimotor conditioning. The resistive device is needed for resistive exercise which the treadmill does not provide. Therefore, only the treadmill and resistive device are needed for the astronauts to fulfill their fitness requirements. The second functional space that is not included in the DEV's habitable volume is the logistic - 2 (temporary stowage). Due to the shape of the DEV, all storage, including temporary stowage will be located in the elliptical caps of the DEV. This storage will be easily accessible through a latch in the floor of the DEV.

The habitable volume is restricted to the cylindrical part of the DEV, and storage is within the elliptical caps. However, the cockpit cuts into the storage volume, taking away 1.76m^3 of volume. The cylinder has also been extended to increase storage space. The cylindrical volume is determined using Equation 5.1.

$$V_{cylinder} = \pi r^2 h \tag{5.1}$$

The final dimensions can be seen in Table 5.2.

The total habitable volume comes out to 2.06m^3 more than the minimum required habitat for a total of 62.05m^3. As for storage, that is calculated using the formula from Equation 5.2.

Variable	Dimension	Units
R_{DEV}	2.70	m
$h_{cylinder}$	2.60	m
$V_{cylinder}$	59.55	m^3
$V_{passage}$	0.76	m^3
$V_{cockpit}$	1.74	m^3
$V_{habitable}$	62.05	m^3

Table 5.2: Habitable volume dimensions

$$V_{ellipse} = \frac{4}{3}\pi abc \tag{5.2}$$

Where a and b are the semi-major axes and c is semi-minor axis. These values are seen in Table 5.3. Due to the size of the water supply and other pieces of equipment, the bottom storage has been increased to include more volume. This is done by elongating the cylindrical portion of the DEV to a total height of 3.2m where 0.6m of that height contributes to storage and the rest to habitable volume. This is reflected in Table 5.3

Variable	Dimension	Units
a	2.70	m
b	2.70	m
c	1.00	m^3
$V_{storage}$	44.28	m^3
V_{total}	41.78	m^3

Table 5.3: Storage/systems volume dimensions

The resulting design of the DEV living and storage volume, developed using CAD, is shown in Figures 5.18 and 5.19.

Now that the shell is designed, some of the DEV's features are developed. The final DEV CAD is seen in Figures 5.20 and 5.21. A cut out of the DEV with an interior view is seen in Figures 5.22, 5.23, and 5.24.

Beginning with the exterior, there are a limited number of items located on the outside of the DEV. The radiators must be located on the outside due to heat radiation which will be discussed more in the Thermal Control section of the report. The other items located

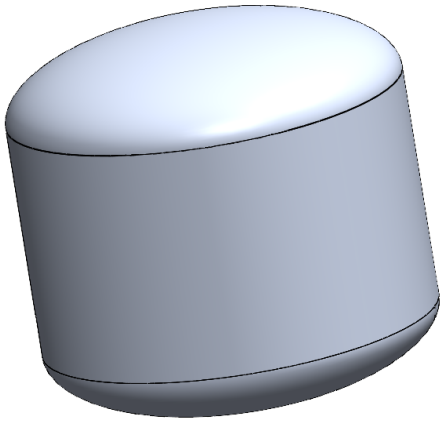

Figure 5.18: DEV habitable volume shell CAD

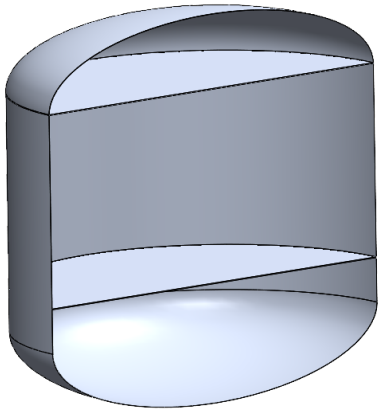

Figure 5.19: DEV habitable volume CAD cut out view

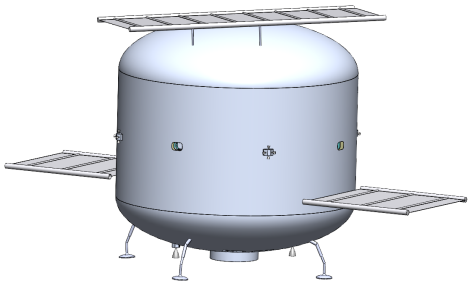

Figure 5.20: Final DEV CAD side view

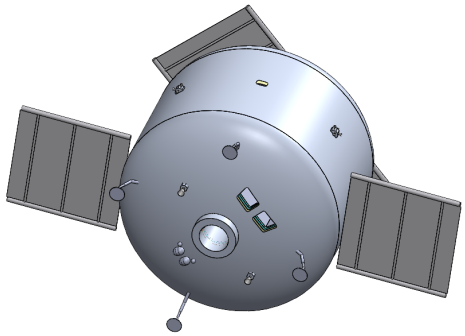

Figure 5.21: Final DEV CAD bottom view

on the exterior include: propellant tanks, MDE, RCS thrusters, docking port, and legs.

The propellant is moved outside due to the health risk they would impose on the crew if inside the habitat. Both MMH and N_2O_4 are highly toxic and should have no direct contact with people. Keeping them on the outside of the DEV is crucial for the crews health and safety. Since they are outside of the DEV, they are properly shielded with micrometeorite and radiation shielding. The size of the tanks are minimal enough, so building an entire service module like on Orion (the ESM) would add undesired additional mass.

The MDEs are located on the bottom of the DEV. They are space 2.48m apart, 1.24m from the center of the DEV. Having two engines is crucial for the safety of the crew. If one engine fails, there needs to be a back up in order for the crew to not become stranded. However, with two engines, a problem that would be encountered is with only one engine

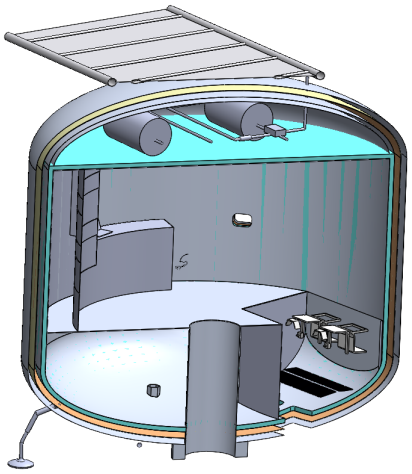

Figure 5.22: Final DEV CAD side view

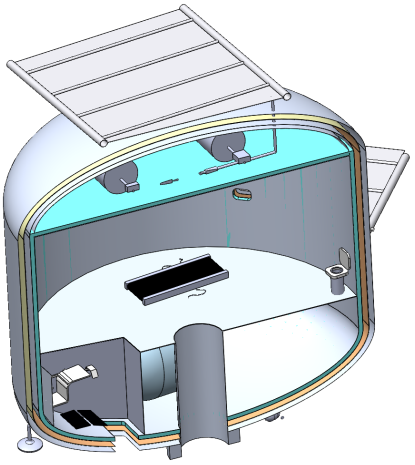

Figure 5.23: Final DEV CAD bottom view

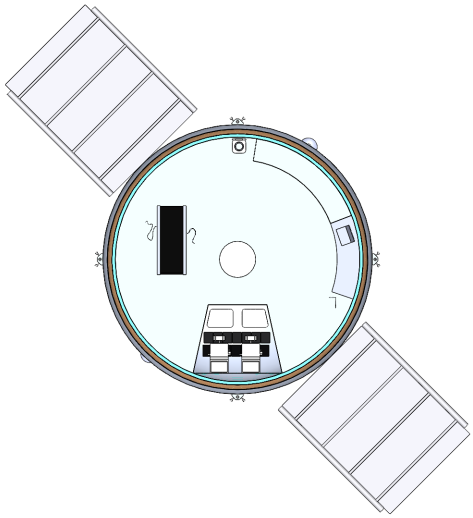

Figure 5.24: Final DEV CAD bottom view

thrusting, a moment is created. To counteract this, an RCS engine will be used. The goal is to have the sum of moments at the center of mass to be zero when not rotating. A moment calculation is done to determine the distance at which the MDE must be located at. Solving Equation 5.3 results in a value of 1.24m.

$$\sum M_0 = 0 = r_{MDE} \times F_{MDE} + r_{RCS} \times F_{RCS} \tag{5.3}$$

Where M_0 is the moment about the center of gravity, r_{MDE} is the perpendicular dis-

tance between the MDE and center of mass, F_{MDE} is the thrust of one of the MDEs, r_{RCS} is the perpendicular distance between the RCS and center of mass, and F_{RCS} is the thrust of one of the RCS thrusters at the same place but opposite side of the DEV. These values are seen in Table 5.4, along with the resulting location of the MDE.

Variable	Dimension	Units
F_{RCS}	200	N
r_{RCS}	3.10	m
F_{MDE}	500	N
r_{MDE}	1.24	m

Table 5.4: MDE and RCS thruster locations from moment calculation

The RCS thrusters are located about the center of mass, evenly distributed about the exterior of the DEV which can be seen in Figure 5.18 and 5.19. There are a total of 16 RCS thrusters. The 16 thrusters are divided into four groups with four thrusters in each group. Two thrusters are pointing opposite directions vertically, one pointing towards the top (direction of nuclear reactor) and the other towards the bottom (same direction as the MDEs). The remaining two are pointing outward at a $90°$ from each other and $45°$ tangent to the DEV's shell. The vertical thrusters allow for rotations about the x and y-axes and precise up and down movements. The remaining two thrusters will be used for rotations about the z-axis and sideways movements. A closer look at the RCS configuration is seen in Figure 5.25.

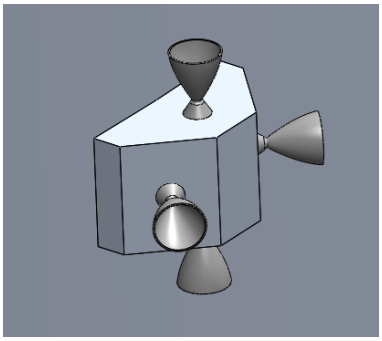

Figure 5.25: RCS thruster configuration on DEV

The ultimate goal of the RCS thrusters is to allow 6 degrees of freedom which this

thruster design fulfills.

The docking feature is the same as the docking system used on the IPV. The docking is located underneath the DEV since the radiator is located on the top of the vehicle. Since the docking is located on the same side as the MDEs and due to the need for precision, only the RCS thrusters will be used for the docking process. The chosen docking system will be discussed further in the assembly section.

Lastly, for the exterior of the DEV, there are four legs located on the bottom of the vehicle. These legs are mainly for redundancy due to the lack of gravity on Deimos's surface. Unlike the Lunar Lander that needed legs that would support the weight of the vehicle, the lack of gravity on Deimos means that there will be no weight needing to be support. Therefore, that will not be the main responsibility of the legs, instead they are there for protection purposes. If the DEV accelerates too fast when approaching Deimos and hits, the legs are there to prevent damage to the vehicle. Important equipment such as the docking port, MDE, propellants, and sensors are located on the bottom of the DEV, making them more susceptible to getting damaged when touching down on Deimos' surface. Additionally, the implementation of the FTIR probes into the legs allows scientific operations while Deimos is in contact with the lunar surface. Landings will be done using RCS thrusters, so it is not expected that rough landings will occur; however, there are times that this problem could arise.

Connecting exterior to interior, there are a total of six windows on the DEV. The largest and most important are the windows on the bottom of the DEV. These windows can be seen in Figure 5.21, located adjacent to the docking port. Inside, they are located in the cockpit. It is important for the crew to see the docking and undocking process without needing to rely on cameras. Cameras have the possibility to malfunction and stop working so having windows is crucial. There are four other windows located around the exterior of the habitat. From NASA's *Deep Space Habitability Design Guidelines Based on the NASA NextSTEP Phase 2 Ground Test Program*, for long term missions, only one viewing window is

needed [41]. Since the bottom windows will be able to only see the ground, more windows are added to increase outside visibility. These windows allow for a nearly complete 360° view around the spacecraft. As seen in the DEV, the windows measure 0.2m by 0.3m. In order to minimize risk, these windows are made purposefully small. Larger windows are more likely to get damaged, and shielding becomes difficult for both micrometeorites and radiation. These windows will be made up of the same makeup as the windows on Orion. The windows are made up of three layers: fused silica thermal pane, an acrylic pressure pane and a redundant pane [42]. The windows on Orion have been rigorously studied and tested at NASA and they are a strong choice for the DEV.

5.3.2 IPV

The IPV habitable space will stay connected to the IPV throughout the duration of the mission. During excursions to Deimos, the two crew members not descending to the surface will remain in this space. Two configurations were considered for the IPV habitable space: one that creates artificial gravity, shown in Figures 5.27 and 5.26, and one that does not, shown in Figures 5.28 and 5.29. The concept that creates artificial gravity is not chosen due to its high level of complexity compared to the other concept. Drugs to combat bone density loss during extended space missions are proven to be effective and are currently used, so creation of artificial gravity for the purpose of combating bone density loss is not necessary.

The capsule is divided into three sections: mission-related tasks, non-mission-related tasks, and storage. The total volume of the habitable space is $172m^3$. The internal diameter is $5.5m$ and the internal overall height is $8.98m$. The decision making process for the overall shape follows the same process as the DEV. The mission-related section contains seats for the crew members while the IPV is thrusting. It contains all scientific and technical equipment necessary for the mission. There is a window that overlooks the docking area, seen in Figures 5.30 and 5.31, made of fused silica thermal pane with an acrylic

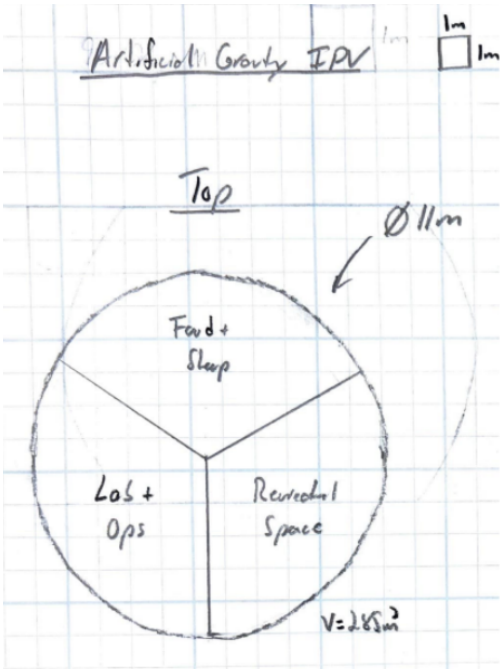

Figure 5.26: IPV Habitable Space Concept With Artificial Gravity - Internal View

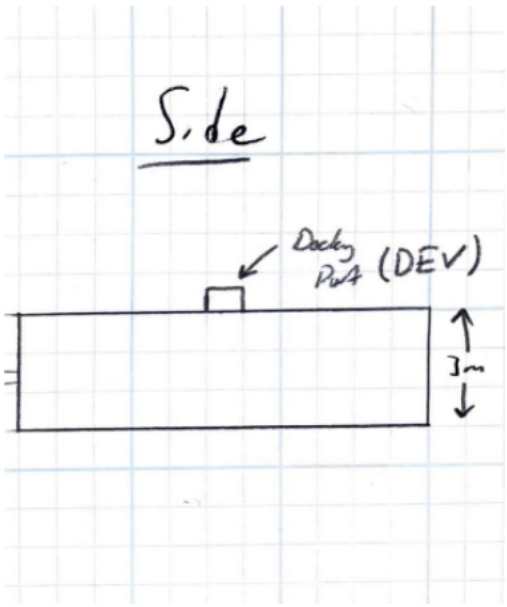

Figure 5.27: IPV Habitable Space Concept With Artificial Gravity - External View

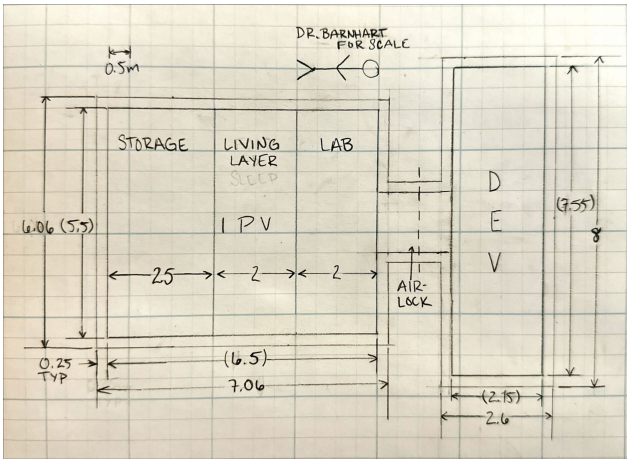

Figure 5.28: IPV Habitable Space Concept Without Artificial Gravity - External View

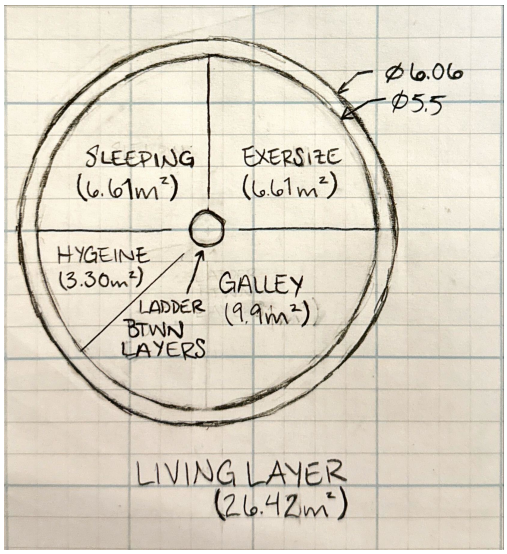

Figure 5.29: IPV Habitable Space Concept Without Artificial Gravity - Internal View

pressure pane and a redundant pane, in the same manner as the DEV window. The non-mission section consists of a sleeping area, a personal hygiene area, and space for social activities, exercise, food-related tasks, and medical tasks, as shown in Figure 5.34. The area amounts dedicated to each task was determined in the same manner as the DEV, dis-

cussed in Section 5.3.1. The storage section contains food storage. Between the sections, there is a pass-through allowing the crew members to easily move between sections.

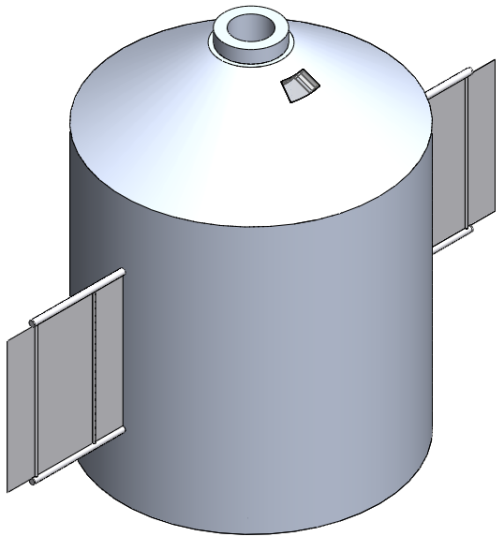

Figure 5.30: IPV Habitable Space Exterior Isometric View

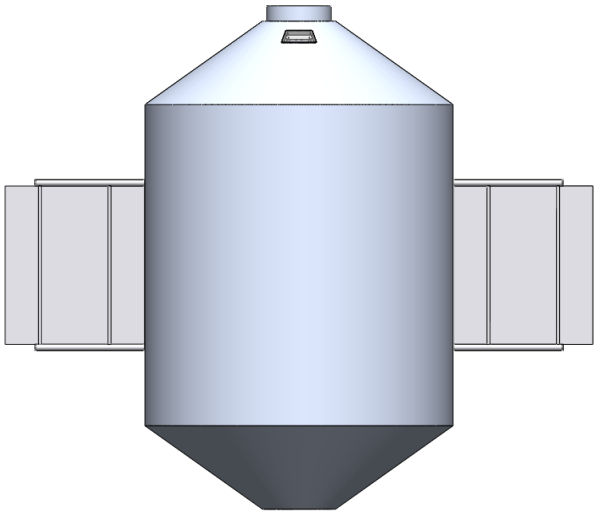

Figure 5.31: IPV Habitable Space Exterior Side View

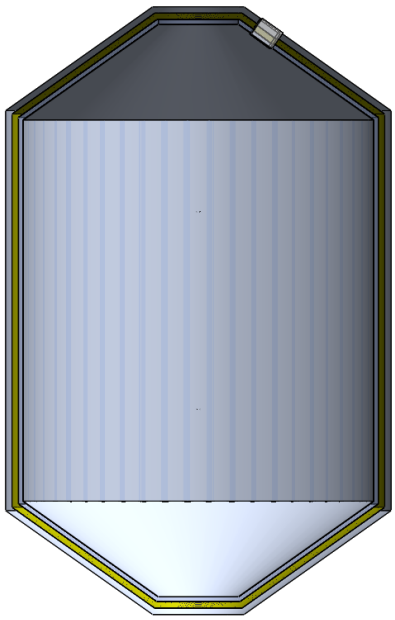

Figure 5.32: IPV Habitable Space Cross Section

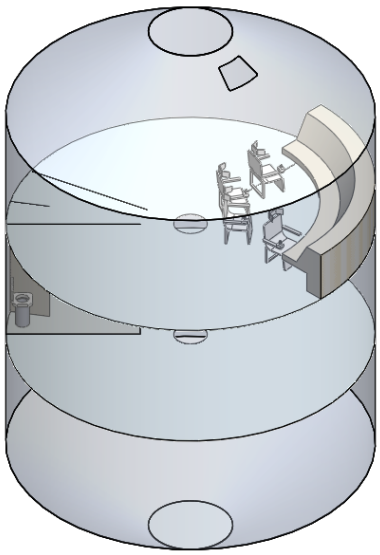

Figure 5.33: IPV Habitable Space Internal Isometric View

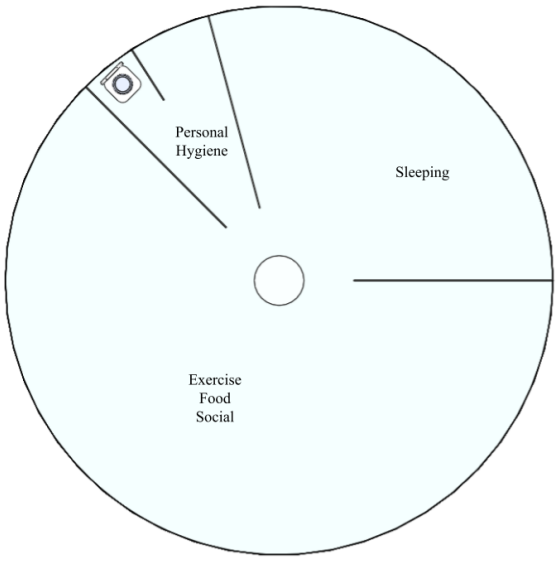

Figure 5.34: IPV Habitable Space: Internal View of Non-Mission Area

5.4 Mars Surface Assets

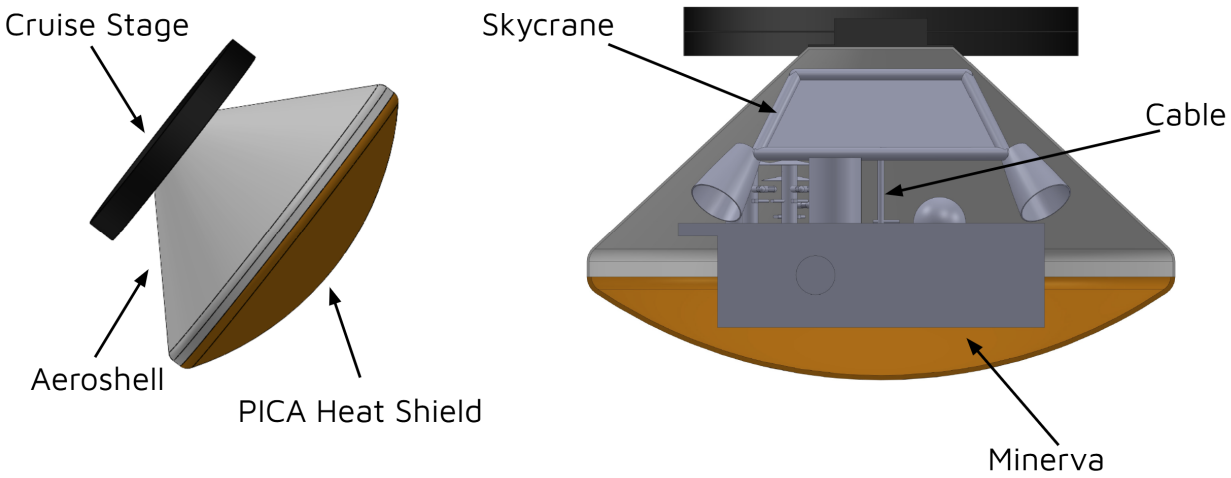

Figure 5.35: Mars Surface Assets

The mars surface assets can be seen above in figure 5.35. Details on each individual component can be found in Sections 14.1.2 , 14.1.5, and 14.1.7. The expected masses are detailed in Table 5.5.

Component	Mass (mT)
Heat Shield	0.13
Aeroshell	1.19
Cruise Stage	0.57
Skycrane	1.37
Rover	0.70
Total	3.96

Table 5.5: Detailed Masses of the Components of the Mars Surface Asset

The ΔV calculated in 16.6 is within margins for the cruise stage. The cruise stage's purpose is to handle the interplanetary trajectory, making course corrections as necessary. It is modeled after the Curiosity rover cruise stage. The Mars assets are contained within the aeroshell and PICA heat shield, as discussed in 14.1.2. The rover will then be transported to the Martian surface using a skycrane.

5.5 Mass Budgets

A full mass breakdown of the unfueled interplanetary vehicle at Earth departure can be found in Table 5.6. This mass breakdown is divided into the subsystems of the IPV, and more detailed breakdowns of these individual subsystems can be found later in this section. Additionally, although this mission uses 6 SLS launches, the total mass of the IPV, and the number used to calculate the necessary mass of propellant, is 750 mT, or 5 SLS launches. The mass provided by the sixth launch is used for any systems that must be launched but will not be part of the IPV at Earth departure. This includes but is not limited to, Orion capsules, the LEO assembly vehicle and assembly equipment, life support for the assembly crew, payload adapters, and any structural supports within the fairings during launch. The addition of the sixth launch also allows for the components to be packaged within fairings of a reasonable height.

Total Fueled IPV Mass at Departure = 750 mT		
Total LH_2 Propellant Mass = 508.5 mT (66.2 Percent of Total)		
Component	**Mass (mT)**	**Percent of Total Dry Mass**
Engines (NTP + OMS + OMS Propellant)	40.71	16.9
Structure	18.30	7.6
DEV	20.47	8.5
IPV Hab	16.74	6.9
Propellant Tanks	82.35	34.0
Life Support	24.14	10.0
Power/Heat Rejection	5.55	2.3
TMSA	4.00	1.7
Margin	31.62	12.2
Total Dry Mass No Margin	212.1	

Table 5.6: Total Dry Mass Breakdown.

5.5.1 DEV Mass Breakdown

Table 5.7 shows the detailed mass breakdown of the Deimos Excursion Vehicle without life support supplies. The mass primarily comes from propulsion systems, shielding, and power systems.

Mass does not include life support supplies(food, water, etc.)		
Component	**Mass (mT)**	**Percent of Total Mass**
Propulsion Systems + Propellant	1.66	8.1
Pressure Vessel Structure	1.28	6.3
Nuclear Power Systems	3.40	16.6
Supplimental Batteries	3.50	17.1
Radiation Shielding	6.93	33.9
MMOD Shielding	3.70	18.1
Total Mass	20.47	

Table 5.7: DEV Mass Breakdown.

5.5.2 IPV Habitat Mass Breakdown

Table 5.8 shows the detailed mass breakdown of the Interplanetary Vehicle Habitat without life support supplies. The mass primarily comes from shielding, both radiation and micrometeoroid.

Mass does not include life support supplies(food, water, etc.)		
Component	**Mass (mT)**	**Percent of Total Mass**
Radiation Shielding	11.47	68.5
MMOD Shielding	1.87	11.2
Pressure Vessel Structure	2	11.9
Water Recycling System	1.39	8.3
Total Mass	16.74	

Table 5.8: IPV Habitat Mass Breakdown.

5.5.3 Propulsion Systems Mass Breakdown

Table 5.9 shows the detailed mass breakdown of the propulsion systems for the IPV. This broken into two major engines: the nuclear thermal engine and the orbital maneuvering engine. Additionally, mass for piping both within the nuclear thermal engine as well as for fuel and ullage are specified.

Component	**Mass (mT)**	**Percent of Total Mass**
Core	1.79	4.40
Inner Reflector	.47	1.15
Outer Reflector	3.25	7.98
Turbomachinery	.29	.71
Nozzle	.90	2.21
Structure	.40	.98
Valves/Piping	.15	.37
Ullage/Propellant Piping	.33	.81
OMS Engine + Propellant	19.46	47.80
Total Mass	40.71	

Table 5.9: Propulsion Systems Mass Breakdown.

5.5.4 Power and Heat Rejection Systems Mass Breakdown

Table 5.10 shows the detailed mass breakdown of the power systems for the IPV. This consists of power systems, such as batteries and solar panels, and heat rejection systems, such as radiators.

Component	Mass (mT)	Percent of Total Mass
Cable Mass	.3	5.41
Radiator Mass	3.40	61.26
Batteries for Bimodal/Thrusting Switch	1.50	27.03
Solar Panels	.35	6.31
Total Mass	5.55	

Table 5.10: Power Systems Mass Breakdown.

5.5.5 Propellant Tank Mass Breakdown

The 4 main propellant tank classes on the IPV are the EDT (4), MDT (2), MCT (2), ECT (1). As detailed in Section 8.4.3, these tanks are constructed in a layered manner, and include a Primary Structure, MLI, and MMOD Shielding. Table 5.11 shows a detailed mass breakdown per layer for each major tank on the IPV.

Layer (mT)	**EDT (x4)**	**MCT (x2)**	**MDT (x2)**	**EDT (x1)**
LH_2	64.25	47.90	34.40	90.05
Primary Structure	3.83	2.53	1.44	6.30
MLI	0.50	0.43	0.34	0.71
MMOD	6.01	4.56	3.19	7.72
Total Mass	73.8	55.3	40.21	101.91

Table 5.11: IPV Major Tank Mass Breakdown

5.5.6 Assembly Components Mass Breakdown

As mentioned earlier in the section, an additional launch is used both to simplify packaging and account for components used during assembly that will be left in low Earth orbit. Table 5.12 shows a detailed mass breakdown of these components.

It is important to note that any extra structural mass needed during launch, such as struts, are not accounted for by this mass budget. However, since the total IPV budget is 750 mT, there is an additional 150 mT for all assembly and launch components provided

Component	Mass (Mass
Assembly Vehicle	4.56
Orion Capsules (2)	66.0
Payload Adapters	7.54

Table 5.12: Assembly and Launch Systems Mass Breakdown.

by the additional sixth launch.

6 Assembly

6.1 Assembly Functional Block Diagram

Below is the Functional Block Diagram for the Assembly subsystem. The subsections are broken into Launch Packaging, Assembly Steps, and Assembly Vehicle.

6. Assembly			
6.1 Block Diagram	6.2 Launch Packaging	6.3 Assembly Steps	6.4 Assembly Vehicle

Table 6.1: Assembly Functional Block Diagram

6.2 Launch Packaging and Timing

The packaging for the first three SLS launches is shown in Figure 6.1 below:

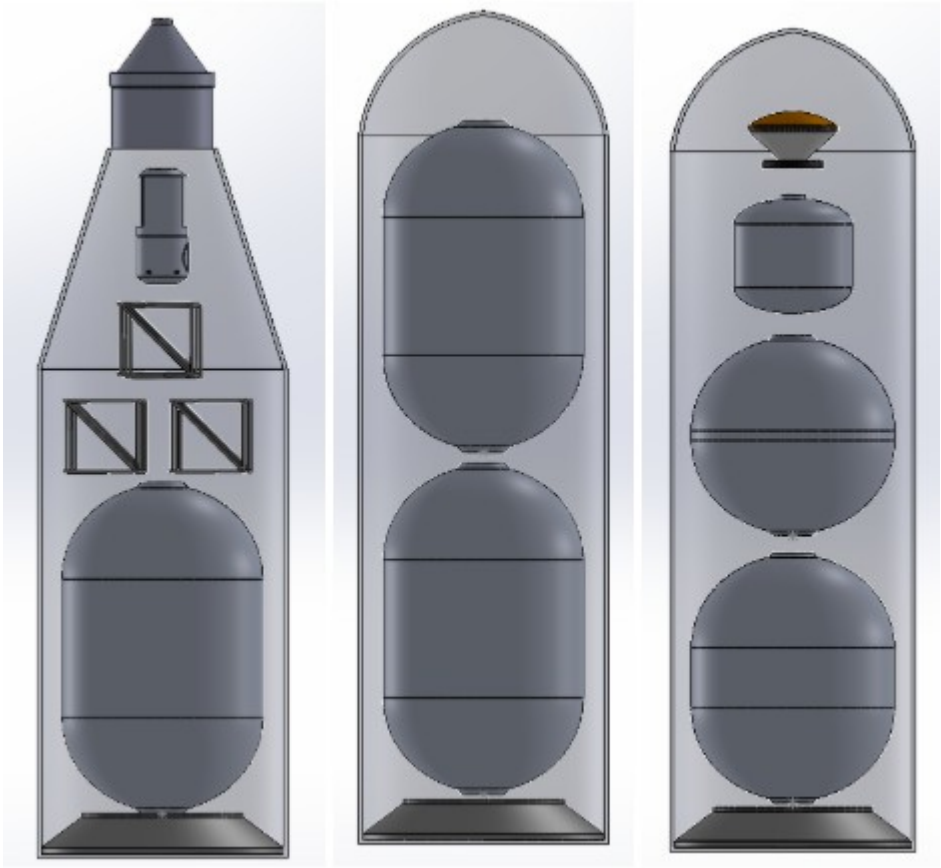

Figure 6.1: SLS Launch 1,2,3

The mass breakdown for each launch is reflected in Table 6.2.

Launch 1		**Launch 2**		**Launch 3**	
Component	**Mass (kg)**	**Component**	**Mass (kg)**	**Component**	**Mass (kg)**
Adapter	1,300.00	Adapter	1,300.00	Adapter	1,300.00
Earth Departure Tank	73,500.00	Earth Departure Tank	73,500.00	Mars Departure Tank	41,000.00
Truss + Structural	9,202.00	Earth Departure Tank	73,500.00	Mars Capture Tank	55,300.00
Assembly Vehicle	4,555.00			DEV	20,000.00
Orion Capsule and ESM	33,000.00			TMSA	4,000.00
Total	**121,577.00**	**Total**	**148,300.00**	**Total**	**121,600.00**

Table 6.2: Mass Breakdown for Launch 1,2,3

The packaging for the last three SLS launches is shown in Figure 6.2 below:

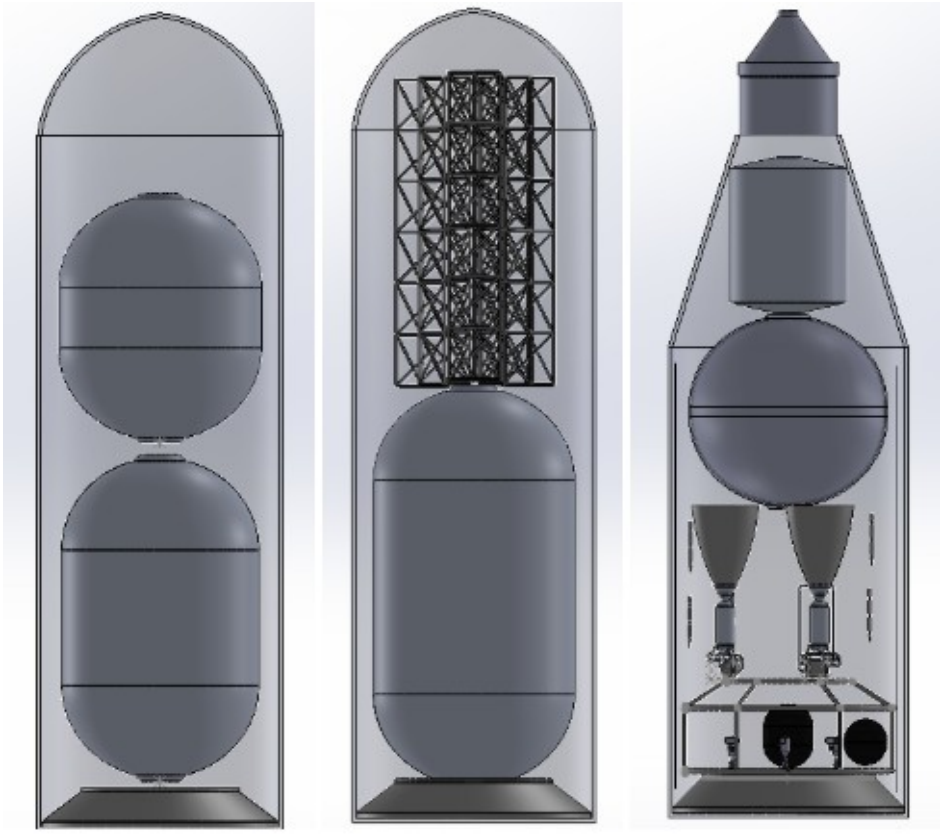

Figure 6.2: SLS Launch 4,5,6

The mass breakdown for each launch is reflected in Table 6.3.

Launch 4		Launch 5		Launch 6	
Component	**Mass (kg)**	**Component**	**Mass (kg)**	**Component**	**Mass (kg)**
Adapter	1,300.00	Adapter	1,300.00	Adapter	1,300.00
Mars Capture Tank	55,300.00	Earth Capture Tank	101,700.00	Engines	22,000.00
Earth Departure Tank	73,500.00	Truss	9,100.00	Mars Departure Tank	41,000.00
Earth Departure Tank	73,500.00	OMS Tanking	17,269.00	Orion Capsule and ESM	33,000.00
				IPV Hab	40,000.00
				Radiators	5,000.00
Total	**130,100.00**	**Total**	**129,369.00**	**Total**	**142,300.00**

Table 6.3: Mass Breakdown for Launch 4,5,6

6.3 Assembly Steps

After the first launch, the assembly vehicle first docks at Orion, then the assembly vehicle and the assembly crew construct the main truss structure as shown in Figure 6.3. This truss structure acts as the centerpiece of the IPV, and all other components are attached to this.

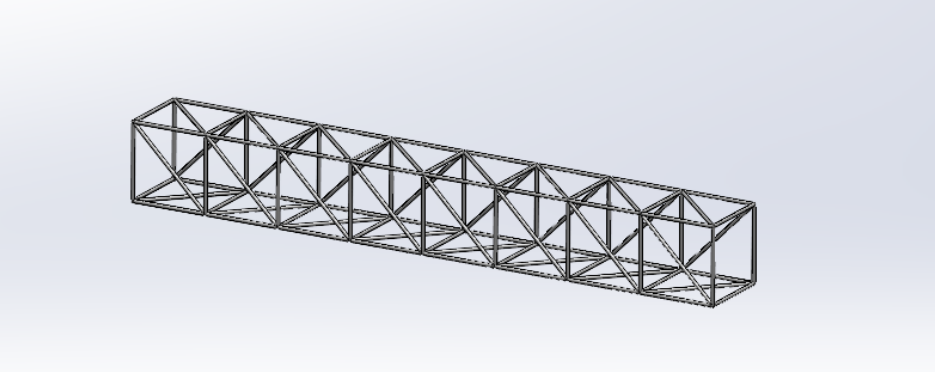

Figure 6.3: Assembly Step 1

Upon completion of the truss assembly, the assembly vehicle docks to the first Earth Departure Tank shown in Figure 6.4 and positions it next to the main truss structure for docking. The assembly crew completes any fine detail connections.

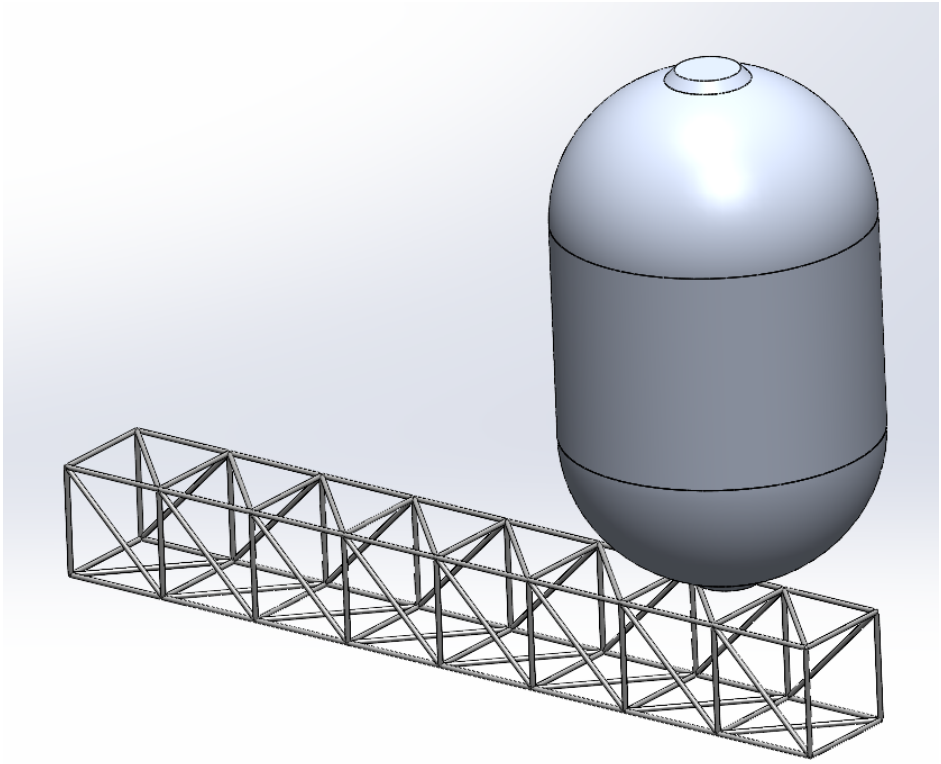

Figure 6.4: Assembly Step 2

This process is repeated for the next two Earth Departure Tanks shown in Figure 6.5.

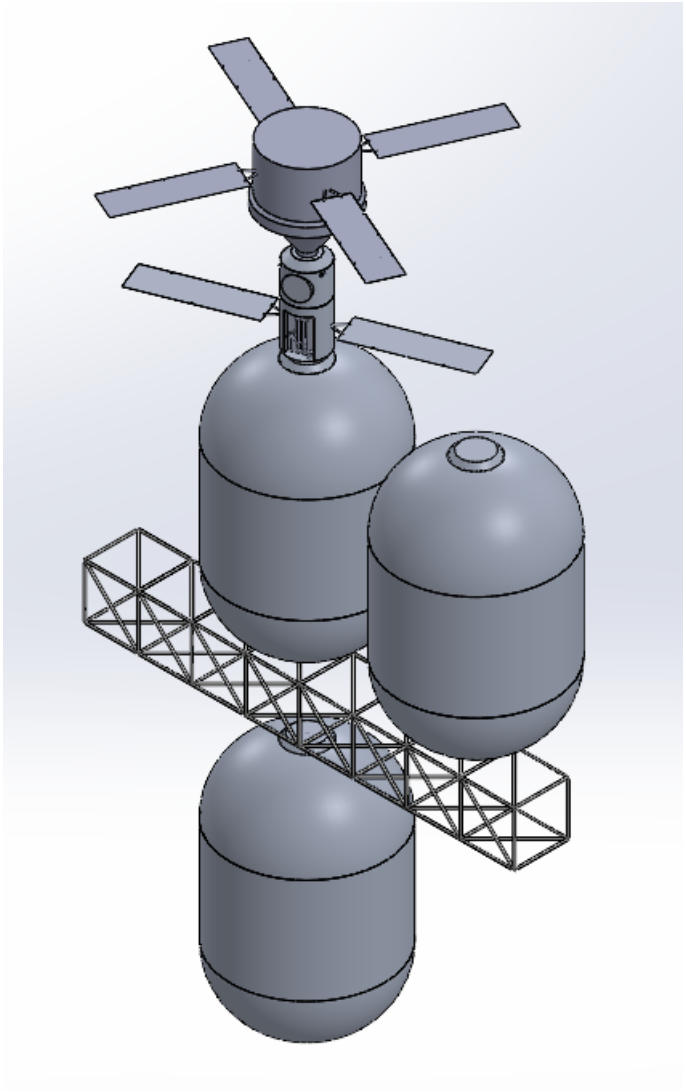

Figure 6.5: Assembly Step 3

Next, the first Mars Departure Tank and the first Mars Capture Tank are similarly assembled. The TMSA is positioned near the main truss structure by the assembly vehicle and fastened by the vehicle and the crew. The DEV uses its own RCS to stay positioned near the IPV as shown in Figure 6.6.

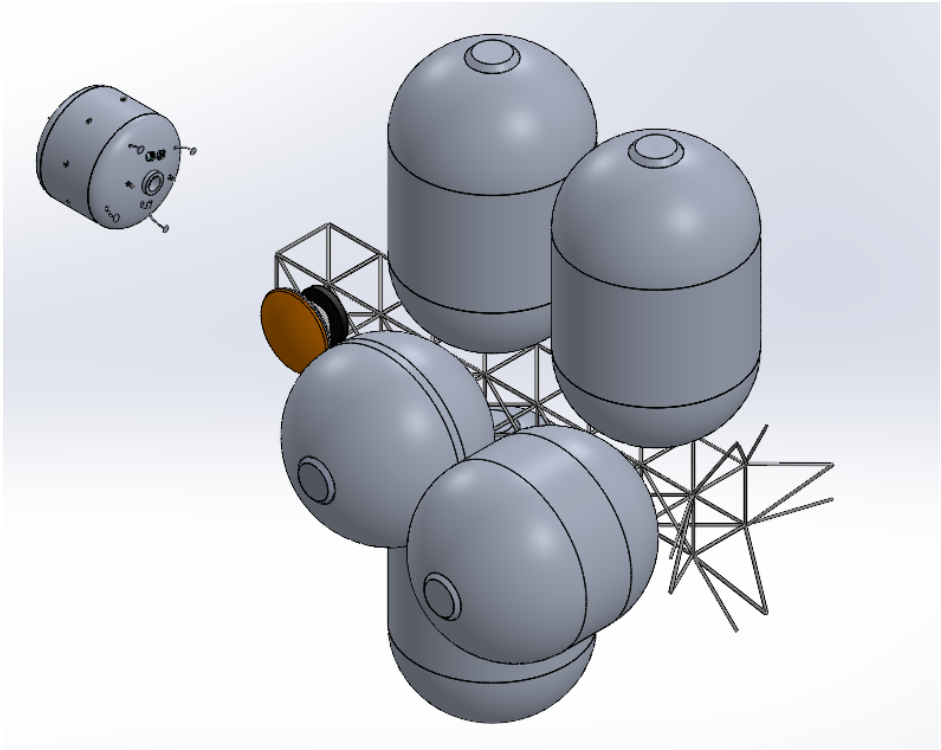

Figure 6.6: Assembly Step 4

Then, the second Mars Capture Tank and final Earth Departure Tank are assembled as shown in Figure 6.7.

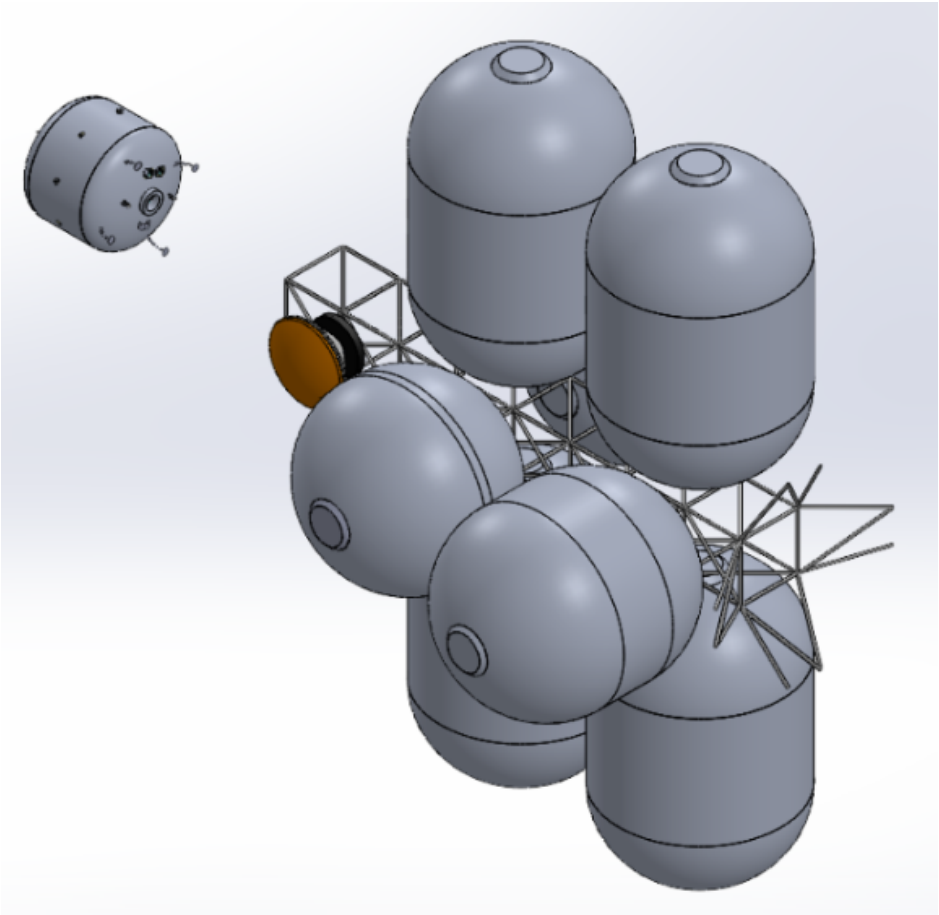

Figure 6.7: Assembly Step 5

Next, the largest tank, the Earth Capture Tank, and the associated truss structure are assembled as shown in Figure 6.8.

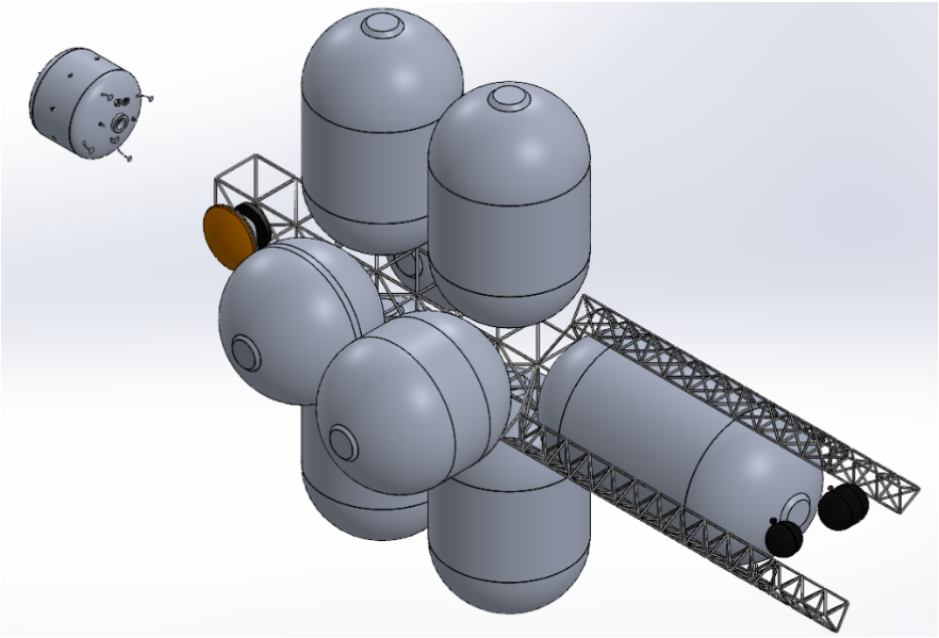

Figure 6.8: Assembly Step 6

Finally, the IPV Hab, thrust structure, engines, and radiators are assembled as shown in Figure 6.9.

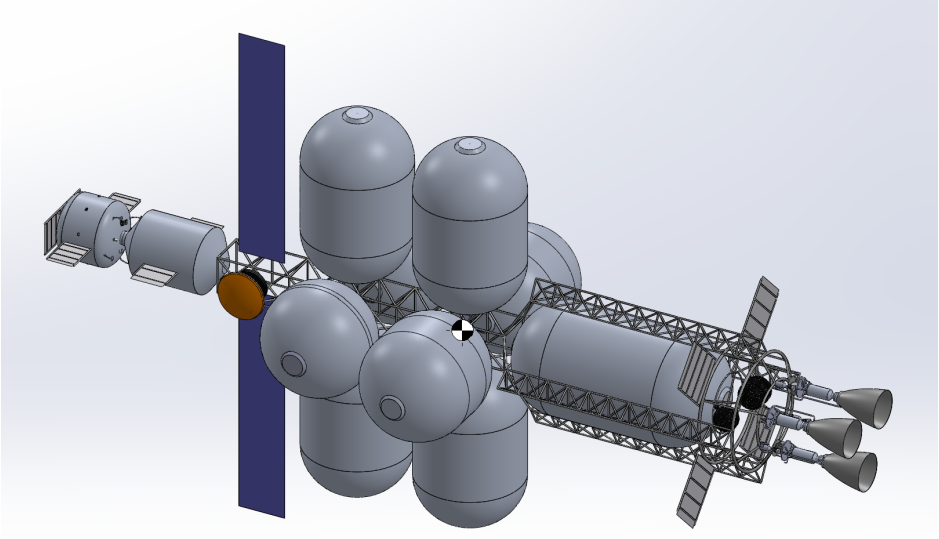

Figure 6.9: Assembly Step 7

To assemble the trusses in orbit, ultrasonic spot welding is utilized to join the truss members together. A welding tool on the assembly vehicle joins the truss members to-

gether. Then, the welding tool vibrates at a certain frequency, which heats the materials of the trusses to thermoplastic conditions [43]. This makes a permanent molecular bond between each of the members [43]. This method is how the main truss, the triangular trusses, and the connection truss are assembled and connected together in orbit, and how the triangular trusses are joined to the thrust structure. A diagram showing a sample assembly with the ultrasonic spot welding method is shown in Figure 6.10 [1]:

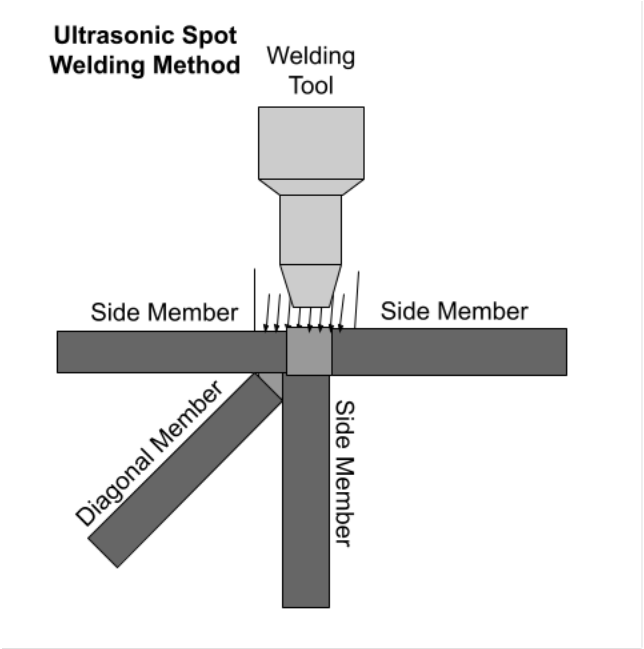

Figure 6.10: Ultrasonic Spot Welding Method [1]

6.4 Assembly Vehicle

The assembly vehicle is a crew-operated module that supports the in-orbit construction of large spacecraft structures in LEO. Its primary function is to transport, position, and fasten large components that cannot be pre-assembled upon launch. The assembly vehicle supports faster mission timelines and is essential to keep to the overall assembly timeline of 3 months for the mission to Deimos.

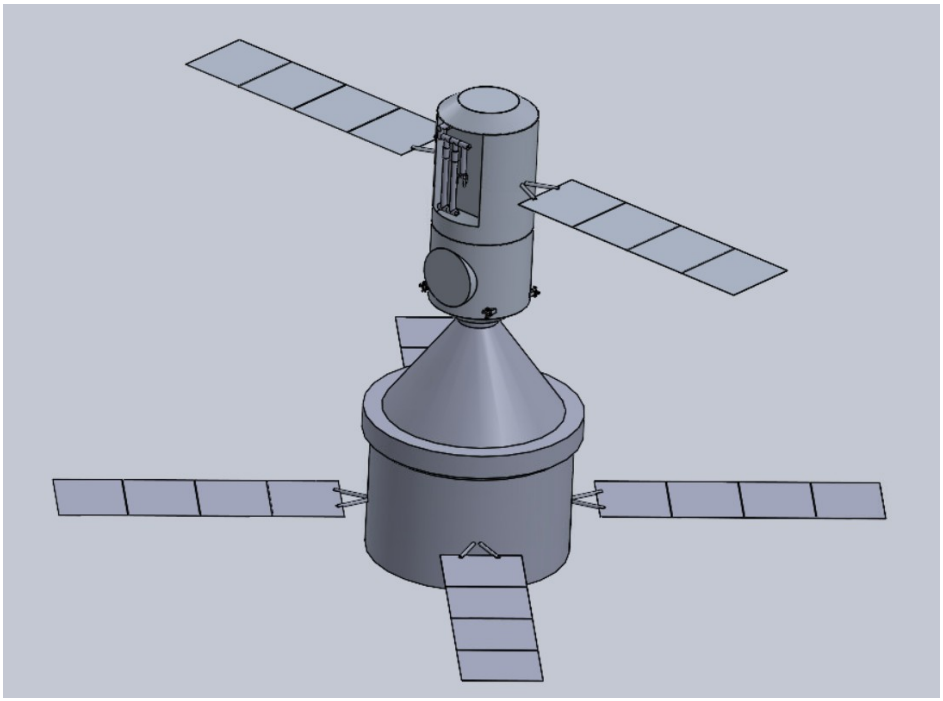

Figure 6.11: Assembly Vehicle with Orion Capsule

The assembly vehicle includes a pressurized crew cabin with life support and storage for supplies to support a crew of two for a 100-day mission. The hull is cylindrical, made of Aluminum 2219-T62, and measures 5 meters in height with a radius of 1.25 meters. A top-mounted docking port allows attachment to incoming modules and fuel tanks, a side-mounted airlock allows EVA operations, and a bottom-mounted NASA Docking System (NDS) allows direct connection with the Orion capsule and the ESM, which provides supplemental power and propulsion. Two robotic arms, each 7.5 meters in length and 0.076 meters in radius, are mounted to the sides of the body. These are made from a combination of Titanium & Carbon Fiber.

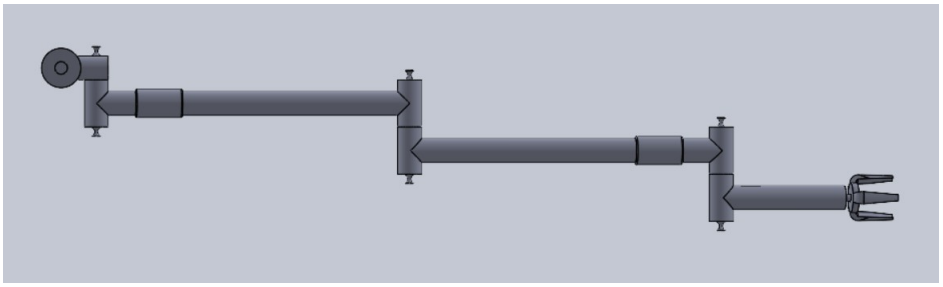

Figure 6.12: Assembly Vehicle Arms

The assembly vehicle contains 28 m² of solar arrays to provide 5.5 kW of additional power. Power is distributed to critical systems, including rendezvous control, capture mechanisms, and robotic operations. Additionally, the assembly vehicle is equipped with four RCS thruster blocks for added control.

Robotic functionality is a key part of the assembly vehicle. The two arms are equipped with a latching end effector that is used for grabbing trusses or latching onto the spacecraft itself. One arm can be used as an anchor point while the other carries out tasks. Additionally, tools such as welding heads and wire cutters are included in a separate attachment that connects to the latching end effector for assembly details, besides moving around larger structures. Therefore, the arms can keep components in position while the crew secures them, as well as secure components itself.

Table 6.4 summarizes the vehicle's key dimensions and materials:

Component	**Value**
Height	5.0 m
Radius	1.25 m
Wall Thickness	0.001 m
Body Material	Aluminum 2219-T62
Arm Material	Titanium & Carbon Fiber
Arm Length	7.5 m
Arm Radius	0.076 m
Arm Wall Thickness	0.006 m
Solar Panel Area	28 m²

Table 6.4: Physical Specifications of Assembly Vehicle

Since the assembly vehicle supports the crew for three months during assembly, additional life support is included. The life support system includes storage for oxygen, water, food, and nitrogen. Supplies are calculated for two crew members over 100 days, with a redundancy factor of 1.75 as shown in Table 6.5:

The overall mass budget for the assembly vehicle is shown in Table 6.6:

Operationally, the assembly vehicle docks to incoming modules using the top port. Astronauts and autonomous tools make final mechanical and electrical connections. This

Resource	Daily Use (kg/CM/day)	Total Needed (kg)
Oxygen	0.89	311.5
Water	6.47	2264.5
Food	0.80	280.0
Nitrogen	–	75.0
Total	–	**2931**

Table 6.5: Life Support Mass Breakdown

Mass Budget	Mass (kg)
RCS	178
Solar Panels	42
Body Mass	1200
Total Arm Mass	205
Life Support	2931
Total Mass	**4556**

Table 6.6: Assembly Vehicle Mass Breakdown

process allows larger, more complex systems to be assembled in space than would otherwise be possible. Furthermore, the assembly vehicle is essential to assemble the spacecraft within a relatively short assembly window. Additionally, since the overall assembly time is reduced, boil-off is reduced, which lowers the required launch mass and results in significant mission cost savings. Finally, the assembly vehicle reduces risk for the assembly crew and can be reused for future large-scale missions.

7 Mission and Operational Capabilities

7.0.1 Deimos Landing and Excursion Concept of Operations

The DEV will make two, 135 day trips to the surface of Deimos, each time operated by a different pair of crew members. This ensures that all 4 crew members participate in a surface stay on Deimos. During these trips to the surface, the crew members will perform science operations that will investigate the origin and composition of Deimos. In order to effectively execute these operations, a designated landing zone on the surface of Deimos is selected. The landing zone can be seen on a surface map of Deimos, shown in Figure 7.1.

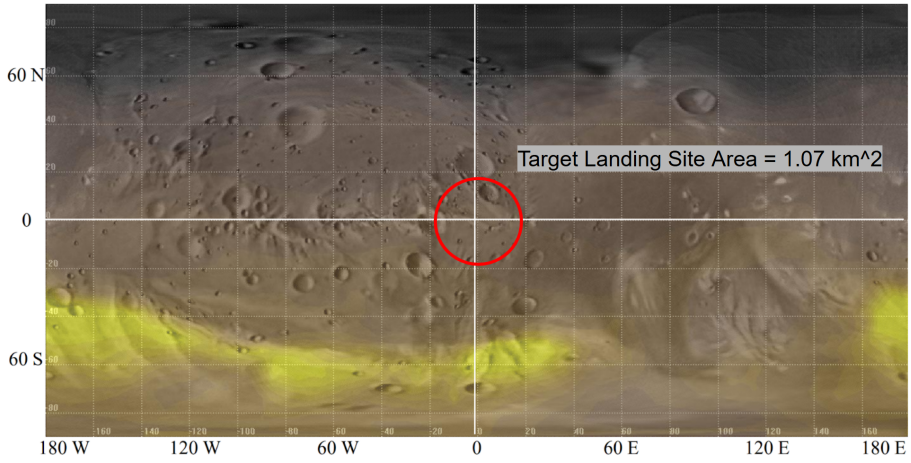

Figure 7.1: Deimos Landing Zone[2]

The landing zone is located at the coordinates: 0-20° North, South, East, and West, with the origin of this surface map located in the center of the section of Deimos. This location will have a constant view of the surface of Mars, which occurs because of the tidally locked nature of Deimos in relation to Mars. The selection of this landing zone is made in accordance with the selection criteria found in Table 7.1.

Selection Criteria:	Reasoning:
Low Solar Radiation	Minimize radiation exposure
Diverse Surface Composition	Maximize science discoveries
Line of Sight to Mars	Potential TMSA operation capabilities

Table 7.1: Deimos Landing Zone Selection Criteria

The selected landing zone has a 1.07 square kilometer area, in which there are several craters of different sizes, providing a variety of locations for analysis. Additionally, the landing zone is not in a constant solar radiation zone, which can be seen highlighted in yellow. The avoidance of these zones allows for a decrease in radiation exposure for the crew members piloting the DEV. This also ensures radiators can effectively remove heat from the DEV's power cycles and the habitat volume.

While in the landing zone, the DEV will conduct scientific operations at each landing site. During the 135 day duration, the DEV will move to 10 sites where these operations will be conducted. The maneuvers between sites will be conducted via RCS propulsion, allowing for precise 20 meter movements across the lunar surface. These maneuvers will allow for a diverse investigation of the lunar surface and regolith layer of the moon. These maneuvers allow for science operations to be conducted at 20 different sites, without requiring round trip transit to the IPV. A 5% propellant margin has been allocated for maneuvers that may require more than the estimated 20 meter transfer distance. This is because there may be potential hazards identified by LiDAR surface scanning or crew observation that could require extra avoidance. Additionally, the potential of landing in a crater with a depth of greater than 20 meters has been identified as a possible risk and is a driver of the 5% propellant margin decision. A simple, not to scale, concept of operations can be seen in Figure 7.2.

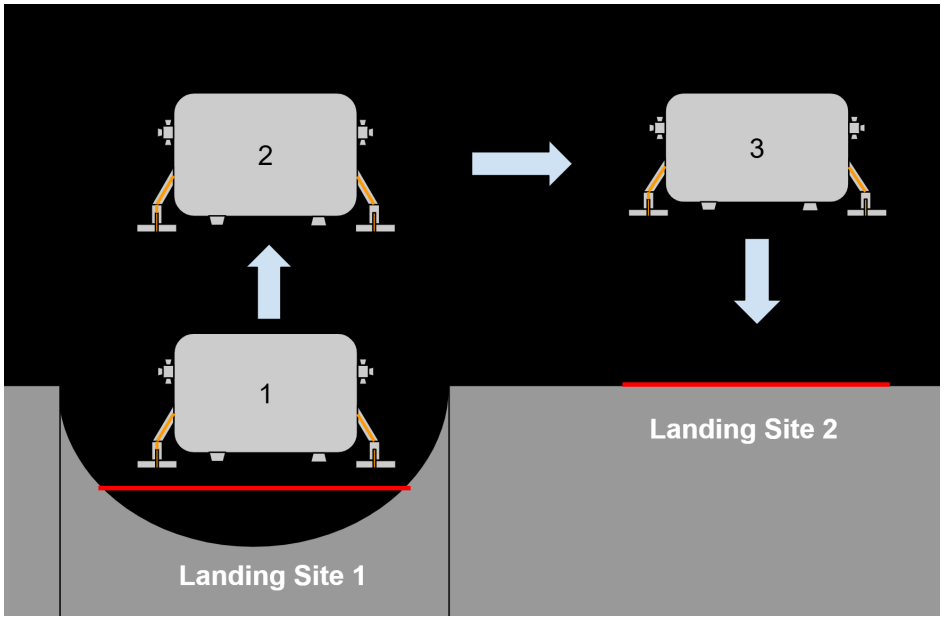

Figure 7.2: Deimos Crater Landing Operations

The operations of the DEV on the surface of Deimos allow for full analysis of its surface and regolith substrate over an area. The operations outlined also provide a comprehensive plan that maximizes propellant use efficiency and allows for constant science operation.

7.1 Mission Profiles and Options

7.1.1 Isp and Initial Mass Selection

Using the calculations outlined in Section 16.4, values for Isp and initial launch mass for the IPV can be compared to decide which combination yields the best resulting final mass. A summary of the comparison can be found in Table 7.2.

Calculated with ΔV = 11.86 km/s: From Table 16.3				
Isp (sec)	m_0/m_f	m_0 (mT)	No. of Launches	m_f (mT)
850	4.149	600	4	144.6
850	4.149	750	5	180.8
950	3.572	600	4	168.0
950	3.572	750	5	210.0

Table 7.2: Comparison of Isp and Mass Ratio Values.

For this mission, the last option shown in Table 7.2 is chosen, with the IPV having a total mass budget of 750mT, resulting in a dry final mass of around 210mT. However, in reality the dry return mass is lower, due to propellant boil off, tank jettisoning, and resources left behind on Deimos.

7.1.2 Robotic Resupply

As part of the mission requirements, calculations are performed to verify if the mission can be extended beyond its initial time frame by utilizing a robotic resupply. The mission would be extended by 780 days, which is the synodic period for a Hohmann transfer between Earth and Mars. Oxygen, water, food, and propellant would require resupply. For oxygen, water, and food, the amounts consumed per day calculated above were multiplied by the additional days, and then a redundancy was included for all three items. These values are discussed in Section 12.1. For the propellant, the boil-off rates for the Mars departure and Earth capture tanks, since those are the only tanks remaining when the mission reaches Deimos, calculated above were multiplied by the trip time to Mars and the additional wait time at Mars. These two additional amounts of boil-off were added together to reach the total boil off that would occur if the mission were to be extended. The boil-off rates are discussed in Section 10.5.2. The masses needed for an extended mission are listed in Tables 7.3, 7.4, 7.5, and 7.6. The total additional mass needed to resupply the mission for an extension is 38.10mT.

Oxygen	
kg/person/day	0.89
Redundancy	2
Extra for 780 day wait time (mT)	5.55

Table 7.3: Oxygen Resupply Values

Water	
kg/person/day	4.03
Redundancy	2
Extra for 780 day wait time (mT)	25.15

Table 7.4: Water Resupply Values

Food	
kg/day	3.20
Redundancy	1.4
Extra for 780 day wait time (mT)	3.49

Table 7.5: Food Resupply Values

Propellant		
	Mars Depart Tanks	Earth Capture Tank
Trip to Mars boil off (mT)	0.33	0.95
780 day wait time boil off (mT)	0.98	2.75
Extra needed (mT)	1.31	2.6

Table 7.6: Propellant Resupply Values

7.2 Human Systems Integration

According to the NASA Human Systems Integration Handbook, HSI is, "a required interdisciplinary integration of the human as an element of the system to ensure that the human and software/hardware components cooperate, coordinate, and communicate effectively to successfully perform a specific function or mission" [27]. HSI differs from SE&I in that HSI is a component of SE&I, but focuses in greater detail on human interactions with the environment. The HSI handbook divides HSI into six main, interconnected categories: Human Factors Engineering, Operations, Maintainability and Supportability, Habitability and Environment, Safety, and Training [27]. Due to this project only being designed to the PDR stage, training is not considered.

7.2.1 Human Factors Engineering

HFE concerns the design of everything human crew members will interact with as well as what tasks are performed by humans versus what tasks are performed by ma-

chines [27]. Some HFE considerations do not enter until the detailed design stage, but the foundations are considered for this design. The primary consideration occurs during the assembly in LEO. The robotic assembly vehicle performs the bulk of the assembly tasks, as described in Section 6.4. The crew will remotely operate the assembly vehicle and will only perform EVAs for detailed assembly procedures.

7.2.2 Operations

Operations considerations in HSI involve analysis of the entire mission timeline to create a mission that is cost-effective without sacrificing mission or human success [27]. The Deimos landing site for this mission is chosen to have minimal solar radiation exposure, which lowers the crew members' daily exposure.

7.2.3 Maintainability and Supportability

Maintainability and supportability ensures the entire lifespan of the mission is considered in the design [27]. Any maintenance that needs to be performed during the mission shall be simplified and be able to be performed safely. Any tools or parts needed for maintenance and repairs shall be included. For this mission, the amount of consumables needed, such as water and food, are calculated with a reasonable safety margin, as shown in Section 12.

7.2.4 Habitability and Environment

Habitability and Environment concerns how the spaces the crew inhabits are designed to uphold the other HSI categories as well as the health of all crew members [27]. Designated areas for non-mission tasks are included in both the IPV and DEV habitable areas. These areas include space for exercise to help combat bone density loss 5.3. All habitable areas are temperature and pressure regulated. The vehicle is designed to keep the crew members' daily radiation dose below the maximum daily limit, shown in Section

12.4. There is a window in the IPV and DEV habitable areas, in the mission task area, for viewing of docking procedure as well as crew well being.

7.2.5 Safety

Safety considerations in HSI involve implementing safety measures for crew and the systems throughout the lifespan of the mission [27]. FMECA is performed to identify the major risks of the mission, so mitigation plans can be created. Radiation shielding is implemented to protect against solar radiation and radiation from the NTP engines.

7.3 Logistics

This mission timeline in Figure 7.3 outlines a series of six launches between July 7, 2041, and October 5, 2041, with a two-week launch cadence. Over a one-year period starting in July 2041, the components are stacked in the VAB. Then, over an additional three-month period, the components are assembled in LEO. Finally, the entire spacecraft departs from LEO on October 19, 2041. After an 8.5-month interplanetary transit, the IPV arrives at MPO on July 3, 2042. The mission includes a 1.24-year stay in Mars orbit, during which the crew performs operations, including 135-day surface shifts to Deimos in the DEV. The IPV departs MPO on September 28, 2043, and returns to LEO on June 13, 2044.

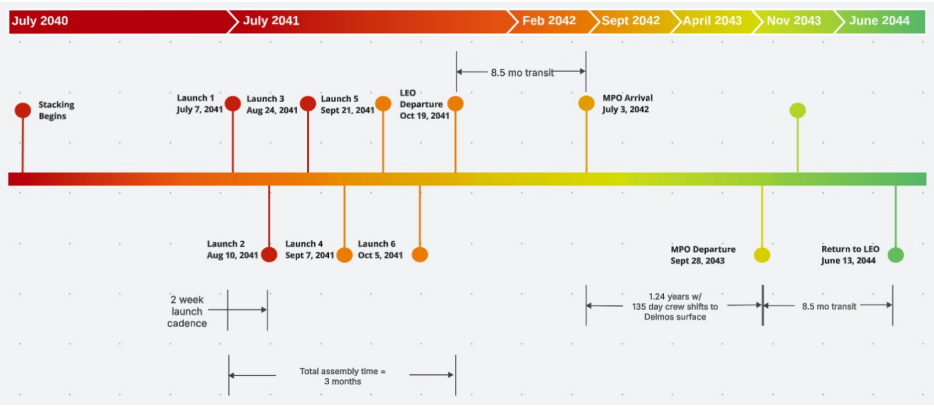

Figure 7.3: Mission Timeline

7.4 Economics and Development Plan

The preliminary cost breakdown for the Crewed Mission to Deimos is shown in Figure 7.4. The values presented are estimates for the primary flight system components, launch vehicles, mission operations, and indirect costs, expressed in millions of U.S. dollars. The total projected mission cost is approximately $329 billion.

Line Item Name	DDT&E [M]	Production [M]	Total [M]
Mission to Deimos	**$ 267,712.0**	**$ 20,954.7**	**$ 288,666.7**
Flight System/Spacecraft	**$ 59,566.0**	**$ 7,662.3**	**$ 67,228.3**
Crewed Vehicle	$ 40,985.0	$ 7,369.9	**$ 48,354.9**
IPV Hab	$ 1,315.2	$ 325.6	**$ 1,640.8**
DeV	$ 6,083.2	$ 1,520.8	**$ 7,604.0**
Assembly Vehicle	$ 1,904.0	$ 476.0	**$ 2,380.0**
TMSA	$ 3,260.0	$ 1,740.0	**$ 5,000.0**
Structures	$ 202.9	$ 45.3	**$ 248.2**
Tanks	$ 423.1	$ 71.8	**$ 494.9**
Thermal Protection	$ 56.3	$ 7.4	**$ 63.7**
Propulsion			
NTR Engines	$ 16,372.2	$ 397.4	**$ 16,769.6**
RCS	$ 5,961.1	$ 1,561.6	**$ 7,522.7**
Avionics			
GNC & CCDH	$ 1,052.0	$ 595.4	**$ 1,647.4**
Power	$ 449.3	$ 28.1	**$ 477.4**
Crew Systems	$ 3,905.7	$ 600.5	**$ 4,506.2**
Integration, Assembly, Checkout	$ 337.8	$ 292.4	**$ 630.2**
System Test Operations	$ 11,577.8	-	**$ 11,577.8**
Ground Segment	$ 6,665.4	-	**$ 6,665.4**
Launch Vehicles	**$ 16,000.0**	**$ 13,000.0**	**$ 29,000.0**
6 SLS	$ 15,000.0	$ 12,000.0	**$ 27,000.0**
2 Orion	$ 1,000.0	$ 1,000.0	**$ 2,000.0**
Operations	**$ 78,798.0**	-	**$ 78,798.0**
Program Development Studies	$ 1,098.0	-	**$ 1,098.0**
Mission Support	$ 14,700.0	-	**$ 14,700.0**
Mission Operations	$ 63,000.0	-	**$ 63,000.0**
Total Indirect Cost	**$ 113,348.0**	-	**$ 113,348.0**
Tracking and Data Acquisition	$ 24,000.0	-	**$ 24,000.0**
Construction of Facilities	$ 14,348.0	-	**$ 14,348.0**
Research and Program Management	$ 75,000.0	-	**$ 75,000.0**
Total	**$ 267,712.0**	**$ 20,954.7**	**$ 288,666.7**
Total Including 14% Margin	**$ 305,191.7**	**$ 23,888.4**	**$ 329,080.1**

Figure 7.4: Total Budget

7.4.1 Spacecraft Cost

The baseline budget is developed using NASA's Project Cost Estimating Capability (PCEC). This tool creates detailed cost projections across a mission's lifecycle using historical data from previous NASA missions with similar requirements and spacecraft mass as a primary input. PCEC provides an accurate estimate by breaking down the total spacecraft mass by subsystem (e.g., structures, tanks, propulsion, avionics, power, and life support), then applying cost models tailored to each subsystem, rather than using a one-size-fits-all approach. PCEC outputs design, development, testing, and evaluation (DDT&E) costs and production costs for each subsystem [44].

Additionally, several new vehicles must be developed to support this mission. For example, the DEV and the assembly vehicle cost $7.6 billion and $2.4 billion, respectively. Both the DEV and assembly vehicle costs are estimated by using previous NASA studies and designs of similar mass and functionality [45] [46]. Additionally, subsystems such as the TMSA, which do not require as much new technology, are scaled based on mass to existing technologies. The TMSA is double the mass of the Curiosity rover, which cost about $2.5 billion, so the cost of the TMSA is $4 billion total [47]. The mission also requires the development of advanced composite propellant tanks and NTR engines, so an additional 20% margin is added to the baseline cost of the tanks and engines to account for further research.

A significant portion of the total spacecraft budget is driven by propulsion costs, primarily due to the mass and complexity of the nuclear thermal propulsion system. The mission requires three NTR engines, which together account for 34.7% of the total spacecraft cost. The DDT&E cost for NTRs is estimated at $16.4 billion, with each engine costing approximately $0.4 billion to produce.

Furthermore, crew systems, which include life support, habitation, and other supplies, represent another significant part of the spacecraft budget, 9.3%. The health and safety of the crew are critical to the mission and require an appreciable percentage of the total mass.

The cost breakdown of the spacecraft by subsystem is represented in Figure 7.5 below:

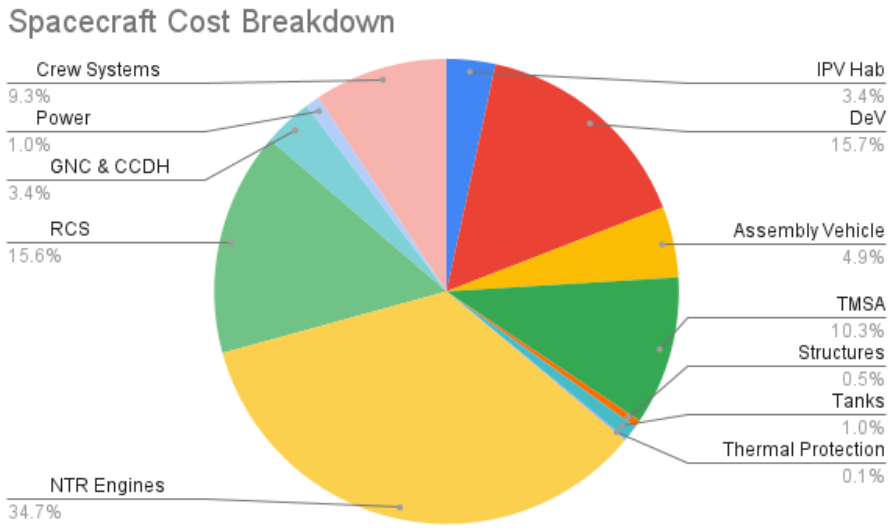

Figure 7.5: Spacecraft Cost Breakdown

7.4.2 Launch Vehicle Cost

The mission requires six SLS launches and two Orion capsules to deliver the spacecraft components to LEO for final assembly. Each SLS launch costs $2.5 billion to launch and $2 billion to produce, leading to a total cost of approximately $27 billion for all six SLS rockets [48]. An additional $1 billion is allocated for each Orion capsule and ESM, bringing the total launch vehicle cost to $29 billion.

Infrastructure development on the ground is necessary to support the two-week launch cadence. Therefore, five additional mobile launchers and high bays are built at Kennedy Space Center. Each mobile launcher costs $2.7 billion, and each high bay costs $169.6 million [49] [50]. Therefore, the total cost for the construction of facilities is $14.3 billion.

7.4.3 Operations and Indirect Cost

Generally, the best way to estimate costs is by direct analogy with the costs of similar missions and mass-cost estimating factors. According to a study from NASA Ames Re-

search Center, the cost of a mission to Mars is two to three times as expensive as any one of the Apollo, space shuttle, or ISS programs [51]. Operations and indirect costs from the Apollo program are used to estimate operations and indirect costs for the mission to Deimos. First, costs are scaled to reflect today's dollars, and then scaled by an additional factor of three to account for increased size and complexity. The total baseline cost for the crewed mission to Deimos is $289 billion. Additionally, a mass-cost estimating factor based on the ISS is used to verify the cost. The total current cost of the ISS is $150 billion for 420 mT or $0.36 billion per metric ton [51]. If the spacecraft's total mass is 750 mT, multiplying by $0.36 billion per metric ton gives a total cost of $270 billion, which is very close to the $289 billion estimate.

The cost breakdown of the spacecraft by subsystem is represented in Figure 7.6 below:

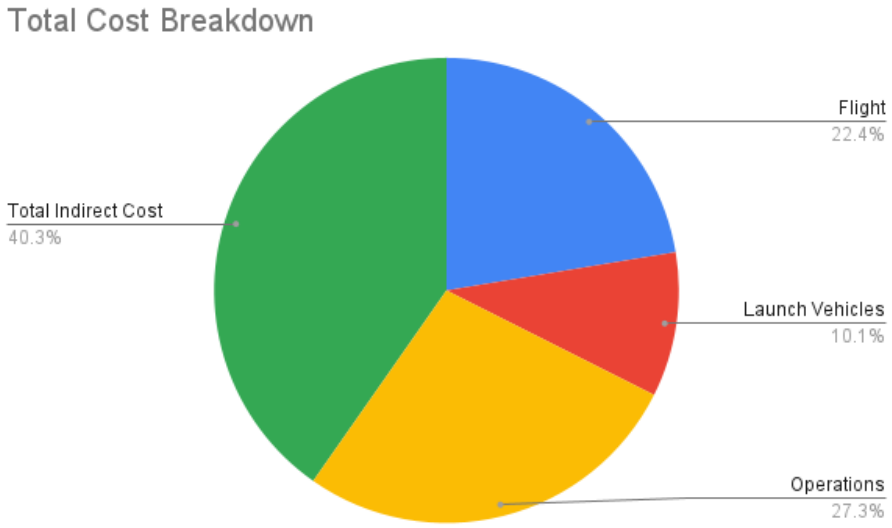

Figure 7.6: Total Cost Breakdown

7.4.4 Cost Risk Analysis

According to NASA's Cost Estimating Handbook, the cost estimate must include an appropriately chosen level of unallocated future expense (UFE) to achieve a desired confidence level [52]. Therefore, a 14% margin is chosen to account for uncertainty and UFE.

This brings the total baseline cost of $289 billion to $329 billion.

7.4.5 Annual Cost Breakdown

To estimate the annual budget distribution for the mission to Deimos, the annual James Webb Space Telescope (JWST) annual budget distribution is used as a reference, given its comparable development timeline [53]. By considering JWST's year-by-year spending as a percentage of its total cost and applying those same proportions to this mission's budget, an annual budget is constructed as shown in Figure 7.7 below:

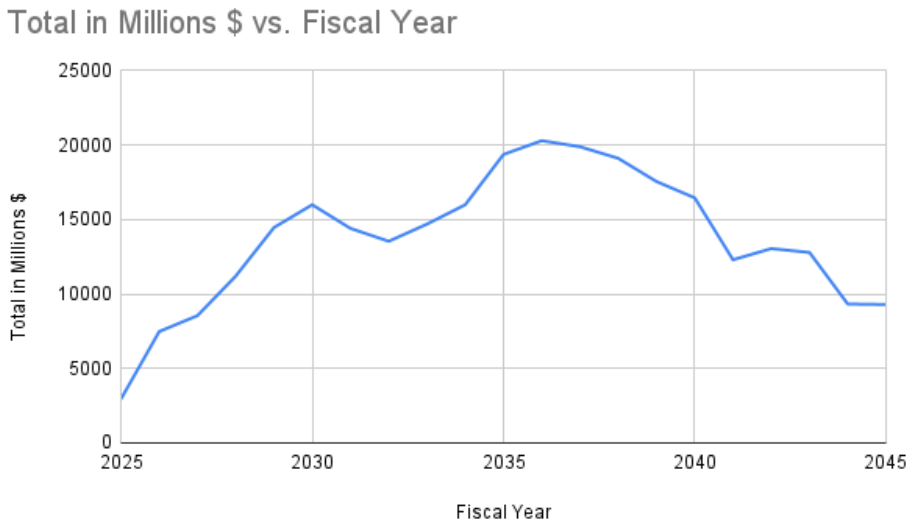

Figure 7.7: Annual Cost Breakdown

The annual budget is influenced by the overall project timeline:

Timeframe	Project Stage
2025–2028	Pre-Phase A: Concept Studies
2028–2031	Phase A: Concept and Technology Development
2031–2035	Phase B: Preliminary Design and Technology Completion
2035–2040	Phase C: Final Design and Fabrication
2040–2045	Phase D: System Assembly, Integration, Test, and Launch

Table 7.7: Project Timeline

As expected, Phase C (2035–2040) incurs the highest costs because it involves procuring materials and fabricating all the major systems and subsystems.

8 Structural Design

8.1 Structures Functional Block Diagram

Below is the Functional Block Diagram for the Structures subsystem. The subsections are referred back to the Master Functional Block Diagram.

<table>
<tr><td colspan="6">Structures</td></tr>
<tr><td>Habitable Structures</td><td>Propellant Tanks</td><td rowspan="2">Trusses</td><td>Radiation Shielding</td><td rowspan="2">Insulation</td><td>MMOD Shield</td></tr>
<tr><td>DEV Primary Structure</td><td>IPV LH_2 Tanks</td><td>Main Truss</td><td>DEV Shielding</td><td>Propellant Tanks</td><td rowspan="2">Habitats</td></tr>
<tr><td>IPV Hab Primary Structure</td><td>DEV Tanks</td><td>Triangular Truss</td><td>IPV Hab Shielding</td><td rowspan="2">Habitats</td><td>Propellant Tanks</td></tr>
<tr><td></td><td>OMS MMH N_2O_4 Tanks</td><td>Connection Truss</td><td rowspan="2"></td><td rowspan="2">Radiators</td><td rowspan="2"></td></tr>
<tr><td></td><td>Ullage Tanks</td><td>Thrust Structure</td></tr>
</table>

Table 8.1: Structures FBD

There are several design drivers that are constant across all structural aspects of the vehicle. First, the factor of safety for all structures is in accordance with NASA-STD-5001 [31]. The launch loading factors are summarized in the following table, taken from Ref [54].

Variable	Value	Units
LF_ϕ	4.1	G
LF_θ	3	G
$F.S.$	1.5	-

Table 8.2: Load Factors and Factor of Safety

The rest of the design drivers include finding materials that have high tensile and yield

strengths while having light masses to bear the loads during launch loading. Once these materials are utilized, the structural components are sized to have launch loading stresses below the allowable stress of their respective material that is fit with the factor of safety of 1.5.

8.2 Material Properties

Tables 8.3 and 8.4 summarize the material properties in structural analyses using Refs [55] and [56].

Variable	Value	Units
α_{wind}	20	°
$X_{t,composite}$	1200	MPa
$V.F$	0.7	
$\alpha_{th_{CF}}$	$-9.00 * 10^-7$	$m/m°C$

Table 8.3: Cycom-5250-4 Material Properties

Variable	Value	Units
X_{tu}	414	MPa
X_{ty}	290	MPa
t_l	0.29	mm
E	73.1	GPa
v	0.33	
α_{th_l}	$2.23 * 10^-5$	$m/m°C$

Table 8.4: Aluminum 2219-T62 Material Properties

8.3 Habitat Primary Structure

8.3.1 Design Decisions

An isogrid structure is chosen for the habitable vehicles to improve stiffness and rigidity at a low mass penalty. By stiffening a membrane with a triangular pattern, the isogrid material acts analogously to an isotropic material.

NASA's Isogrid Design Handbook is utilized for the preliminary design of the isogrid structure for the cylindrical section of the IPV Hab and the DEV. An iterative design approach is employed to arrive at a design geometry which satisfies all structural requirements. A MATLAB code is developed that computes the structural loading and mass of the isogrid cylindrical section when provided with a geometrical layout. Aluminum 2219-T62 is considered as the primary structure material for both habitable structures. Material properties for Aluminum 2219-T62 are provided in Table 8.4.

8.3.2 Isogrid Analyses

Using NASA's Isogrid Design Handbook [57], a structure is analyzed given loading and internal pressure inputs along with the isogrid geometry. Isogrid geometry is given in Figure 8.1. The analysis considers t, b, d, h, and N_c along with structure internal radius, R_i, and length, L, to be inputs. It should be noted that an unflanged isogrid is considered for simplicity of analysis. The isogrid structure is analyzed by an averaging method such that the grids are considered as a continuous sheet of metal with the modified elastic properties. Section 4.2 of NASA's Isogrid Handbook, Cylinders in Compression and Bending, is used to gather the necessary equations for the analysis.

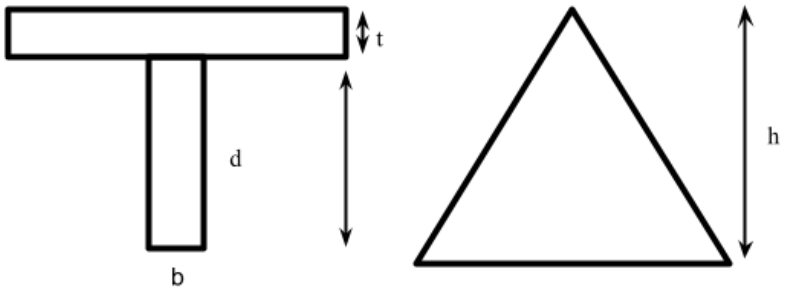

Figure 8.1: Isogrid Geometry

First, the non-dimensional isogrid geometry parameters are computed for the chosen geometry using Equations (8.3), (8.4), and (8.5).

$$d = t_w - t \tag{8.1}$$

$$h = \frac{D_o \pi}{N_c} \tag{8.2}$$

$$\alpha = \frac{bd}{th} \tag{8.3}$$

$$\delta = d/t \tag{8.4}$$

$$\beta = [3\alpha(1+\delta)^2 + (1+\alpha)(1+\alpha\delta^2)]^{1/2} \tag{8.5}$$

Next, the equivalent thickness and Young's Modulus values are computed using Equations (8.6) and (8.7).

$$t^* = \frac{t\beta}{1+\alpha} \tag{8.6}$$

$$E^* = \frac{E(1+\alpha)}{\beta} \tag{8.7}$$

Utilizing the non-dimensional geometric parameters, t_{eff} and t_{equiv} are computed. t_{eff} represents the transformed monocoque cylinder thickness for structural stiffness properties, while t_{equiv} represents the equivalent mass monocoque cylinder thickness.

$$t_{eff} = t(1+\alpha) \tag{8.8}$$

$$t_{equiv} = t(1+3\alpha) \tag{8.9}$$

The experimentally derived constants for cylindrical isogrid structures are used from NASA's Handbook.

$$c_0 = 0.397$$

$$c_1 = 10.2$$

$$c_2 = 0.616$$

The internal pressure and launch loading are now applied. The axial and lateral loading factors are taken from Table 8.2 and applied to the estimated mass of the IPV Habitat and DEV. Structures are considered to be in a combined axial and bending loading.

Axial Loading:

$$N_\phi = \frac{F_a * FS}{2\pi R} \tag{8.10}$$

Bending Loading:

$$N_b = \frac{M * FS}{\pi R^2} \tag{8.11}$$

Combined Loading Condition:

$$N_a + N_b = N_{cr} \tag{8.12}$$

Using the non-dimensional geometrical parameters defined previously, 3 critical stresses are defined: General Instability, Skin Buckling, and Rib Crippling using Equations (8.13),(8.14), and (8.15).

General Instability

$$N_{cr(1)} = c_0 E \frac{t^2}{R} \beta \tag{8.13}$$

Skin Buckling:

$$N_{cr(2)} = c_1 E t (1 + \alpha) \frac{t^2}{h^2} \tag{8.14}$$

Rib Crippling:

$$N_{cr(3)} = c_2 E t (1 + \alpha) \frac{b^2}{d^2} \tag{8.15}$$

After the critical stresses are computed, it is verified the structure geometry can withstand the allowable pressure loading using Equation (8.17). At the optimal structure geometry, all critical stresses should be equal to each other. To achieve this, the geometrical inputs are iterated until critical stresses are converged satisfactorily.

Input			Output		
Parameter	Value	Unit	Parameter	Value	Unit
Skin Thickness	2	mm	Allowable Loading	309.8	kN/m
Rib Thickness	1.5	mm	General Instability	310.5	kN/m
Rib Depth	19.1	mm	Skin Buckling	497.2	kN/m
Number of Cells	150	-	Rib Crippling	623.9	kN/m
Inner Diameter	5.5	mm	Burst Pressure	335.4	kPa
Length	6.5		Allowable Pressure	223.6	kPa
			t_{equiv}	2.745	mm
			Mass	876.8	kg

Table 8.5: IPV Hab Cylindrical Section Isogrid Parameters

Then, the burst pressure is expressed as:

$$p_{allow} = FS * p_{design} \tag{8.16}$$

$$p_{burst} = \frac{F_{tu} t(1+\alpha)}{R} \tag{8.17}$$

where $p_{burst} = p_{allow}$ at the optimal geometry. The critical stresses computed above are transformed into failure loads with Equation (8.18).

Computing Failure Loads:

$$L_{cr(n)} = 2\pi N_{cr(n)} R \tag{8.18}$$

where n is represents one of the 3 failure mode values N_{cr}.

An iterative MATLAB code (in Appendix) is utilized to generate the following outputs for the primary structure of the IPV Hab and the DEV.

The mass of the cylindrical primary structure sections for both the DEV and the IPV Hab is then approximated from the t_{equiv} value by computing the volume of the cylindrical shell and multiplying by the density of Aluminum 2219-T62.

Input			Output		
Parameter	Value	Unit	Parameter	Value	Unit
Skin Thickness	1.7	mm	Allowable Loading	241.4	kN/m
Rib Thickness	1.5	mm	General Instability	222.9	kN/m
Rib Depth	16.9	mm	Skin Buckling	217.53	kN/m
Number of Cells	125	-	Rib Crippling	668.72	kN/m
Inner Diameter	5.4	mm	Burst Pressure	191.3	kPa
Length	4	m	Allowable Pressure	286.92	kPa
			t_{equiv}	2.256	mm
			Mass	436.2	kg

Table 8.6: DEV Cylindrical Section Isogrid Parameters

8.3.3 Habitable Pressure Vessel Closures Analysis

The ASME Boiler and Pressure Vessel Code Section VIII [58] is used to calculate the required thickness of pressure vessel closure for the IPV Hab and DEV due to internal pressure loading. Equations (8.21) and (8.20) are used to determine the thickness of the elliptical closures on the DEV, while Equation (8.19) is used to determine the thickness of the conical to cylindrical taper on the IPV Hab.

$$t = \frac{PD_0}{2\cos(\alpha)(\sigma_{allow} + 0.4P)} \tag{8.19}$$

$$t = \frac{PD_0K}{2\sigma_{allow} - 0.2P} \tag{8.20}$$

$$K = \frac{1}{6}[2 + (\frac{D}{2h})^2] \tag{8.21}$$

Table 8.7 provides the geometrical layout and thicknesses for the IPV Hab pressure vessel closures. Aluminum 2219-T62 is utilized for the closure structure.

Table 8.8 provides the geometrical layout and thicknesses for the DEV pressure vessel closures. Aluminum 2219-T62 is again utilized for the closure structure.

Parameter	Value	Units
Outer Diameter	5.5	m
Pressure	101.325	kPa
$\alpha_{conical}$	60	°
t		mm

Table 8.7: IPV Hab Pressure Vessel Closure Parameters

Parameter	Value	Units
Outer Diameter	5.4	m
Pressure	101.325	kPa
K	1.54	-
t	2.5	mm

Table 8.8: DEV Pressure Vessel Closure Parameters

8.4 Propellant Tank Pressure Vessel Analysis

At the beginning of the Preliminary Design Phase, the team has chosen to utilize hybrid composite tanks in order to reduce the mass of the propellant tank primary structures. This subsection discusses the following topics regarding propellant tanks: important design decisions, analyses methods, results, CAD models, risk mitigations, and mass breakdowns.

8.4.1 Design Decisions

As shown in the figure above, these types of tanks utilize a layered carbon fiber outer skin bonded to a metallic liner. One of the only preliminary design procedures for these composite pressure vessels is netting theory, and therefore is utilized in these analyses. The composite layer is considered to be composed of a helical and a hoop layer. The helical wind layers carry the majority of the axial loads, while the hoop layers carry the majority of the circumferential loads The metallic liner is necessary to prevent permeation of cryogenic hydrogen through the composite layers [59]. The metallic liner is considered to carry no loads in the analyses, and is held a constant thickness throughout all propellant tank analyses. The choice of a hybrid composite-metallic tank construction poses issues

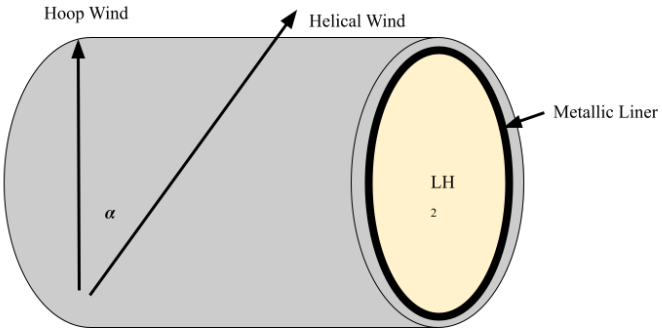

Figure 8.2: Hybrid Composite Tank Notional Diagram

with differing coefficients of thermal expansion, which are addressed in the risk mitigation section.

Cycom 5250-4 is selected for the composite material [56]. In accordance to NASA-STD-5001 [31], a factor of safety of 1.5 is applied to all propellant tank structures. Aluminum 2219-T62 is selected for the metallic liner material.

8.4.2 Analyses

Two main analyses are performed for the propellant tank structures. First, the composite layer helical and hoop wind thicknesses are sized based on pressure, tensile, and bending loading. Second, a simple thermal expansion analysis is conducted to better understand the issues with hybrid composite tank construction. Figure 8.2 shows a notional diagram of the different tank layers and winds.

Netting Theory Analyses Netting theory [60] assumes loads are only carried by the fibers, and that the tube wall acts as a membrane, carrying no out of plane bending or shear

loads. The loads are solely carried in the direction of the fiber wind, and also consider no load to be supported by the matrix holding the fibers in place.

First, the case of internal pressure loading on each tank is considered using Equations (8.22) (8.23) for hoop, θ, and axial pressure loads,ϕ, respectively.

$$N_{\theta,P} = PR \tag{8.22}$$

$$N_{\phi,P} = PR/2 \tag{8.23}$$

Next, the maximum SLS launch loading factors as seen in Table 8.2 are applied. The axial loading is considered to be applied to the cross sectional circumference of the tank, while the lateral launch loads are transformed into an equivalent bending moment at one end of the tank using Equations (8.24) and (8.25).

$$N_{\theta,launch} = \frac{W * LF * L/2}{\pi^2 R} \tag{8.24}$$

$$N_{\phi,launch} = \frac{W * LF}{2\pi R} \tag{8.25}$$

Under the combined loading conditions experienced by the propellant tanks, the total loadings are defined by Equations (8.26), and (8.27). Figure 8.3 shows the loading types experienced by each propellant tank upon launch.

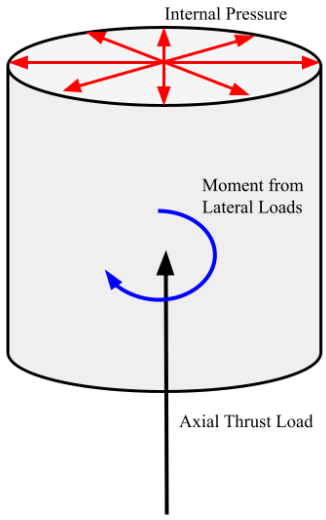

Figure 8.3: Payload Loading

$$N_{\theta,tot} = N_{\theta,launch} + N_{\theta,P} \tag{8.26}$$

$$N_{\phi,tot} = N_{\phi,launch} + N_{\phi,P} \tag{8.27}$$

Then, using the previously defined helical winding angle, the fiber thicknesses for the helical and hoop layers can be computed using Equations (8.29) and (8.30) for helical and hoop thickness, respectively.

$$\sigma_{allow} = X_{ty}/F.S. \tag{8.28}$$

$$t_{\alpha f} = \frac{N_{\phi}}{\sigma_{allow}\cos^2(\alpha)} \tag{8.29}$$

$$t_{90f} = \frac{N_\theta - N_\phi \tan^2(\alpha)}{\sigma_{allow}} \tag{8.30}$$

To find the thickness of both wind layers, the volume fraction of the composite must be considered. The volume fraction of composite describes the volume ratio of composite fibers to resin matrix. Using appropriate values from Equations (8.29), (8.30), and Table 8.3, the final thickness is found with Equation (8.31).

$$t = \frac{t_{\alpha f} + t_{90f}}{V.F.} \tag{8.31}$$

Tank Endcap Analysis Standard pressure vessel ellipsoidal end cap equations are used from Reference [58]. Equations (8.21) and (8.20) are used to find the thickness of the ellipsoidal pressure vessel wall. It should be noted that the metallic liner thickness remains identical to the previous analysis for the cylindrical portion of the tank.

Thermal Expansion Analyses A metallic liner on the inside of tank is necessary due to hydrogen permeation through the composite layer. The hybrid construction of these tanks has proven to be a problem point due to differing coefficients of thermal expansion between the composite layer and the metallic liner. As the outside of the tank cools in temperature from ambient temperature down to the temperature of the cryogenic hydrogen, the metallic liner shrinks in size while the composite remains approximately the same. A simple thermal expansion analysis is considered to investigate this problem. First, the circumference of the tank is calculated and is then used to calculate the length change with Equation (8.32) for the metallic liner and carbon fiber layers. L_2 and L_1 represent the circumference of the tank at the decreased temperature state and ambient temperature state, respectively.

$$L_2 = L_1 \alpha * (T_2 - T_1) + L_1 \tag{8.32}$$

Table 8.9 summarizes results of thermal expansion coefficients for the largest tank radius. Between states, there is a maximum of approximately $3cm$ space between the metallic liner and the composite layer.

Variable	Value	Units
R_1	4.9	m
L_1	30.787	m
T_1	21	$°C$
T_2	-250	$°C$
L_2	39.060	m
R_2	4.870	m

Table 8.9: Thermal Expansion Analysis Results

8.4.3 Propellant Tank Construction

The IPV LH_2 tanks are composed of three layers: primary structure, MLI, and MMOD shielding. The MLI and MMOD shielding layers are analyzed in Sections 10.5 and 8.8, respectively. Figure 8.4 displays a notional diagram of the ordering of the tank layers. Appendix A.3 contains dimensioned drawings for all propellant tanks showing the layer thicknesses for each IPV tank. A complete mass breakdown for each propellant tank is located in Section 5.5.

8.4.4 Results

Primary Structure Tables 8.11 and 8.10 provide calculated geometric parameters and mass estimates for the IPV LH_2 and IPV OMS propellant and ullage tank primary structures.

Figure 8.4: Propellant Tank Construction Notional Diagram

Parameter	EDT	MCT	MDT	ECT	Unit
P	234	234	234	234	kPa
R	4.75	4.9	4.9	4.9	m
L	15.6	11.94	9.41	19.82	m
$t_{\alpha_{wind}}$	0.92	0.92	0.91	0.96	mm
$t_{\alpha_{90}}$	1.60	1.60	1.46	1.72	mm
t_{total}	3.60	3.60	3.38	3.83	mm
t_{endcap}	0.74	0.77	0.77	0.77	mm
t_l	0.29	0.29	0.29	0.29	mm
m_{struct}	3830	2530	1442	6302	kg
V_{prop}	901.5	676.4	485.4	1271.1	m^3

Table 8.10: Primary Structure Breakdown for IPV LH_2 Tanks

Parameter	OMS Oxi	OMS Fuel	OMS He, Oxi	OMS He, Fuel	Unit
P	200	200	14000	14000	kPa
R	1.1	1.25	0.15	0.19	m
L	2.05	3.25	0.3	0.37	m
$t_{helicalwind}$	0.42	0.47	1.49	1.88	mm
$t_{hoopwind}$	0.68	0.78	2.45	3.10	mm
t_{total}	1.57	1.79	5.63	7.13	mm
t_{endcap}	1.57	1.79	5.63	7.13	mm
t_l	0.15	0.15	0.15	0.15	mm
m_{struct}	34	102	3	5	kg
V_{prop}	5.26	12.23	0.01	0.03	m^3

Table 8.11: Primary Structure Breakdown for IPV OMS Tanks

8.4.5 Propellant Tank CAD

Figure 8.5 shows the tank locations in the Assembled IPV configuration.

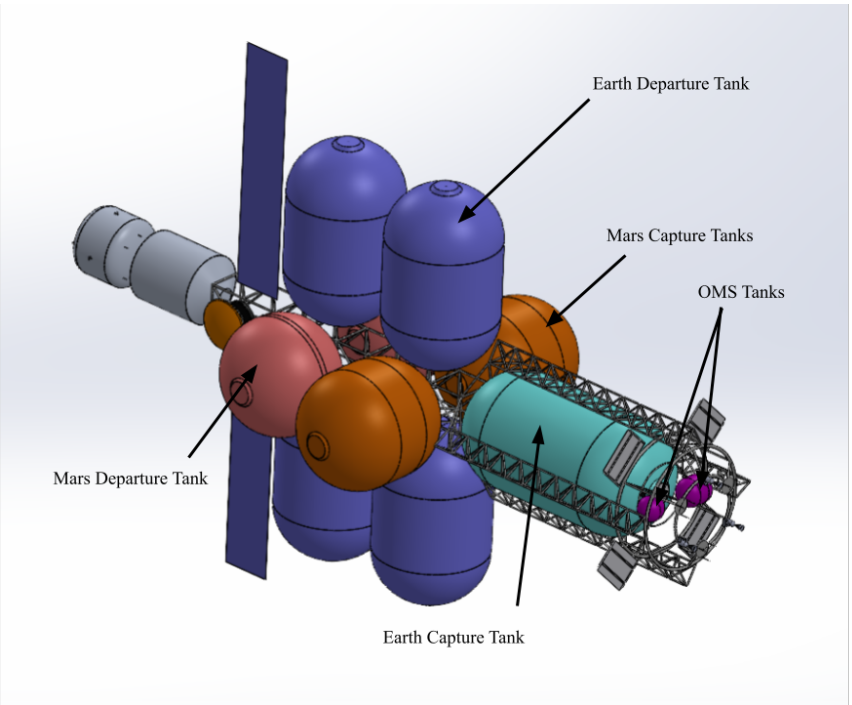

Figure 8.5: Assembly CAD Diagram with Labeled Tank Locations

8.5 Truss Structures

8.5.1 Design Decisions

This particular section will go over the design and analysis of the trusses for the IPV. The primary trusses consist of the engine thrust structure that attaches the engines to the IPV, four sets of triangular truss sections that attach from the thrust structure to the main truss, the main box truss section that attaches from the triangular truss sections to the habitat, and the truss connections that connect the main truss and the triangular trusses. All the truss members that make up the sections are hollow cylindrical beams and hollow rings. The maximum loading conditions that the trusses take under during the duration of the mission are during SLS launch loading, seen in Table 8.2.

The components of the truss members are broken down into two components: a straight

hollow cylinder and a hollow cylindrical ring. These components are made of different materials: for the straight hollow cylinders, the material chosen is the IM7/5555 Graphite/Epoxy composite, chosen for the material's high failure strength in the longitudinal direction and extremely low density[15]. For the hollow ring, the material chosen is Aluminum-Beryllium Metal (AlBeMet) AM162 Alloy, chosen for the material's high yield strength in the transverse direction and low density[16]. These properties are referred in Table 8.12:

Material Properties	IM7/5555 Graphite/Epoxy	AlBeMet AM162	Units
X_{fl}	1330	322	MPa
X_{ft}	111	165	MPa
E	107	193	GPa
Density	1500	2071	kg/m^3
Allowable X_{fl}	886.67	214.67	MPa
Allowable X_{ft}	74	110	MPa
ν	0.28	0.17	-

Table 8.12: Truss Component Material Properties [15][16]

8.5.2 Truss Analysis and Sizing

To size the straight hollow cylinders for all the trusses, the load on each truss is first computed with a factor of safety of 1.5 used, and the truss members undergoing axial and lateral launch loading. The forces computed for the members are:

$$F_\phi = mLF_\phi FS \tag{8.33}$$

$$F_\theta = mLF_\theta FS \tag{8.34}$$

Where ϕ is the axial direction and θ is the lateral direction. Note that for the diagonal members in each of the trusses, the forces subjected onto them are a combination of the

axial and lateral loads. This is computed as the resultant of the lateral and axial loads:

$$F_{diagonal} = \sqrt{F_{\phi}^2 + F_{\theta}^2} \tag{8.35}$$

Once the forces are computed, Euler's Buckling Analysis is done to find the area moment of inertia for each truss member [61]. This is given through equation 8.36:

$$I_{member} = \frac{F L_{member}^2}{\pi^2 E} \tag{8.36}$$

L_{member} is the length of the member and E is the elastic modulus of the material used in the members. Once the area moment of inertia is calculated, the area moment of inertia is expressed in Equation 8.37 since the truss is a hollow cylinder:

$$I_{member} = \frac{\pi}{4}(R_o^4 - R_i^4) \tag{8.37}$$

R_o is the outer radius and R_i is the inner radius of the member [61]. The inner radius can be substituted as a function of the thickness and the above equation can be used to calculate the outer radius. For all of the members, a thickness-to-outer radius ratio n is selected. The function for inner radius is in Equation 8.38:

$$R_i = R_o - t_{member} \tag{8.38}$$

With the equation for thickness t_{member} in terms of outer radius being

$$t_{member} = nR_o \tag{8.39}$$

the function for inner radius in terms of outer radius is written in Equation 8.40:

$$R_i = R_o(1 - n) \tag{8.40}$$

Then, substituting the inner radius function into the equation for the area moment of inertia, the outer radius for each member can be found:

$$R_o = (\frac{4I_{member}}{\pi(1-(1-n)^4)})^{1/4} \tag{8.41}$$

Once the outer radius is found for each member, the cross-sectional area can be determined for member:

$$A_{member} = \pi(R_o^2 - R_i^2) \tag{8.42}$$

With this, the stress on the hollow cylinder can be found:

$$\sigma_{current} = \frac{F}{A_{member}} \tag{8.43}$$

This stress can be compared to the allowable stress of the material, which is calculated using the formula below:

$$\sigma_{allowable} = \frac{X_{failure}}{FS} \tag{8.44}$$

For the truss rings, the analysis is the same, except that the lateral stress on the rings are different. The lateral stress on the rings are approximated as twice the axial stress, due to the lateral loads and approximations as a thin cylinder [62].

$$\sigma_{lateral} = 2\sigma_{axial} \tag{8.45}$$

The sizing methods for the truss rings are the same, the only difference is the material being used is AM162 AlBeMet alloy.

8.5.3 Main Truss

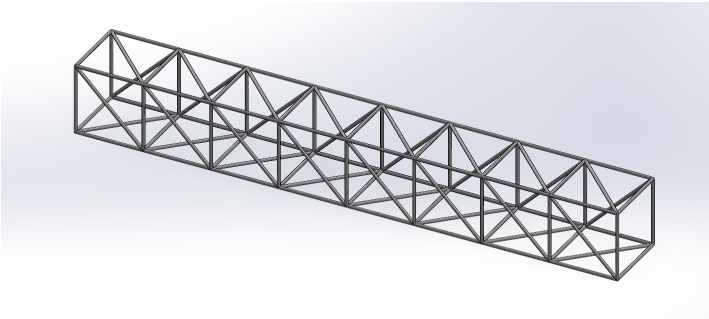

Figure 8.6: Main Truss

For designing the main truss, most of the analysis considers buckling analysis for each of the straight hollow cylinders. 1 cell of the main truss consisted of a box cross-section and each face of the cell consisted of 1 diagonal member and 4 side members. The thickness-to-outer radius ratios for the main truss members are 0.3 for the side members and 0.4 for the diagonal members.

Using Euler's Buckling Analysis for the straight hollow cylinders, the main truss's members are sized and analyzed, comparing the final stresses on the members to the allowable stresses of the IM7/5555 composites. Running the analysis, the dimensions, mass, and stresses of each member of the main truss is in Table 8.13:

Truss	Main Truss		Units
Components	Side	Diagonal	
Number of cells	8		-
Number of members	8	4	-
L_{member}	3.5	4.95	m
D_o	0.154	0.15	m
t_{member}	0.023	0.021	m
Max $\sigma_{current}$	507.8	491.8	MPa
$\sigma_{allowable}$	886.67		MPa
m_{member}	3.18	2.022	mT
m_{total}	5.202		mT

Table 8.13: Dimensions, Stresses, and Mass of Main Truss

From Table 8.13, it is seen that all of the main truss components' maximum stress values from launch loading are well within the longitudinal allowable stress of the IM7/5555 composite; therefore, the main truss is structurally sound.

Additionally, the load paths of the main truss during the mission are included. The main loads that the main truss will endure in the mission are loads from the Earth Departure, Mars Departure, and Mars Capture Tanks, as well as the loads from the solar panels, habitat module, and connection truss. The load paths on the full main truss are shown in Figure 8.7:

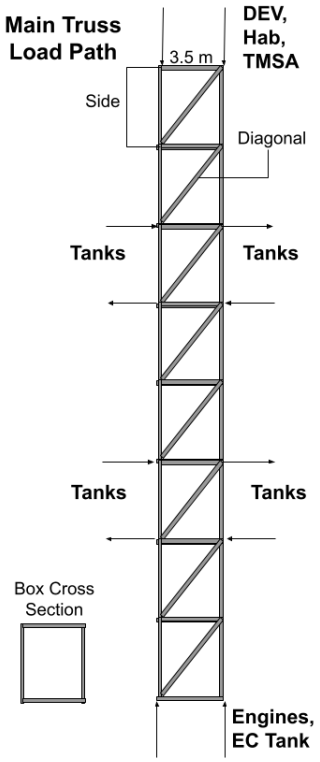

Figure 8.7: Main Truss Load Paths

8.5.4 Triangular Truss

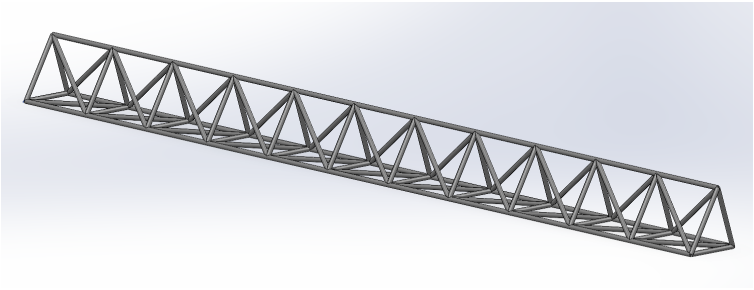

Figure 8.8: Triangular Truss

For designing the triangular trusses, the process for analysis and sizing of the individual truss members are the same as the main truss. The only difference is that there are only 3 faces per cell, as opposed to the 4 faces per cell in the main truss due to the triangular cross-section. The number of diagonal and side members in each face remains the same. The thickness-to-outer radius ratios for the triangular truss members are 0.3 for the side

members and 0.4 for the diagonal members. 4 of these triangular trusses will be used for the spacecraft to ensure that the loading of the engines are not thrusting into the Earth Capture propellant tank during the mission.

Using Euler's Buckling Analysis for the straight hollow cylinders, the triangular truss's members are sized and analyzed, comparing the final stresses on the members to the allowable stresses of the IM7/5555 composites. Running the analysis, the dimensions, mass, and stresses of each member of the triangular truss is in Table 8.14:

Truss	Triangular Trusses		
Components	Side	Diagonal	Units
Number of cells	44		-
Number of members	9	3	-
L_{member}	2	2.82	m
D_o	0.118	0.115	m
t_{member}	0.018	0.017	m
Max $\sigma_{current}$	860.5	468.4	MPa
$\sigma_{allowable}$	886.67		MPa
m_{member}	6.178	2.922	mT
m_{total}	9.1		mT

Table 8.14: Dimensions, Stresses, and Mass of Triangular Truss

From Table 8.14, it can be seen that all of the triangular truss components' maximum stress values from launch loading are well within the longitudinal allowable stress of the IM7/5555 composite; therefore, the triangular trusses are structurally sound.

The load paths of the triangular truss during the mission are included. The main loads that the triangular truss will endure in the mission are loads from the connection truss and loads from the engine thrust structure. The load paths on the triangular truss are shown in Figure 8.9:

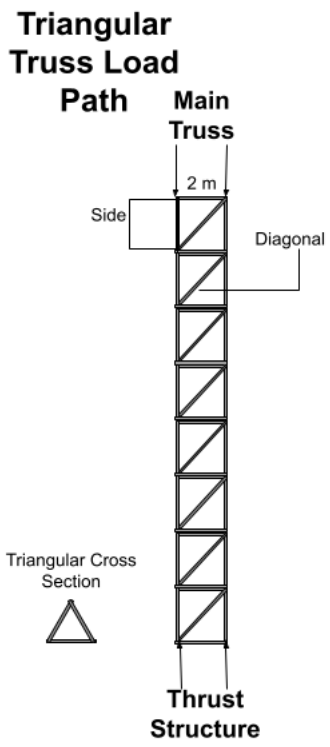

Figure 8.9: Triangular Truss Load Paths

8.5.5 Connection Trusses

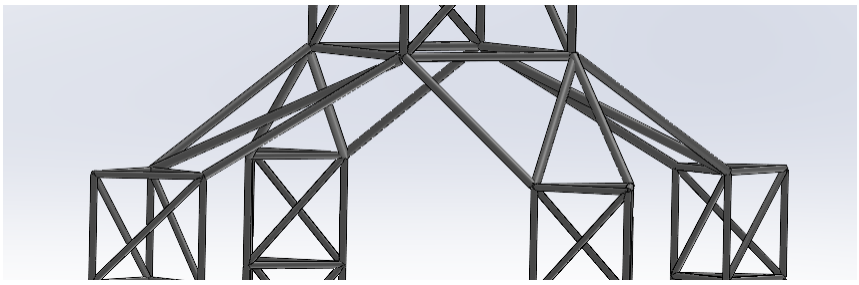

Figure 8.10: Connection Truss

The members that connect to the trusses are evaluated similarly to the main and triangular trusses. There are 4 connection faces that go from the main truss to 1 of the triangular trusses. Each face consists of 2 external members that connect from the trusses on each edge, as well as 1 internal middle member for stability. The thickness-to-outer radius ratio chosen for the connection truss members is 0.1.

Using Euler's Buckling Analysis for the straight hollow cylinders, the connection truss's members are sized and analyzed, comparing the final stresses on the members to the allowable stresses of the IM7/5555 composites. Running the analysis, the dimensions, mass, and stresses of each member of the connection truss are shown in Table 8.15:

Components	Middle Members from Main to Triangular	External Members from Main to Triangular	Units
Number of Members	4	8	-
L_{member}	5.062	4.316	m
D_o	0.1750	0.1547	m
t_{member}	0.0175	0.0155	m
Max $\sigma_{current}$	129	151.8	MPa
$\sigma_{allowable}$	886.67	886.67	MPa
m_{member}	0.3503	0.2631	mT
m_{total}	0.6134		mT

Table 8.15: Dimensions, Stresses, and Mass of Connection Truss

From Table 8.15, it can be seen that all of the maximum stress values of the connection truss components from launch loading are well within the longitudinal allowable stress of the IM7/5555 compound it is made of; therefore, the connection trusses are structurally sound.

The load paths of the connection truss during the mission are included. The main loads that the connection truss will endure in the mission are loads from the main truss and loads from triangular trusses. The load paths on the connection truss are shown in Figure 8.11:

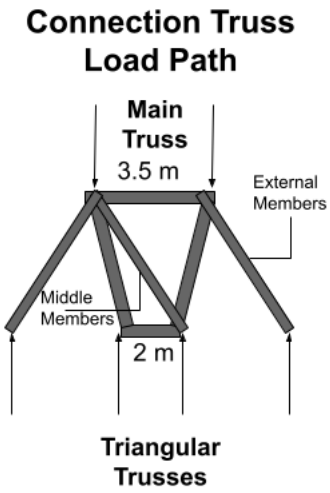

Figure 8.11: Connection Truss Load Paths

8.5.6 Engine Thrust Structure

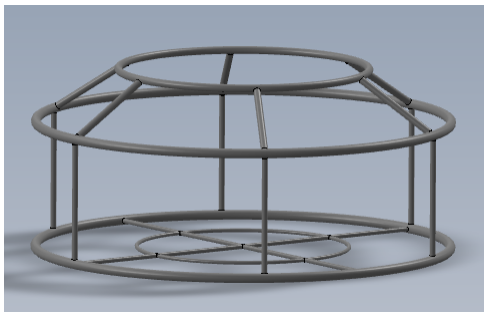

Figure 8.12: Engine Thrust Structure

The engine thrust structure is designed differently from the other trusses. This structure has to fit and mount 3 *Harmonia* Nuclear Thermal Rocket Engines that will be used during travel, as well as 3 engines for the OMS. Additionally, the thrust structure will store the propellant tanks for the orbital maneuvering system. This truss also has to connect to the triangular truss members as well to ensure that no thrusting is set into the Earth Capture tank, and be able to fit the propellant tanks for the orbital maneuvering system engines. The members of this structure undergoing launch loading includes 3 hollow rings, 6 vertical truss members that connect the 2 larger rings, and 6 diagonal truss members that connect the smaller ring to the larger rings. The thickness-to-outer radius ratio for

the thrust structure members is 0.1.

Using Euler's Buckling Analysis for the straight hollow cylinders and the ring truss analysis, the thrust structure's members are sized and analyzed, comparing the final stresses on the members to the allowable stresses of the IM7/5555 composite for the cylindrical members and the AlBeMet AM162 alloy for the rings. Running the analysis, the dimensions, mass, and stresses of each member of the thrust structure are in Table 8.16:

Truss	Engine Thrust Structure				
Section	Connections to Triangular Trusses		Connections to Engines		
Components	Horizontal Rings	Vertical Members	Diagonal Members	Horizontal Ring	Units
Number of Members	2	6	6	1	-
L_{member}	34.558	3	2.31	19.792	m
D_o	0.25	0.152	0.186	0.2	m
t_{member}	0.025	0.015	0.019	0.02	m
D_{ring}	11	N/A	N/A	6.7	m
Max $\sigma_{current}$	55.6	184.9	149	86.9	MPa
$\sigma_{allowable}$	110	886.67	886.67	110	MPa
$m_{component}$	2.529	0.174	0.207	0.478	mT
m_{total}	3.388				mT

Table 8.16: Dimensions, Stresses, and Mass of the Thrust Structure

From Table 8.16, it can be seen that all of the thrust structure cylindrical members' maximum stress values from launch loading are well within the longitudinal allowable stress of the IM7/5555 composite, and all of the thrust structures' rings have maximum lateral stress values that are well within the transverse allowable stress of the AlBeMet AM162 alloy; therefore, the thrust structure is structurally sound.

The load paths of the thrust structure during the mission is included. The main loads that the thrust structure will endure in the mission are loads from the triangular trusses and the loads from the engines. The load paths on the thrust structure are shown in Figure 8.13:

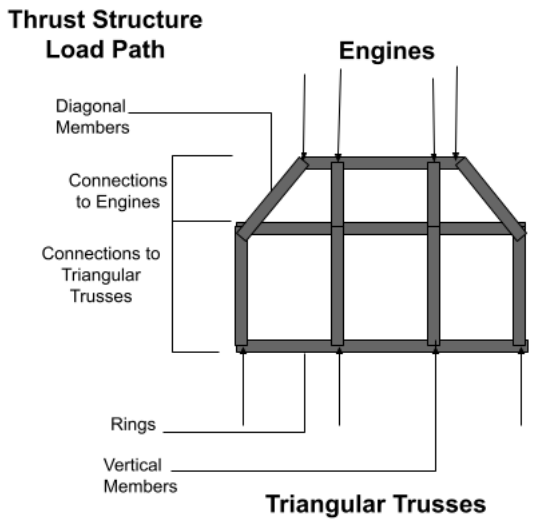

Figure 8.13: Thrust Structure Load Paths

8.6 Payload Adapter

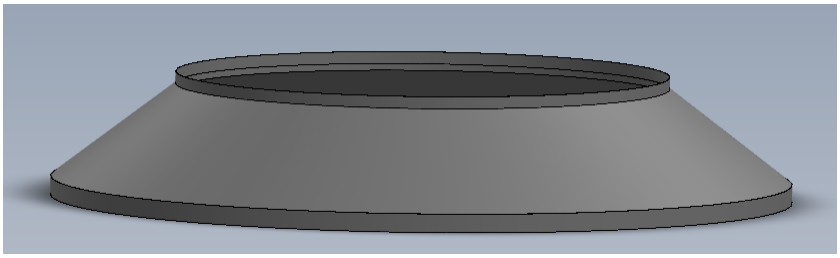

Figure 8.14: Payload Adapter

8.6.1 Design Decisions

A payload adapter has been developed to fit all 6 SLS launches. The design for the payload adapter is similar to the SLS Launch vehicles [63]. Geometrically, the payload adapter is made of 2 rings and a conical frustum to adapt the payload to the rest of the SLS rocket. The 2 rings are made of AlBeMet AM162 alloy, and the frustum is made out of T800S carbon fiber composite [17]. The material properties for the components are in Table 8.17:

Material Properties	AlBeMet AM162	T800S Carbon Fibre	Units
X_{fl}	322	3000	MPa
X_{ft}	165	64	MPa
E	193	294	GPa
Density	2071	1800	kg/m^3
Allowable X_{lf}	214.67	2000	MPa
Allowable X_{tf}	110	42.67	MPa
ν	0.17	0.35	-

Table 8.17: Material Properties for Payload Adapter Components [16][17]

Since these are only used in launch loading, the payload adapters are sized and fitted for launch and are mainly designed to fit the propellant tanks and the engines based on the launch packaging. Critical compression and bending analysis will be conducted on the payload adapters, fitted with a factor of safety of 1.5 [64].

8.6.2 Payload Adapter Analysis

To size the payload adapter, the top has to be designed to fit the payload it interacts with. Launches 1 through 5 all have the same payload adapter, as the payload it fits through are the propellant tanks. Launch 6 has a different payload adapter to fit the IPV engines. The base of the payload adapter has to fit to the rest of the SLS Launch Vehicle [63]. For the payload adapter, the conical frustum can be analyzed for critical buckling forces [64]. Approximating as a thin cone, the critical force is calculated as

$$F_{critical} = \gamma \frac{2\pi E t^2 cos^2(\alpha)}{\sqrt{3(1-\nu^2)}} \tag{8.46}$$

Where α is the angle between the vertical and the surface of the frustum, ν is the Poisson's ratio, t is the thickness of the frustum, and E is the Young's modulus. γ is an empirical

factor that can be calculated [64]. For thin conical frustums, the γ parameter is

$$\gamma = \frac{0.83}{\sqrt{(1 + 0.01\frac{\rho_o}{t})}} for \frac{\rho_o}{t} \leq 212 \tag{8.47}$$

Where ρ_o is the knockdown factor dependent on the top outer radius of the frustum and the angle α. The equation to find ρ_o is below:

$$\rho_o = \frac{R_o}{cos(\alpha)} \tag{8.48}$$

Once this is calculated, the stress is found by dividing the critical force by the cross-sectional area of the top of the frustum. This can then be compared to the current axial stresses to see if the frustum can handle the loads. For the payload adapter, the rings are flat and thin. Approximating the rings as thin cylinders, the critical stresses for bending and compression can be calculated [64]. Sizing the diameters of the rings are due to the top and base diameters of the conical frustum. With a chosen thickness, the stresses can be computed as

$$\sigma_{critical} = \gamma \frac{E}{\sqrt{3(1 - \nu^2)}} \frac{t}{R_o} \tag{8.49}$$

Where E is the Young's modulus, ν is the Poisson's ratio, and r is the radius of the ring. The γ is an empirical factor dependent on the type of stress. For compression stress, γ is

$$\gamma_{compression} = 1 - 0.9(1 - e^{-\Phi}) \tag{8.50}$$

For the critical bending empirical factor, gamma is

$$\gamma_{bending} = 1 - 0.731(1 - e^{-\Phi}) \tag{8.51}$$

Where Φ is dependent on the radius-to-thickness ratio. For thin cylinders, Φ is equated as

$$\Phi = \frac{1}{15}\sqrt{\frac{R_o}{t}} \tag{8.52}$$

Once these stresses are calculated, they are compared to the actual axial and lateral stresses from the loading conditions to see if they can handle the loads.

8.6.3 Payload Adapter Results

Conical Frustum Using the analysis of critical stresses via approximating the frustum as a thin cone, the dimensions, mass, and critical stresses of the frustum of the payload adapter is in Table 8.18:

PLA	Launch 1-5	Launch 6	Units
α	52.8	45	$^\circ$
D_b	12		m
D_t	8	9	m
$t_{frustum}$	0.010		m
$h_{frustum}$	1.520		m
Max $\sigma_{cr,c}$	89		MPa
Max $\sigma_{cr,b}$	129		MPa
Max $\sigma_{current}$	28.83	25.63	MPa
$m_{frustum}$	0.858	0.901	mT

Table 8.18: Dimensions, Stresses, and Mass of Payload Adapter Frustum

From Table 8.18, it is seen that the frustum's maximum stress values from launch loading are well within the critical compression and bending stresses for both payload adapters made of T800S Carbon Fiber; therefore, the frustum of the payload adapters are structurally sound.

Rings Using the analysis of critical stresses via approximating thin cylinders for the rings, the dimensions, mass, and critical stresses of the rings of the payload adapter are in Table 8.19:

PLA	Launch 1-5	Launch 6	Units
D_b	12.000		m
D_t	8.000	9.000	m
t_{rings}	0.010		m
h_{rings}	0.300		m
Base $\sigma_{cr,b}$	25.41		MPa
Base $\sigma_{cr,c}$	41.87		MPa
Top $\sigma_{cr,b}$	47.36	39.58	MPa
Top $\sigma_{cr,c}$	70.32	60.46	MPa
Base Max $\sigma_{current}$	11.05		MPa
Top Max $\sigma_{current}$	16.58	14.73	MPa
$m_{ring,base}$	0.234		mT
$m_{ring,top}$	0.156	0.175	mT

Table 8.19: Dimensions, Stresses, and Mass of Payload Adapter Rings

From Table 8.19, it can be seen that the rings' maximum stress values from launch loading are well within the critical compression and bending stresses for both payload adapters made of the AlBeMet AM162 alloy; therefore, the rings of the payload adapters are structurally sound. The total mass for each payload adapter is about **1.25 mT** for Launches 1-5 and **1.3 mT** for Launch 6.

8.6.4 Payload Adapter Load Paths

The load paths of the payload adapter during launch are included. The main loads that the payload adapter will endure are loads from the payload and loads from the rest

of the SLS Launch Vehicle. The load paths on the payload adapter are shown in Figure 8.15:

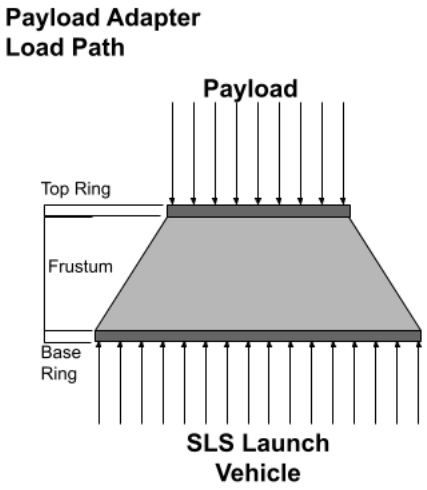

Figure 8.15: Payload Adapter Load Paths

8.7 Launch Vibration Analysis

8.7.1 Analysis Approach

Upon launch of the IPV components by the SLS, the payloads experience significant vibrational loading. The main limiting consideration of this vibrational loading is the resonance phenomena. When the frequency of forcing applied by the SLS, ω_f, upon launch equals the resonant frequency of the stacked payloads, ω_n, detrimental structural effects can occur. To prevent this, the resonant frequency of the stacked payloads must be determined through a simplified analysis. During the launch and ascent regime of flight, there are three basic types of flight environments that are considered: low frequency dynamic response, high frequency random vibration environment, and high frequency acoustic pressure environment. To simplify the analysis, only low frequency dynamic response loading is investigated in the analysis. Since the specific forcing functions for the SLS launcher are not readily available, the SLS Mission Planner's Guide is consulted to determine the minimum acceptable payload cantilevered fundamental frequencies. The

objective of the analysis is to ensure that each payload stack has a fundamental frequency that is at least 1.5 times greater than the minimum acceptable payload cantilevered fundamental frequency (NASA-STD-5002 Section 4.7.2 [65]). Table 8.20 displays the minimum acceptable cantilevered frequencies in order to apply certain design load factors.

Parameter	Value	Unit
$\omega_{n_{lat}}$	8	Hz
$\omega_{n_{axial}}$	15	Hz

Table 8.20: Minimum Acceptable Payload Cantilevered Fundamental Frequency

To examine the payload stacked cantilevered fundamental frequencies for each launch configuration, a simplified mass-spring model is analyzed. Figure 8.16 displays the mass-spring configuration for both the axial and lateral modes. In the axial cantilever bending mode, it is assumed that all payloads are supported individually by a rigid external support structure located in the fairing. In the lateral cantilever bending mode, it is assumed that the payload stack acts as a single cantilever beams. Each item being launched is considered to be a mass, m, with stiffness, k. Damping is not considered in the model due to its small effect on the natural frequency of the system. The forcing function of the SLS is not considered because it is not readily publicly available. Additionally, the low number of SLS launches means that there is not an adequate amount of flight data. Figure 8.16 considers a case in which there are three payload elements on a launch. The analysis is easily expanded for launches containing more or less individual payload elements. In both axial and lateral vibrational analyses, a diagonal mass matrix is constructed. A general form of this matrix is shown in Equation (8.53). n denotes the number of payload elements in each launch.

$$[m] = \begin{bmatrix} m_p & 0 & 0 & 0 \\ 0 & m_{n-2} & 0 & 0 \\ 0 & 0 & m_{n-1} & 0 \\ 0 & 0 & 0 & m_n \end{bmatrix} \tag{8.53}$$

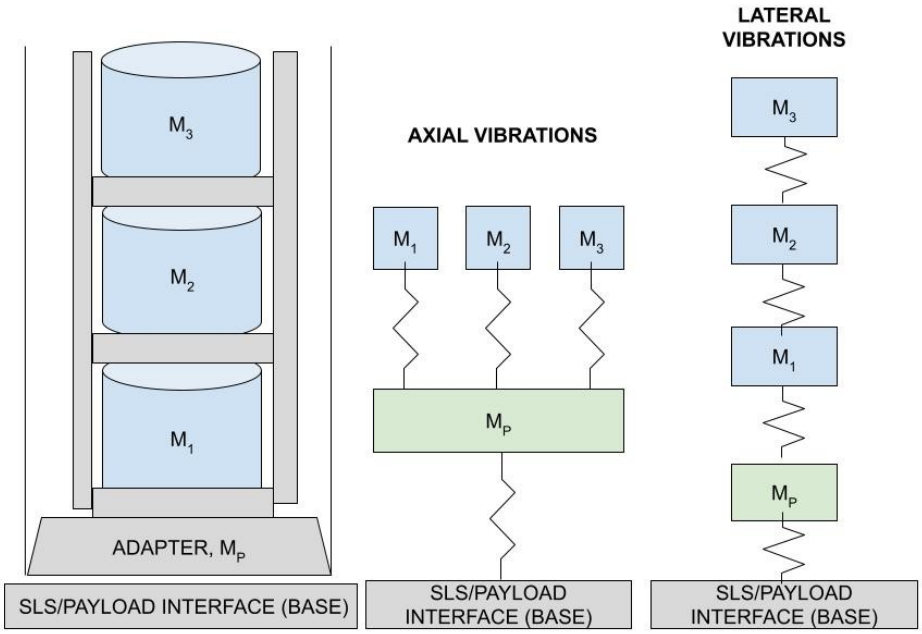

Figure 8.16: Vibration Analysis Model

For both modes of vibrations, Equation (8.54) is used to compute the natural frequency for each payload stack configuration and mode. The generalized eigenvalue problem is solved in each case.

$$[K][x] = [\lambda][M][x] \tag{8.54}$$

The natural frequencies of the system are expressed in Equations 8.55 and (8.56).

$$\omega_n = \sqrt{[\lambda]} \tag{8.55}$$

$$f = \frac{\omega_n}{2\pi} \tag{8.56}$$

Axial Stiffness Matrix Derivation for General Case In both the axial and the lateral cases, Lagrange method is used to compute the stiffness matrices for a system with n payloads attached to the payload adapter. First, the axial stiffness matrix is derived. The

Lagrangian is defined as:

$$L = T - V \tag{8.57}$$

The general differential for the Lagrangian is written in Equation 8.58.

$$\frac{d}{dt}\left(\frac{\partial L}{\partial \dot{x}_i}\right) - \frac{\partial L}{\partial x_i} = 0 \tag{8.58}$$

The kinetic energy, T, can be defined as:

$$T = \frac{1}{2}M_p\dot{x}_p^2 + \sum_{i=1}^{n}\frac{1}{2}m_i\dot{x}_i^2 \tag{8.59}$$

For this particular arrangement, the potential energy, V is defined in Equation (8.60)

$$V = \sum_{i=1}^{n}\frac{1}{2}k_i(x_p - x_i)^2 \tag{8.60}$$

Equation (8.60) is expanded into Equation (8.61).

$$V = \frac{1}{2}\left(\sum_{i=1}^{n}k_i\right)x_p^2 - \sum_{i=1}^{n}k_i x_p x_i + \sum_{i=1}^{n}\frac{1}{2}k_i x_i^2 \tag{8.61}$$

$$\mathbf{x} = \begin{bmatrix} x_p \\ x_1 \\ x_2 \\ \vdots \\ x_n \end{bmatrix} \tag{8.62}$$

After the necessary derivatives are taken and the equations of motion are written in matrix form, the stiffness matrix can be expressed in a general form with Equation (8.63).

$$\mathbf{K_a} = \begin{bmatrix} \sum_{i=1}^{n} k_i & -k_1 & -k_2 & \dots & -k_n \\ -k_1 & k_1 & 0 & \dots & 0 \\ -k_2 & 0 & k_2 & \dots & 0 \\ \vdots & \vdots & \vdots & \ddots & \vdots \\ -k_n & 0 & 0 & \dots & k_n \end{bmatrix} \tag{8.63}$$

Lateral Stiffness Matrix Derivation for a General Case In a similar method to the axial stiffness matrix, the lateral stiffness matrix is defined in Equation (8.65). The kinetic energy is identical to the axial vibration mode. In the lateral case, the potential energy can generally be expressed in Equation (8.64)

$$V = \frac{1}{2}k_p x_p^2 + \sum_{i=1}^{n} \frac{1}{2}k_i (x_{i-1} - x_i)^2 \tag{8.64}$$

After taking necessary derivatives and writing the equations of motion in matrix form yet again.

$$\mathbf{K_l} = \begin{bmatrix} k_p + k_1 & -k_1 & 0 & \dots & 0 \\ -k_1 & k_1 + k_2 & -k_2 & \dots & 0 \\ 0 & -k_2 & k_2 + k_3 & \dots & 0 \\ \vdots & \vdots & \vdots & \ddots & -k_n \\ 0 & 0 & 0 & -k_n & k_n \end{bmatrix} \tag{8.65}$$

For the first mass-spring element:

$$M_p \ddot{x}_p + (k_p + k_1)x_p - k_1 x_1 = 0$$

For the intermediate masses:

$$m_i\ddot{x}_i + (k_i + k_{i+1})x_i - k_i x_{i-1} - k_{i+1}x_{i+1} = 0, \quad i = 1, \ldots, n-2$$

For the last mass:

$$m_{n-1}\ddot{x}_{n-1} + k_n x_{n-1} - k_n x_{n-2} = 0$$

Computing Individual Payload Element Stiffnesses A series of MATLAB codes to analyze the lateral and axial natural frequencies are in Appendix A.1.2. The stiffness of each individual payload element is computed by treating the each element as a cantilever beam. The lateral mode individual stiffnesses for each payload element, n, are calculated using Equation (8.66).

$$k_{l_n} = \frac{EI_{xx}}{L^3} \tag{8.66}$$

For a square beam, I_{xx} is expressed as

$$I_{xx} = \frac{bd_o^3}{12} - \frac{bd_i^3}{12} \tag{8.67}$$

For a cylindrical shell, I_{xx} is expressed as

$$I_{xx} = \frac{\pi}{4}(r_o^4 - r_i^4) \tag{8.68}$$

The axial mode individual stiffnesses for each payload element, n, are calculated using Equation (8.69).

$$k_{a_n} = \frac{EA_{cs_n}}{L} \tag{8.69}$$

8.7.2 Analysis Results

Tables 8.21 - 8.24 shows the stiffness and mass of each individual payload element for each launch. Table 8.25 also shows the lowest stacked payload natural frequency output

from the MATLAB code.

	Launch 1		Launch 2		Launch 3	
Stiffness	**Component**	$k_l\ (N/m)$	**Component**	$k_l\ (N/m)$	**Component**	$k_l\ (N/m)$
k_1	Adapter	6.11E+12	Adapter	6.11E+12	Adapter	6.11E+12
k_2	ED	9.43E+09	EDT	9.43E+09	MC	1.56E+10
k_3	Truss	4.23E+10	EDT	9.43E+09	ED	9.43E+09
k_4	Assem	1.53E+10			IPV Hab	6.34E+09
k_5	Orion	4.54E+09				

Table 8.21: Payload Element Stiffnesses for Launches 1-3

	Launch 4		Launch 5		Launch 6	
Stiffness	**Component**	$k_l\ (N/m)$	**Component**	$k_l\ (N/m)$	**Component**	$k_l\ (N/m)$
k_1	Adapter	6.11E+12	Adapter	6.11E+12	Adapter	6.11E+12
k_2	MD	3.07E+10	ECT	4.90E+09	Engines	3.11E+11
k_3	MC	1.56E+10	Truss	3.21E+10	MDT	3.07E+10
k_4	DeV	3.95E+10			Orion	4.54E+09
k_5	TMSA	2.00E+09			IPV Hab	6.34E+09

Table 8.22: Payload Element Stiffnesses for Launches 4-6

	Launch 1		Launch 2		Launch 3	
Mass	**Component**	$m\ (kg)$	**Component**	$m\ (kg)$	**Component**	$m\ (kg)$
m_1	Adapter	9.43E+02	Adapter	9.43E+02	Adapter	9.43E+02
m_2	ED	7.35E+04	EDT	7.35E+04	MCT	5.53E+04
m_3	Truss	5.97E+03	EDT	7.35E+04	EDT	7.35E+04
m_4	Assem	9.40E+02			IPV Hab	4.30E+04
m_5	Orion	3.30E+04				

Table 8.23: Payload Element Masses for Launches 1-3

	Launch 4		Launch 5		Launch 6	
Mass	**Component**	$m\ (kg)$	**Component**	$m\ (kg)$	**Component**	$m\ (kg)$
m_1	Adapter	9.43E+02	Adapter	9.43E+02	Adapter	9.43E+02
m_2	MD	4.10E+04	ECT	1.02E+05	Engines	1.80E+04
m_3	MC	5.53E+04	Truss	9.94E+03	MDT	4.10E+04
m_4	DeV	2.00E+04			Orion	3.30E+04
m_5	TMSA	4.00E+03			IPV Hab	6.34E+09

Table 8.24: Payload Element Masses for Launches 4-6

Launch Number	ω_{n_a}	ω_{n_l}
1	25.74	38.2
2	25.23	35.6
3	25.56	42.4
4	31.3	54.8
5	20.3	33.7
6	27.1	32.5

Table 8.25: Axial and Lateral Natural Frequencies for All Launches

8.8 Micro-meteoroid and Orbital Debris Shielding

A major risk for the spacecraft is MMOD in Earth orbit, during interplanetary travel, and in Mars orbit. Thus, shielding for protection against MMOD is implemented. Using the NASA "Handbook for Designing MMOD Protection," the type and sizing of the shielding is calculated [29]. The handbook provides equations and constants for those equations, which are listed in Table 8.26.

Constants	
c_0	0.38
c_b	0.15
c_{n-k}	0.23
c_w	8.84 s/km

Table 8.26: Constants for MMOD Shielding Equations

The maximum characteristics of MMOD were assumed to be a diameter of 1 cm, density of 2.5 g/cm^3, and an impact velocity normal to the shield of 10.5 km/s, a worse case scenario, as shown in Table 8.27 [29].

Maximum Allowable MMOD		
Diameter (cm)	d	1
Density (g/cm^3)	ρ_p	2.5
Mass (g)	M_p	1.31
Impact Velocity (km/s), normal to shield	V_n	10.5

Table 8.27: Maximum Allowable MMOD

From these values, a maximum mass is calculated to be 1.31g using equation 8.70.

$$M_p = \frac{4}{3}\pi \left(\frac{d}{2}\right)^3 \rho_p \tag{8.70}$$

The type of shielding chosen is a triple-wall Nextel/Kevlar stuffed Whipple shield. A Whipple shield consists of a "bumper wall", a space under vacuum, and then a "rear wall"; sometimes doubling as the pressure vessel wall. The bumper wall is the outermost wall and serves the purpose of breaking up the MMOD. The smaller pieces decrease in

velocity as they travel through the vacuum, and the impact is lessened on the rear wall due to the decrease in velocity as well as the impact being spread out over a larger surface area. The rear wall is designed to prevent fragments from penetrating the pressure vessel. This method of shielding has the same effectiveness as a single-wall shield, but has a lower mass. The addition of a Nextel layer and a Kevlar layer between the bumper and rear walls increases the effectiveness of the shielding. Nextel is a ceramic fabric and Kevlar is a high strength fabric. Nextel breaks the MMOD down further, then the Kevlar slows the debris and stops some fragments from reaching the rear wall. The fabric layers are placed halfway between the bumper and rear wall.

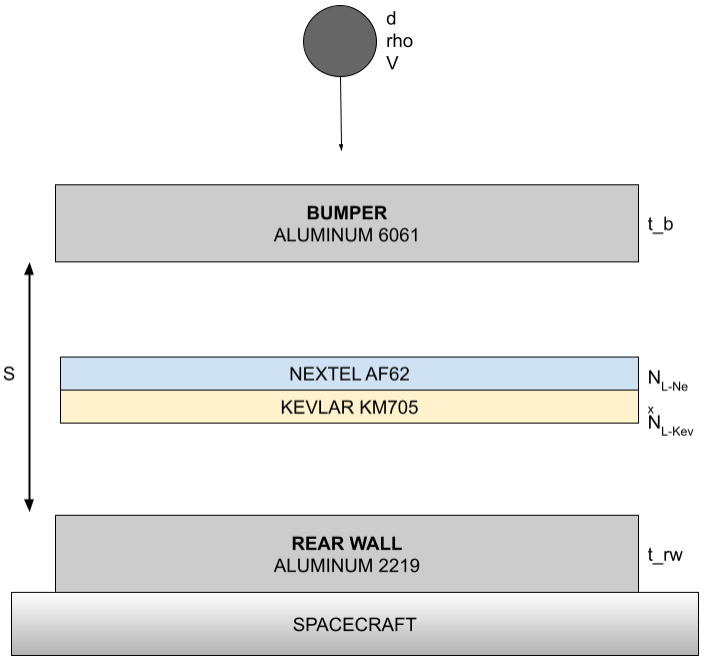

Figure 8.17: MMOD Shield Notional Diagram

The materials for each layer are chosen for consistency with NASA handbook JSC-64399 [29]. The material properties are listed in Table 8.28 [66].

The handbook provides equations for calculating the thicknesses of each layer. The bumper thickness is calculated using Equation 8.71.

$$t_b = c_b d \rho_p / \rho_b \tag{8.71}$$

Material Properties		
Al 6061-T6		
Density (g/cm^3)	ρ_b	2.7
Nextel AF62		
Areal Density (g/cm^2)	m_{Nextel}	0.1
Areal Density Fraction	f_{Nextel}	0.75
Kevlar KM2 705		
Areal Density (g/cm^2)	m_{Kevlar}	0.023
Areal Density Fraction	f_{Kevlar}	0.25
Al 2219-T87		
Density (g/cm^3)	ρ_w	2.84
Yield Strength (ksi)	σ	57

Table 8.28: MMOD Shield Material Properties

The Nextel and Kevlar combined areal density is calculated using Equation 8.72, which results in a value of 0.575 g/cm^2.

$$m_{Nextel-Kevlar} = c_{N-K} d \rho_p \tag{8.72}$$

From that value, the number of Nextel and Kevlar layers are calculated, using the areal density fractions for each material, Equations 8.73 and 8.74 respectively.

$$n_{Nextel} = \frac{m_{N-K} f_{Nextel}}{m_{Nextel}} \tag{8.73}$$

$$n_{Kevlar} = \frac{m_{N-K} f_{Kevlar}}{m_{Kevlar}} \tag{8.74}$$

It is determined that five layers of Nextel and seven layers of Kevlar are required to satisfy the design parameters. The spacing between the bumper and rear wall is chosen to be S = 20cm. This is chosen to be thicker than the shields tested in JSC-64399 as a larger distance allows the MMOD to have a larger decrease in velocity, which in turn allows the layers to be thinner. Thinner layers lead to less mass. The thickness of the rear wall is calculated with Equation 8.75.

$$t_w = c_w[\frac{c_0 d\rho_p}{(t_b\rho_p + m_{Nextel-Kevlar)}}]^{1.1} M_p^{1/3} V_n (cos^{0.5}\theta)\rho_w^{-1} S^{-2} (\sigma/40)^{-0.5} \tag{8.75}$$

The impact angle as measured from normal to the shielding, θ, is $0°$, since the calculations are performed assuming the worst scenario, where the MMOD is impacting normal to the shielding. The thicknesses for all layers are listed in Table 8.29. The rear wall on the IPV does not act as the pressure vessel wall, as there is insulation and radiation shielding between the rear wall and the pressure vessel wall, as discussed in Sections 10.5 and 12.4, respectively. A drawing of a cross section of MMOD shielding on the IPV Hab can be seen in Appendix A.4. Each layer is included in the CAD model as separate parts, so the materials can be assigned correctly.

Layer	Material	Thickness (m)
Rear Wall	Al 2219-T87	0.000774
Vacuum	-	0.0993
Kevlar	KM2 705	0.00100
Nextel	AF-52	0.00160
Vacuum	-	0.0981
Bumper	Al 6061-T6	0.00139

Table 8.29: Thicknesses of MMOD Shielding Layers

9 Propulsion

9.1 Introduction

There are four main propulsion methods for the IPV and DEV. The IPV's main propulsion system is an NTP system nicknamed Harmonia. The IPV also has a bi-propellant gas generator engine cycle to assist in small orbital maneuvers and to perform orbital corrections as needed within its propellant margins. The Deimos Excursion Vehicle is equipped with RCS as well as a bi-propellant pressure-fed system for travel between the IPV and Deimos.

	11. Propulsion		
11.1 Nuclear Thermal	11.2 IPV OMS	11.3 DEV RCS	11.4 DEV Main Thrusters
11.1.1 Overview	11.2.1 OMS Engine	11.3.1 Overview	11.4.1 Overview
11.1.2 Turbomachinery	11.2.2 Engine P&ID	11.3.2 Performance	11.4.2 Performance
11.1.3 Reactor Design	11.2.3 Engine Analysis	11.3.3 Design	11.4.3 Design
11.1.4 Performance	11.2.4 Trade Study		11.4.4 Operations
11.1.5 Nozzle Geometry	11.2.5 CAD		
11.1.6 Specific Impulse	11.2.6 Results		
11.1.7 Ullage and Fuselage			
11.1.8 Start Up and Cool Down			

9.2 Nuclear Thermal Propulsion

9.2.1 Overview

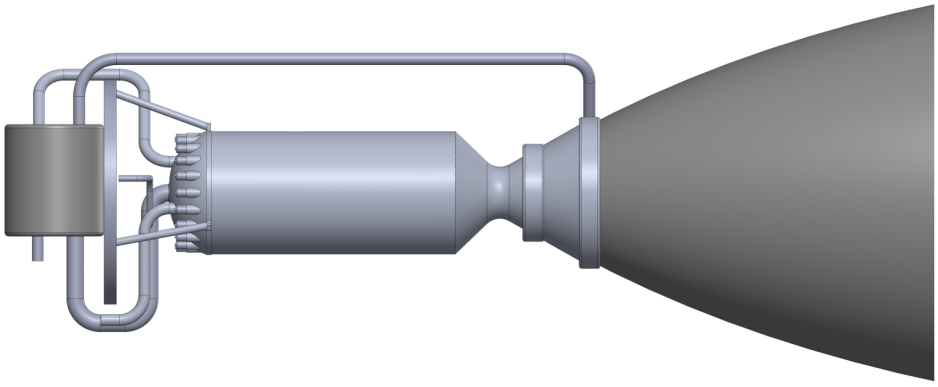

Figure 9.1: Harmonia Engine Assembly

Isp	Thrust (kN)	$\dot{m}$ (kg/s)	A_e/A_{th}	T_0 (K)	P_0 (MPa)
951	354	38	300	2700	0.504

Table 9.1: Hormonia Overall Performance

The Harmonia engine system Utilizes an expander cycle. The propellant selected for the NTP is hydrogen given its low molecular weight and the related benefit of chemical simplicity. The propellant is stored cryogenically at 20K and pumped as a liquid into the nozzle throat and reactor where it acts as a coolant. The system employs a five stage pump to increase the pressure of the propellant to drive it against the head loss through the downstream pipe systems. Heat is extracted from the nozzle and reactor walls by the pre-turbine propellant. The subsequent turbine extracts the necessary work from the propellant fluid in order to drive the pump with the capacity to power an electrical generator as needed. Propellant then flows through the reactor where the primary heating occurs through a parallel array of nuclear cores. Through the nozzle, the high pressure, high temperature hydrogen expands, converting internal energy into a high exhaust velocity.

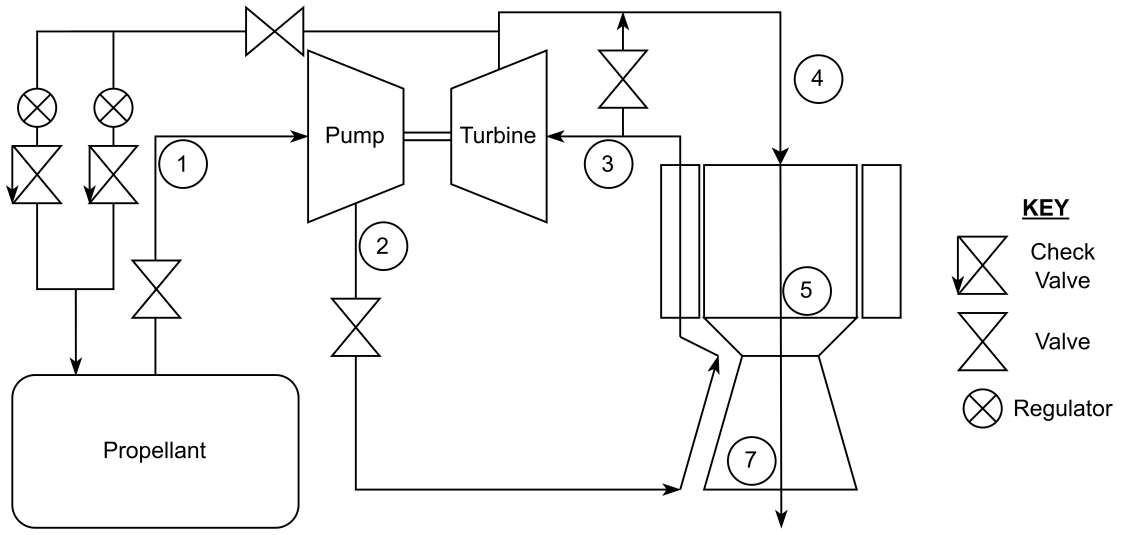

Figure 9.2: P&ID for the Harmonia Expander Engine

Table 9.2: Thermodynamic Flow States

Thermodynamic Flow States

	State	ṁ (kg/s)	T (K)	P (MPa)	h (kJ/kg)	s (kJ/kg K)	M	A / A*
1	**Propellant Tanks**	38	20	0.225	403.34	17.1		
2	**Pump Outlet**	38	61.28	11	629.66	28.55		
3	**Turbine Inlet**	38	400	11	5474.1	38.22		
4	**Reactor Inlet**	38	349.6	1.2	4675	45.86	0	
5	**Reactor Outlet**	38	2700	0.504			1	
6	**Throat**	38					1.001	5
7	**Exhaust**	38	30.112	8.3 Pa	566.72	65.46	8.83	300

9.2.2 Turbomachinery

In order to overcome head loss through the propellant pipes, a pump is utilized to increase the pressure of the hydrogen before it reaches the turbine. Head loss is calculated using the Darcy equation, (9.1). From the Darcy equation, the pressure loss through the pipe is calculated using equation (9.2). This pressure is subtracted from the total pressure rise through the pump. The friction factor is estimated using an approximate Reynolds

number [67].

$$H_f = f\frac{L}{D}\frac{v^2}{2g} \tag{9.1}$$

$$\Delta P = \rho g H_f \tag{9.2}$$

Inputs	f	L (m)	D (m)	v (m/s)	g (m/s^2)	ρ (kg/m^3)
Value	0.01	90	0.16	25	9.80665	71

Table 9.3: Head Loss Input Values

Outputs	H_f (m)	Δ P (MPa)
Value	199	0.137

Table 9.4: Head Loss Output Values

In order to avoid increasing the complexity of turbomachinery, the turbo pumps are not geared and therefore all have the same angular speed ω. The overall speed is set by the first pump stage. The initial pump specific speed is assumed to be 1. The maximum difference in pressure is calculated using the minimum pressure required to avoid cavitation (9.4).

$$\omega = \frac{n_{s_p}(P_{out} - P_{in})^{3/4}}{\rho^{1/4}\sqrt{\dot{m}_p}} \tag{9.3}$$

$$P_{in_{min}} = (1-\alpha)\sigma(P_{out} - P_{in}) + P_v \tag{9.4}$$

The suction speed parameter S_s is used to confirm that there is no cavitation in the pump. All S_s values are kept below 5.

$$S_s = \frac{\omega\rho^{1/4}\sqrt{\dot{m}_p}}{(P_{in} - Pv)^{3/4}} \tag{9.5}$$

$$d_{s_p} = \frac{D_p[\rho(P_{out} - P_{in}]^{1/4}}{\sqrt{\dot{m}_p}} \tag{9.6}$$

Stage	0	1	2	3	4	5
Pressure (kPa)	225	1306	2861	4737	7422	11133
n_{s_p}	1	0.75	0.7	0.65	0.6	
S_s	4.8515	0.9174	0.4941	0.3352	0.2381	
σ	0.25	1	1.75	2	2.25	
$P_{in_{min}}$ (kPa)	150	1306	2861	4737	7422	
d_{s_p}	2.5	3.0	4.0	4.0	4.0	
Dp (m)	0.0351	0.0321	0.0408	0.0373	0.0344	
ω (RPM)	21400					

Table 9.5: Pump States

In order to increase turbine efficiency, the single stage turbine shaft is geared so that the turbine shaft rotates at 1/5 the speed of the pumps. The turbine specific speed is calculated with this ratio in mind and the diameter of the turbine is calculated using an assumed specific diameter of 1.75 in order to achieve an efficiency of 80%.

$$n_{s_t} = \frac{\omega\sqrt{\dot{m}_t}}{\sqrt{\rho}(h_{in} - hout)^{3/4}} \tag{9.7}$$

$$d_{s_t} = \frac{D_t\sqrt{\rho}(h_{in} - h_{out})^{1/4}}{\sqrt{\dot{m}_t}} \tag{9.8}$$

Inputs	ω (rad/s)	$\dot{m}_t$ (kg/s)	h_{in} (J/K)	h_{out} (J/K)	ρ (kg/m^3)	d_{st}
Value	449	38	5474.1	4675	6.44645	1.75

Table 9.6: Turbine Input Values

Output	n_{st}	D_t (m)
Value	1.74	0.8

Table 9.7: Turbine Output Values

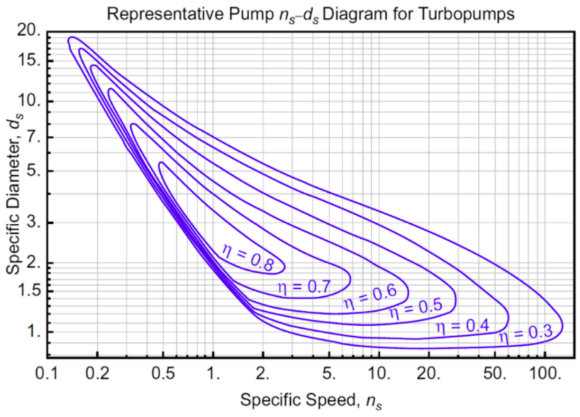

Figure 9.3: Pump efficiency [3]

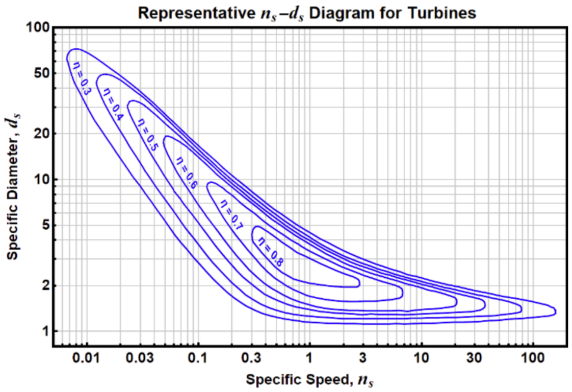

Figure 9.4: Turbine Efficiency [3]

Based on the above charts and data, the pump efficiency can be estimated to 33% and turbine efficiency can be estimated to be 80%. Due to the uncertainty of this preliminary design, the mass of the pump and turbine is estimated by comparing similar assemblies that have already been designed [68] [69].

Pump Length (cm)	Pump Diameter (cm)	Pump Mass (kg)	Turbine Length (cm)	Turbine Diameter (cm)	Turbine Mass (kg)
32	4	208	40	80	82

Table 9.8: Pump and Turbine Sizing

From these turbine and pump results, the thermodynamic state of the propellant across the turbo machinery is summarized in Table 9.2. From this, the power required by the pump and the power generated by the turbine can be found with Equations 9.9 and 9.10.

$$P_t = \dot{m}(h_3 - h_4) = 18.4MW \tag{9.9}$$

$$P_p = \dot{m}(h_2 - h_1) = 18.2MW \tag{9.10}$$

9.2.3 Reactor Design

The mass and volume of the Harmonia reactor is extrapolated from the NERVA NRX engine [70]. Despite the fact that it's performance is lower than required for this mission, it serves as a servicable foundation for estimating the basic properties of the engine. The UC-graphite composite fuel elements are coated in a layer of ZrC to resist corrosion from the hydrogen. The reactor consists of 300 fuel elements and 140 tie tubes. Each fuel element has 25 fluid channels each with a diameter of 2 mm. The inner and outer reflector radii are estimated based on previous designs [70].

	Hex Elements	Length (cm)	Mass (kg)
NERVA NRX	256	78.74	409
Harmonia	440	200	1791
Mass Multiplier	1.72	2.546	4.38

Table 9.9: Reactor Sizing

The main factors contributing to the performance of the reactor are length, hydraulic diameter, and friction factor. An increased $\frac{L}{D}$ corresponds to a higher maximum hydrogen temperature through the reactor. The length of the reactor was capped at 2 meters to save mass and volume. Previously, the NERVA design utilized passage diameters $(D_H)$of 2.5 mm [70]. This geometry yields a $\frac{L}{D}$ of 1000. Using this geometry, the pressure drop and temperature through the reactor can be calculated. [71]

$$\frac{T_t}{T_s} = \frac{1}{1+\sqrt{1+\left(\frac{\pi D}{2C_f L}\right)^2}}\left[1+\frac{T_{t1}}{T_s}\sqrt{1+\left(\frac{\pi D}{2C_f L}\right)^2}-\left(1-\frac{T_{t1}}{T_s}\right)\cos\left(\frac{\pi x}{L}\right)\right] \tag{9.11}$$

$$\frac{T_w}{T_s} = \frac{1}{1+\sqrt{1+\left(\frac{\pi D}{2C_f L}\right)^2}}\left[1+\frac{T_{t1}}{T_s}\sqrt{1+\left(\frac{\pi D}{2C_f L}\right)^2}+\left(1-\frac{T_{t1}}{T_s}\right)\left(\frac{\pi D}{2C_f L}\sin\left(\frac{\pi x}{L}\right)-\cos\left(\frac{\pi x}{L}\right)\right)\right] \tag{9.12}$$

Input	Ts (K)	Tt1 (K)	L (m)	D (m)	C_f
Value	3000	350	2	0.002	0.005

Table 9.10: Reactor Input Values

Output	T_{t2} (K)
Value	2780

Table 9.11: Reactor Output Values

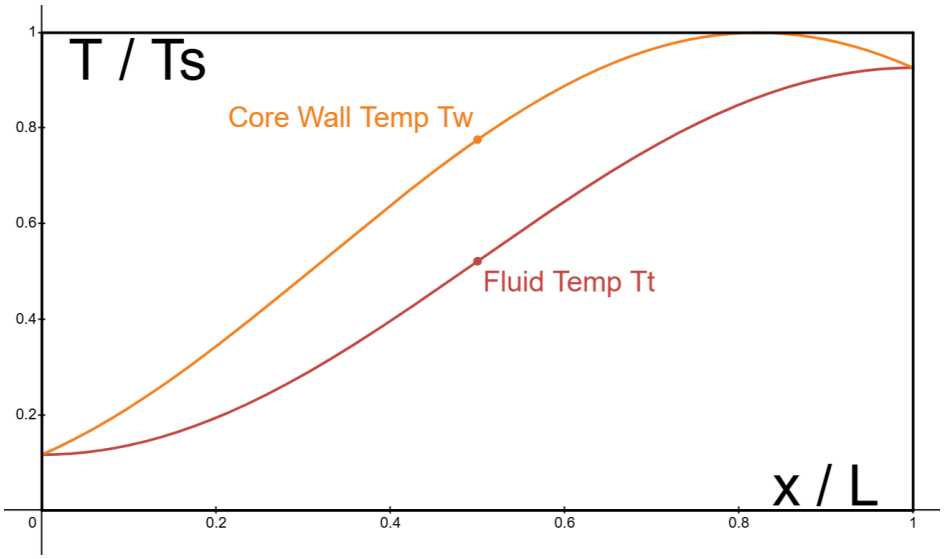

Figure 9.5: Wall and Fluid Temp vs Reactor Length

$$\frac{p_2}{p_1} = \frac{1+\gamma M_1^2\left(1-\frac{C_f L}{D}\right)}{1+\gamma M_2^2\left(1+\frac{fL}{D}\right)} \tag{9.13}$$

P1 (MPa)	P2 (MPa)
1.2	0.504

Table 9.12: Reactor Pressure Drop

The Harmonia reactor is surrounded by 3 layers of radiation shielding and contains 2 layers of internal reflecting material. The internal reflector is made of beryllium and surrounds the hex elements. The beryllium acts as a proven way to effectively scatter neutrons [72].

Reactor Radius (cm)	Inner Reflector Thickness (cm)	Volume (m^3)	Density (kg/m^3)	Reflector Mass (kg)
37.5	10	0.251	1850	465

Table 9.13: Inner Reflector Sizing

The outer radiation shielding and reflector is made of beryllium, tungsten, lithium hydride, and boron carbide. The beryllium reflector is located on the inside of the pressure vessel walls. Conversely, the outside of the pressure vessel contains the radiation shielding materials. The first layer is a thin sheet of tungsten, followed by a thicker layer of lithium hydride and boron carbide [73] [74].

Layer	Thickness (cm)	Inner Radius (cm)	Outer Radius (cm)	Volume (m^3)	Density (kg/m^3)	Mass (mT)
Boron Carbide	2	65.2	67.2	0.166	2,520	.4
Lithium Hydride	12.5	52.7	65.2	0.926	820	.8
Tungsten	0.5	52.2	52.7	0.033	19,450	.6
Al-6061	2.2	50	52.2	0.141	2,700	.4
Beryllium	10	40	50	0.565	1,850	1
					TOTAL	3.2

Table 9.14: Outer Reflector and Shielding Sizing

9.2.4 Performance

The performance of Harmonia is defined by specific impulse and thrust. Specific impulse (directly proportional to exhaust velocity) is determined primarily from the reactor exit fluid temperature and the nozzle expansion ratio and determines the minimum mass of propellant needed. Thrust is then determined by the mass flow rate of propellant and determines the IPV's acceleration and thus burn time for each major mission maneuver. In this analysis, a mass flow rate is chosen which would correspond to a thrust that would result the desired burn characteristics.

9.2.5 Nozzle Geometry

The method of characteristics for axially symmetric nozzles is a relatively simple way to calculate the contour of a rocket nozzle. However, since the expansion ratio is fairly large (300) and the hydrogen is being expanded to vacuum condition, normal method of characteristics produces a nozzle that is over 9 meters long. Because of volume and mass constraints and packing conditions, it is not possible to have a nozzle that large. It is then required to shorten the nozzle using Rao's method. This method removes the portion of the nozzle that is concave up and only marginally decreases performance. The required equations are listed below. The nozzle used on the Harmonia engine uses an 80% nozzle ratio.

$$x = 1.5R_t \cos\theta \tag{9.14}$$

$$y = 1.5R_t \sin\theta + 1.5R_t + R_t \tag{9.15}$$

$$x = 0.382R_t \cos\theta \tag{9.16}$$

$$y = 0.382R_t \sin\theta + 0.382R_t + R_t \tag{9.17}$$

$$x(t) = (1-t)^2 N_x + 2(1-t)tQ_x + t^2 E_x \tag{9.18}$$

$$y(t) = (1-t)^2 N_y + 2(1-t)tQ_y + t^2 E_y \tag{9.19}$$

$$Q_x = \frac{C_2 - C_1}{m_1 - m_2} \tag{9.20}$$

$$Q_y = \frac{m_1 C_2 - m_2 C_1}{m_1 - m_2} \tag{9.21}$$

$$m_1 = \tan(\theta_n) \tag{9.22}$$

$$m_2 = \tan(\theta_e) \tag{9.23}$$

$$C_1 = N_y - m_1 N_x \tag{9.24}$$

$$C_2 = E_y - m_2 E_x \tag{9.25}$$

$$L_N = n_{bell\%} \frac{(\sqrt{\epsilon} - 1)R_t}{\tan(15)} \tag{9.26}$$

Throat Diameter (cm)	Exit Diameter (cm)	Area Ratio
20	348	300

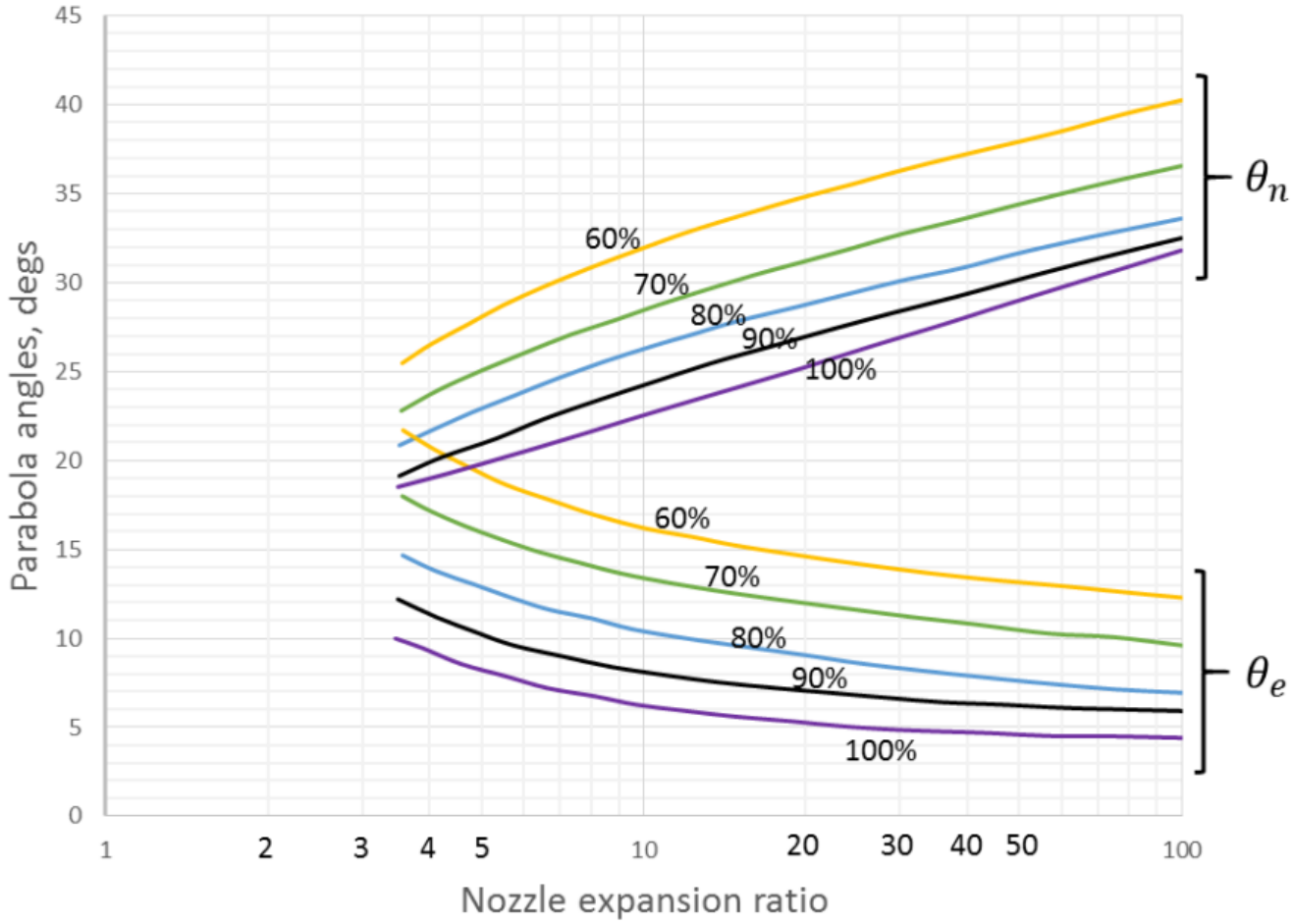

Figure 9.6: Bell nozzle percentage [4]

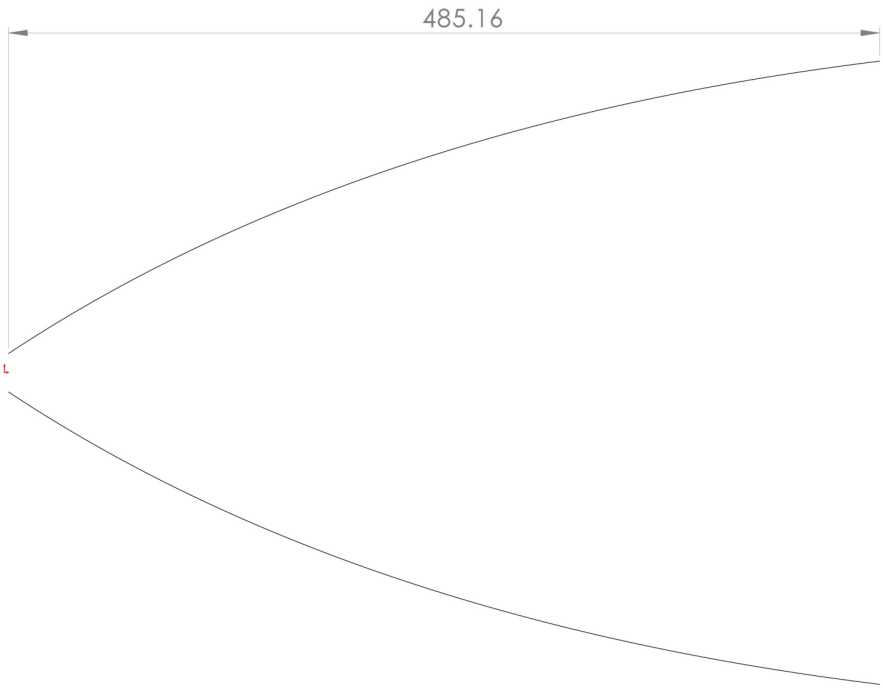

Figure 9.7: 2D Nozzle Geometry

The nozzle mass is calculated by relating the volume and mass of the RL10C-2-1 engine nozzle to the volume of the Harmonia nozzle assuming both are solid cones. The volume equation used to make this comparison is listed below. The RL10C-2-1 was chosen due to its recent design, similar area ratio, and large size. [75]

$$V = \frac{\pi}{3}(R^2 H - r^2 h) \tag{9.27}$$

	Nozzle Length (m)	Exit Diameter (m)	Volume (m^3)	Mass (mT)
RL10C-2-1	4.15	2.15	5.02	0.3
Harmonia	4.85	3.48	15.38	0.92

Table 9.15: Nozzle Sizing

9.2.6 Specific Impulse

The specific impulse can be calculated from the exhaust velocity and pressure area specific thrust over the reference acceleration of earth surface gravity where the exhaust velocity is the nozzle exit mach number multiplied by the speed of sound [76].

$$I_{sp} = \frac{u_e + \frac{F_{pressure}}{\dot{m}}}{g_0} \tag{9.28}$$

$$u_e = M_e\sqrt{\gamma R T_0} = \sqrt{\frac{2}{\gamma - 1}\left(1 - \left(\frac{P_e}{P_0}\right)^{\frac{\gamma-1}{\gamma}}\right)(\gamma R T_0)} \tag{9.29}$$

$$c_p = \frac{\gamma R}{\gamma - 1} \tag{9.30}$$

$$I_{sp} = \frac{\sqrt{2c_p T_0\left(1 - \left(\frac{P_e}{P_0}\right)^{\frac{\gamma-1}{\gamma}}\right)} + \frac{P_e A_e}{\dot{m}}}{g_0} \tag{9.31}$$

The total temperature leaving the reactor assuming a half sine core power axial density distribution is given as a function of x = axial distance / reactor length in Equation 9.11 where

$$T_0 = T_s \cdot T_{tvS}(1)$$

. The key parameters and results relevant to the specific impulse are summarized as follows.

g_0	$\dot{m}$	γ	c_p	C_f	L/D_H	T_s	T_0	$\frac{P_e}{P_0}$
9.80665	38	1.315	17,871	0.0025	1000	3000	2792	5.34×10^{-5}

$1 - \left(\frac{P_e}{P_0}\right)^{\frac{\gamma-1}{\gamma}}$	$\frac{P_e A_e}{\dot{m} g_0}$	I_{sp}
0.905	0.69	951.9

The fluid temperature leaving the reactor T_0 is sensitive to the friction factor C_f which needs experimental verification but is assumed for this analysis to be 0.0025.

The ratio of specific heats γ is a function of temperature, which changes more smoothly than predicted by classical mechanics (Primarily due to the non-discrete transition between the vibrational fluid energy modes becoming available and to a lesser extent the effects of chemical "freezing") over the extreme temperatures from the nozzle entrance to exit. The specific impulse equation is highly sensitive to γ primarily from the $c_p = \frac{\gamma}{\gamma-1}$ term. At the hottest fluid temperature, γ becomes as low as 1.215 and at the cold exhaust, γ becomes as high as 1.430 as calculated with Gordon and McBride's NASA CEA code. Assuming an effective γ of 1.315, the calculations agree with the outputs of CEA.

9.2.7 Ullage and Fuel Systems

Fluid piping for propulsion systems is required for two reasons: moving propellant from the tanks into the engines, and moving ullage gas into the tanks to fill them as they drain. For the nuclear thermal propulsion system, hydrogen gas is used as the ullage, which is directly from the turbine in the engine cycle.

The fluid systems layout is as follows. The liquid propellant is piped from each of the tanks into the Earth Capture Tank, which is then drained into the engines. This is done for two reasons: first, only one fluid connection is needed for the inlet of the engine. Second, the total amount of piping is decreased since it is not needed for the length of the Earth Capture Tank. The ullage gas is taken directly from the turbine in the engine, and is pumped to each individual tank. For this reason, the total length of ullage piping is greater than the total length of propellant piping. The piping itself is run alongside the Earth Capture Tank until it reaches the main truss, at which point it runs inside the main truss. This is done to protect the piping from micrometeoroids and other space debris without adding shielding to the pipes themselves. A flow diagram showing the ullage and propellant flow through the IPV is shown in Figure 9.8.

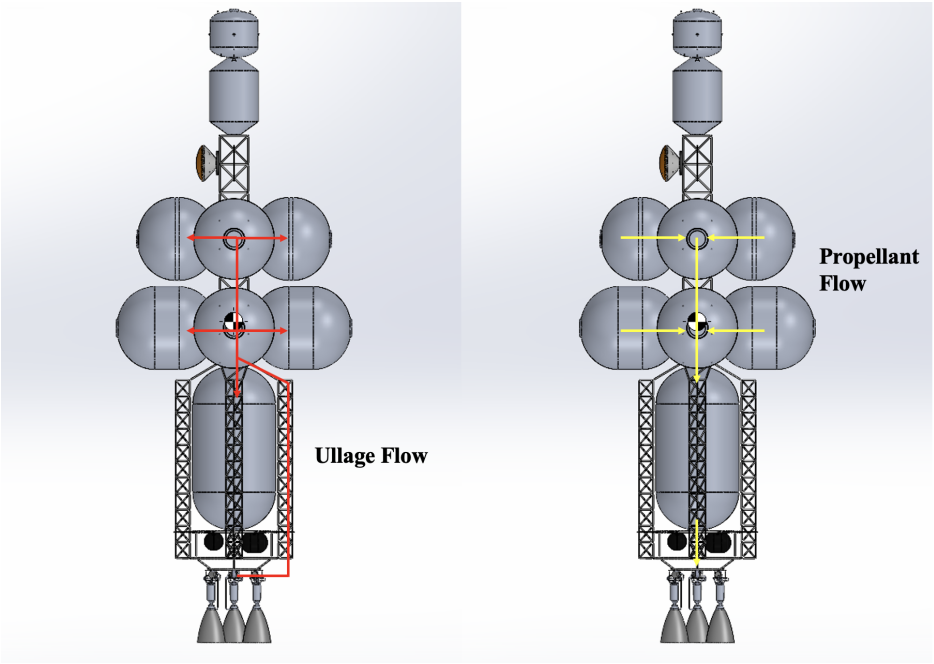

Figure 9.8: Ullage and Propellant Piping Flow Diagram

First, the total ullage mass, or the mass of the gas required to fully fill all propellant tanks, is calculated. The equations used to do the following calculations come from Reference [77].

$$\dot{V}_{propellant} = \frac{\dot{m}_{propellant}}{\rho_{propellant}} \tag{9.32}$$

$$\dot{V}_{propellant} = \dot{V}_{ullage} \tag{9.33}$$

$$\dot{m}_{ullage} = \dot{V}_{ullage}\rho_{ullage} \tag{9.34}$$

$$m_{ullage} = \dot{m}_{ullage}\frac{V_{tank}}{\dot{V}_{ullage}} \tag{9.35}$$

These calculations are performed for all propellant tanks, and the resulting masses are summed to obtain a total ullage mass. These values are then used to perform calculations to size the pipes.

$$D_{propellant} = \sqrt{\frac{4}{\pi}\frac{\dot{m}_{propellant}}{U_{propellant}\rho_{propellant}}} \tag{9.36}$$

For sizing the ullage piping, a maximum speed is chosen to prevent the gas flow from choking and inducing shocks. Since the sonic speed of gaseous hydrogen is around 1500 $\frac{m}{s}$, a maximum speed is chosen at 800 $\frac{m}{s}$ for safety. Then, using equation (9.36), the diameter for the ullage piping is calculated.

$$D_{ullage} = \sqrt{\frac{4}{\pi} \frac{\dot{m}_{ullage}}{U_{ullage} \rho_{ullage}}} \tag{9.37}$$

After obtaining the diameters, the thicknesses of the propellant and ullage piping are calculated. These values are obtained using Reference [78].

$$t_{pipe} = \frac{PD}{2(SEW + PY)}) \tag{9.38}$$

Using the values for thickness, diameter, total length of piping for ullage and propellant, and the material density of the chosen piping material, a total piping mass is calculated.

$$m_{piping} = \rho_{material}[(L_{ullage} 2\pi \frac{D_{ullage}}{2} t_{ullage}) + (L_{propellant} 2\pi \frac{D_{propellant}}{2} t_{propellant})] \tag{9.39}$$

However, this only accounts for the internal pressure forces acting on the pipes during use. Structural calculations must also be performed to account for the launch loading conditions when the pipes are launched on the SLS.

First, a thickness is guessed to calculate the mass of the piping. This is then be converted into a force, and subsequently a stress, which is then compared to the ultimate strength of the material. If the calculated stress is too low, a new thickness is guessed, and the process is iterated again.

The mass of the piping is calculated using (9.39), replacing the values for t_{ullage} and $t_{propellant}$ with the guess values.

$$F_{axial} = m_{piping} a_{launch} \tag{9.40}$$

$$\sigma_{actual} = \frac{F_{axial}}{2\pi \frac{D}{2} t_{guess}} > \sigma_{allowable} \tag{9.41}$$

The resulting piping mass from both of these methods are compared, and the larger mass is taken as the final value. A breakdown of all relevant values for the propulsion fluid system can be found in Table 9.16, and a summary of the results can be found in Table 9.17.

Tank Dimensions from Section 8.4.2		
Thermodynamic State Values from Section 9.2		
Selected Material: Al 6061-T6 B210: Reference [78]		
Variable	Value	Units
Propellant Mass Flow Rate	38	kg/s
Ullage Mass Flow Rate	.096	kg/s
Propellant Density	71.44	kg/m^3
Ullage Density	.18	kg/m^3
Propellant Velocity	25	m/s
Ullage Velocity	800	m/s
Propellant Pressure	.225	MPa
Ullage Pressure	1.2	MPa
Material Allowable Stress	96.53	MPa
Material Quality Factor	.8	
Material Weld Joint Reduction	1	
Material Coefficient	.4	
Propellant Piping Length	50	m
Ullage Piping Length	100	m
Launch Load	10	g

Table 9.16: Relevant Values for Fluid Pipe Sizing Calculations.

Variable	Value	Units
Propellant Pipe Diameter	16.46	cm
Ullage Pipe Diameter	1.36	cm
Propellant Pipe Thickness for Internal Pressure	.27	mm
Ullage Pipe Thickness for Internal Pressure	.12	mm
Pipe Mass for Internal Pressure	20.2	kg
Propellant Pipe Thickness for Launch Loads	4	mm
Ullage Pipe Thickness for Launch Loads	4	mm
Allowable Stress with 2 FoS	144.8	MPa
Propellant Pipe Actual Stress	13.57	MPa
Ullage Pipe Actual Stress	2.24	MPa
Pipe Mass for Launch Loads	325.3	kg

Table 9.17: Summary of Pipe Sizes and Masses for Fuel and Ullage Systems.

As seen in Table 9.17, the total mass due to the launch loading conditions is higher than the total mass due to the internal pressure. Therefore, this mass, along with the corresponding thicknesses, are used in the design of the propellant and ullage piping.

9.2.8 Start Up and Cool Down

As the propellant is actively used to keep the fuel rods from exceeding allowable temperatures and is the only means of heat power disposal aside from the comparatively weak radiation potential, this design continues to run propellant out of the rocket after each burn until the temperature of the reactor reaches suitable levels for its next mode of operation, a continuous electrical power generation cycle (Section 11.6). To determine the time and mass of propellant required for this cool down process, a lumped capacitance model is employed. The rate of heat extracted from the solid reactor is equal to that required to heat the propellant to its exit temperature.

$$\dot{Q} = \dot{m} c_p \Delta T_{fluid} \tag{9.42}$$

Therefore, a model of the fluid exit temperature as a function of time can inform the rate of heat loss from the fuel rods which can be directly related to the average temperature of the solid reactor. The lumped capacitance model uses this average temperature. Using the assumption that the temperature profile roughly maintains the same shape over the reactor's length as calculated in Equation 9.11 for the steady state thrusting mode. From the instantaneous rate of heat loss,the fluid and solid core temperature profiles are updated iteratively.

$$T_{fluid,new} = T_1 + (T_{fluid,previous} - T_1) \cdot e^{-t/\tau} \tag{9.43}$$

From this approach, there is a trade off between time to cool down and mass flow rate during cool down. For a time of 13 minutes to be achieved, a mass flow rate of 0.5 kg/s is employed resulting in the expenditure of 0.390 mT of propellant.

The start up process is comparatively mass efficient. The soon to be hot surfaces are primed with the cryogenic fluid propellant before reaching the steady operational heat flux levels during thrusting, though this can be achieved with a lower flow rate.

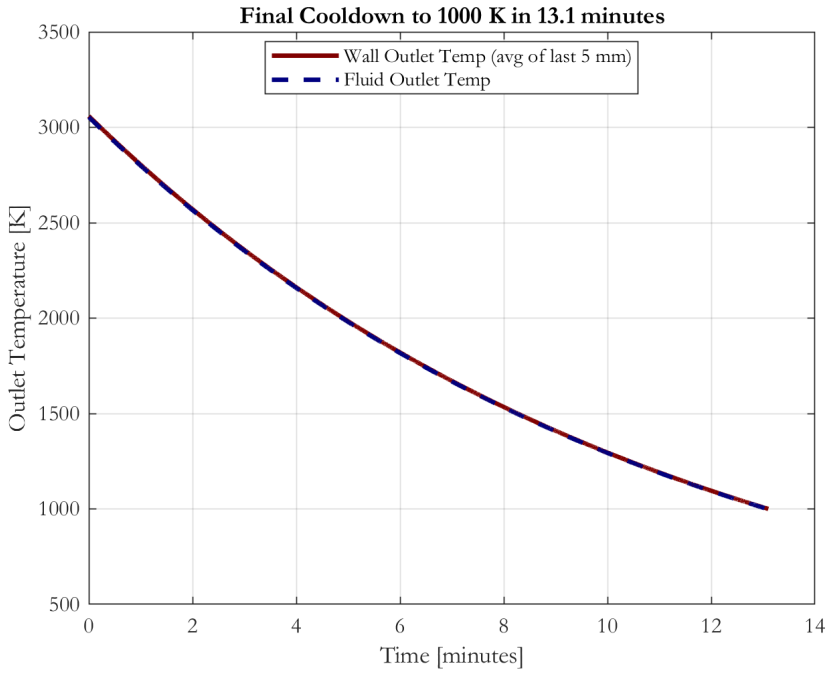

Figure 9.9: Final Cooldoen to 1000K Plot

9.3 IPV Orbital Maneuvering System

9.3.1 OMS Engine

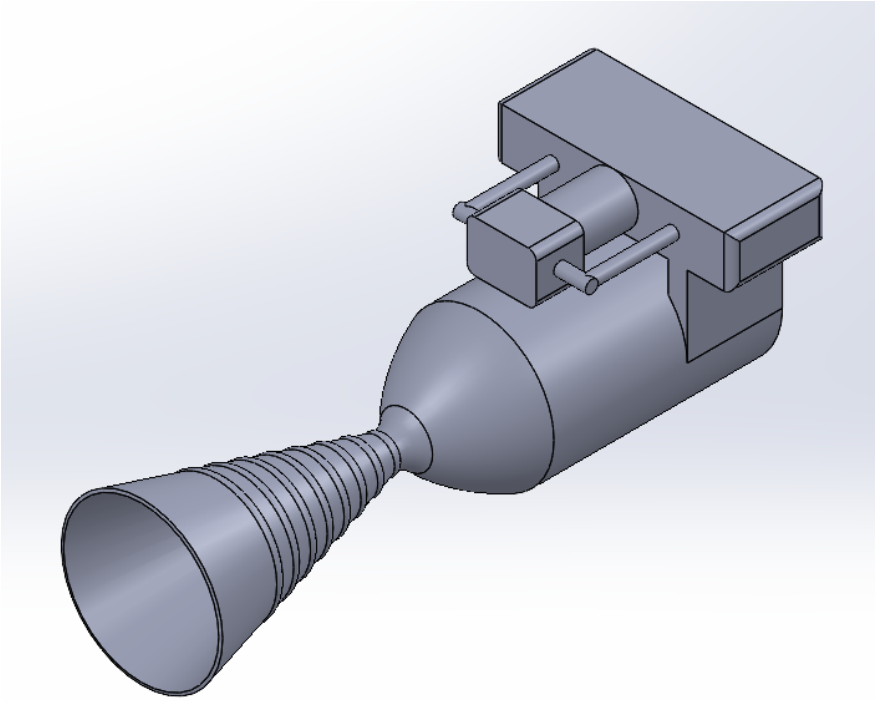

Figure 9.10: OMS Engine CAD

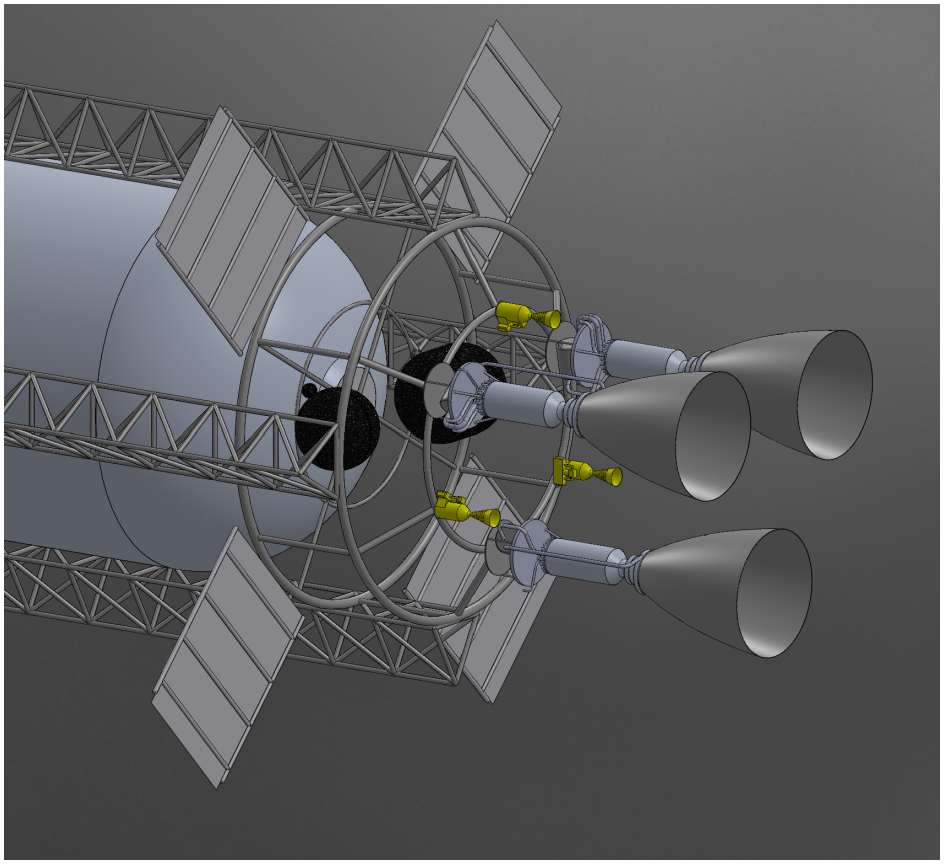

Figure 9.11: OMS Engine Placement

The OMS is used to provide propulsion for the Interplanetary Vehicle while in the Mars Orbit phase of the mission. It will complete maneuvers that will ensure the vehicle stays on the correct path during the mission while the primary propulsion system is not in the thrusting mode. The OMS includes 3 engine units in a triangular pattern located around the nuclear thermal propulsion engines, shown in Figure 9.11 . This triangular pattern ensures the systems capability of performing all maneuvers necessary to the mission. The OMS engines utilize a gas generator engine cycle with MMH as the fuel and N_2O_2 as the oxidizer. These propellants are selected due to the fact that they are hypergolic and have a simpler means of storage. Hypergolic propellants, which ignite on contact, simplifies the engine cycle since no ignition system is needed. The storage of these propellants also lowers the complexity with the fact that they are not cryogenic. The specific impulse benefits associated with the use of other propellants such as LH_2/LO_2 is outweighed by the added

complexity of cryogenics.

9.3.2 Engine P&ID

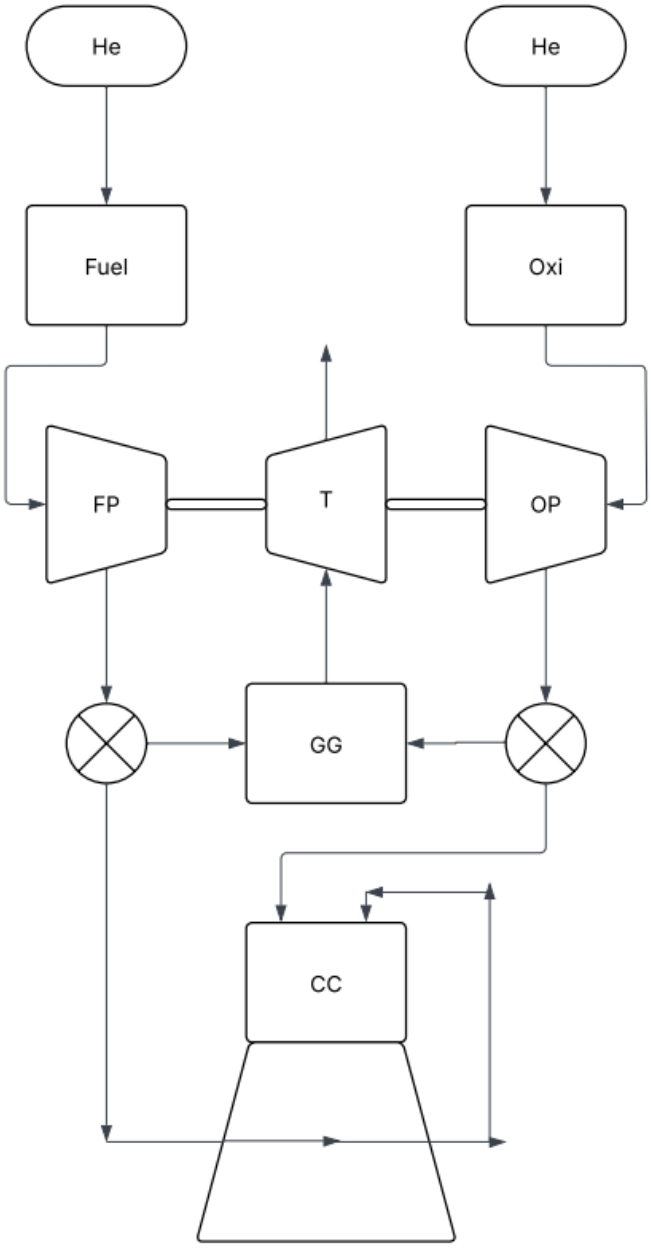

Figure 9.12: OMS Engine P&ID

The P&ID in Figure B.1 gives a breakdown of the gas generator bi-propellant engine cycle that is used in the design of the OMS. The cycle is broken down into several compo-

nents including the propellant feed system, fuel and oxidizer pumps, turbine, gas generator, and the combustion system. The propellant feed system is broken into helium-backed fuel and oxidizer tanks. This helium acts as the ullage to ensure the system operates at a consistent pressure. The fuel and oxidizer turbo pumps are mechanically linked to the turbine via a central shaft. These pumps are used to increase the pressure of the propellants as they enter the combustion chamber or the gas generator, ensuring an efficient injection. The turbine uses the hot exhaust of the gas generator to drive the fuel and oxidizer pumps on the shared shaft. The gas generator uses a finite portion of fuel and oxidizer to combust and produce the exhaust for the turbine. This comes with the trade-off of losing some specific impulse, but the cycle still exceeds the minimum Isp requirement. After the turbomachinery the fuel is then directed through a regenerative cooling system in order to keep the nozzle below critical temperatures. After this, the fuel and oxidizer are fed into the combustion chamber where the high-pressure propellants are combusted. The combustion then expands through the nozzle to generate thrust.

9.3.3 Engine Analyses

The OMS is iterated in design using a spreadsheet, and models the performance based on selected engine requirements and key assumptions. Table 9.18 shows the selected engine requirements.

m_{overall}	505	mT
F_{T}	35	kN
ΔV	150	m/s
Fuel	MMH	-
Oxidizer	N_2O_2	-
$\rho_{N_2O_2}$	1440	kg/m^3
$\rho_{\text{hydrazine}}$	880	kg/m^3
P_{c}	6890	kPa
T_{c}	2995	K
C_{p}	2.8	kJ/kgK
γ	1.35	-

Table 9.18: OMS Analysis Initial Values

These initial values are chosen to either fit the mission needs or are chosen relative to a similar engine cycle. The thrust and ΔV are estimated on the basis of the requirements of the mission. The overall mass is estimated based on the mass of the vehicle after certain burns. These calculations are sectioned by the mass and ΔV at those mission phases. These values are summed together for the overall cycle analysis. The equations used are shown below[71].

$$\dot{m}_{\text{tot}} = \frac{F_T}{I_{sp} \cdot g_0} \quad (\text{kg/s}) \tag{9.44}$$

$$m_{\text{fuel}} = m_0 \left(1 - e^{\frac{-\Delta V}{I_{sp} \cdot g_0}}\right) \quad (\text{kg}) \tag{9.45}$$

$$m_{\text{oxi}} = \frac{O/F}{(O/F) + 1} \cdot m_p \quad (\text{kg}) \tag{9.46}$$

$$\dot{m}_{\text{fuel}} = \frac{1}{1 + (O/F)} \cdot \dot{m}_{\text{tot}} \quad (\text{kg/s}) \tag{9.47}$$

$$\dot{m}_{\text{oxi}} = \frac{O/F}{(O/F) + 1} \cdot \dot{m}_{\text{tot}} \quad (\text{kg/s}) \tag{9.48}$$

$$m_{\text{prop}} = m_{\text{fuel}} + m_{\text{oxi}} \tag{9.49}$$

$$V_{\text{tank,fuel}} = \frac{m_p}{\rho_{\text{hydrazine}}} \quad (\text{m}^3) \tag{9.50}$$

$$V_{\text{tank,oxi}} = \frac{m_{\text{oxi}}}{\rho_{N_2O_4}} \quad (\text{m}^3) \tag{9.51}$$

$$A^* = \frac{F_T}{C_f \cdot P_\text{c}} \tag{9.52}$$

$$A_e = \varepsilon \cdot A^* \tag{9.53}$$

$$P_e = P_\text{c} \left(1 + \frac{\gamma - 1}{2} M_e^2\right)^{-\frac{\gamma}{\gamma - 1}} \tag{9.54}$$

$$C_f = \left[\sqrt{\frac{2\gamma^2}{\gamma - 1}\left(\left(\frac{2}{\gamma + 1}\right)^{\frac{\gamma+1}{\gamma-1}}\left(1 - \left(\frac{P_e}{P_\text{c}}\right)^{\frac{\gamma-1}{\gamma}}\right)\right)} + \frac{P_e}{P_\text{c}} \cdot \frac{A_e}{A^*}\right] \tag{9.55}$$

$$\epsilon = \frac{A^*}{A} = \frac{1}{M_e}\left[\frac{2}{\gamma + 1}\left(1 + \frac{\gamma - 1}{2} M_e^2\right)\right]^{\frac{\gamma+1}{2(\gamma-1)}} \tag{9.56}$$

$$I_{sp} = \frac{1}{g_0} \cdot \sqrt{\frac{2\gamma}{\gamma - 1} \cdot R \cdot T_c \cdot \left(1 - \left(\frac{P_c}{P_e}\right)^{\frac{\gamma-1}{\gamma}}\right)} \tag{9.57}$$

$$\dot{m} = \rho v A \tag{9.58}$$

Equation (9.56) is set to zero to solve for the mach number at the nozzle exit. With the initial values chosen or found, the values in Table 9.19 are attained using the previous equations.

$\dot{m}_{\text{tot}}$	10.9	kg/s
m_{prop}	17.3	mT
m_{fuel}	10.2	mT
m_{oxi}	7.08	mT
$\dot{m}_{\text{fuel}}$	4.5	kg/s
$\dot{m}_{\text{oxi}}$	6.4	kg/s
V_{fuel}	11.6	m^3
V_{oxidizer}	4.90	m^3
A_e	0.20	m^2
A^*	0.003	m^2
D_{throat}	0.10	m
P_{nozzle}	5.12	kPa
C_{F}	1.77	-
η_{nozzle}	0.90	-
M_{exit}	5.59	-

Table 9.19: Initial Calculations

This process is repeated three more times to take into account the varying masses through the different burns of the trajectory, shown in Table 9.20 below.

	Overall Mass	ΔV
Earth Departure	505	50
Mars Capture	410	25
Mars Departure	315	25
Earth Capture	248	50

Table 9.20: Mass and ΔV Breakdown

These broken-down mass points and the values that are found with them are shown

in Table 9.21.

	Earth Departure	**Mars Capture**	**Mars Departure**	**Earth Capture**
m_{overall}	505000	410000	315000	248000
F_{T}	35000	35000	35000	35000
ΔV	50	25	25	50
$Fuel$	Hydrazine	Hydrazine	Hydrazine	Hydrazine
$Oxidizer$	N_2O_4	N_2O_4	N_2O_4	N_2O_4
$\rho_{N_2O_4}$	1440	1440	1440	1440
$\rho_{\text{hydrazine}}$	880	880	880	880
Ae/A*, ϵ	55	55	55	55
P_{c}	6890	6890	6890	6890
T_{c}	2995	2995	2995	2995
C_p	3.06	3.06	3.06	3.06
O/F	1.44	1.44	1.44	1.44
m_{prop}	7810	3180	2440	3833
m_{fuel}	4610	1878	1442	2262
m_{oxi}	3201	1304	1001	1571
$\dot{m}_{\text{fuel}}$	4.5	4.5	4.5	4.5
$\dot{m}_{\text{oxi}}$	6.4	6.4	6.4	6.4
V_{fuel}	5.2	2.1	1.6	2.6
V_{oxidizer}	2.2	0.9	0.7	1.1

Table 9.21: Mass Breakdown for Mission Points

With these sectioned calculations, a more realistic estimate for the propellant mass and volume can be found. With those masses found, values for the overall cycle are calculated, as shown in Table 9.22.

With the general values found, the analysis for the components of the turbomachinery

m_{overall}	505000	kg
F_{T}	35000	N
ΔV	150	m/s
$Fuel$	MMH	-
$Oxidizer$	N_2O_4	-
$\rho_{N_2O_4}$	1442	kg/m^3
$\rho_{\text{hydrazine}}$	880	kg/m^3
Ae/A*, ϵ	55	-
P_{c}	6890	kPa
T_{c}	2995	K
C_p	2.84	kJ/kgK
O/F	1.44	-
γ	1.35	-
I_{sp}	327	s
$\dot{m}_{\text{tot}}$	10.9	kg/s
m_{prop}	17.2	mT
m_{fuel}	10.2	mT
m_{oxi}	7.08	mT
$\dot{m}_{\text{fuel}}$	4.50	kg/s
$\dot{m}_{\text{oxi}}$	6.44	kg/s
V_{fuel}	11.60	m^3
V_{oxidizer}	4.90	m^3
A_e	0.20	m^2
A^*	0.003	m^2
D_{throat}	0.10	m
P_{nozzle}	5.12	kPa
C_{thrust}	1.77	-
η_{nozzle}	0.90	-
M_{exit}	5.59	-

Table 9.22: Calculations with Overall Mass

and other components are calculated. For the pumps, the outlet pressure and mass flow rate are needed to find the total shaft power required to operate the engine cycle. It is assumed that the outlet pressure is the chamber pressure. The mass flow rates used are also previously calculated in the previous steps of the analysis. The injector pressure drop is assumed to reach the selected combustion chamber pressure. The inlet pressure will be the tank pressure when storing the propellants. With these values, the shaft power is calculated with the following equations [79].

$$P_{\text{shaft,oxi}} = \frac{\dot{m}_{\text{oxi}}}{\rho_{\text{oxi}}} \left(P_{\text{out,oxi}} - P_{\text{in,oxi}} \right) \tag{9.59}$$

$$P_{\text{shaft,fuel}} = \frac{\dot{m}_{\text{fuel}}}{\rho_{\text{fuel}}} \left(P_{\text{out,fuel}} - P_{\text{in,fuel}} \right) \tag{9.60}$$

With these the following values are found in Table 9.23.

Fuel Pump		
ΔP_{inj}	1.20	-
$P_{\text{in,f}}$	200	kPa
$P_{\text{corr,fuel}}$	8268	kPa
$P_{\text{out,f}}$	6890	kPa
$\dot{m}_f$	4.47	kg/s
$P_{\text{shaft,f}}$	40.97	kW
Oxidizer Pump		
$P_{\text{in,ox}}$	200	kPa
$P_{\text{corr,oxi}}$	8268	kPa
$P_{\text{out,ox}}$	6890	kPa
$\dot{m}_{ox}$	6.44	kg/s
$P_{\text{shaft,ox}}$	35.99	kW
$P_{\textbf{shaft,tot}}$	76.96	kW

Table 9.23: Pump Analysis

The calculations for the gas generator show how much propellant is needed to generate enough power for the pumps. The relative Isp loss from taking a portion of the propellant is also calculated to show the trade-off with using a gas generator cycle. Table 9.24 shows the assumed values or values found via CEA for the gas generator.

T_{ti}	**1343**	**K**
C_p	5.49	kJ/kg·s
P_{ti}/P_{te}	18.0	-
O/F	0.25	-
γ_{gg}	1.24	-
η_{pump}	0.70	-
η_{turb}	0.70	-
ρ_{gg}	8.62	kg/m^3

Table 9.24: Gas Generator Inputs

The turbine inlet temperature, specific heat, and the gas density are all values found using CEA. The rest of the values are inputs or assumed values for the calculations. The following equations are used to calculate the gas generator characteristics.[80]

$$\eta_{\text{gg}} = 1 - \left(\frac{P_{\text{te}}}{P_{\text{ti}}}\right)^{\frac{\gamma-1}{\gamma}} \tag{9.61}$$

$$\dot{m}_{\text{gg}} = \frac{P_{\text{pump}}}{\eta_t \cdot \eta_{\text{gg}} \cdot C_p \cdot T_{\text{ti}}} \tag{9.62}$$

$$\dot{m}_{\text{oxi}} = \frac{\dot{m}_{\text{gg}} \cdot (O/F)}{(O/F) + 1} \tag{9.63}$$

$$\dot{m}_{\text{fuel}} = \frac{\dot{m}_{\text{gg}}}{1 + (O/F)} \tag{9.64}$$

$$C_{\text{gg}} = \sqrt{2 \cdot C_p \cdot T_{t,\text{out}} \cdot \left(1 - \left(\frac{P_e}{P_{\text{te}}}\right)^{\frac{\gamma-1}{\gamma}}\right)} \tag{9.65}$$

$$C = \sqrt{2 \cdot C_{p,n} \cdot T_c \cdot \left(1 - \left(\frac{P_n}{P_c}\right)^{\frac{\gamma-1}{\gamma}}\right)} \tag{9.66}$$

$$I_{sp,\text{loss}} = -I_{sp} \cdot \left(\frac{\dot{m}_{\text{gg}}}{\dot{m}_{\text{tot}}}\right) \cdot \left(1 - \frac{C_{\text{gg}}}{C}\right) \tag{9.67}$$

With these equations, the following values are found in Table 9.25.

T_{ti}	**1343**	**K**
C_p	5.49	kJ/kg·s
P_{ti}/P_{te}	18.00	-
O/F	0.25	-
γ_{gg}	1.24	-
η_{pump}	0.70	-
η_{turb}	0.70	-
ρ_{gg}	8.62	kg/m^3
$P_{\text{pump,tot}}$	109.9	kW
η_{gg}	0.423	-
$\dot{m}_{gg}$	0.0504	kg/s
$\dot{m}_{oxi}$	0.0101	kg/s
$\dot{m}_{fuel}$	0.0403	kg/s
C_{gg}	2442	m/s
C	3432	m/s
$\Delta I_{sp,rel}$	-0.4362	s
$I_{sp,\text{corr}}$	327	s

Table 9.25: Gas Generator Analysis

The nozzle geometry calculations show the general sizing of the nozzle needed to expand the combustion products effectively. Table 9.26 contains the input values, where

the expansion ratio and nozzle angle are assumed values, while the throat and chamber diameters are known from the previous step of the analysis.

D_t	**0.06**	**m**
D_c	0.45	m
R_t	0.03	m
α°	15	degrees
α	0.26	radians
ε	55	-

Table 9.26: Nozzle Geometry Inputs

The nozzle length and the upstream wall radius are found with the following equations.[81]

$$R_u = 0.494 \cdot R_t \tag{9.68}$$

$$L = \frac{R_t\left(\sqrt{\varepsilon}-1\right) + R_u \cdot \sec(\alpha - 1)}{\tan(\alpha)} \tag{9.69}$$

When finding the upstream radius, through empirical data the upstream radius is on the order of 0.5-1.5 times the value of the throat radius. The SSME is 0.494 times the value of the throat radius. With these equations, Table 9.27 is calculated with the nozzle geometry characteristics.

D_t	**0.06**	**m**
D_c	0.45	m
R_t	0.03	m
α	15	degrees
α	0.26	radians
ε	55	-
R_u	0.02	m
L	0.80	m

Table 9.27: Nozzle Geometry Analysis

The analysis for the regenerative cooling of the nozzle is modeled as a simple heat transfer process, making conservative assumptions for the wall of the nozzle and the heat transfer coefficients. Table 9.28 shows the assumed and input values of the analysis.

T_g	**2995**	**K**
T_{cool}	298	K
t_w	0.002	m
k_w	43	W/m·C
h_g	657	W/m^2·K
h_c	26000	W/m^2·K
ε_g	0.05	-

Table 9.28: Regenerative Cooling Inputs

Using the following equations, the heat transfer characteristic values are found [76].

$$\dot{Q}_w = \frac{T_{tg} - T_c + \left(\frac{\varepsilon_g \sigma T_g^4}{h_g}\right)}{\left(\frac{1}{h_g} + \frac{t_w}{k_w} + \frac{1}{h_c}\right)} \tag{9.70}$$

$$\dot{Q}_r = \varepsilon_g \sigma T_g^4 \tag{9.71}$$

$$\dot{Q}_c = \dot{Q}_w - \dot{Q}_r \tag{9.72}$$

$$T_{wg} = T_g - \frac{\dot{Q}_c}{h_g} \tag{9.73}$$

$$T_{wc} = \frac{\dot{Q}_w}{h_c} + T_c \tag{9.74}$$

With these equations, the full cooling analysis is complete, shown in Table 9.29.

T_g	**2995**	**K**
T_{cool}	298	K
t	.002	m
k_w	43	W/m·C
h_g	657	W/m^2K
h_c	26000	W/m^2K
ε_g	0.05	-
$\dot{Q}_w$	1.89	MW/m^2
T_g	459	K
T_{cool}	371	K
$\dot{Q}_r$	228	kW/m^2
$\dot{Q}_c$	1.67	MW/m^2

Table 9.29: Regenerative Cooling Analysis

For ullage, the design incorporates high-pressure helium tanking to ensure correct propellant pressure throughout the engine cycle. The analysis found the sizing of the ullage

tanks to back the propellants. The tank sizing and pressures are reported in the tank section.

A general mass estimation is in use for the OMS. The following analysis breaks down the components of the cycle and finding the estimated mass on an individual level.

The turbine mass is approximated using a specific power density. The design incorporates a 1.25 kW/kg power density for the turbine resulting in a mass estimation of roughly 62 kg [82].

The nozzle mass approximation is calculated by assigning a material and density to the nozzle, as well as a nozzle volume. With this the mass of the nozzle is calculated as about 227 kg.

The gas generator mass is approximated by finding the volume of the generator and using the density of the assigned material. The design incorporates hastelloy as the material and the following equation is used to approximate the mass of the gas generator [83].

$$m_{\text{gg}} = 1.5 \times \rho_{\text{gg},m} \cdot \frac{4}{3}\pi \left(R_{\text{gg}}^3 - r_{\text{gg}}^3 \right) \tag{9.75}$$

This incorporates a 50% reduction factor to account for the total mass of the generator, and not just the chamber walls. From this, the mass is approximated to be roughly 122 kg.

The mass of the pumps are to be approximated as 50 kg each.

The piping mass is found using the assumption that 43% of the overall mass of the turbomachinery is allocated to the piping and valving. With this, the piping mass is calculated to be 219 kg. With the use of these analyses, the entire OMS mass is estimated, as seen in Table 9.30 [84].

Subsystem	Mass (kg)
Propellant	17269.3
Pumps	100
Turbine	61.6
Nozzle	227.5
Gas Generator	122.1
Piping Estimation	219.1
Engine Mass	730.2
Total	18729.7

Table 9.30: OMS Mass Breakdown

9.3.4 Trade Studies

The propellant selection process is between the use of cryogenics such as LOX/LH2 and hypergolics such as the chosen MMH/N2O4. Cryogenics offer a higher Isp, on the order of 400s, but come with the need of boil-off mitigation. Having a lower Isp is more suitable for this specific system due to the lower Isp needs to meet the mission requirements. Hypergolic propellants are chosen to lower the complexity of the OMS, due to having self-ignition and simpler storage.

Originally an electric pump fed system was sized that would be a simple and would be reliable choice to meet mission requirements. Through further analysis it is determined that this would be very costly in terms of the amount of power needed to feed the propellants. Another concept of design is a pressure-fed system, this is considered due to the lack of turbomachinery needed for the cycle. This is ultimately not selected due to sizing of the tanks and the complexity of propellant storage resulting in a high minimum mass. It is decided to move forward with the gas generator cycle due to its balanced mass and power needs to meet the mission requirements.

When determining the performance needs of the OMS, the team decided that having an OMS that has a lower performance, when compared to cryogenics, is in accordance with the requirements of the mission. The OMS does not need high Isp capabilities to meet the lower propulsion requirements for the OMS. With these trade-offs in consideration, it is decided to move forward with the bipropellant gas generator engine cycle for the OMS.

9.3.5 Results

I_{sp}	**327.2**	s	Injector Pressure Drop	0.2	20%	**Regenerative Cooling**		
Corrected I_{sp}	326.8	s	**Fuel Pump**	**-**	-	$\dot{Q}_w$	1894191	W/m^2
F_T	35000.0	N	Corrected Exit Pres.	8268.000	kPa	T_g	459.11	K
ΔV	150.0	m/s	$\dot{m}$	4.469	kg/s	T_{cool}	371.00	K
O/F	1.4	-	Oxi Pump	-	-			
P_c	6890.0	kPa	Corrected Exit Pres.	8268.000	kPa	V_{He}	0.0392	m^3
T_c	2995.0	K	$\dot{m}$	6.435	kg/s	V_{Prop}	16.5	m^3
ε	55.0	-	Total Shaft Power	76.964	kW	m_{prop}	17269	kg
D_c	0.4	m	**Gas Generator**	**-**	-	m_{He}	8.8523	kg
D_t	0.1	m	$\dot{m}_{\text{in}}$	0.0504	kg/s	m_{engine}	730	kg
$\dot{m}_{\text{tot}}$	10.9	kg/s	O/F	0.25	-	Number of Engines	3	-
Nozzle Angle	15.0	degrees	Chamber Temp	1343.0000	K			
Nozzle Length	0.8	m						
M_e	5.6	-	Relative I_{sp} Loss	-0.4362	s	$m_{\textbf{tot}}$	19460	kg

Table 9.31: OMS Design Characteristics

9.4 MDE

9.4.1 Overview

The main propulsion system on the DEV consist of two pressure fed engines. Both engines use bipropellant combustion in order to produce their thrust. The propellant used for this is MMH as the fuel and N_2O_4 as the oxidizer. Due to the lower thrust needed for the engines, a simple pressure-fed system is all that is needed. This pressure-fed system utilizes He to pressurize the propellant. This way, there is no need for pumps and more complex turbomachinery which would contribute to increases mass and risk. Both the MDE and RCS use the same propellant tanks. The full P&ID can be seen in 9.13.

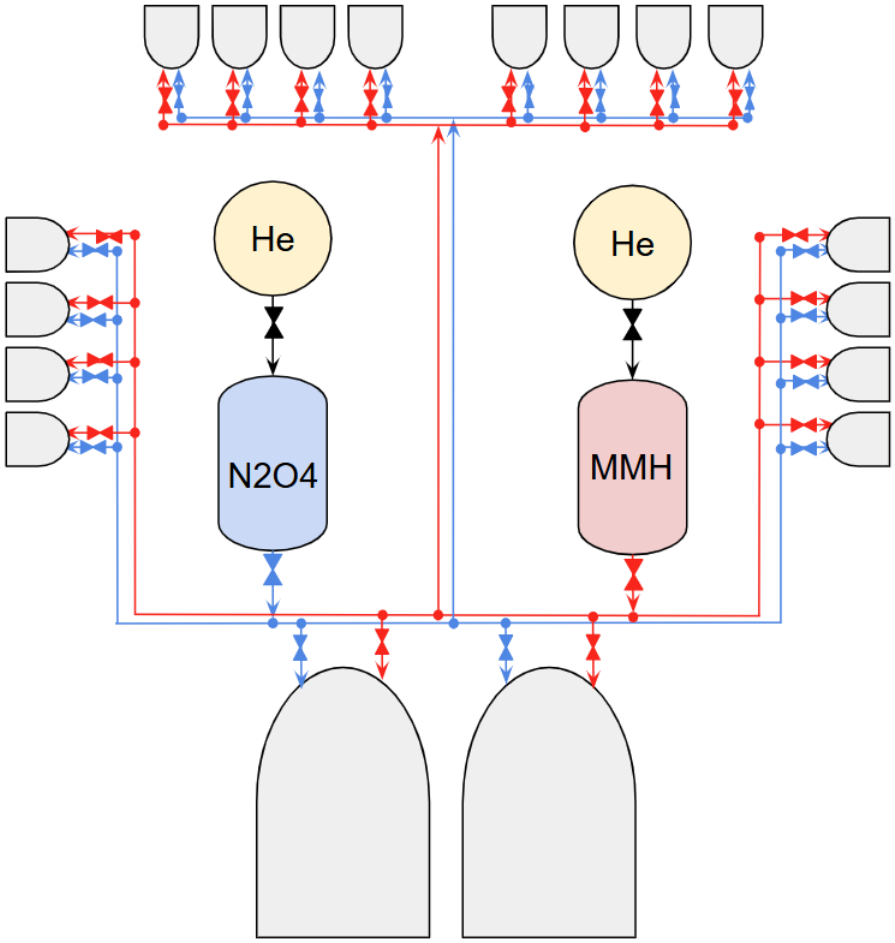

Figure 9.13: DEV P & ID with both RCS and MDE engines.

9.4.2 Performance

In order to design the nozzle, combustion chamber, and tanks, a performance analysis must be completed. First, a number of parameters must be chosen in order to begin the calculations. The parameters that are chosen can be seen in Table 9.32. The only value that is not chosen is the Isp which had been first estimated to be 325s but was recalculated later for accuracy.

A typical Isp for these types of smaller engines range from 300 s to 350 s. Due to low ΔV requirement determined in the DEV Trajectory Section, a low Isp is acceptable. A ΔV of less than 4 m/s is needed per transit between Deimos and the IPV. This means a low

Variable	Value	Units
Isp	324	seconds
Thrust	500	N
A_e/A^*	100	
T_0	3000	K
P_0	1	MPa
O/F	1.6	MPa

Table 9.32: Main DEV Engine Performance.

thrust is needed which resulted in 500 N being picked. The value of T_0 is found using CEA. P_0 is chosen due to recommendation in the *Design of Liquid Propellant Rocket Engines* textbook [85]. The O/F ratio is an optimized ratio commonly used in MMH and N_2O_4 bi-propellant engines. Using the same process as the OMS engine, the desired values are calculated. These values are seen in 9.42.

Variable	Value	Units
M_e	4.58	
P_e	0.80	kPa
C_f	2.01	
A^*	0.00025	m^2
A_e	0.025	m^2
$\dot{m}_{MMH}$	0.06	kg/s
$\dot{m}_{N_2O_4}$	0.10	kg/s
$\dot{m}_{propellant}$	0.16	kg/s

Table 9.33: Main DEV Engine Performance.

Since this is a pressure fed system, the design of the propellant tanks are crucial. Table 9.34 shows the values selected and calculated for the tanks pressures and volumes.

Variable	Value	Units
P_{MMH}	2.50	MPa
$P_{N_2O_4}$	2.50	MPa
P_{He}	30.00	MPa
V_{MMH}	0.014	m^3
$V_{N_2O_4}$	0.014	m^3

Table 9.34: Pressure and volume of propellant tanks.

A pressure drop of 20% is estimated for this system. The RCS combustion chamber has

a higher pressure that is twice as much as the pressure in the MDE combustion chamber. Therefore, flow for the MDE must be throttled using a valve within the flow system before entering the chamber in order to drop to 1 MPa.

The volumes for the propellant tanks are found using Boyle's law:

$$P_1 V_1 = P_2 V_2 \tag{9.76}$$

Using the mass discussed in the DEV Trajectory section of the report, the volume of the propellant is calculated. The volumes at normal atmospheric conditions, uncompressed (101.325kPa) and at room temperature (293.15K), are found to be $0.340m^3$ and $0.352m^3$ of N_2O_4 and MMH, respectively. When pressurized, the volume is compressed resulting in the much smaller volume, resulting in the values in the table.

It is important to know how much volume of He is needed to pressurize the pressure-fed propulsion system. These values are calculated using the following set of equations [85].

$$m_{He} = \frac{P_{propellant} V_{propellant}}{R_{He} T_{He}} \tag{9.77}$$

$$V_{He} = \frac{m_{He}}{[\frac{P_i - P_f}{R_{He} T_{He}}]} \tag{9.78}$$

All the volumes for these calculations including the inputs are in Table 9.35

This is assuming that the pressure will begin at 30 MPa and once all the propellant is gone, the He will still be pressurized to 2.7 MPa, so it is still able to pressurize the propellant until the tanks are empty.

Due to the high temperature within the combustion chamber, regenerative cooling is needed. The same method is used as in the OMS engine. The cooling loop uses MMH as the coolant fluid. It passes by the chamber and nozzle as it makes it way to the injectors in the combustion chamber. The inputs are seen in Table 9.36 while the outputs are in Table

Variable	Value	Units
P_{MMH}	2.50	MPa
$P_{N_2O_4}$	2.50	MPa
P_i	30.00	MPa
P_f	30.00	MPa
V_{MMH}	0.014	m^3
$V_{N_2O_4}$	0.014	m^3
$m_{He_{MMH}}$	2.50	MPa
$m_{He_{MMH}}$	2.50	MPa
$V_{He_{MMH}}$	0.0013	m^3
$V_{He_{N_2O_4}}$	0.0013	m^3
R_{He}	2077.1	$\frac{J}{kgK}$
T_{He}	293.15	K

Table 9.35: Helium tank values

9.37, showing that the temeprature of the wall is cooled down significantly.

Variable	Value	Units
$T_{0_{propellant}}$	3000	K
$T_{0_{coolant}}$	298.15	K
t_{wall}	0.002	m
k_{wall}	109	$\frac{W}{mK}$
$h_{propellant}$	657	$\frac{W}{m^2K}$
$h_{coolant}$	26000	$\frac{W}{m^2K}$
$\epsilon_{propellant}$	0.05	

Table 9.36: MDE: regenerative cooling inputs.

Variable	Value	Units
Q_{total}	1.936	$\frac{MW}{m^2}$
T_{wall} (propellant side)	403.122	K
T_{wall} (coolant side)	367.603	K
$Q_{radiation}$	259.635	$\frac{kW}{m^2}$
$Q_{convection}$	1.706	$\frac{MW}{m^2}$

Table 9.37: MDE: regenerative cooling results.

9.4.3 Design

The nozzle and combustion chamber design of the MDEs are developed using the values calculated in the performance section above. The nozzle design uses the Rao's method to make a parabolic contour. In order to develop the correct nozzle contouring using this method, a MATLAB script is developed.

MATLAB Inputs		
Variable	Value	Units
R_{th}	0.009	m
R_e	0.089	m
ϵ	100	
Length %	80	%

Table 9.38: MDE: Rao's method MATLAB inputs.

The values for R_{th}, R_e, and ϵ come from the performance analysis of the nozzle. Where R_{th} is the radius of the nozzle's throat , R_e is the radius of the exit of the nozzle, and the length percentage was chosen arbitrarily. The chosen value of 80% is commonly used for rocket engine nozzles. At 80%, the efficiency has reached a plateau. Increasing to 100% length will only increase the efficiency slightly.

Using these values and the Rao's method, the nozzle contour can be determined. The first calculation is to contour the throat. The x coordinate is calculated using Equation 9.14, and the y coordinate is calculated using Equation9.15. A range of $-135° \leq \theta \leq -90°$ is plugged in for θ with a step size of $1°$. This range is typical for many engine nozzles. Next is determining the exit section of the throat. This is found using Equations 9.16 and 9.17 to find the x and y coordinates, respectively. The range for θ used in these equations is a range from $-90° \leq \theta \leq (\theta_n - 90)°$ where θ_n is $32°$. This value is found using Figure 9.6, based on the percent bell length and area ratio. Next is to determine the coordinates for x and y along the parabolic part fo the nozzle. These values were found using Equations 9.18 and 9.19, respectively. The value for t is a range of numbers from 0 to 1. The step size chosen for this is 0.05 for precision but also to minimize run time. The values for N_x,

Q_x, E_x, N_y, Q_y, and E_y were calculated using Equations 9.20 all the way to Equation 9.25. These values are seen in Table 9.41.

Variable	Value	Units
N_x	0.002	m
N_y	0.009	m
E_x	0.242	m
E_y	0.089	m
m_1	0.625	m
m_2	0.132	m
C_1	0.008	m
C_2	0.057	m
Q_x	0.099	m
Q_y	0.070	m

Table 9.39: Values for Rao's method on MDE nozzle (throat is located at 0).

N_x and N_y are the last values in the throat exit calculations for the x and y coordinates, respectively. E_x and E_y are the length of the nozzle, L_N, and exit radius, R_e. L_N is calculated using 9.26. The final contour produced by these numbers is seen in Figure 9.14.

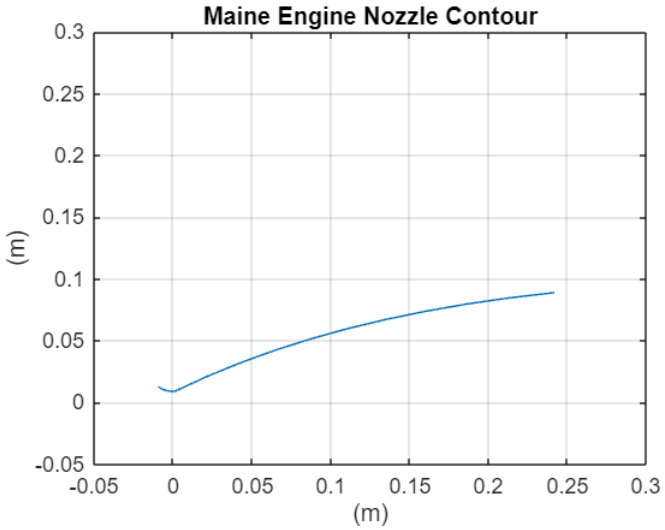

Figure 9.14: MDE Nozzle Contour.

Now that the nozzle is designed, the combustion chamber can be designed. First the characteristic length must be determined. Figure 9.15 shows the recommended characteristic lengths for different propellant mixtures. For MMH and N_2O_4, the recommended

characteristic length is $30in$ to $35in$. To be safe, a characteristic value of 35in is chosen, which is equal to 0.889m. The volume of the chamber can be calculated rearranging Equation 9.79

TABLE 4-1.–*Recommended Combustion Chamber Characteristic Length* (L*) *for Various Propellant Combinations*

Propellant combination	Combustion chamber characteristic length (L^*), in.
Chlorine trifluoride/hydrazine-base fuel	30-35
Liquid fluorine/hydrazine	24-28
Liquid fluorine/liquid hydrogen (GH_2 injection)	22-26
Liquid fluorine/liquid hydrogen (LH_2 injection)	25-30
Hydrogen peroxide/RP-1 (including catalyst bed)	60-70
Nitric acid/hydrazine-base fuel	30-35
Nitrogen tetroxide/hydrazine-base fuel	30-35
Liquid oxygen/ammonia	30-40
Liquid oxygen/liquid hydrogen (GH_2 injection)	22-28
Liquid oxygen/liquid hydrogen (LH_2 injection)	30-40
Liquid oxygen/RP-1	40-50

Figure 9.15: Recommended characteristic length.

$$L^* = \frac{V_c}{A_t} \tag{9.79}$$

Using Equation 9.80, the combustion chamber dimensions are calculated. An input for the combustion chamber cross section area is chosen in order to have only one unknown variable. The resulting values are seen in 9.40.

$$v_c = A_t[L_c\epsilon_c + \frac{1}{3}\sqrt{\frac{A_t}{\pi}}\cot(\theta)(\epsilon_c^{1/3} - 1)] \tag{9.80}$$

Where L^* is the characteristic length, A_t is the throat area, V_c is the combustion chamber volume, ϵ_c is the ratio of the combustion chamber area to the throat area ($\frac{A_c}{A_t}$), L_c is the chamber length, and A_c is the chamber area.

Variable	Value	Units
L^*	0.889	
A_t	0.00025	m^2
V_c	0.00022	m^3
ϵ_c	8.401	
L_c	0.110	m
A_c	0.002	m^2

Table 9.40: Combustion chamber calculation for MDE.

Figure 9.16 shows the final assembly of the nozzle and combustion chamber of the MDE. The final CAD drawing with overall dimensions is seen in the appendix.

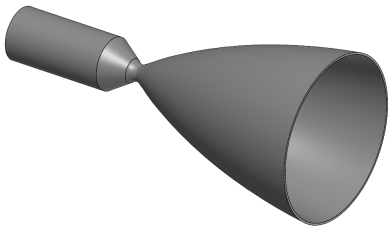

Figure 9.16: CAD of MDE.

9.5 DEV RCS

9.5.1 Overview

The purpose of RCS thrusters are to make small maneuvers and rotations. The DEV must be able to do this for both the transit to and from Deimos as well as maneuvering on Deimos's surfaces. These movements require precise control which is why these engines are needed. They are much smaller than a typical engine. As discussed in the vehicle design section, the DEV contains a total of 16 RCS thrusters which allows for 6 degrees of freedom. There are four clusters of four thrusters evenly located around the outside of the habitat. These thrusters utilize the same propellant system as the MDE, using MMH and N_2O_4. This also means that they use a pressure fed system as well, which is more common for RCS thrusters to use.

9.5.2 Performance

As with the MDE, the RCS thrusters follow the same analysis as the OMS engines. The input and results are seen in Tables 9.41 and 9.42.

Variable	Value	Units
Isp	328	seconds
Thrust	200	N
$\dot{m}$	53.42	g/s
A_e/A^*	60	
T_0	3081	K
P_0	2	MPa

Table 9.41: DEV RCS Performance.

Variable	Value	Units
M_e	4.32	
P_e	2.86	kPa
C_f	2.01	
A^*	0.000051	m^2
A_e	0.0031	m^2
$\dot{m}$	53.42	g/s

Table 9.42: RCS Performance.

The RCS thrusters use the same propellant and helium tanks as the MDE engines. Those results are seen in Table 9.34 and 9.35. The benefits of using one set of propellant and helium tanks is to decrease mass. Having multiple tanks and multiple piping systems results in a significant increase of mass. The tanks are also so small in size already that there is no need for multiple tanks.

Since bi-propellant combustion is being used, the walls of the combustion chamber and nozzle heat up. The temperature for combustion is quite high, so this system also requires regenerative cooling. The RCS uses the same regenerative cooling system as both the OMS and MDE. The inputs and obtained values from the analysis are seen in Tables 9.43 and 9.44.

Variable	Value	Units
$T_{0_{propellant}}$	3081	K
$T_{0_{coolant}}$	293.15	K
t_{wall}	0.002	m
k_{wall}	109	$\frac{W}{mK}$
$h_{propellant}$	657	$\frac{W}{m^2K}$
$h_{coolant}$	26000	$\frac{W}{m^2K}$
$\epsilon_{propellant}$	0.05	

Table 9.43: RCS: regenerative cooling inputs.

Variable	Value	Units
Q_{total}	2.009	$\frac{MW}{m^2}$
T_{wall} (propellant side)	412.286	K
T_{wall} (coolant side)	375.422	K
$Q_{radiation}$	255.552	$\frac{kW}{m^2}$
$Q_{convection}$	1.754	$\frac{MW}{m^2}$

Table 9.44: RCS: regenerative cooling results.

9.5.3 Design

The RCS thruster's nozzle and combustion chamber use the same development process as the MDE. Beginning with the nozzle design, the inputs are seen in Table 9.45 and the resulting values are seen in Table 9.46.

MATLAB Inputs		
Variable	Value	Units
R_{th}	0.004	m
R_e	0.032	m
ϵ	60	
Length %	65	%

Table 9.45: RCS: Rao's method MATLAB inputs.

There are a few design choices that separate the RCS thrusters from the MDE. The first difference is that the percentage bell length is only 65%. Although this value is less efficient

than a 80% nozzle, RCS nozzles tend to be shorter. This is due to factors such as length and area ratio. RCS thruster prefer to be more compact due to their position outside of spacecrafts. The area ratio chosen for this specific RCS thruster is on the larger side for RCS systems which is due to desiring a higher Isp. RCS will be used more than the main engines when maneuvering around the surface of Deimos. A higher Isp means a better efficiency. The amount of mass that can be taken to Deimos must be limited, so anywhere where propellant mass can be minimized is important.

Variable	Value	Units
N_x	0.0009	m
N_y	0.0043	m
E_x	0.0655	m
E_y	0.0313	m
m_1	0.7536	m
m_2	0.1317	m
C_1	0.0036	m
C_2	0.0226	m
Q_x	0.0306	m
Q_y	0.0267	m

Table 9.46: Values for Rao's method on RCS nozzle (throat is located at 0).

The resulting contour is seen in Figure 9.17

The combustion chamber is then design using the same methods as the MDE. Table 9.47 shows these results.

Variable	Value	Units
L^*	0.889	
A_t	0.00005	m^2
V_c	0.00005	m^3
ϵ_c	15.650	
L_c	0.057	m
A_c	0.0008	m^2

Table 9.47: Combustion chamber calculation for RCS.

Figure 9.18 shows the completed combustion chamber and nozzle CAD of the RCS thrusters.

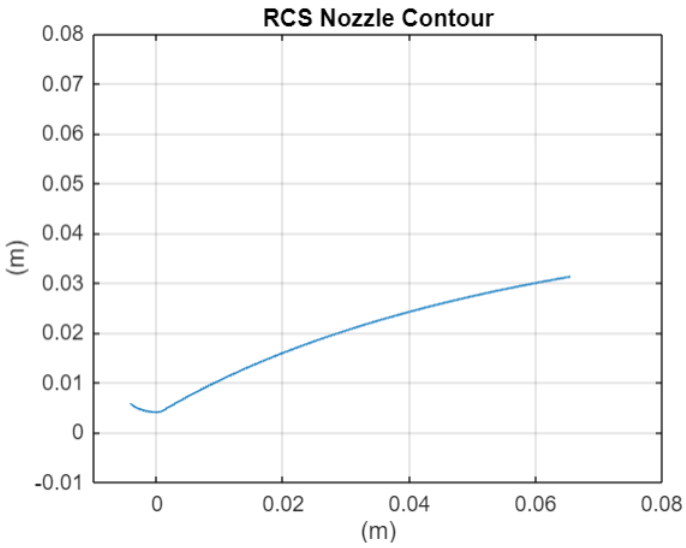

Figure 9.17: DEV RCS Nozzle Contour.

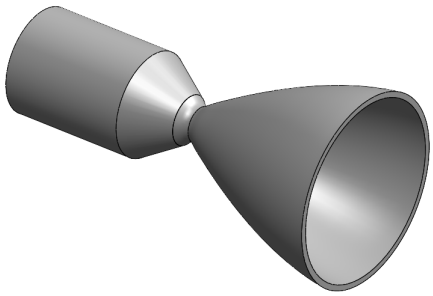

Figure 9.18: DEV RCS Nozzle Contour.

The final CAD drawing with overall dimensions of the nozzle and combustion chamber can be found in the appendix.

10 Thermal Control

10.1 FBD of Thermal Control Systems

Below is an overall Functional Block Diagram (FBD) of the systems within Thermal Control. There are four major categories within Thermal Control Systems: Heat Exchangers, Pumps, Radiators, and MLI. These represent the key systems within Thermal Control, with additional sub-categories shown beneath them in Table 10.1.

Thermal Control Systems			
Heat Exchanger	**Pumps**	**Radiators**	**MLI**
Overall Heat Transfer Coefficient	Power Required	Fluid Temperature Change	Boil-Off Rate
Materials	Pump Diameter	Fin Temperature Change	Materials
Design	Specific Speed and Diameter	Materials	Thickness
		Placement	
		Design & Redundancy	

Table 10.1: Functional Block Diagram for Thermal Control Systems

The following sections contain detailed analysis, results, and design decisions for each of these categories.

10.2 Piping and Instrumentation Diagrams of Heat Rejection Systems

Figures 10.1 and 10.2 display the flow diagrams for the two types of ATCS used on the IPV for the resulting high and low temperature systems. The Type A system shown in Figure 10.1 is responsible for the control systems, such as the bimodal and DEV reactors that operate at high temperatures, while the Type B system shown in Figure 10.2 is responsible for the control of the lower temperature systems, such as the habitable locations and electronic equipment on board. Due to the DEV separating from the rest of the IPV for extended periods of time, one of each system type is located on both the IPV Hab and DEV, resulting in a total of four closed-loop systems with both the IPV Hab and DEV

being able to reject waste heat from both temperature ranges independently of each other.

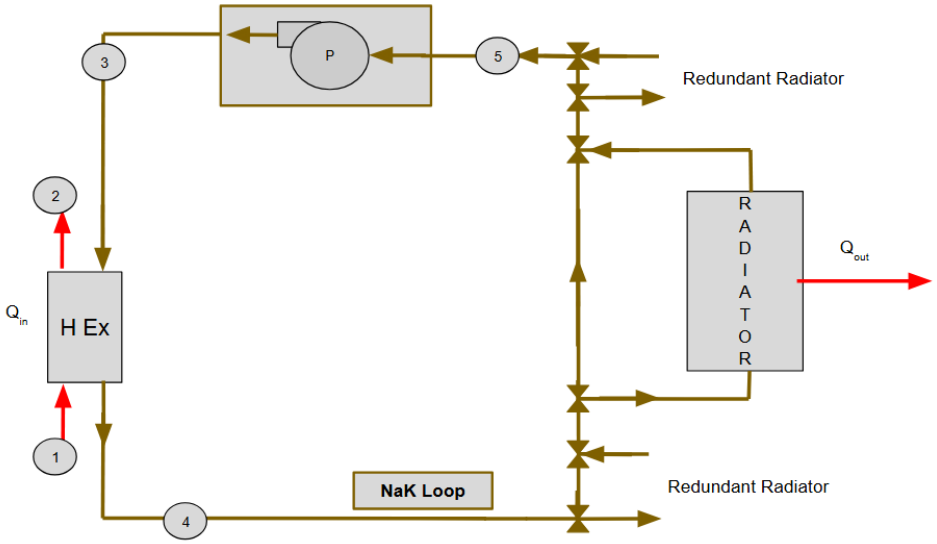

Figure 10.1: Type A NaK Eutectic Thermal Rejection Loop Block Diagram

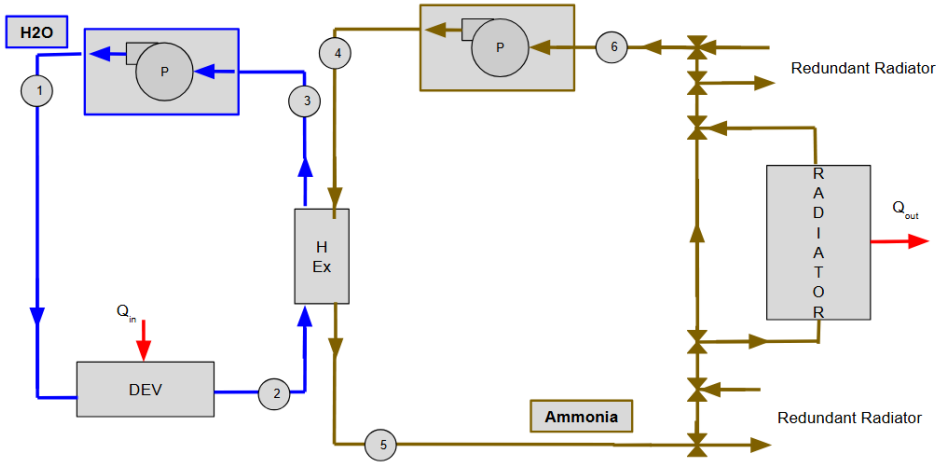

Figure 10.2: Type B Water-Ammonia Thermal Rejection Loop Block Diagram

Each ATCS is made of a few key components that will be further analyzed in Subsections 10.3.2 -10.4. A finned-tube heat exchanger is used to transfer thermal energy between the different fluid loops transporting the thermal energy in the system. The second major component is the radial pump, which ensures consistent pressure and fluid flow through the network of piping throughout the closed-loop system. The last major component in

the ATCS is the radiators, which dissipate thermal energy transferred to them by rejecting it to space.

10.3 ATCS State Analysis

The steady state power cycle operational conditions are determined for each state along the paths of the ATCS shown in the Figures 10.1 and 10.2. The initial pressure and temperature conditions are chosen for each of the specific system types. For the Type A systems, the initial power cycle states is determined in Section 11 where the temperature and pressure drop across the heat exchanger in the system is given by states 6 to 1 from Tables 11.8 and 11.18 for the bimodal and DEV reactors respectively. To find the steady-state conditions for each type A loop, these initial conditions, along with the resulting Q_{out} are needed.

Then, assuming isentropic conditions across the heat exchanger, the resulting temperature difference for the NaK across the heat exchanger is found using Equation 10.1.

$$\Delta T = \frac{Q_{out}}{\dot{m} \cdot C_p} \tag{10.1}$$

Using the resulting values in Section 11, a max NaK temperature was selected at values of 620 K and 660 K for the Bimodal and DEV, respectively. The maximum possible temperature for the eutectic is not chosen in order to reduce the resulting size necessary for the heat exchanger. The initial temperature and initial pressure are chosen based on a closely related design from Reference [7]. Using the initial temperature and pressure, the state before and after the radiator is determined. Table 10.2 shows the resulting pressures and temperatures for each state of the two Type A ATCSs.

		Bimodal:	**DEV:**
	$Q\ (kW)$	***77.2***	***115.3***
State 1	$T\ (K)$	648	608
	$P\ (MPa)$	2.5	2.5
State 2	$T\ (K)$	500	450
	$P\ (MPa)$	2.5	2.5
State 3	$T\ (K)$	574	618
	$P\ (MPa)$	0.27	0.27
State 4	$T\ (K)$	595	647
	$P\ (MPa)$	0.27	0.27
State 5	$T\ (K)$	586	618
	$P\ (MPa)$	0.12	0.12
State 6	$T\ (K)$	N/A	N/A
	$P\ (MPa)$	NA	NA

Table 10.2: Type A ATC: Thermodynamic State Table

Similar to the analysis for the Type A ATCS, the resulting pressures and temperatures for the Type B ATCS are determined. However, instead of the steady state power cycle operational conditions determined from the reactor power cycles, the initial values for both the water and ammonia must first be determined. The low temperature Type B loops, water and ammonia cycles are chosen in reference to the ATCS currently operating on the ISS, as it is a similar system currently in operation, given in Reference [86]. These initial temperatures and pressures are chosen in order to ensure that both the water and ammonia remain well within the liquid phase throughout operation. The resulting thermal heat transfer out,Q_{out}, is again determined by Section 11

Using equations presented in the following Section 10.3.1 to account for the frictional pressure losses through the network of pipes used to collect heat from the DEV and HAB,

the pressure drop across the water loop is determined. Using the pressures and initial temperatures, all the states are then determined using the Equation 10.1 as shown above for steady state conditions throughout the Type A ATCS. All other sub-components within each loop are once again assumed to be isentropic, and the pressures and temperatures for each state along both Type B loops are shown in Table 10.3.

		HAB:	**DEV:**
	$Q\ (kW)$	***15***	***10***
State 1	$T\ (K)$	283.2	283.9
	$P\ (MPa)$	0.5	0.5
State 2	$T\ (K)$	285.5	285.4
	$P\ (MPa)$	0.493	0.497
State 3	$T\ (K)$	283.2	283.9
	$P\ (MPa)$	0.493	0.497
State 4	$T\ (K)$	282.7	282.8
	$P\ (MPa)$	1.2	1.2
State 5	$T\ (K)$	284.4	283.9
	$P\ (MPa)$	1.2	1.2
State 6	$T\ (K)$	282.7	282.8
	$P\ (MPa)$	0.9	0.9

Table 10.3: Type B ATC: Thermodynamic State Table

10.3.1 Pressure Drop Across Looped Piping

The habitable waste heat rejection systems for the DEV and the IPV Hab consist of tightly looped piping to remove excess waste electrical heat from the habitat modules and move the heat into the radiators for dissipation into space. The analysis of the interaction between the habitation module waste heat, the H_2O working fluid, and the pipe walls is

treated as two distinct processes. First, the energy balance equation is used to calculate the change in enthalpy from the heat addition from habitation module waste heat. Next, the pressure loss from the tubing is estimated through the use of the Darcy Weisbach equation and a Moody Diagram to obtain the relevant flow coefficients. Figure 10.3 below shows the heat addition and pressure loss steps side by side.

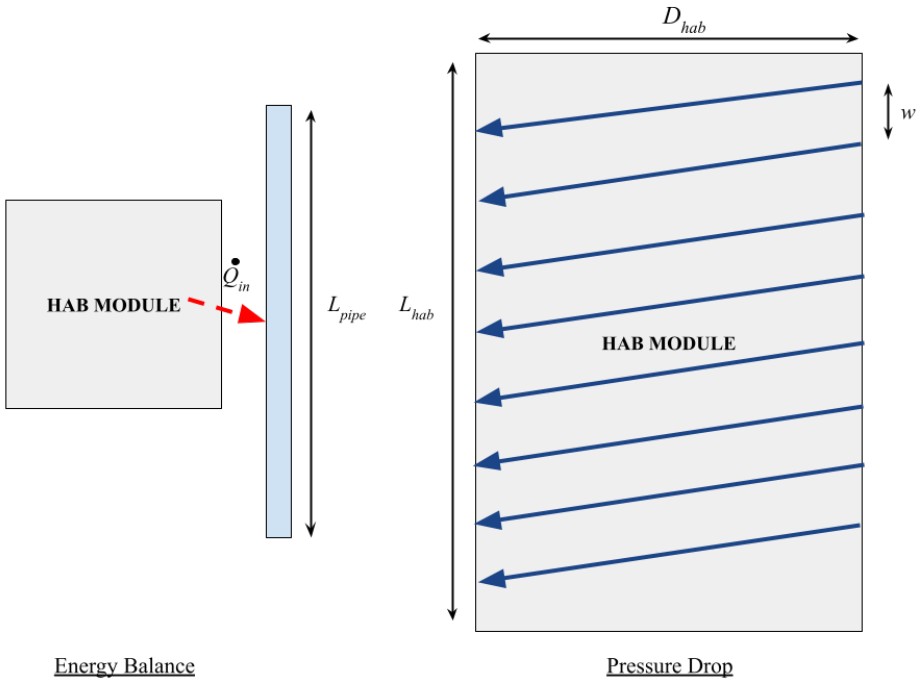

Figure 10.3: Habitation Waste Heat Analysis Approach

For the energy balance portion of the analysis, State 1 is considered to be before the heat addition process, while State 2 is considered to be after.

$$\dot{m}h_1 + \dot{Q_W} = \dot{m}h_2 \tag{10.2}$$

State 1 is considered to be an input condition, with T_1 and P_1 being specified for the analysis. REFPROP integrated into Microsoft Excel is used to calculate the thermodynamic properties at the output, State 2. After h_1 is computed with REFPROP, h_2 is computed with simple algebraic manipulation of Equation (10.2). Tables 10.3 provides the input, output,

and maximum heat rejection capabilities for the DEV and IPV Hab systems.

Second, the pressure drop across the tightly wound piping is calculated. Using Figure 10.3, the piping layout is chosen for DEV and the IPV Hab. Any conduction or convection between the working fluid and the pipe wall is not considered in this analysis, as the heat addition process is considered to act at a single time and location. Based on a constant pipe diameter and a chosen piping separation, w_{pipe}, the total length of the pipes is calculated. The total length of each pipe wind is simply the circumference of the cylindrical habitat section. To calculate the total length, the length of one wind is multiplied by the number of total winds, N, which is expressed as $N = L_{hab}/w_{pipe}$. Then, the total length of the fully wound pipe is simply $L_{pipe} =_{hab}$. Next, the pressure drop is computed with the Darcy Weisbach equation [77].

$$\Delta P = f_d \frac{L_{pipe}}{d_{pipe}} \frac{\rho v^2}{2} \tag{10.3}$$

In order to obtain a value for f_d, the Reynolds Number, Re, is computed using REFPROP to solve for the kinematic viscosity based on the heated H_2O conditions (State 2). The local flow velocity in the pipe, u, is computed from the cross sectional area of the circular pipe and the chosen mass flow rate, $\dot{m}$.

$$u = \frac{\dot{m}}{\rho A} \tag{10.4}$$

The Reynolds number is then found:

$$Re = \frac{\rho u D}{\mu} \tag{10.5}$$

Finally, the friction factor is found from a Moody diagram (Figure 10.4) based on the calculated Reynolds number. The computed parameters for the IPV Hab and DEV pressure drop are listed in Table 10.4. As $Re \leq 2300$, the flow is considered laminar on the Moody Diagram and the f_d values are inferred from the chart.

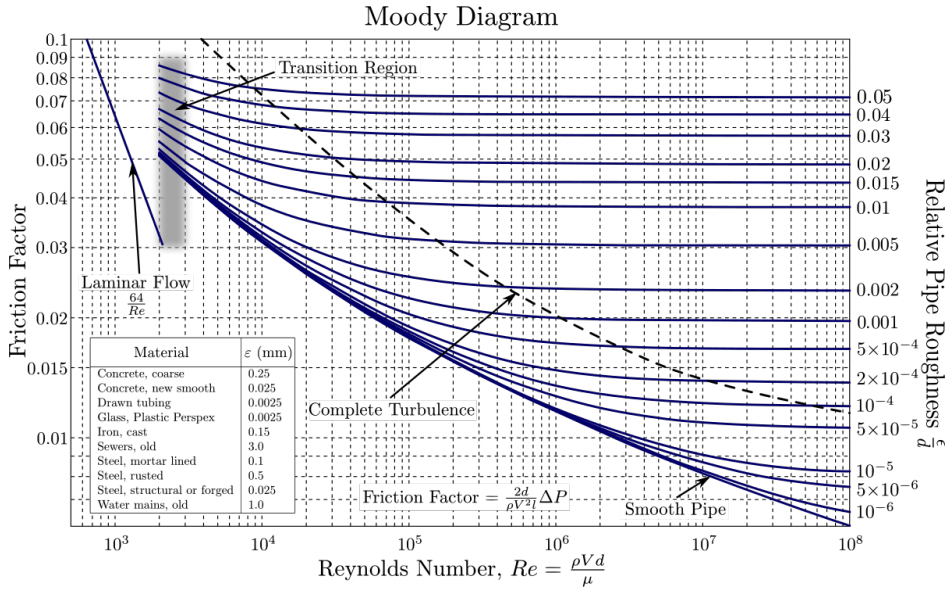

Figure 10.4: Heat Rejection Moody Diagram

Equation (10.3) is now used to solve for the pressure drop.

Table 10.4 displays the results of the previously mentioned analysis.

Parameter	Hab	DEV	Unit
D	5.50	5.40	m
L	7.50	3.20	m
w	0.25	0.25	m
d	0.10	0.10	m
C	17.28	16.96	m
N	30.00	12.80	-
$Lpipe$	518.36	217.15	m
L/d	5183.63	2171.47	-
ρ_2	999.57	1000.16	kg/m^3
μ_2	0.01	0.02	
u_2	0.20	0.20	m/s
Re	1696.17	1356.97	-
f_d	0.06	0.06	-
Δ_P	5918.53	2477.87	Pa
$Delta_P$	5.92	2.48	kPa
P_2	0.49	0.50	kPa
P_2/P_1	0.988	0.995	

Table 10.4: ATCS Type B Pressure Drop Analysis

10.3.2 Heat Exchanger Analysis

The ATCS uses a cross-flow, fin-and-tube heat exchanger to efficiently transport the thermal energy from one set of fluids to another. Due to the complex geometry of the resulting design, several design assumptions are made in order to perform the analysis. The resulting analysis is simplified to an aligned tube bank in order to use an appropriate Nusselt number correlation found by [5]. The convective coefficient through both fluids

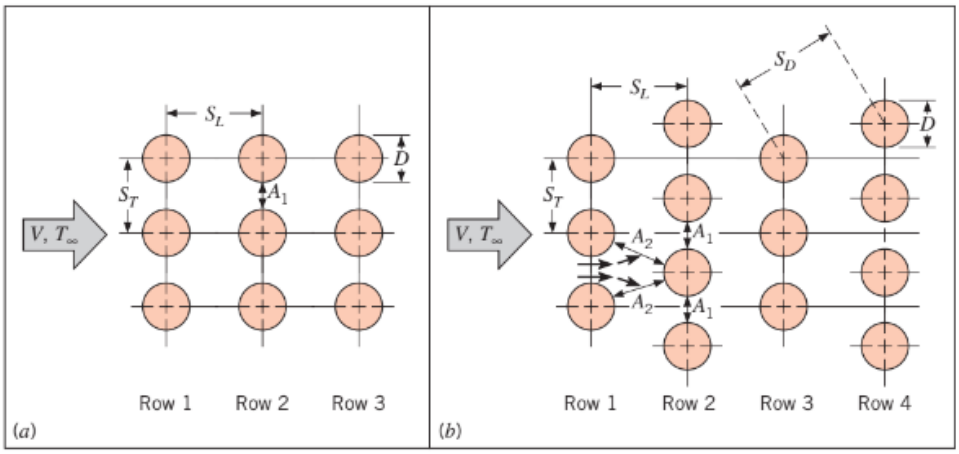

FIGURE 7.12 Tube arrangements in a bank. (*a*) Aligned. (*b*) Staggered.

Figure 10.5: Diagram of staggered and inline tube banks showing chosen dimensions

within the heat exchangers are then calculated. Table 10.5 shows the resulting design assumptions made for each heat exchanger. Figure 10.5 depicts a diagram of the design length presented in Table 10.5 and is taken from Reference [5].

	Type A		**Type B**	
	Bimodal	**DEV**	**HAB**	**DEV**
A	0.5	0.5	0.2	0.3
$S_t\ (m)$	0.04	0.04	0.04	0.04
$S_L\ (m)$	0.02	0.02	0.02	0.02
$D_i\ (m)$	0.01	0.02	0.025	0.01
t (m)	0.001	0.01	0.03	0.005
$N_t\ (m)$	230	234	180	225
N-h (m)	23	26	20	25

Table 10.5: ATCS Heat Exchanger: Chosen Design Parameters

Analysis begins with determining the Reynolds number of both fluids using Equation 11.29 below. The Prandtl number is also determined using Equation 10.7 for each fluid.

$$Re = \frac{\dot{m}_{He-Xe} \cdot D_o}{\mu \cdot A_{c-s}} \tag{10.6}$$

$$Pr = 0.001 \cdot \mu \cdot \frac{Cp}{k} \tag{10.7}$$

$$T_{avg_{He-Ne}} = \frac{(T_3 + T_2)}{2} \tag{10.8}$$

Using Equation 10.8, another Prandtl number is calculated using the average temperature across the heat exchanger. This separate Prandtl number will be further referenced as Pr_s throughout the analysis. Next, the convection coefficient is determined for the fluid flowing through the in-line tube banks. Using Equations 10.9 and 10.10, the Nusselt number approximations for the eutectic and ammonia are given by Reference [5].

$$Nu_{NaK} = 5.0 + 0.025(Re \cdot Pr)^{0.8} \tag{10.9}$$

$$Nu_{H2O} = 0.023 Re^{0.8} \cdot Pr^{0.4} \tag{10.10}$$

The resulting convective coefficient is determined using Equations 10.11 and 10.12.

$$h_{NaK} = 5\left(\frac{k}{D_i}\right) + 0.025(k)^{0.2}\left(\frac{4\dot{m}C_p}{\pi \cdot N_t}\right)^{0.8}\left(\frac{1}{D_i}\right)^{1.8} \tag{10.11}$$

$$h_{H2O} = 0.023 \cdot \left(\frac{\dot{m}}{A_{cs}}\right)^{0.8}\left(\frac{C_p \cdot D}{\mu}\right)^{0.4}\left(\frac{k}{D}\right)^{0.6} \tag{10.12}$$

The Nusselt number for the fluid flowing across the in-line tube bank is modeled using Equation 10.13 below, taken from Reference [5]

$$Nu_D = 0.27 \cdot Re^{0.63} \cdot Pr^{0.36}\left(\frac{Pr}{Pr_s}\right)^{1/4} \tag{10.13}$$

Equation 10.13 is rewritten in the form of Equation 10.14 below, resulting in the convective coefficient for the fluid flowing across the tube bank.

$$h_{TB} = \left(\frac{k}{Re}\right)\left[0.27 \cdot Re^{0.63} \cdot Pr^{0.36}\left(\frac{Pr}{Pr_s}\right)^{1/4}\right] \tag{10.14}$$

Then, assuming copper as the primary conductive material, the resulting thermal resistance through the entire heat exchanger is determined using Equation 10.15 below.

$$U = \left[\frac{1}{h_{NaK/H2O}} + \frac{t}{k_{wall}} + \frac{1}{h_{TB}}\right]^{-1} \tag{10.15}$$

Then, using the temperatures flowing into and out of each portion of the heat exchanger, the log-mean temperature is calculated using Equation 11.34.

$$T_{lm} = \frac{(T_{3_{He-Xe}} - T_{2_{He-Xe}}) - (T_{4_{NaK}} - T_{1_{Nak}})}{\ln\left[\frac{T_{3_{He-Xe}} - T_{2_{He-Xe}}}{T4_{NaK} - T1_{NaK}}\right]} \tag{10.16}$$

Finally, with the resulting T_{lm} and U, the heat exchangers' effective surface area is calculated using Equation 10.17. The resulting calculated values for each heat exchanger are given in Tables 10.6 & 10.7.

$$A = \frac{Q_{out}}{U \cdot T_{lm}} \tag{10.17}$$

Parameter	Bi-Modal	DEV
$\dot{m}$ NaK (kg/s)	1.5	1.5
$\dot{m}$ He-Xe (kg/s)	1.1	0.8
T_{lm} (K)	123.22	118.64
A (m^2)	27.07	45.54
UA (W/K)	752.51	702.01

Table 10.6: Heat Exchanger Analysis within the Type A: ATCS

Parameter	HAB	DEV
$\dot{m}\ H_2O\ (kg/s)$	1.6	1.6
$\dot{m}\ CH_3\ (kg/s)$	3	3
$T_{lm}\ (K)$	1.93	1.29
$A\ (m^2)$	30.03	8.01
$UA\ (W/K)$	7794.73	7794.73

Table 10.7: Heat Exchanger Analysis within the type B ATCS

10.3.3 Radial Pump Analysis

The pumps within each fluid loop in the ATCS provide the pressure needed to counteract losses generated by flowing through the extensive network of piping. As an isentropic analysis across each of the states throughout each system was already determined, the resulting pressure increase across the pump is already known. Adiabatic efficiency is then determined using Equation 10.18 to determine the adiabatic head change across the pump.

$$H_{ad} = \frac{\eta_p(P_2 - P_1)}{\rho} \tag{10.18}$$

Using REFPROP, integrated into Microsoft Excel, the density of the fluid is then determined for the two states. Next, using the density and the mass flow rate, the volumetric mass flow rate is calculated using equation 10.19.

$$Q = \frac{\dot{m}}{\rho} \tag{10.19}$$

Then, inputting a common motor rpm value and other relevant information into equation 10.20, the non-dimensional specific speed is calculated. The non-dimensional speed is then multiplied by a scaling factor in order to use Figure 10.6 below to determine a potential desired specific diameter for the pump for the highest possible compressive efficiency as mentioned in [87].

$$N_s = \frac{N * Q^{1/2}}{H_{ad}^{3/4}} \tag{10.20}$$

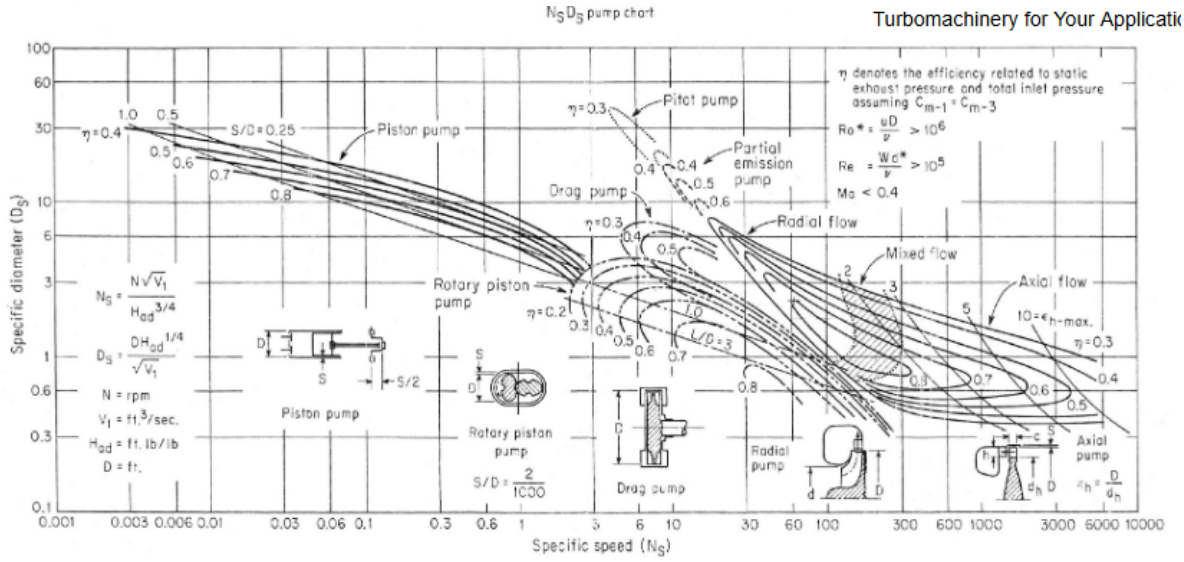

Figure 10.6: Specific Speed vs. specific diameter plot for various pump designs and pressure efficiencies

For all resulting pumps, the compressive efficiency is selected to be 0.8. As a result, the specific diameter is determined and input into equation 10.21 below, the resulting pump diameter is calculated.

$$D_s = \frac{D \cdot (H_{ad})^{1/4}}{Q^{1/2}} \tag{10.21}$$

Finally, the analysis of the pumps concludes with using equation 10.22 to determine an initial estimate of the power required to continuously operate the resulting ATCSs along the IPV. Table 10.8 presents the results of this analysis for all pumps used in all four of the ATCSs on the IPV, displaying each pump's respective rpm, power, efficiency, and both dimensional and non-dimensional specific speeds and diameters.

$$P_{pump} = Q(P_2 - P_1) \tag{10.22}$$

	Bi-Modal	NaK DEV	H2O HAB	NH3 HAB	H2O DEV	NH3 DEV
RPM	7200	7200	3600	14400	3600	14400
$W_{pump}\ (W)$	302	302	800	2250	3965	2250
Efficiency	0.8	0.8	0.8	0.8	0.8	0.8
$D\ (cm)$	2.3	1.5	15.00	4.0	15.0	4.0
N_S	0.607	0.718	0.802	0.512	1.357	0.512
D_S	2.888	1.241	0.997	1.359	0.837	1.359

Table 10.8: ATSC: Pump Analysis Results

10.4 Radiators

Radiators are a crucial element in the operations of this spacecraft. Without the ability to reject heat, power production becomes impossible, and habitat volumes overheat. There are a series of radiators spread throughout the spacecraft to manage heat rejection for power sources and solar irradiation absorbed by habitat volumes. On the IPV, heat rejection is needed for the bimodal power system, which is the principal power production unit on the spacecraft, and the IPV Habitat, which absorbs solar irradiation. The DEV requires its own independent radiators for its power generation system, as well as any solar irradiation it absorbs, as it must operate alone for extended durations.

Eutectic NaK is used for the working fluid of radiators for the heat rejection of the power cycles because of its excellent thermal conductivity as a liquid metal, and the higher operating temperatures of these power cycles. For heat rejection of habitat volumes, ammonia is used as the working fluid in the radiators because of its high range of operating temperatures and because it has a relatively high thermal capacity.

A manifold design is chosen for the radiators, which is described later in Section 10.4.2, given its design is more inherently safe as compared to other designs. In addition, this design is easy to mount to the IPV vehicle and the DEV because of the location of its inlets

and outlets.

Radiator placement and arrangement justification is discussed in Section 5.1.4, and will not be reiterated in this section of the report.

10.4.1 Radiator Analysis Model

Fundamentally, these radiators must change the working fluid temperature in the radiator by some amount to make an effective power cycle. This temperature delta is determined from the heat rejection analysis, and more specifically, heat exchanger analysis, described earlier. It is important to note that operating the working fluid at higher temperatures and minimizing the temperature delta is a priority for ensuring radiators are as small as possible. This is because operating at higher temperatures means more energy can be transferred through the working fluid. Additionally, minimizing the temperature delta reduces the amount of heat transfer, thus the size of the radiators is decreased.

The radiator analysis consists of two, one-dimensional heat transfer models for convection and conduction. The convection model is needed to update how the radiators' working fluid decreases in temperature, while the conduction model is needed to size the radiator fins. A diagram of the radiator analysis model is shown in Fig. 10.7.

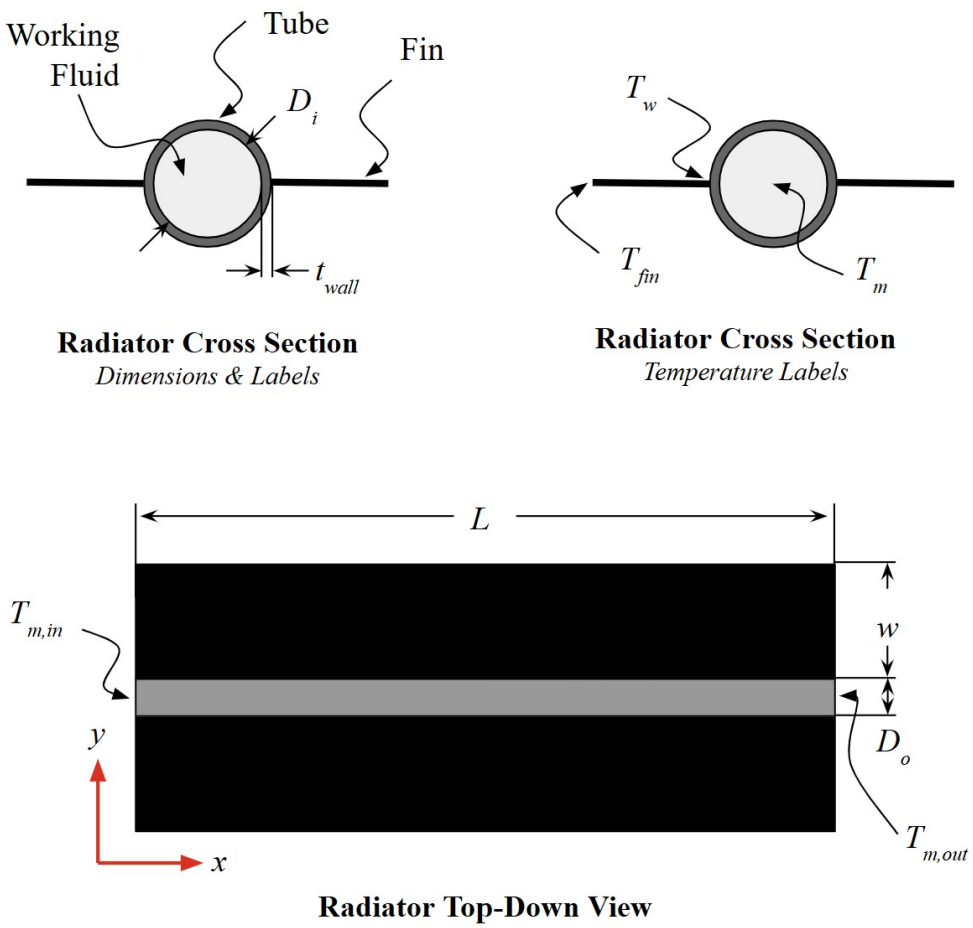

Figure 10.7: Radiator Analysis Model Diagram

The convection model is based on a heat transfer balance of convection from the working fluid to the radiation coming off the radiator across a small, approximately differential, element. A given mean fluid input temperature is provided, $T_{m,in}$, with a target output mean fluid output temperature of $T_{m,out}$. These temperatures are used to drive the system, as ultimately the radiator needs to cool down the fluid temperature to $T_{m,out}$. This differential model is mathematically represented in Eq.(10.23), where the rate of convective heat transfer, $\dot{Q}_{conv}$, is set equal to the rate of radiative heat transfer, $\dot{Q}_{rad}$. Applying Newton's Law of Cooling and the Stefan-Boltzmann Law to this equation, the result shown in Eq.(10.24) is obtained, which is further simplified in Eq.(10.25).

$$\dot{Q}_{conv} = \dot{Q}_{rad} \tag{10.23}$$

$$\Delta x \, \pi \, D_i \, h \, (T_{m,x} - T_w) = \Delta x \, (\pi \, D_o + w) \, \epsilon \, \sigma \, (T_w^4 - T_s^4) \tag{10.24}$$

$$\Rightarrow D_i \, h \, (T_{m,x} - T_w) = D_o \, \epsilon \, \sigma \, (T_w^4 - T_s^4) \tag{10.25}$$

Here, Δx represents some small step size in the x-direction, D_i is the inner diameter of the tube, h is the heat transfer coefficient, $T_{m,x}$ is the mean fluid temperature at increment x, T_w is the wall temperature of the tube, D_o is the outer diameter of the tube, w is a guessed radiator width, ϵ is the emissivity of the radiator, σ is the Stefan-Boltzmann constant, and T_s is the temperature of space. Fig. 10.7 labels many of these parameters for clarification, as well as the coordinate system for this analysis. Note that for the first approximately differential element, $T_{m,x} = T_{m,in}$.

Calculating the heat transfer coefficient h of the working fluids for the different radiators requires the use of some empirical driven equations referenced in *Fundamentals of Heat and Mass Transfer* [5]. For the NaK eutectic fluid, a correlation between the Nusselt number, Nu, and the Péclet number, Pe, is used to find h. This equation, Eq. (10.26), is valid if Pe ≥ 100, which is true for all radiator calculations. The Nusselt number and Péclet number are defined below, with additional quantities defined.

$$\mathrm{Nu}_D = 5.0 + 0.025 \, \mathrm{Pe}^{0.8} \tag{10.26}$$

$$\mathrm{Nu}_D = \frac{h \, D_i}{k} \tag{10.27}$$

$$\mathrm{Pe} = \mathrm{Re} \cdot \mathrm{Pr} = \left(\frac{V \, D_i}{\nu} \right) \left(\frac{\nu}{\alpha} \right) \tag{10.28}$$

$$\alpha = \frac{k}{\rho \, c_p} \tag{10.29}$$

$$h = \frac{k}{D_i}\left[5.0 + 0.025\ \left(\frac{V\ D_i\ \rho\ c_p}{k}\right)^{0.8}\right] \tag{10.30}$$

Thermodynamic properties for NaK, such as c_p and k, are found in a "SODIUM-NaK Engineering Handbook" from 1972 [88]. A list of equations for these thermodynamic properties is found in Appendix D under Section D.1.

To find the heat transfer coefficient of ammonia, which is used for rejection heat from the habitat volumes, a different relation is used. This is the Dittus-Boetler equation, written in Eq.(10.31), for cooling, which is a decent approximation of the heat transfer coefficient for ammonia if $0.6 \leq \mathrm{Pr} \leq 160$, $\mathrm{Re}_D \geq$ 10,000, and if $L/D \geq 10$. All these conditions are meant for both radiators using ammonia.

$$\mathrm{Nu}_D = 0.023\ \mathrm{Re}_D^{4/5}\ \mathrm{Pr}^{0.3} \tag{10.31}$$

Combining Eq.(10.31) with the equation for the Nusselt number, Eq.(10.27), the following result is found for calculating the heat transfer coefficient of ammonia:

$$h = 0.023\left(\frac{k}{D}\right)\ \mathrm{Re}_D^{4/5}\ \mathrm{Pr}^{0.3} \tag{10.32}$$

Using Eq.(10.25), with the appropriate calculation for h depending on working fluid type, T_w can be solved for using a numerical method, with the use of a few assumptions. These include assuming negligible friction loss, a constant temperature distribution across the radiator fin, and assuming that conduction across the wall thickness of the tube is negligible. Once T_w is solved for, $\dot{Q}$ can be found by either calculating $\dot{Q}_{conv}$ or $\dot{Q}_{rad}$. This is done using Newton's Law of Cooling, which is shown in Eq.(10.33).

$$\dot{Q} = \dot{Q}_{conv} = \Delta x\ \pi\ D_i\ h\ (T_{m,x} - T_w) \tag{10.33}$$

The mean fluid temperature on the other side of the (approximate) differential ele-

ment, $T_{m,x+1}$, can be evaluated using a general heat transfer equation, shown in Eq.(10.34), and simplified in Eq.(10.35).

$$\dot{Q} = \dot{m}\ c_p\ (T_{m,x}\ - T_{m,x+1}) \tag{10.34}$$

$$\Rightarrow T_{m,x+1} = \frac{-\dot{Q}}{\dot{m}\ c_p} + T_{m,x} \tag{10.35}$$

Here, $\dot{m}$ is the mass flow going through the radiator, and c_p is the specific heat capacity of the working fluid in the radiator. Calculations proceed by taking $T_{m,x+1}$ as the temperature at the start of the next differential element, and then continuing through this calculation process until $T_{m,out}$ is reached on the last differential element. Upon this calculation, the total length L (shown in Fig.10.7) can be found for this radiator.

The above analysis guesses a width w for the radiator, but this length is based on the assumption that the radiator fins have a constant temperature profile, which is not the case because of conduction across the radiator fin. As a result, a conduction analysis must be done along the length of the radiator fin in the y-direction.

This becomes a problem of equating the rate of conduction to the rate of radiation along the fin in the y-direction, which is expressed in Eq.(10.36). Applying Fourier's Law (approximated for a small differential-like element) and the Stefan-Boltzmann Law to this equation yields Eq.(10.37), which is further simplified and rearranged in equations (10.38) and (10.39). In Eq.(10.37), A_c is defined as the cross-sectional area of the fin, while A_s represents the surface area of the fin. Therefore $A_c = L\ t$, where t is the thickness of the radiator fin, and $A_s = L\ \Delta y$, where Δy is some small, approximately differential, element in the y-direction.

$$\dot{Q}_{cond} = \dot{Q}_{rad} \tag{10.36}$$

$$-k\ A_c\ \frac{(T_y - T_{y+1})}{\Delta y} = \Delta y\ A_s\ \epsilon\ \sigma\ (T_{y+1}^4 - T_s^4) \tag{10.37}$$

$$\Rightarrow k\ t\ (T_y - T_{y+1}) = \epsilon\ \sigma\ (T_{y+1}^4 - T_s^4)\ \Delta y^2 \tag{10.38}$$

$$\Rightarrow -k\ t\ T_{y+1} - \epsilon\ \sigma\ \Delta y^2\ T_{y+1}^4 = -k\ t\ T_y - \epsilon\ \sigma\ \Delta y^2\ T_s^4 \tag{10.39}$$

To begin calculations, the temperature at the base of the fin for iteration 1 is needed, T_1. From the convection analysis, a series of wall temperatures, T_w 's, are calculated. An average of these temperatures is taken, to get an average wall temperature, $\bar{T}_w$. This value can then be used for T_1, from which Eq.(10.39) can be used to solve for T_{y+1} using a numerical method, as the equation cannot be solved for otherwise given its non-linear nature. T_{y+1} can then be used as T_y of the next differential element. Calculations continue until a desired temperature at the end of the fin, T_{fin}, matches the temperature at the end of the last differential element, T_n, where n is the total number of iterations.

From this conduction analysis, a new width for the radiator fin is found, which can be defined as w_{sel}. This width is likely different from the one guessed in the conduction analysis. As a result, this analysis may need to be run a few times until w and w_{sel} are the same. From running these analyses, it is known that this process converges very quickly, and is not laborious in nature. Given L is only defined by the convection analysis, this dimension does not need the same treatment.

Given the computational nature of this analysis, a MatLab program exists to solve this problem. A code listing of this program can be view in Appendix D under Section D.3.

10.4.2 Radiator Design

With w and L defined, the total radiator area, A, required can be calculated as $A = L\ w$. With this area, along with the other parts of the geometry defined from the convection analysis, the radiators size can be fully defined. However, unlike the radiator analysis model diagram shown in Fig. 10.7, the radiator design is not one very long tube with two fins sticking out from either side of the tube. This would be impractical to implement on the spacecraft, so instead a manifold-like design is used instead. This is shown in Fig.

10.8, where there is one vertical pipe that contains warm fluid, which is then forced across smaller tubes that connect to the radiator fins. These smaller pipes then connect to another vertical pipe that now contains the colder fluid. These smaller pipes reflect the analysis model shown in Fig. 10.7, except now there are multiple of them stacked on top of each other. In this way, the analysis previously described still works for this radiator layout.

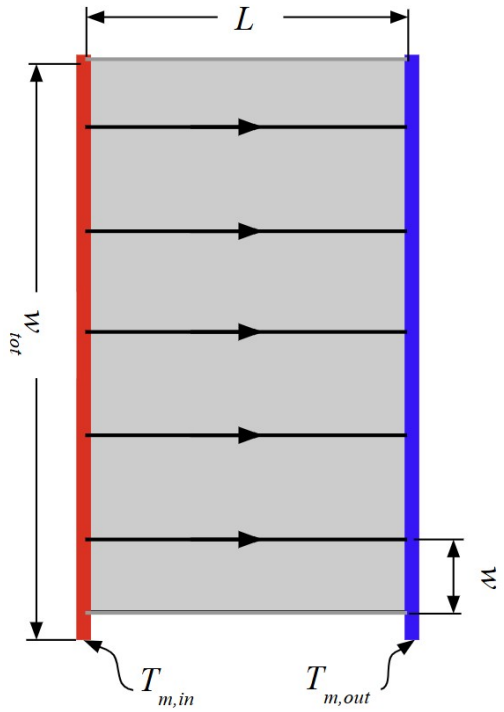

Figure 10.8: Radiator Design

It is important to note that the previously described analysis assumes that the hot and cold vertical tubes have a constant mean fluid temperature profile. In reality, this temperature profile decreases slightly due to radiation from the vertical tube to space. However, the analysis would become significantly more complicated if this was taken into account, and would likely have a negligible effect on results.

Although not reflected in CAD models, these radiators are designed to fold out and deploy. This is mainly done to improve the ease of packing the radiators into a fairing, and also because if these radiators were fully deployed in launch, they would most likely

break. This is because these radiators are not designed for significant structural loading when deployed, as they would be prone to breaking due to vibrations. The point at which these radiators would fold would be located at the midline between a tube-fin section, like the one shown in Fig. 10.7. This would allow one of these sections to be intact for a fold, preserving the effectiveness of the design.

As described in Section 5.1.4, insulation is required on some parts of the radiators in order to minimize view factor problems with propellant tanks. This insulation will be comprised of a high-temperature MLI, with layers of fibrous insulation between ceramic foils [89]. Analysis of such an MLI requires experimental testing or advanced thermal FEA, which is not required for this preliminary analysis. However, given the effectiveness of low temperature MLI's, these high-temperature MLI's should also be very effective.

The materials chosen for the radiator include not only the high-temperature MLI's, but also the material that the radiator themselves are made of. The radiators are made of aluminum given its relatively high conductivity as a metal, as well as its low density for a metal. These properties balance the conduciveness of the metal with its weight when compared to other options such as copper, which is far too heavy. Additionally, aluminum is a robust structural material as well, meaning these radiators should withstand loads during launch.

To increase the emissivity of the radiators, a special coating will be added to the radiators to increase the effectiveness of radiative heat transfer. A standard coating for these kinds of applications is PCCM (Protective Coating for Ceramic Materials), which was later privatized by Wessex, and re-branded as Emisshield. This product has the ability to reach emissivities of up to 0.9, making the coating ideal for this application [90]. An emissivity of 0.9 was therefore used for the analysis of these radiators.

10.4.3 Radiator Models and Results

Using all the analysis described, in addition to the design decision discussed above, a series of results is obtained for all radiators on the spacecraft. Important key parameters regarding the results of the heat transfer analysis can be found in Table 10.9. Note that A is the total area of the radiator.

Radiator Name	Working Fluid	$T_{m,in}$ (K)	$T_{m,out}$ (K)	T_{fin} (K)	Total Area, A (m^2)
Bimodal Power Cycle Radiators	NaK	620	549.7	525	21.78
DEV Power Radiators	NaK	660	596.8	600	15.4
IPV Hab Radiators	Ammonia	283.15	282.75	281	7.8
DEV Hab Radiators	Ammonia	283.9	282.8	282	17.9

Table 10.9: Radiator Analysis Key Parameters and Results

Additionally, a series of plots is generated that show temperatures as a function of distance for the radiators. Two of these plots are shown below for the bimodal power system, with the others listed in Appendix D, Section D.2. Fig. 10.9 shows how the temperature of the fluid and the wall of the pipe change as a function of distance in the x-direction. Additionally, Fig. 10.10 shows how temperature varies across the fin in the y-direction for the bimodal radiator.

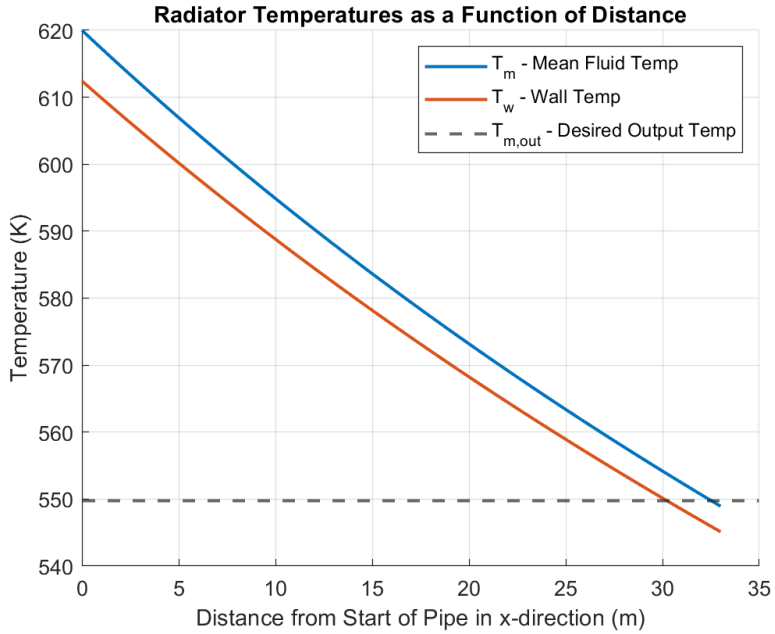

Figure 10.9: Bimodal Radiator Temperature in x-direction

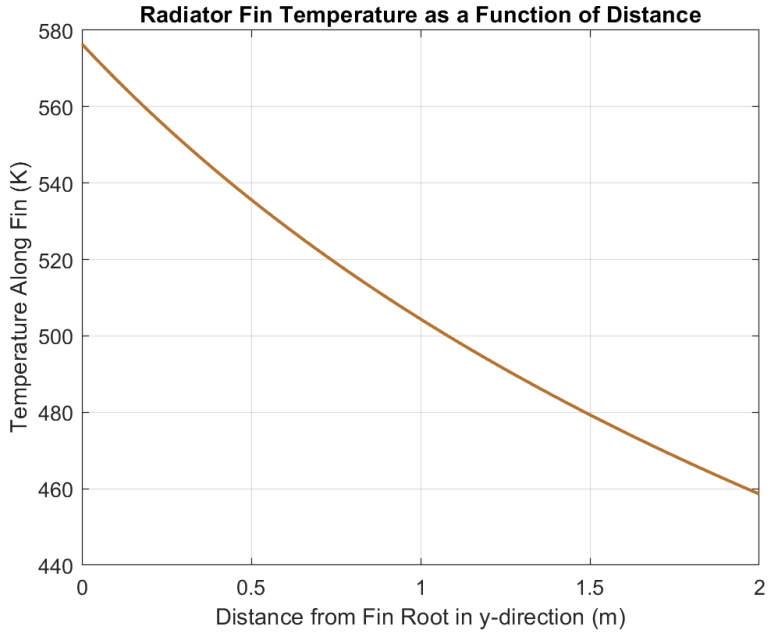

Figure 10.10: Bimodal Radiator Temperature in y-direction

Furthermore, a series of dimensions is calculated for each radiator, which can be seen in Table 10.10. Note that N is the number of tube-fin sections, like the one shown in Fig. 10.7, stacked on top of one another in the radiator. Additionally, t is the thickness of the radiator fins, and m is the mass of the radiator.

Radiator Name	L (m)	w (m)	w_{tot} (m)	N	D_i (m)	t_{wall} (mm)	t (mm)	m (kg)
Bimodal Power Cycle Radiator	4.25	0.66	5.64	4	0.1	10	5	515
DEV Power Radiator	2.5	0.4	3.38	4	0.05	5	5	165
IPV Hab Radiator	3.1	0.66	2.73	2	0.05	5	5	148
DEV Hab Radiator	3	0.39	6.6	8	0.05	5	5	376

Table 10.10: Radiator Dimensions

Fig. 10.11 shows a CAD model of the bimodal radiator, which is very similar to the other CAD models for other radiators.

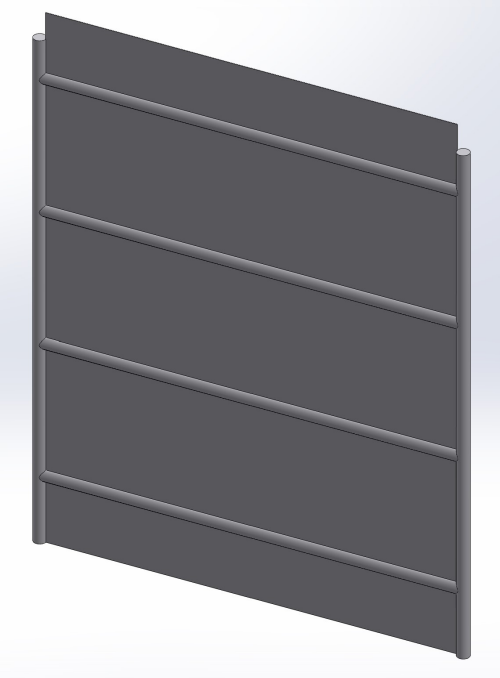

Figure 10.11: Bimodal Radiator CAD Model

10.4.4 Radiator Risks and Mitigation

The last key consideration for radiators is their redundancy in order to decrease risk in this subsystem. This is crucial, as if a radiator becomes dysfunctional because of a micro-meteorite impacts or some other reason, power cycles and temperature regulation control are no longer possible. As a result, there is redundancy on all radiators, such that if one fails, there is at least one back-up radiator.

For the bimodal radiators, there is quadruple redundancy, given that this system is the most crucial power generation system on the spacecraft. If the bimodal power cycle fails, then the vast majority of power production ceases, justifying this level of redundancy. All other radiators will have double redundancy, given their less critical nature to the mission, and given that many of them are fairly small and have a lower chance of getting impacted by a micrometeorite.

10.5 Multilayer Insulation

Passive thermal control resulting from an MLI layer is crucial to mission success, as without it, the resulting boil-off from the cryogenic propellant and waste heat to be rejected from the HAB and DEV would be far too large to feasibly do with the ATCS. The entire MLI for all components will be made using a double aluminized Mylar reflector layer, shown from NASA's "Multilayered Insulation Material Guidelines" to be $0.05mm$ thick and having an absorptivity of $\alpha = 0.14$. The separator between each reflector layer will be comprised of a Dacron mesh of $0.16mm$ thickness. Figure 5.10 below provides a small cross-sectional conceptual diagram of the MLI used throughout the IPV.

Note that the majority of the MLI is internalized below the MMOD shielding in the design to protect it from orbital debris; however, a separate layer of aluminized Mylar is used on the outer layer of the Tanks, HAB, and DEV to ensure a low initial absorptivity and hot side temperature of the MLI.

10.5.1 Thermal heat flux through the MLI

The analysis of the resulting heat flux through the MLI is broken down into two distinct processes. First is determining the resulting hot side temperature of the MLI. First, the radiation heat transfer equation can be used to determine the resulting rate of heat being transferred to the outer surface of the IPV. Using equation 10.40 below, the resulting heat flux across the outer layer of each tank can be determined.

$$q \cdot A_s = \sigma \epsilon A_t ({T_h}^4 - {T_c}^4) \tag{10.40}$$

$$A_s = \left[4\pi \frac{(R^{2P}) + (R^P \cdot 2 \cdot H_D \cdot R^P) + (R^P \cdot 2 \cdot H_D \cdot R^P)^{\frac{1}{P}}}{3} + 2\pi \cdot R \cdot H_c \right] /2 \tag{10.41}$$

Then, using equation 10.41, the resulting surface area exposed to the sun throughout transit can be calculated. With these two results, the next task is to use the radiation heat transfer equation again to determine the resulting surface temperature of the IPV. The radiation heat transfer equation, rewritten below, is then used to solve for the IPV surface temperature. Inputting the solar flux and solar exposed surface area for the heat transfer rate and assuming the ambient temperature to be negligible, the resulting surface temperature of the IPV can be obtained from Equation 10.42.

$$T_h = \left[\frac{[G_s\alpha + q_1 \cdot \epsilon * sin^2(\rho) + G_s * a_b * \alpha * Ka * sin^2(\rho)] \cdot A_s}{\sigma \epsilon A_t} + {T_c}^4 \right]^{1/4} \tag{10.42}$$

Once the surface temperature of the IPV is known, the analysis can then move on to the second process of determining the resulting heat flux transferred through the MLI. For this, the MLI general equation derived by Lockheed Martin's MLI Final report is used [91]. The general MLI formula is shown in equation 10.43 below.

$$q = \frac{[3.07x10^{-11} * ({T_h}^2 - {T_c}^2) - 2.13x10^{-14}({T_h}^3 - {T_c}^3)] * \overline{N}^{3.91}}{N_s + 1} + \frac{8.03x10^{-10} \cdot 0.031}{N_s}({T_h}^{4.67} - {T_c}^{4.67}) \tag{10.43}$$

$$\overline{N} = \frac{10}{t_{seperator} + t_{reflector}} \tag{10.44}$$

Inputting the layer density given from equation 10.44, the individual layer thicknesses determined from Reference [92], a $T_c = 20K$ as the cold side temperature for the MLI due to the boiling point of the Cryogenic H2, and an initial total layer count, the heat flux passing through the MLI can be calculated.

10.5.2 Boil-Off Rate

The Boil-off rate is the rate per day at which the cryogenic propellant boils away. This change of phases results in the unusable by the NTP engine for thrusting. The Boil-off rate for each tank is calculated using equation 10.45 taken from Reference [93].

$$BOR(\%perday) = \frac{Q_i \cdot 100 \cdot 24 \cdot 3.6}{H_v \cdot M} \tag{10.45}$$

Inputting the respective H_v for the LH2 of 421.77 kJ/kg as the enthalpy of vaporization and the M as the mass of LH2 within the tank, and the resulting heat flux and surface area of the tank, the Boil-Off rate can be calculated as a % per day. Then the resulting boil-off mass for each tank can be modeled as an exponential decay function as shown in equation 10.46 below.

$$M_{boiloff} = M_{LH2}\left[\frac{1}{exp(\frac{-BOR \cdot t}{100})} - 1\right] \tag{10.46}$$

10.5.3 Results

The resulting layers surrounding the propellant tanks, DEV, and HAB are selected to optimize the resulting combined mass of the propellant lost due to boil-off and the mass used for the MLI, resulting in a minimized total mass used for each tank during transit. Table 10.11 below shows the resulting layer count surrounding each section of the IPV, the resulting total thickness of the MLI shielding, the Mass of the MLI, the mass of boiled-off propellant from each tank throughout the mission, and the resulting total mass lost by the boil-off propellant and MLI shielding.

	Earth Departure	Mars Capture	Mars Departure	Earth Capture	Hab	Dev
Layer Count	282	240	270	550	10	5
MLI Thickness (cm)	5.94	5.05	5.68	11.58	0.21	0.11
MLI Mass (mT)	3.83	1.56	1.23	1.24	0.3	0.2
Boil Off Mass (mT)	3.89	1.02	1.06	3.6	N/A	N/A
Total Mass (mT)	7.72	2.58	2.29	4.83	0.3	0.2

Table 10.11: Results from the MLI analysis showing minimized resulting minimized Mass

11 Power

11.1 Power Requirements

11.1.1 IPV

The power requirements are derived based on existing systems, trade studies, and analog field tests. The power requirements are broken down into the following subsystems:

1. Life Support
2. Avionics
3. Operations
4. Communications
5. Margin

The power requirement for life support is derived from Table 3.13 located in Appendix E.1[13]. This data is based on existing ISS ECLSS technology from Table 3.13 are then modified for this specific mission. The life support power usage is scaled based on the number of astronauts (4 for IPV and 2 for DEV). However, it is important to note that there is still a baseline power usage that cannot be scaled. The biomass power consumption is completely removed, and the other values are scaled accordingly.

In order to estimate the power consumption of the avionics a trade study of an NTP rocket [94] and MUSTANG avionics unit [95] is examined. Avionics such as Guidance, Navigation and Control (GN&C), Command and Data Handling (C&DH), RCS thrusters, and thermal systems are taken into account.

Operational power is evaluated on analog field tests performed by NASA. In particular, power usage from habitats (on Earth) are retrieved from HI-SEAS [96] and Desert RATS (2010) [14]. The power draw from Desert Rats is esimated from the current draw from

the Desert RATS field test in Figure E.2 located in Appendix E.7. Lastly, a 30% margin was added in accordance with ARC STD 8070.1 [18].

IPV Peak Power Usage	
Subsystem	**Power (kWe)**
Life Support	7.69
Avionics	3.59
Operations	7.00
Communications	1.00
30% Margin	5.78
Total	**25.07**

IPV Nominal Power Usage	
Subsystem	**Power (kWe)**
Life Support	5.71
Avionics	1.47
Operations	4.50
Communications	1.00
30% Margin	3.80
Total	**16.49**

11.1.2 DEV

DEV Peak Power Usage	
Subsystem	**Power (kWe)**
Life Support	7.96
Avionics	2.50
Operations	4.50
Communications	1.00
30% Margin	4.79
Total	20.75

DEV Nominal Power Usage	
Subsystem	**Power (kWe)**
Life Support	6.93
Avionics	1.20
Operations	3.00
Communications	1.00
30% Margin	3.64
Total	15.76

11.2 Batteries

In order to maintain a conservative estimate for power storage using methods, the nickel-hydrogen (Ni-H2) aboard the ISS is used to calculate battery storage for the IPV and DEV. The ISS has recently upgraded to lithium-ion batteries, which are able to store twice as much charge and are significantly smaller. However, the design life (number of discharges) of lithium-ion batteries is much lower than their Ni-H2. The specifications for both battery types are provided below [97]:

ISS Ni-H2 Batteries	
Weight (kg)	170
Storage (kWh)	4

Table 11.1: Ni-H2 Batteries

ISS Li-Ion Batteries	
Weight (kg)	106
Storage (kWh)	4

Table 11.2: Li-ion Batteries

In addition, Table 11.3 specifies the depth of discharge (DOD) of batteries under cyclic operation [18]:

Number of Cycles	**Allowable DOD**
<100	<70%
100 < # cycles < 5,000	<60%
5,000 < # cycles < 30,000	<40%
> 30,000	<20%

Table 11.3: Battery Depth of Discharge Limits [18]

The values in Tables 11.1 and 11.3 are used to calculate the number of batteries needed for two limiting scenarios: the switchover from engine thrusting operations to bimodal and singular reactor failure on the DEV. In case two, the batteries must be able to supply the peak power usage (25.1 kWe) to the IPV for one hour at a DOD of 70%. For case two, the batteries must be able to supplement (3 kWe) the singular reactor to power all

Bimodal Switchover		**DEV Reactor Failure**	
Number of Batteries	Weight (mT)	Number of Batteries	Weight (mT)
9	1.53	21	3.57

Table 11.4: Battery Requirements

essential systems (ex. life support, and avionics) for the total transit time between Deimos (19 hrs). Equation 11.1 details these calculations:

$$\text{number of batteries} = \frac{P_e * t}{\text{storage capacity} \times \text{DOD}} \tag{11.1}$$

The NiH_2 batteries aboard the ISS are used as a conservative estimate. The results are shown below:

11.3 Solar Arrays

$$P_e = \eta_s(A)(S) \tag{11.2}$$

The Roll Out Solar Arrays (ROSA) currently used on the ISS are used as a baseline for solar array power generation. ROSAs, which are supplied by Redwire, have the following properties [98]:

Solar Panels	
Efficiency (%)	30.70%
Power to Mass (W/kg)	100
Stowed Power Density (kW/m^3)	40

The ROSA panels, supplied by Redwire, have been proven in operations aboard the ISS and many other satellites. Additionally, their compact size and lightweight construction make them the optimal choice. The mean solar irradiance at Mars of 588.6 $\frac{W}{m^2}$ is acquired from ASTM E-490 and used to size the solar panel arrays on the IPV accordingly [99]. Using Equation 11.2 and the mean solar irradiance at Mars the minimum solar panel area for both the IPV and DEV peak power requirements is calculated:

Minimum Solar Panel Area	
IPV	138.90 m^2
DEV	111.23 m^2

Table 11.5: Minimum Solar Panel Area for Peak Power Consumption

11.4 Fuel Cells

Fuel cells are a common power generation method for a variety of applications. In particular, the space shuttle used fuels "due to their high conversion efficiency and high energy density" [100]. Fuel cells are evaluated as a possible short-term power generation method for both the DEV and IPV. A simple stoichiometric equation is as follows for hydrogen and oxygen:

$$2H_2 + O_2 \longrightarrow 2H_2O \tag{11.3}$$

The efficiency of a fuel cell is defined below:

$$\text{efficiency} = \frac{V_c}{1.48} \tag{11.4}$$

The space shuttle fuel cells have an efficiency of 70% leading to a voltage per cell (V_c) of 1.036 V. The oxidizer and fuel usage rates are then determined based on the power required(P_e) and Equations 11.5 and 11.6.

$$H_2 \text{ usage} = 1.05 \times 10^{-8} \frac{P_e}{V_c} \text{kg} s^{-1} \tag{11.5}$$

$$O_2 \text{ usage} = 8.29 \times 10^{-8} \times \frac{P_e}{V_c} \text{kg} s^{-1} \tag{11.6}$$

The rate of water production is:

$$\text{Water Production} = 9.34 \times 10^{-8} \frac{P_e}{V_c} \text{kg} s^{-1} \tag{11.7}$$

The heat produced is

$$\text{Heating rate} = P_e(\frac{1.25}{V_c} - 1) \text{ W} \tag{11.8}$$

Equations 11.5, 11.6, 11.7 and 11.8 were used in preliminary trade studies to determine the viability of fuel cells for temporary power generation. Ultimately, the fuel and oxidizer need to be stored cryogenically, and batteries proved to be a lighter alternative for multiple uses.

11.5 Brayton Cycle Analysis

The IPV and DEV utilize a Brayton cycle as the main source of power generation. Brayton cycles are commonly used in gas turbines and jet engine applications and are modeled using ideal gases. A generic regenerative Brayton cycle diagram is shown below: The state

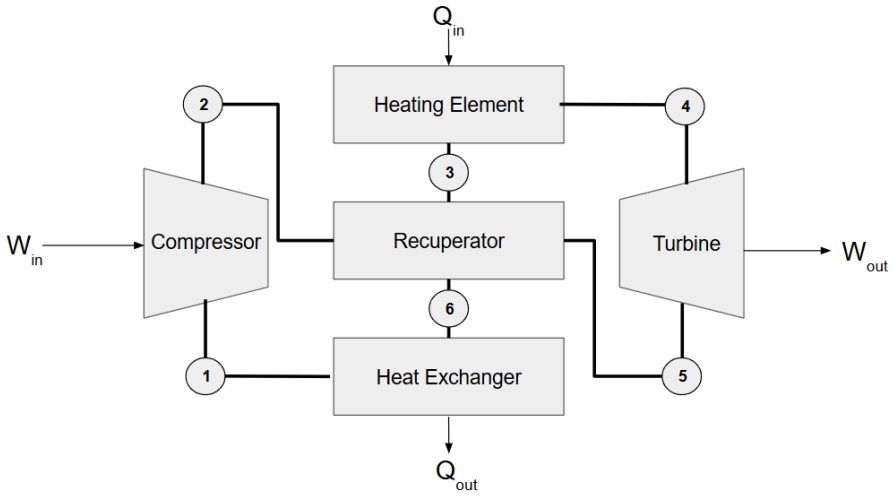

Figure 11.1: Regenerative Brayton Cycle

points identified in Figure 11.1 can be described as the following:

1. Compressor Inlet
2. Compressor Outlet
3. Recuperator Cold Outlet
4. Turbine Inlet
5. Turbine Outlet
6. Recuperator Hot Outlet

The state points are used to analyze the Brayton Cycles for both the Bimodal and DEV Reactor power generation. The following methodology is used to analyze the cycles:

11.5.1 Working Fluid

A Xenon-Helium mixture is chosen for a multitude of reasons: inert, high efficiency, and low weight [101]. In particular, a XeHe with a molar mass of 40g/mol is chosen [7]. The mole fractions are then calculated using the following system of equations:

$$X_{Xe} + X_{He} = 1 \tag{11.9}$$

$$M_{Xe}X_{Xe} + M_{He}X_{He} = 40 \tag{11.10}$$

The mixture properties are determined using ideal gas theory:

$$C_{pmix} = C_{pXe}X_{Xe} + C_{pHe}X_{He} \tag{11.11}$$

$$C_{vmix} = C_{vXe}X_{Xe} + C_{vHe}X_{He} \tag{11.12}$$

$$\gamma_{mix} = \frac{C_p}{C_v} \tag{11.13}$$

$$R_{mix} = C_p - C_v \tag{11.14}$$

11.5.2 Compressor

The following equations detail the compressor analysis:

$$\frac{T_{2s}}{T_1} = (\frac{P_2}{P_1})^{\frac{\gamma_{mix}-1}{\gamma_{mix}}} \tag{11.15}$$

$$T_2 = \frac{T_{2s} - T_1}{\eta_c} + T_1 \tag{11.16}$$

11.5.3 Turbine

The following equations detail the turbine analysis:

$$\frac{T_{5s}}{T_4} = (\frac{P_5}{P_4})^{\frac{\gamma_{mix}-1}{\gamma_{mix}}} \tag{11.17}$$

$$T_5 = T_4 - \eta_t(T_4 - T_{5s}) \tag{11.18}$$

11.5.4 Regenerator

The regenerator is modeled using overall effectiveness as opposed to log-mean temperature. The equations used to model the regenerator are as follows [5]

$$T_3 = \varepsilon_r(T_5 - T_2) + T_2 \tag{11.19}$$

$$T_6 = T_5 - T_3 + T_2 \tag{11.20}$$

11.5.5 Power Optimization

These equations are implemented in a MATLAB script which iterates over possible solution spaces containing $\dot{m}(kg/s)$ and p_2/p_1. The MATLAB script provides key system parameters such as $\dot{Q_{in}}$, $\dot{Q_{out}}$,$\dot{W_{net}}$ and $\eta_{thermal}$. The goal of optimizing the Brayton cycles is to meet the power generation requirements while minimizing radiation area. During the optimization process, $\dot{m}$ and p_2/p_1 also play another role. The pressure drop through the corresponding nuclear reactors is minimized with a small $\dot{m}$ and a large compressor pressure ratio (p_2/p_1). Optimization is performed with the MATLAB script located in Appendix E.6. The results are shown in Figures 11.2 and 11.3.

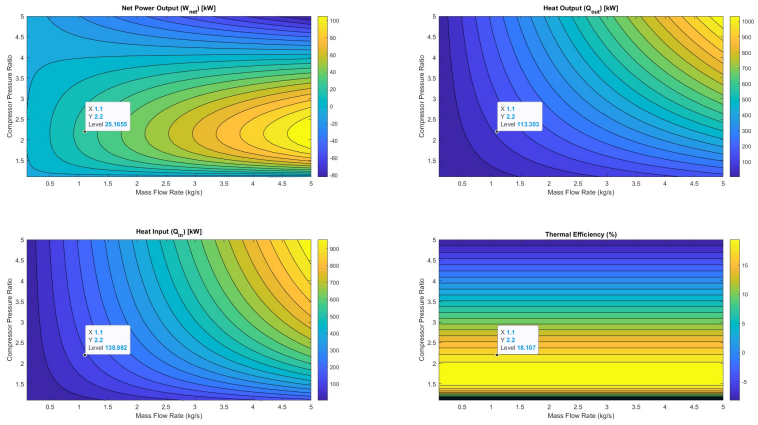

Figure 11.2: Bimodal Cycle Optimization

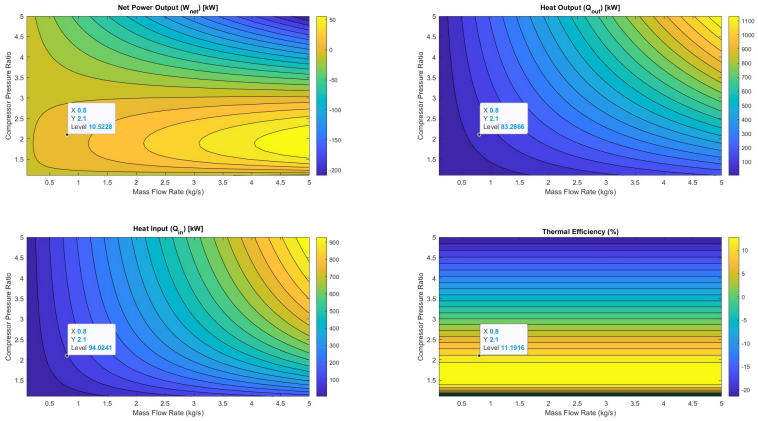

Figure 11.3: DEV Cycle Optimization

11.5.6 Regenerator Sizing

The regenerator is modeled base on effectiveness [5] . An effectiveness of 0.90 is chosen for analysis as it significantly reduces weight and improves thermal efficiency [102]. The regenerator is then sized using an UA value found using Equation 11.21 and Figure 11.4 [5]:

$$\text{NTU} = \frac{UA}{C_{min}} \tag{11.21}$$

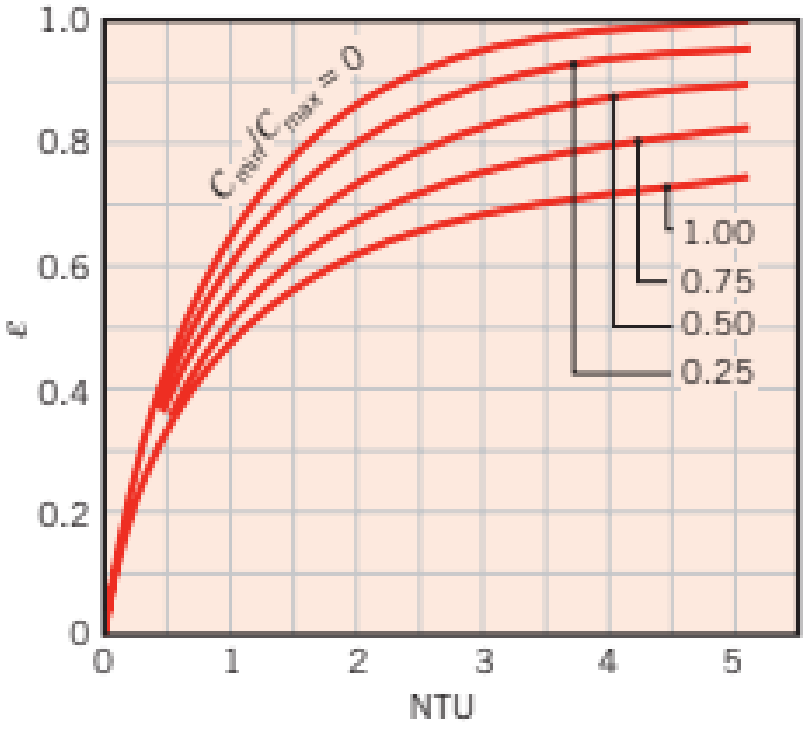

Figure 11.4: Effectiveness for Cross-Flow Heat Exchange[5]

It is assumed that there is a 99% pressure recovery across the regenerator.

11.5.7 Alternator

The alternator is assumed to have a 98% efficiency [101] in converting the mechanical work of the cycle into electricity. Additionally, the alternator was modeled to have 16 poles to achieve a frequency of 20 kHz [103]. The angular speed (rpm) of the turbomachinery is then calculated using the following equation[104]:

$$N = \frac{f_a}{P} \times 120 \tag{11.22}$$

The rotational speed of the turbomachinery is determined to be 150,000 rpm.

11.5.8 Turbomachinery Selection

Balijè's method is used to appropriately size the turbomachinery for both the IPV and DEV Brayton Cycles. Figures 11.5 and 11.6 details isentropic efficiency η as a function of specific diameter (D_s) and specific speed (ω_s) [6] .

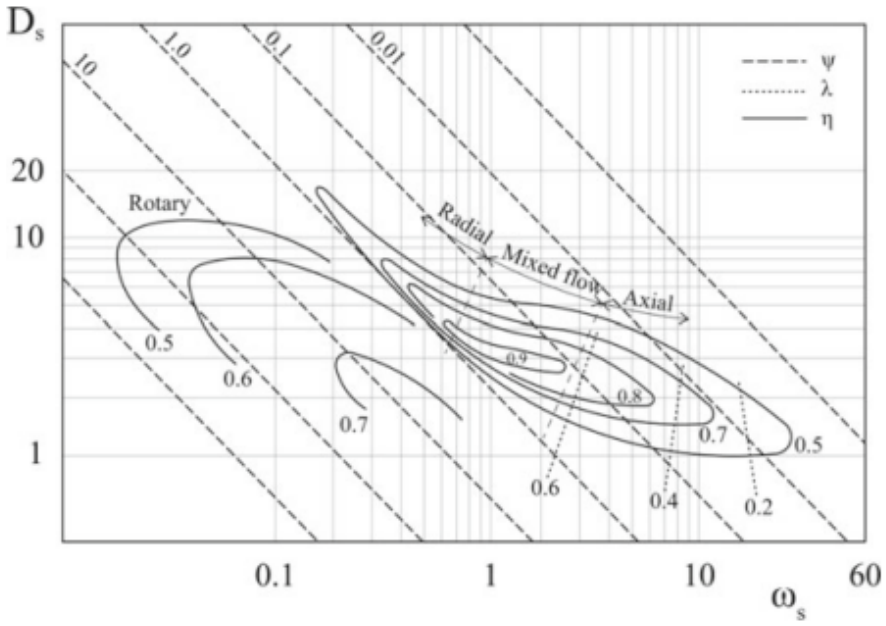

Figure 11.5: Compressors Balijè's Diagram [6]

The speed and diameters of the compressor and turbines are then calculated using Equations 11.23 and 11.24:

$$\omega_s = \omega \frac{\dot{V}^{1/2}}{W^{3/4}} \tag{11.23}$$

$$D_s = D \frac{W^{1/4}}{\dot{V}^{1/2}} \tag{11.24}$$

Using Figures 11.6 and 11.5, and Equations 11.23 and 11.24, the specific speeds and diameter can then be calculated.

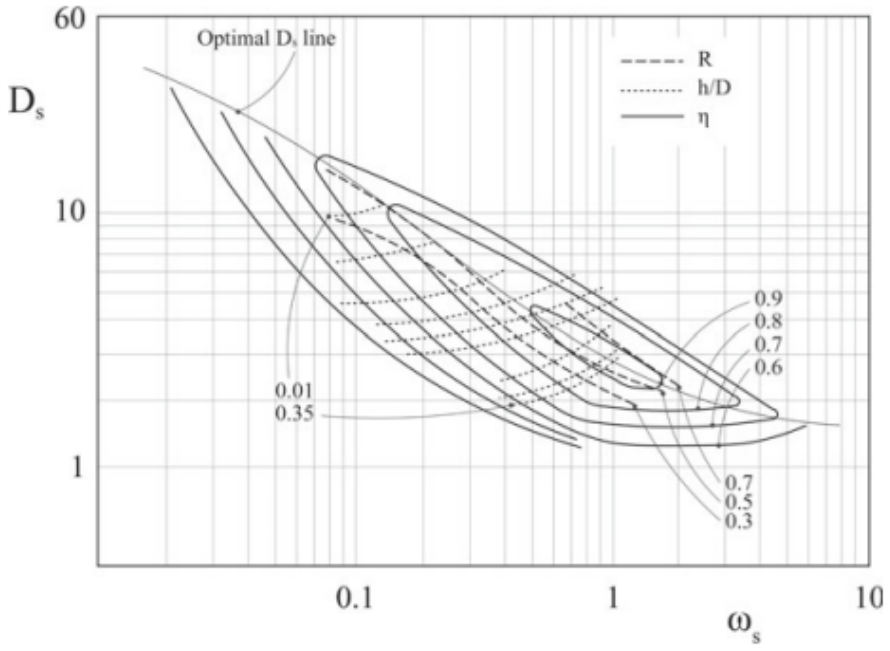

Figure 11.6: Axial Turbines Balijè's Diagram [6]

11.6 Bimodal

When the NTP engines on the IPV are not thrusting, they will be used for Bimodal power generation. The nuclear core of the NTP engine is used to provide Q_{in} to the working fluid in the Brayton Cycle. The working fluid is heated to its maximum temperature of $T_4 = 1000K$ by flowing through the tie tubes of the reactor.

11.6.1 Tie Tube Geometry

The geometry of the tie tubes is chosen in order to maximize pressure recovery. The geometry of the tie tubes below results in a static pressure recovery of $\frac{P_4}{P_3} = 0.98$.

D_{hs}	4 mm
r_o	6 mm
r_i	5.25 mm
f	0.005

Table 11.6: Tie Tube Measurements

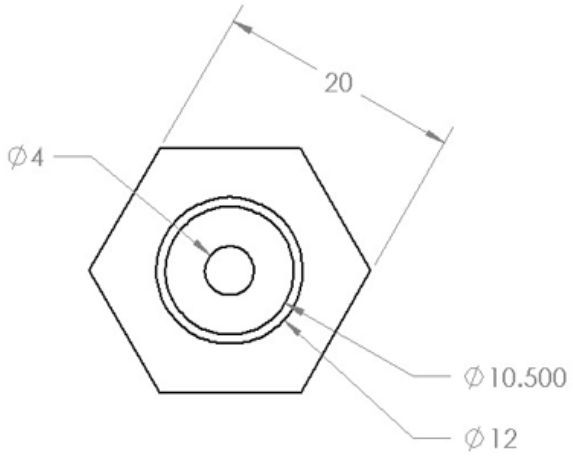

Figure 11.7: Tie Tube Geometry

11.6.2 Tie Tube Pressure Loss

In order to calculate the pressure drop across the tie tubes a differential element setup is used. The differential element is shown below [7]:

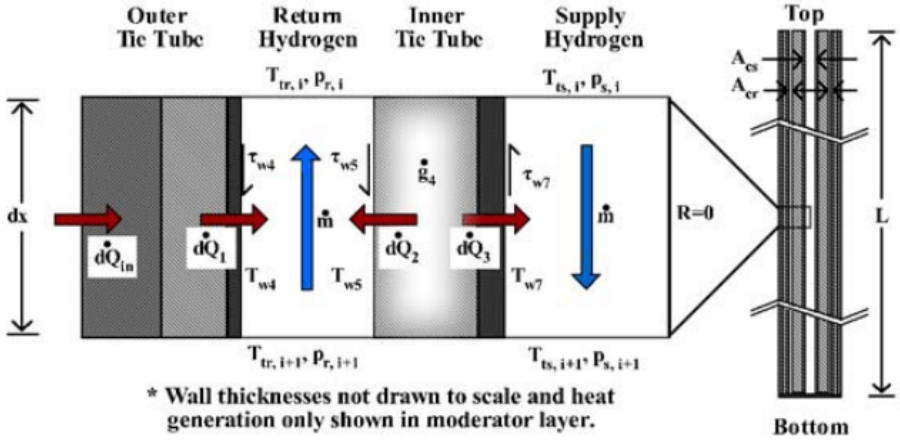

Figure 11.8: Tie Tube Differential Element [7]

The pressure loss across the tie tubes is calculated using the following relations [7]:

$$T_{i+1} = T_i + \frac{d\dot{Q}}{\dot{m}C_p} \tag{11.25}$$

$$p_{si+1} = p_{si} + (\frac{\dot{m}}{A_{cs}})^2(\frac{1}{\rho_{si}} - \frac{1}{\rho_{si+1}} - \frac{1}{\rho_{si} + \rho_{si+1}}\frac{4fdx}{D_h}) \tag{11.26}$$

$$p_{ri+1} = p_{ri} + (\frac{\dot{m}}{A_{cr}})^2(\frac{1}{\rho_{ri}} - \frac{1}{\rho_{ri+1}} + \frac{1}{\rho_{ri} + \rho_{ri+1}}\frac{1}{A_{cr}}(f(dA_3 + dA_4)) \tag{11.27}$$

The length of the tie tubes is split into differential elements. A MATLAB script in Appendix E.3 determines the pressure drop across the tie tubes by guessing the density at the next slice, and then solving for the resultant at each slice. Due to the nature of the solver by guessing density, an increase in differential slices leads to higher accuracy. A sensitivity study using Appendix E.5 is performed to determine an adequate number of slices to use for calculations. The results are shown in Figure 11.9 indicating the pressure recovery across the tie tubes is 98%.

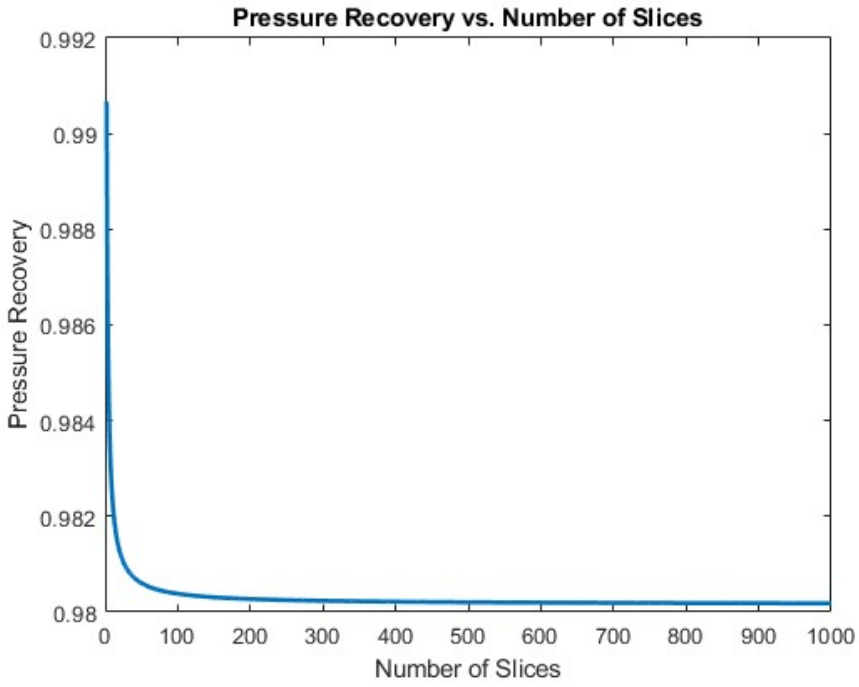

Figure 11.9: Pressure Recovery vs. Number of Slices

11.6.3 Thermodynamic Cycle

Key thermodynamic cycle parameters are displayed below in Table 11.7: The corresponding state points are calculated using the MATLAB Code in Appendix E.1 and dis-

$\dot{m}(kg/s)$	$\frac{p_2}{p_1}$	η_c	η_t	ε_r
1.1	2.2	0.9	0.9	0.9

Table 11.7: Bimodal Cycle Parameters

played in Table 11.8.

State	Temperature (K)	Pressure (MPa)
1	450.0	2.50
2	634.0	5.50
3	757.5	5.45
4	1000	5.34
5	771.2	2.55
6	647.7	2.53

Table 11.8: Bimodal Brayton Cycle State Points

The state points displayed in Table 11.8 are plotted to produce the following P-v diagram:

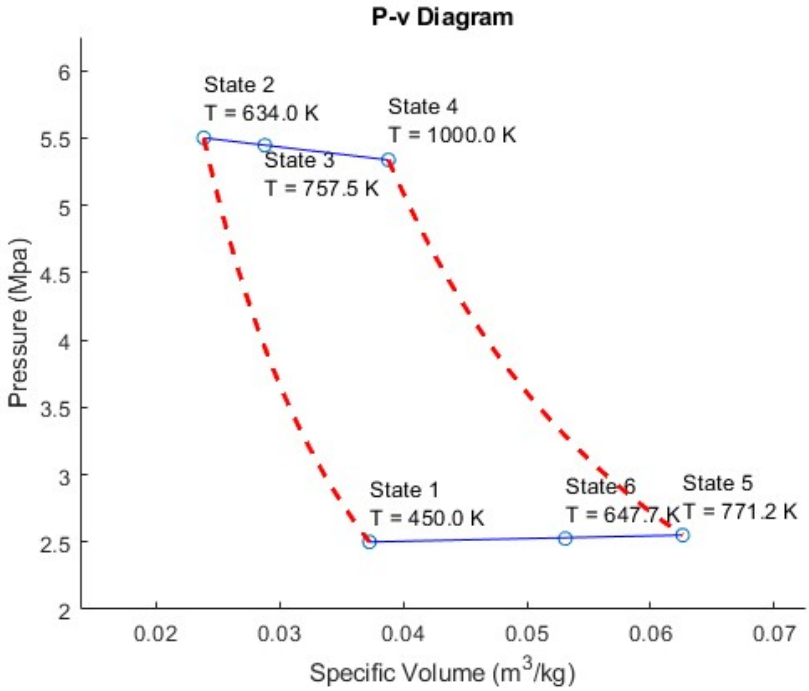

Figure 11.10: Bimodal P-v Diagram

The heat transfer in and out of the cycle along with the net work is then calculated and displayed

Cycle Characteristics	
$\dot{Q_{in}}$ (kWt)	138.98
$\dot{Q_{out}}$ (kWt)	113.3
$\dot{W_{net}}$ (kWe)	25.6
$\eta_{thermal}$ (%)	18.1

Table 11.9: Bimodal Cycle Characteristics

11.6.4 P&ID

The P&ID diagram for the Bimodal Cycle is shown below: Figure 11.11 defines all relevant state points and flow stations. It is important to note that each engine will be equipped with its own turbomachinery in order to ensure redundancy.

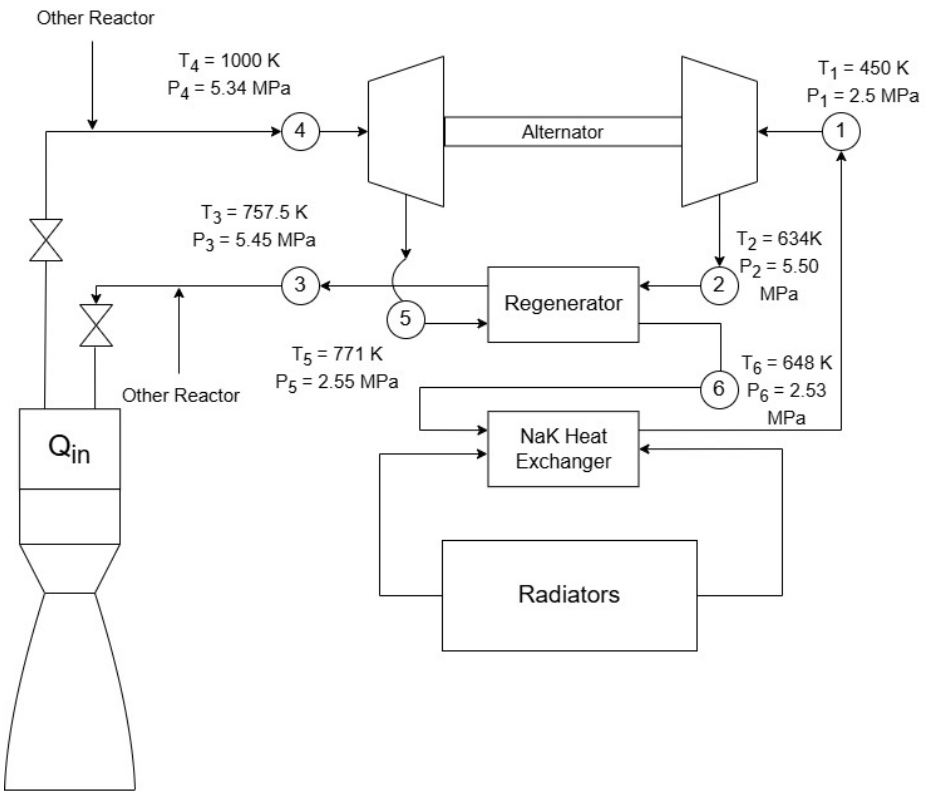

Figure 11.11: Bimodal P&ID

UA	2.6049e+03

Table 11.10: Bimodal Regenerator

11.6.5 Regenerator Sizing

The size of the regenerator in the bimodal Brayton cycle is calculated using Equation 11.21 and Figure 11.4:

11.6.6 Turbomachinery

The compressor and turbine for the Bimodal Brayton Cycle are selected using Figures 11.12 and 11.13. Their properties are shown in Tables 11.12 and 11.11.

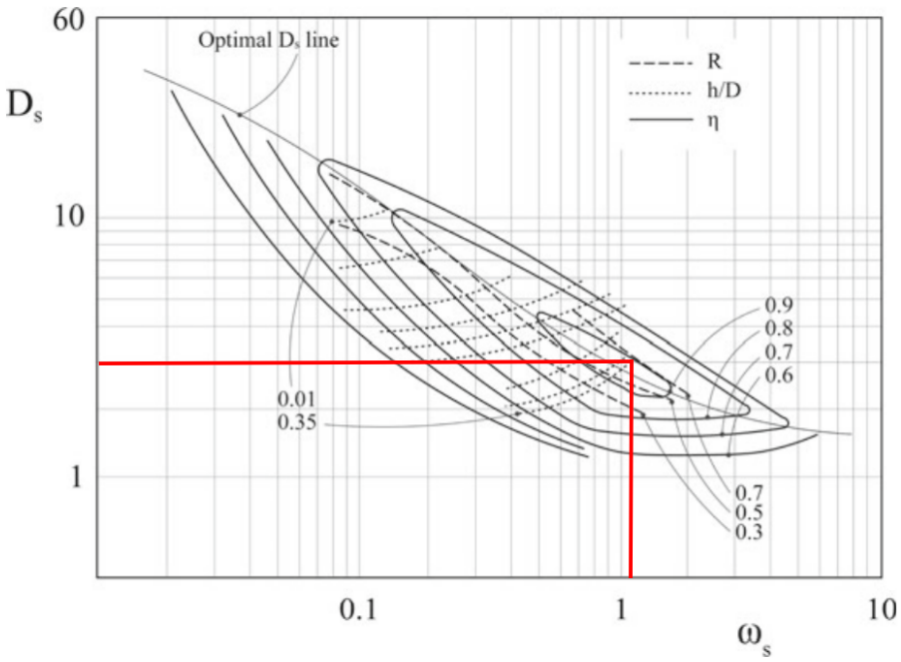

Figure 11.12: Ds-Ns Diagram for Bimodal Turbine [6]

Turbine	
ω_s	1.0450
D_s	3
w (rpm)	150,000
D (m)	0.0434

Table 11.11: Bimodal Turbine

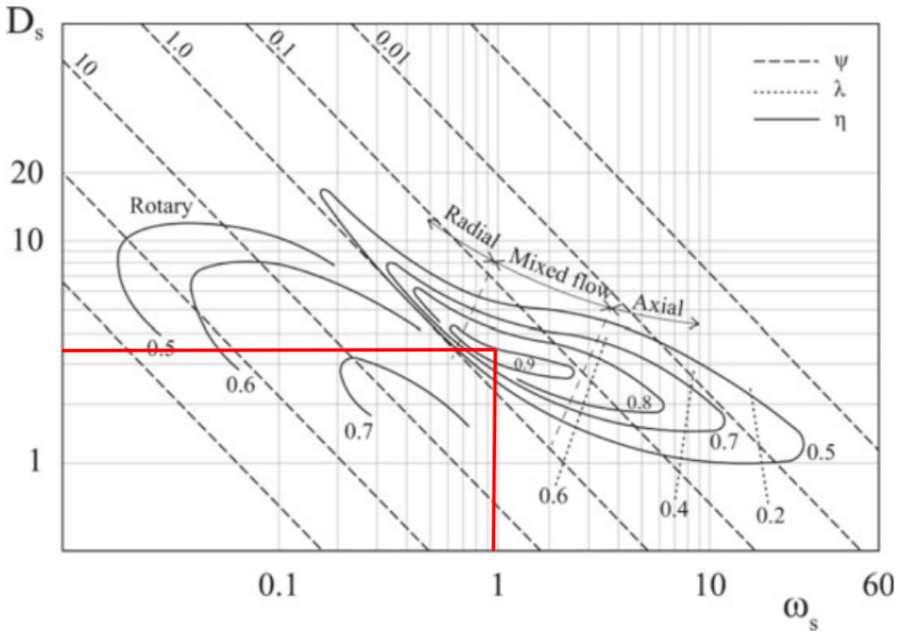

Figure 11.13: Ds-Ns Diagram for Bimodal Compressor [6]

Compressor	
ω_s	0.955
D_s	3.5
w (rpm)	150,000
D (m)	0.0416

Table 11.12: Bimodal Compressor

The turbine and compressor run at the same rotational speed eliminating the need for a gear box and an extra failure mode. Additionally, the turbomachinery rotational speed of 150,000 rpm is correctly sized for an alternator frequency of 20 kHz discussed in Section 11.5.7.

11.7 DEV Nuclear Reactor

11.7.1 Reactor Sizing

The DEV nuclear reactor consists of 5 main components, namely: the core, turbine, recuperator, radiator, and compressor. The state point numbers and connections between components are shown below in Fig. 11.16. The defining requirement of this Brayton cycle is that it needs to be able to produce at least 10.05 kWe from the turbine in order to meet the peak load requirement of 20.1 kWe when two cycles are in operation.

The core's defining requirement is the thermal energy it releases into the system. It needs to inject at least 94.024 kWt of energy into the XeHe mixture, heating up the fluid from 774.4 K in State 3 to 1000K in State 4.

To find the core size and the required amount of uranium it needs to contain, the first step is the define the inputs. Table 11.13 below displays those inputs:

Variable Value	Value	Units
P_t	94	kWt
C	$3 * 10^{10}$	Fissions/(W*s)
$Days$	300	Days
α	1.2	-
$\%_{burnup}$	1.4	Percent
$\%_{Enrichment}$	1.4	Percent
V_r/V_m	1.25	-
N_u	4.72E+22	Fuel atoms/cm^3
D_P	0.003	m
N_p	120	-
T_c	1050	k
T_{in}	774.4	k
T_{out}	1000	k
$\dot{m}$	0.8	kg/s
$\dot{Q}$	-94	kW/s
Pr_{mean}	0.236	-
k_{mean}	0.156	W/(m*k)
μ_{mean}	7.19E-05	Pa*s

Table 11.13: Input Parameters

It has to be checked if the flow through the pipes will be laminar or turbulent, as it dictates the heat transfer coefficient equation that can be used.

$$v_{pipe} = \frac{\dot{m}}{\rho_{mean}(A_{pipe}N_p)} \tag{11.28}$$

$$Re = \frac{\rho_{mean} v_p D_p}{\mu_{mean}} \tag{11.29}$$

With a Reynolds number of 39350, the flow is highly turbulent. Hence, the following equations and calculations are used to find the heat transfer coefficient.

$$Nu = 0.023 Re^{0.8} Pr_{mean}^{0.4} \tag{11.30}$$

$$h = \frac{Nu \cdot k}{D} \tag{11.31}$$

The log mean temperature difference also has to be calculated.

$$\Delta T_1 = T_c - T_{\text{in}} \tag{11.32}$$

$$\Delta T_2 = T_c - T_{\text{out}} \tag{11.33}$$

$$\Delta T_{\text{lm}} = \frac{\Delta T_1 - \Delta T_2}{ln(\frac{\Delta T_2}{\Delta T_1})} \tag{11.34}$$

With all of that done, the required length of the pipe and core can finally be calculated.

$$A_{pipe_{surface}} = \frac{\frac{1000\dot{Q}}{N_p}}{h\Delta T_{\text{lm}}} \tag{11.35}$$

$$L = \frac{A_{pipe_{surface}}}{\pi D} \tag{11.36}$$

The values calculated in Equations (11.29),(11.31) (11.34), (11.36) are displayed in Table 11.14.

Re	$h\{\frac{W}{m^2K}\}$	$\Delta T_{\text{lm}}\{K\}$	$L\{m\}$
39350.62	3179.59	-132.17	0.20

Table 11.14: Values calculated while finding L

The cross-sectional area of the core is based on the volume of uranium that is needed to be brought in order to sustain the output power for 300 days. The following process is modified from the Schwenk and Shannon's Nuclear Power Engineering [105]. The main

difference arises in the burnup percentage. Over the past 70 years, advancements in reactor technology have enabled fuel burnup percentages to exceed the enrichment percentage in [106]. However, to be conservative, the burn up percentage is set to be equal to enrichment percent at 1.4%.

$$F_R = 1000\dot{Q}C \tag{11.37}$$

$$U_{235_{burnrate}} = 235F_R \tag{11.38}$$

$$U_{235_{totalburnt}} = U_{235_{burnrate}}\alpha(Days * 24 * 3600) \tag{11.39}$$

$$N_{FuelAtoms_{Total}} = \frac{U_{235_{totalburnt}}}{235 * \%_{burnup} * 100} \tag{11.40}$$

$$V_{Fuel} = \frac{N_{FuelAtoms_{Total}}}{N_u} \tag{11.41}$$

$$V_m = V_r - V_{Fuel} = V_m * \frac{V_r}{V_m} - V_{Fuel} => V_m = \frac{V_{Fuel}}{\frac{V_r}{V_m} - 1} \tag{11.42}$$

$$V_r = V_{Fuel} + V_m \tag{11.43}$$

Now that to have the volume of the uranium and moderator $(0.0006637\, m^3)$, the calculated length can be used in (11.36) to find the the total diameter of the core.

$$A_r = \frac{V_{Fuel}}{L_{pipe}} + A_{pipe} \tag{11.44}$$

$$D_r = \sqrt{\frac{4A_r}{\pi}} \tag{11.45}$$

The values calculated in Equations (11.41),(11.42) and (11.45) are displayed in Table 11.15.

D_h	3 mm
f	0.005

Table 11.16: DEV Reactor Channel Dimensions

$V_{Fuel}\{m^3\}$	$V_m\{m^3\}$	$D_r\{m\}$
0.0001327	0.0005310	0.073161

Table 11.15: Values calculated while finding L

11.7.2 Reactor Pressure Drop

The methodology to calculate the pressure drop across the DEV reactor is very similar to the pressure drop in the supply line of the tie tubes. The pressure is modeled using a 1-D differential model [7] shown below in Figure 11.14 :

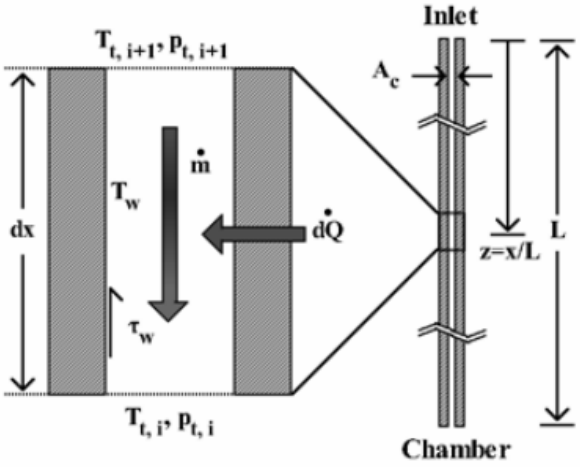

Figure 11.14: DEV Reactor Differential Element [7]

The temperature increase and pressure drop across the elements are defined by the following equations [7]:

$$T_{i+1} = T_i - \frac{d\dot{Q}}{\dot{m}C_p} \tag{11.46}$$

$$p_{i+1} = p_i + (\frac{\dot{m}}{A_{cs}})^2(\frac{1}{\rho_i} - \frac{1}{\rho_{i+1}} - \frac{1}{\rho_i + \rho_{i+1}}\frac{4fdx}{D_h}) \tag{11.47}$$

The pressure recovery across the reactor is calculated to be 98% using Equations 11.47 and 11.47 for the geometry in Table 11.16 using the MATLAB script in Appendix E.4

11.7.3 Thermodynamic Cycle

The key thermodynamic cycle parameters are determined using Section 11.5.5 and are displayed in Table 11.17:

$\dot{m}(kg/s)$	$\frac{p_2}{p_1}$	η_c	η_t	ε_r
0.8	2.1	0.9	0.9	0.9

Table 11.17: DEV Brayton Cycle Parameters

The corresponding state points are calculated using the code in Appendix E.2 and are displayed below:

State	Temperature (K)	Pressure (MPa)
1	500.0	2.50
2	690.5	5.50
3	774.4	5.45
4	1000	5.34
5	783.7	2.55
6	699.8	2.53

Table 11.18: DEV Brayton Cycle State Points

The state points displayed in Table 11.18 are plotted to produce the following P-v diagram:

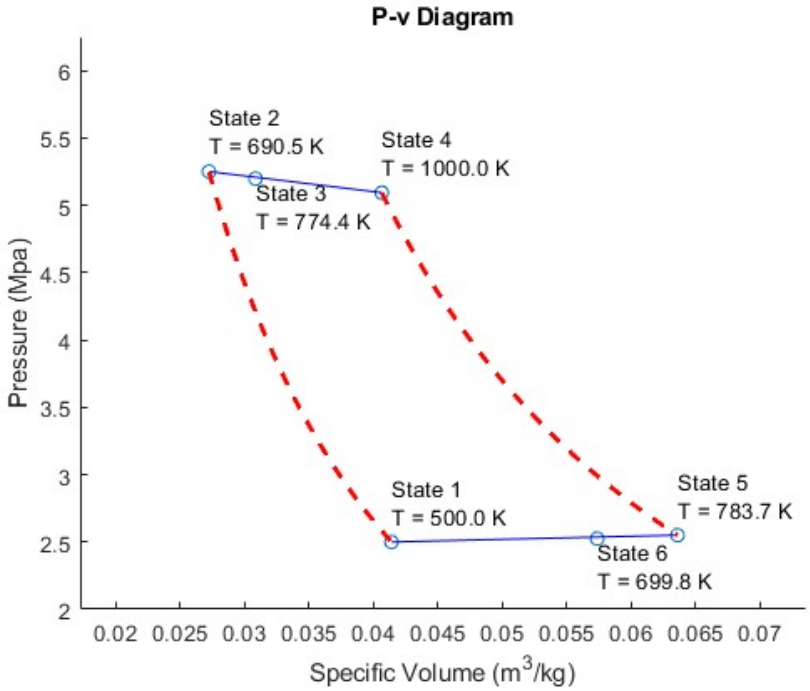

Figure 11.15: DEV P-v Diagram

The cycle characteristics are then calculated:

Cycle Characteristics	
$\dot{Q_{in}}$ (kWt)	94.0
$\dot{Q_{out}}$ (kWt)	83.3
$\dot{W_{net}}$ (kWe)	10.53
$\eta_{thermal}$ (%)	11.2

Table 11.19: DEV Cycle Characteristics

11.7.4 P&ID

The following P&ID displays the flow stations for a singular DEV reactor:

UA	2.6049e+03

Table 11.20: DEV Regenerator

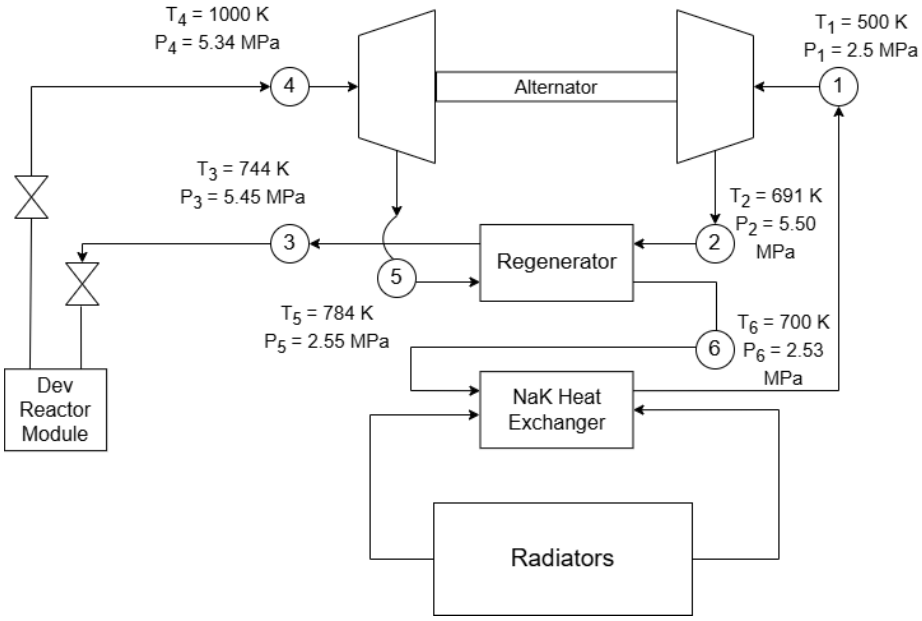

Figure 11.16: DEV P&D

11.7.5 Regenerator Sizing

The size of the regenerator in the bimodal Brayton cycle is calculated using Equation 11.21 and Figure 11.4:

11.7.6 Turbomachinery

Once again the turbomachinery is sized using the process described in Section 11.5.8. The corresponding values are displayed in Tables 11.21 and 11.22.

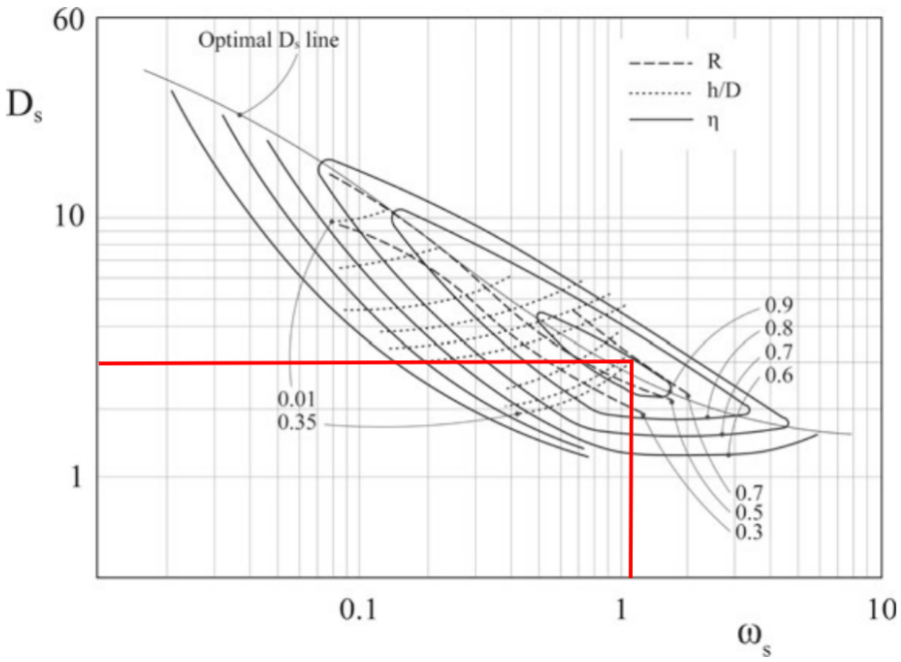

Figure 11.17: DEV Turbine [6]

Turbine	
ω_s	1.0421
D_s	3
w (rpm)	150,000
D (m)	0.0421

Table 11.21: Dev Turbine

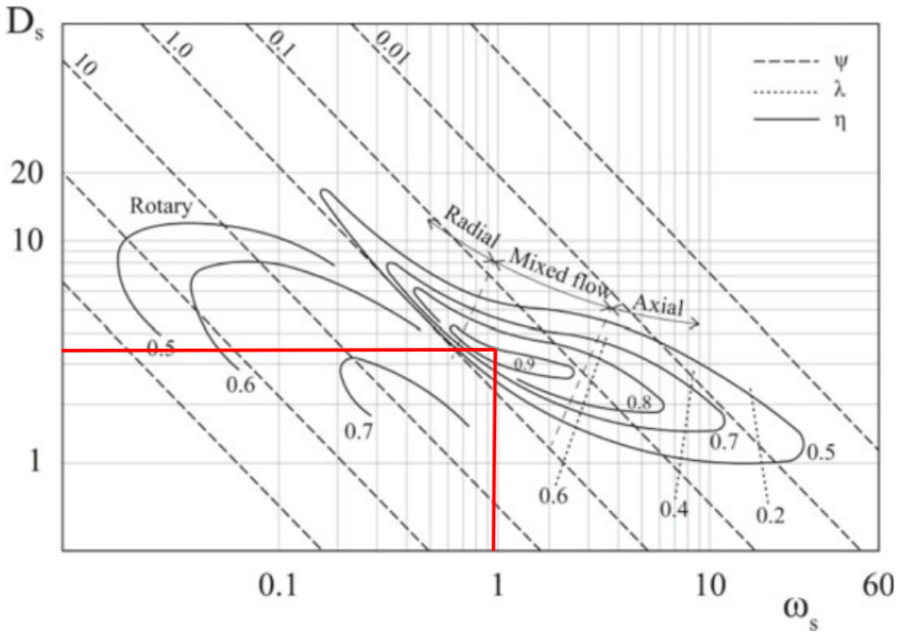

Figure 11.18: DEV Compressor [6]

Compressor	
ω_s	0.93
D_s	3.5
w (rpm)	150,000
D (m)	0.0412

Table 11.22: DEV Compressor

11.8 IPV: Power Management and Distribution

Power Management and Distribution is a key issue among spacecraft. Figure 11.19 details this process:

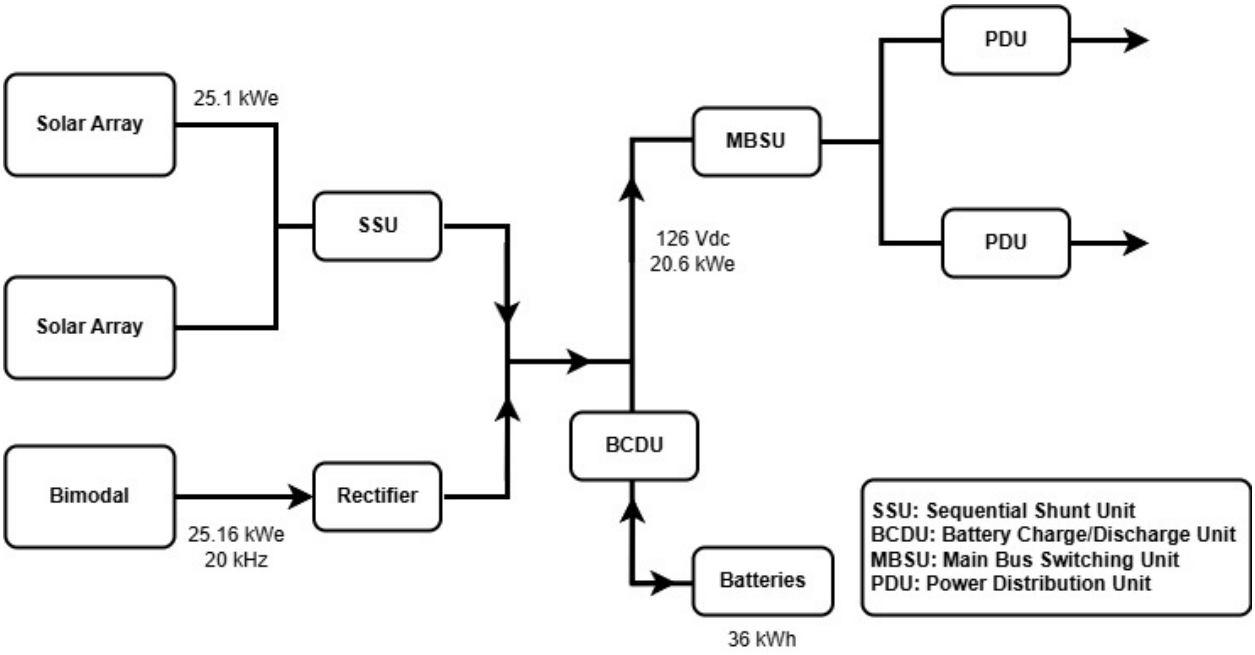

Figure 11.19: IPV Power Management and Distribution

The IPV is equipped with the Bimodal Brayton Cycle that produces 25.16 kWe of energy. If all three reactors fail, the IPV is also equipped with solar arrays to produce the necessary power. The power produced from the Bimodal is ran through a rectifier to convert it to DC power. The power from the solar array (when operational) is ran through a Sequential Shunt Unit (SSU), which regulate the solar arrays' current and voltage [107]. Additionally, the IPV is equipped with 36 kWh to provide power during Bimodal switchover procedures. The batteries are managed using a Battery Charge/Discharge Unit (BCDU) [107]. Lastly, the entire power is managed using a Main Bus Switching Unit (MBSU), where it is then sent out to Power Distribution Units (PDUs) to provide electrical power to all devices.

Parameter	Bimodal	DEV
$\dot{Q}_{in}(kWt)$	139.0	94.0
$\dot{Q}_{out}(kWt)$	113.3	83.3
$\dot{W}_{net}(kWe)$	25.16	10.53
$\eta_{thermal}(\%)$	18.1	11.2
$\eta_{carnot}(\%)$	50.3	54.3

Table 11.23: Power Generation Summary

11.9 DEV: Power Management and Distribution

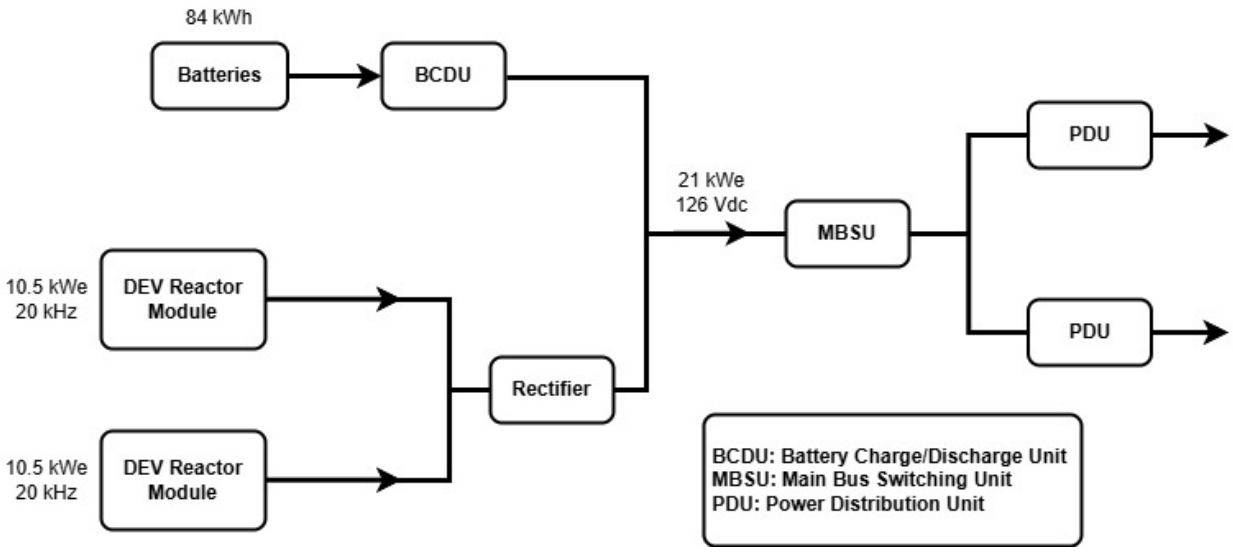

Figure 11.20: DEV Power Management and Distribution

The Power Management and Distribution diagram is displayed in Figure 11.20. The DEV is powered by two reactor modules that produce 10.5 kWe each. That power is then converted to DC using a rectifier. The DEV contains 84 kWh of batteries that are managed by a BCDU to provide 19 hours of supplemental power in the event of one reactor out. The power is then distributed through the DEV using a MBSU and PDUs [107].

11.10 Summary

Table 11.23 displays the thermodynamic cycle characteristics for both the bimodal and DEV Brayton cycles. It is important to note that the DEV contains two reactor modules for

a total power generation of 21 kWe.

12 Life Support

12.1 Trade Studies

The life support system needed for a successful completion of the crewed mission to Deimos needs to have efficient recycling capabilities, sufficient life support supply, and a viable redundancy. These key characteristics are evaluated from the life support needs of the ISS and the standards of NASA. The life support system is designed to maintain the habitable requirements needed to support the life of the needed number of crew members. This mission requires a system to effectively maintain the minimum supplies for four crew members and nine-hundred and seventy-two days. The system will include a WRS that will help reduce the initial mass needed of the life support elements. From the ISS, WRS is capable of maintaining recycling capabilities of approximately 96%. That recycling system undergoes regular maintenance and is capable of having frequent resupply missions, for parts and life support masses. As a preliminary design of the WRS for this mission a recycling capability of 75% efficiency for 80% of the trip is incorporated to take into account the lower frequency of maintenance and no resupply mission capabilities [108]. The mission will also include a high redundancy of masses since there will be unaccounted losses at this point in the design process and for the inability for multiple resupply missions. These unaccounted losses may include system failures, plumbing losses, leaks, or human error. The design includes one resupply mission available if the mission time spent at Deimos is extended. This will in turn require the crew member to maintain a schedule of routinely checking life support supply due to the resupply mission requiring a lengthy duration to reach the crew members. The minimum life support masses needed per day are shown in figures 12.1 and 12.2.

12.2 Block Diagram

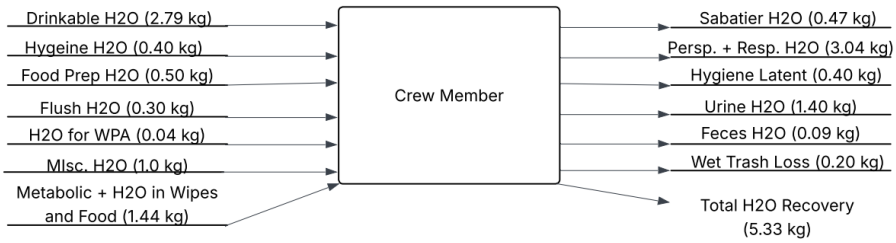

Figure 12.1: H2O Balance [8]

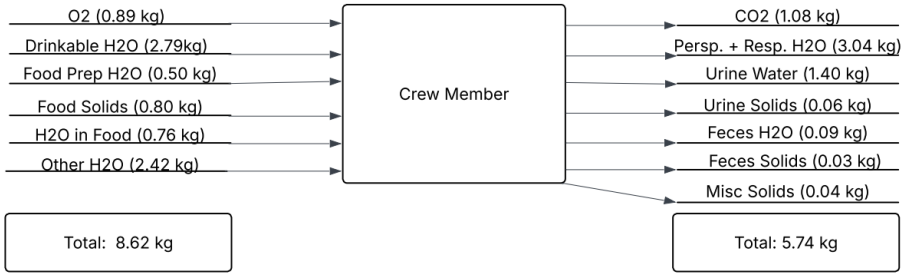

Figure 12.2: Overall Balance [8]

12.3 Results and Risk Mitigation

Similar to the ISS, the initial design for the life support system included an OGA which would require less supplied oxygen and tanking needed for the mission. This would help with the needed overall masses needed at the beginning of the mission. The OGA is capable of running for 40% of the trip duration and running 99% efficient. This design puts significant reliance on the OGA for the supply of the oxygen needed for the mission. With this initial design, it is found to help with initial masses but with a heavy strain on the power required and efficiency levels. Calculations of this initial design is shown in Table 12.1 [109].

Value	Mass (kg)
Oxygen (no redundancy)	3,461.28
Oxygen needed (no generation for 60%)	2,076.77
Oxygen with redundancy (100%)	4,153.54
Water (no redundancy)	15,648.48
Recycled period (80%)	12,518.78
Water lost (25% of recycled)	3,129.70
No recycling (20%)	3,129.70
Total water before O2 gen	6,259.40
Water for oxygen generation (40%)	1,555.20
Total water (no redundancy)	7,814.60
Water with redundancy (100%)	15,629.20
Total Water and O2	19,782.74

Table 12.1: OGA Conceptual Design

Table 12.2 is showing the design that is selected for this mission. This design turns out to require a higher initial mass for the life support elements and would also require significantly more power in order to generate oxygen. It has a lower complexity in terms of supplying the needed life support. This does not put unneeded reliance on a system for the supply of oxygen as well as requiring less maintenance on systems needed for life support.

Value	Mass (kg)
Oxygen per crew per day	-
Oxygen for 4 crew over 972 days	3,461.28
With 100% redundancy	6,922.56
Water per crew per day	-
Water for 4 crew over 972 days	15,648.48
Water during 75% of mission (with recycling)	11,738.04
Water lost during 75% recycling (6% loss)	704.28
Water needed during 25% of mission (no recycling)	3,910.44
Total water needed without redundancy	4,614.72
Water (100% redundancy)	9,229.44
Final Totals:	
Oxygen (with redundancy)	6,922.56
Water (with redundancy)	9,229.44
Total	16,152.00

Table 12.2: Chosen Design

From this the overall Table 12.3 shows the life support mass balance for the mission duration.

	DEV	TOTAL/IPV	Redundancy	Rate	Rate (Mission Scale)
Oxygen	360 kg	6920 kg	100%	.89 kg/day/CM	0.11 mT/Month
Nitrogen	75 kg	1770 kg	50%	80/20 (N/O)	0.43 mT/Month
Water	2640 kg	9230 kg	100%	4.03 kg/day/CM	0.48 mT/Month
Food	345 kg	6220 kg	100%	.80 kg/day/CM	0.10 mT/Month
Water Rec. Sys.	-	1390 kg	75% recycling	-	**Total Mass Consumption Rate**
Habitable Vol.	73 m^3	164 m^3	-	-	**1.11 mT/Month**

Table 12.3: Life Support Mass Balance

12.4 Radiation Shielding

One of the largest challenges of an extended time-duration space mission is the threat that radiation poses to the crew members. Prolonged exposure to constant radiation in space can lead to an increase in the likelihood of exposure-related health issues. Due to this, it is necessary that the design of the habitable volumes of the interplanetary vehicle integrates radiation shielding to ensure the safety of the crew members by limiting their exposure to the allowable dose. This allowable dosage is 1.3 mSv/day for systems in free space from NASA-STD-3001, Volume 1, Revision C, 4.8.5. While the current allowable career dosage in mSv is 600, this would limit current deep space missions to a maximum of eight months, per the current 3% Risk of Exposure-Induced Death (REID) guidelines. It is calculated by the Space Radiation Program at NASA Lyndon B. Johnson Space Center in Houston, Texas, that the current regulations would not allow for a deep space mission to be carried out in accordance to the current guidelines.[110] Operating under these conditions, the radiation shielding solution for this mission is designed in accordance with the NASA-STD-3001 4.8.5 daily allowable radiation exposure dosage allowance.

The radiation shielding solution for this mission is integration of water walls as the primary radiation shield. Water walls are a modular solution to radiation shielding, as the water is contained in polyethylene bags. The polyethylene material is resistant to radiation and will not degrade over the lifetime of the mission, allowing for a very low likelihood of a system failure. The water that is contained in the bags will be Ultrapure Water, to ensure that there are no contaminants that could undermine the effectiveness of the solution. The polyethylene bag that will contain the water can be seen in figure 12.3:

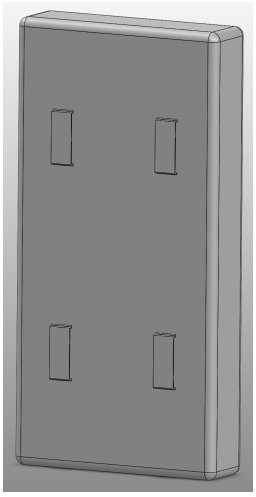

Figure 12.3: Polyethylene Water Wall Bag

The dimensions of this bag are 25x50x7.2 centimeters, with the thickness of 7.2 centimeters being determined by the allowable radiation dosages. The water wall bags will be connected via a semi-rigid grid structure, providing flexible and strong connections that allow for the entirety of both the IPV and DEV habitable volumes to be shielded completely. This solution is adaptable to both structures and allows for minimal design changes necessary to provide a solution to the radiation shielding. Additionally, with the use of water and polyethylene, this is simple, low cost, and does not require complex and expensive research and development to implement and manufacture.

In the decision process to create a solution to protect crew members from the harmful radiation that is ever present in deep space, Aluminum, Liquid Hydrogen, and Water were evaluated to ensure the most efficient shielding method. To make a decision, the main drivers for finding the optimal choice were mass, thickness, and complexity. Radiation shielding is the largest mass component of both habitable volumes, and it is paramount that the mass of the systems are kept to a reasonable level. In conjunction with that, it is necessary to keep the system compact, to allow for optimal packaging and launch configuration. Additionally, the complexity of the systems were also evaluated to minimize the risk associated with the possible failures of the system.

A trade study is used to find the mass as a function of the surface area of each habit-

able volume. These calculations also allow the calculation of the thickness and packaging capabilities of each material. These calculations are based on the material properties for each material, and its allowed radiation dosage per thickness. The calculations for the thickness begin with this graph, marking the allowable radiation per shielding thickness:

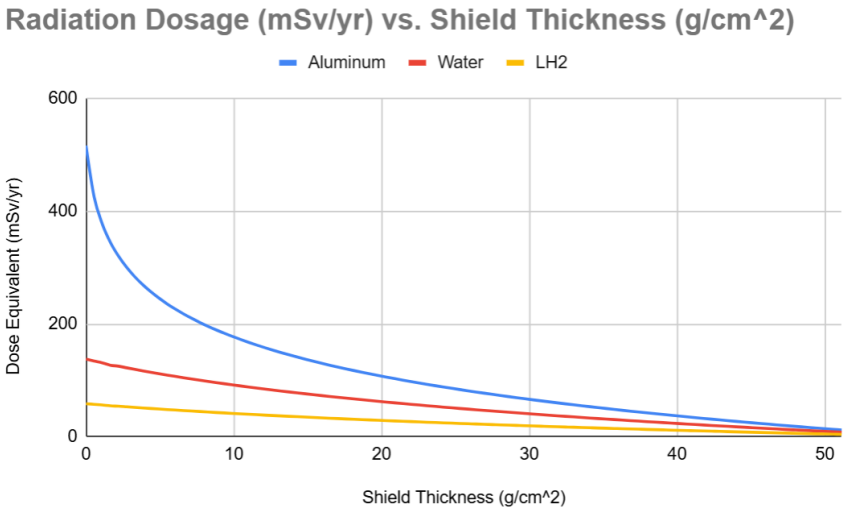

Figure 12.4: Radiation Dosage vs. Shield Thickness[9]

Using this relationship, the thickness of each of the materials is able to be calculated using Equation 12.1.

$$T_{Shielding} = T_s/\sigma \tag{12.1}$$

The total mass of each material in mT is then able to be calculated using Equation 12.2.

$$M_{Shielding} = (T_{Shielding}/\sigma) * 0.01 \tag{12.2}$$

The results for the DEV can be seen in Table 12.4:

Surface Area (m^2)	Material	Shielding Thickness (cm)	Mass (mT)
109.0	Aluminum	17.8	19.4
mSv/Day	LH2	256.0	0.3
1.3	Water	7.2	7.8

Table 12.4: DEV Radiation Shielding Results

The results for the IPV habitable volume can be seen in Table 12.5:

Surface Area (m^2)	Material	Shielding Thickness (cm)	Mass (mT)
159.8	Aluminum	17.8	28.4
mSv/Day	LH_2	256.0	0.4
1.3	Water	7.2	11.5

Table 12.5: IPV Habitat Radiation Shielding Results

While Liquid Hydrogen has the lowest mass, the complications in the systems required for storage for a long term mission make it a non-viable option for this mission profile. Aluminum, while being the least complex solution, has a high mass and thickness in comparison to Water and Liquid Hydrogen. Water provides a solution that has a manageable amount of mass and a thickness that allows for easy and compact packaging. The additional structural aluminum will provide a slight increase in radiation shielding. It is of note that while increasing the thickness of the radiation shielding decreases the total radiation dosage exposure, the exposure decreases significantly less than the respective increase in thickness. The final masses for the IPV and DEV habitable volume radiation shielding are 7.8 and 11.5 mT, respectively, with a uniform thickness of 7.2 cm.

12.5 Adherence to NASA Standards

All life support systems are designed to be in compliance with NASA standards, primarily NASA-STD-3001 Volumes 1 and 2 [30] [111].

13 Risk Assessment

13.1 Risk Matrix

A risk matrix for the mission was developed to analyze mission risks to determine their threat to mission success. To conduct this analysis, a 5x5 matrix was created. In this matrix, the likelihood and consequence of each risk was determined to evaluate the risk severity, and mitigation plan. The likelihood determination factors can be seen in Table 13.1:

Score	**Likelihood of Occurrence (p)**	**p**
5	Near Certainty	$p > 80\%$
4	Highly Likely	$60\% < p < 80\%$
3	Likely	$40\% < p < 60\%$
2	Low Likelihood	$20\% < p < 40\%$
1	Not likely	$p < 20\%$

Table 13.1: Risk Likelihood Criteria [19]

Where p is the percentage chance of a risk occurring, assigning the risk a score on a scale between 1 and 5, with 5 signifying the most likely to occur. The consequence criteria used to evaluate the risks can be seen in Table 13.2:

	1	2	3	4	5
Performance	Minimal consequence to objectives/goals	Minimal consequence to objectives/goals	Unable to achieve particular objective, but remaining goals represent better than minimum success or outcome	Unable to achieve multiple objectives/goals but minimum success can still be achieved	Unable to achieve objectives/goals such that minimum success cannot be achieved or claimed
Human Safety	Discomfort or nuisance	First aid event per OSHA criteria	No lost time injury or illness per OSHA criteria	Lost time injury or illness per OSHA criteria	Loss of life
Asset	Asset has no sign of physical damage	Asset has cosmetic damage and is repairable	Asset is damaged but repairable	Asset is substantially damaged but repairable	Asset is compromised, and unrepairable: a total loss
Schedule	Minimal Consequence	Critical path is not slipped, impact <10 days	Critical path is not slipped, total slack is within 10 days of impacting critical path	Critical path slips	Critical path slips and one or more critical milestones or events cannot be met
Cost	Minimal Consequence	Minor cost consequence, cost variance <5% total baseline	Cost consequence, cost variance <10% total baseline	Cost consequence, cost variance <15% total baseline	Major cost consequence, cost variance >15% total baseline

Table 13.2: Risk Consequence Criteria [19]

The risks were categorized based on these consequence criteria, and were rated a score between 1 and 5, with 5 denoting the most severe outcome. A complete analysis of the risks, type, description, and their corresponding likelihood and consequence ratings were calculated and compiled. The risks and their evaluations are seen in Table 13.3:

ID	Risk	Type	Risk Description	L	C	Mitigation
4	In-Space Assembly	Technical	In Space Assembly Technical Challenges	2	4	Mitigate
1	Boil Off Management	Technical	Development of boil off prevention technologies to meet max allowable limits falls short of goal.	2	2	Mitigate
8	Mass Budget Overrun	Technical	Total mass breakdown over 750mT allocation (past expected dry mass margin)	2	3	Watch
7	SLS Launch Number	Technical	Cannot package all modules into 6 launches (due to mass or geometry)	2	2	Mitigate
2	NTP Engine Isp	Technical	Nuclear Thermal Propulsion does not meet specified 950s Isp.	2	2	Mitigate
10	OMS Mass Overrun	Technical	OMS Secondary Propulsion overruns mass allocation	3	2	Watch
5	Micrometeoroid Shielding	Technical	Shielding unable to meet impact energy requirements while meeting mass allocation	1	2	Mitigate
3	Radiation Protection/Mass	Technical	Radiation Shielding unable to meet mass allocation	1	2	Watch
11	Radiator/Heat Rejection System Mass	Technical	Radiator and heat rejection system mass higher than previously thought	3	3	Watch
12	Lined Composites Tanks	Technical	Thermal expansion, manufacturability concerns	3	3	Mitigate

Table 13.3: Risk Matrix Analysis Table

This table can be visualized using the 5x5 risk matrix:

RISK						
LIKELIHOOD	CONSEQUENCE					
		1	2	3	4	5
	5					
	4					
	3			8, 11, 12		
	2		2, 10, 7	1	4	
	1		3, 5			

Figure 13.1: 5x5 Risk Matrix

The risks are evaluated using a final ranking by multiplying the likelihood and consequence number together. The higher this number, the greater the risk poses to the mission. The range for these values is between 1 and 25, where 25 presents the highest possible risk to the mission. The risks that were identified to have the most potential to cause a mission failure are Mass Budget Overrun, Radiator/Heat Rejection System Mass, and Lined Composite tanks, due to the combination of their likelihood and consequences, giving them a final ranking of 9. These risks were watched throughout the design process, and mitigated with implemented preventative measures when necessary.

13.2 Failure Modes and Criticality Effects Analysis

An analysis of the major components of the IPV, DeV, and TMSA were evaluated using a Failure Modes, Effects, and Criticality Analysis (FMECA) to identify areas of design that have potential failures. The areas of design analyzed include the critical subsystems of the IPV to eliminate as many potential failures as possible. These potential failures are then

prioritized by the severity of their potential effects to determine the order of which they should be addressed. The severity and criteria of these failures can be seen in Figure 13.2:

Failure Severity:
1) Very Low: Minor or no impact on mission life or performance
2) Low: Potential for major or significant degradation of mission or performance
3) Moderate: Significant loss or degradation of mission, or Loss or degradation of a redundant subsystem producing level 3 or 4 severity
4: High: Major Loss or degradation of mission, or Loss or degradation of a redundant subsystem producing levels 4 or 5 severity
5: Very High: Complete loss of mission, or loss or degradation of a subsystem or science leading to a subsystem or science leading to safety or hazard monitoring system failure

Figure 13.2: FMECA Failure Severity Scale[10]

With the severity of the failures defined, a full FMECA analysis was completed:

Item/Functional Identification	Function	Failure Modes and Causes	Mission Phase/Operational Mode	S	Damage Mode	Local Effects	Next Higher Level	End Effects	Remarks
Nuclear Thermal Reactors (NTR)	Provide thrust for main mission operations: Earth and Mars departure and capture burns. Provide power via bimodal operations to provide electrical power generation for the IPV.	Core Meltdown: Insufficient Cooling, Power Surges, Fuel Feed Failure	All Departure and Capture Burns: Main thrust provider, Earth to Mars and Mars to Earth Transits: Bimodal Power generation.	5	Propellant feed is insufficient.	Thrust & Bimodal power generation stall.	Subsystems reliant on power generation begin to fail.	The IPV fails to complete trajectory marks and leads to critical power generation failure.	Failure of the Nuclear Thermal Reactors has the potential to cause a full mission failure.
Propellant Tanks	Storage of the propellant needed to generate thrust through the propulsion system.	Leakage: Impact from Space Debris	Propellant Tank dependent, subsequent tanks are used for specified orbital maneuvers throughout the course of the mission.	3	Pressurization loss due to insufficient stress withstanding capabilities.	Propellant tank becomes depressurized and fuel feed lines become compromised.	Decrease in overall thrust generation capabilities.	The IPV may fail to meet thrust requirements for the mission profile due to insuffient ability to provide propellant.	The failure of the propellant tanks is unlikely due to their robust design which implements MMOD shielding and strong materials.
		Cracking or Fracture: Vibrations, Thermal Cycling	Propellant Tank dependent, subsequent tanks are used for specified orbital maneuvers throughout the course of the mission.	3	Pressurization loss due to critical structural failure.	Propellant tank becomes depressurized and fuel feed lines become compromised.	Decrease in overall thrust generation capabilities.	The IPV may fail to meet thrust requirements for the mission profile due to insuffient ability to provide propellant.	The propellant tanks are unlikely to be affected by thermal cycling issues due to their material selection being adequate for the application.
Radiators	Disperse heat generated by various power cycles in the IPV to ensure operable temperatures for all on board systems.	Coolage Leakant: MMOD impacts	Radiators are active at all stages of the mission profile to ensure all IPV systems are able to operate at temperatures withing their standard operating range.	3	Decrease in heat rejection efficiency due to system degredation.	Radiator becomes less effective at rejecting all heat to space.	Secondary systems begin to operate at suboptimal temperatures.	Overall efficiencies of processes in the IPV, such as thrusting and power generation decrease.	The failure of a radiator will cause cascading effects that will cause systems to run below their peak efficiency levels, however this can be tolerated in moderation due to redundancies built into subsystems.
		Surface Degradation: Thermal Cycling	Radiators are active at all stages of the mission profile to ensure all IPV systems are able to operate at temperatures withing their standard operating range.	2	Effectiveness of heat rejection is decreased due to thermal fatigue.	Radiator becomes less effective at rejecting all heat to space.	Secondary systems begin to operate at suboptimal temperatures.	Overall efficiencies of processes in the IPV, such as thrusting and power generation decrease.	The radiators are unlikely to be affected by thermal cycling issues due to their material selection being adequate for the application.
		Structural Failure: Vibrations and MMOD impacts	Radiators are active at all stages of the mission profile to ensure all IPV systems are able to operate at temperatures withing their standard operating range.	3	Decrease in heat rejection efficiency due to system degredation.	Radiator becomes less effective at rejecting all heat to space.	Secondary systems begin to operate at suboptimal temperatures.	Overall efficiencies of processes in the IPV, such as thrusting and power generation decrease.	The MMOD shielding protects against impacts from small space debris, and the design decreases the chance of these impacts creating a measurable effect on the IPV's mission success is highly unlikely.
Solar Panels	Provide electric power generation for subsystems and ensure complete power geneartion during bimodal operation startup.	Deployment Failure: Actuator Malfunction	Operational during the phase of the NTR bimodal power operation startup, but can supply additional power during all phases of the mission.	1	Reduced surface area due to sustained damage from deployment.	Power generation decreased and less efficient.	Subsystems during bimodal power operation startup may see decreased power and capabilities.	Can lead to partial system failure due to insufficient power generation.	Due to redundancy in the power generation systems, a decrease in solar panel efficiency due to reduced surface area can be tolerated and is low risk to mission success.
		Wiring Failure: Vibration, UV Degredation	Operational during the phase of the NTR bimodal power operation startup, but can supply additional power during all phases of the mission.	1	Reduced power transfer.	Power generation decreased and less efficient.	Subsystems during bimodal power operation startup may see decreased power and capabilities.	Can lead to partial system failure due to insufficient power generation.	Due to redundancy in the power generation systems, a decrease in solar panel efficiency due to reduced power transfer can be tolerated and is low risk to mission success.
		Surface Damage: MMOD	Operational during the phase of the NTR bimodal power operation startup, but can supply additional power during all phases of the mission.	2	Reduced surface area due to sustained damage from impacts.	Power generation decreased and less efficient.	Subsystems during bimodal power operation startup may see decreased power and capabilities.	Can lead to partial system failure due to insufficient power generation.	Due to redundancy in the power generation systems, a decrease in solar panel efficiency due to reduced surface area can be tolerated and is low risk to mission success.

Figure 13.3: Failure Modes and Criticality Effects Analysis (FMECA)

Item/Functional Identification	Function	Failure Modes and Causes	Mission Phase/Operational Mode	S	Damage Mode	Local Effects	Next Higher Level	End Effects	Remarks
Truss Structures	Provide structural integrity during thrusting and secure mounting points for spacecraft systems.	Material Fatigue: Thermal Cycling	Operational during all phases of the mission as a passive component of the IPV.	4	Structural fatigue or fracture resulting in a failure.	Systems become misaligned or detatched.	Subsystems are not able to interact with one another properly, causing failures in systems like propulsion or power generation.	The IPV may fail to continue on projected mission profile due to failures of subsystems.	The truss structure is integral to the success of the IPV, and while a failure could cause a critical failure, the structures have been designed to pass all mission phases with integrated factors of safety in their design.
		Cracking: Vibrations, MMOD impacts	Operational during all phases of the mission as a passive component of the IPV.	4	Localized failure due to impact or vibration caused failures.	Systems become misaligned or detatched.	Subsystems are not able to interact with one another properly, causing failures in systems like propulsion or power generation.	The IPV may fail to continue on projected mission profile due to failures of subsystems.	The IPV could be subject to a critical failure due to cracking from vibrations during transit or launch, which could cause mission delay or failure.
Orbital Maneuvering System (OMS)	The OMS performs fine adjustments in orbital maneuvers and assists in precision burns throughout the mission.	Valve Jamming: Clogging, Insufficient fuel flow.	Used in all phases containing a burn to facilitate course corrections.	3	Loss of maneuverability and precise controls.	Minor corrections of the IPV become difficult to operate.	Subsystems like cooling and propellant feeding may be negatively affected.	The IPV becomes significantly more difficult to maneuver and finish large orbital maneuvers precisely.	While an OMS failure may not cause a full mission failure, it may hinder the IPV's ability to maneuver precisely into the desired locations during each phase of the mission, potentially altering mission objectives.
Micro-Meteoroid and Orbital Debris (MMOD) Shielding	Provides protection for mission critical components that may be susceptible to failures due to high velocity impacts from space debris or micro-meteoroids.	Puncture: Repeated MMOD impacts.	Operational during all phases of the mission as a passive component of the IPV and Dev.	2	Impact affects local area of MMOD shielding.	Decreased protection to vacuum of space for components protected by MMOD shielding.	Damage to subsystems like propellant tanks and habitable volume.	Could cause a total failure of a subsystem if the impact is severe enough to puncture every layer of the MMOD shielding.	The MMOD shielding protects against impacts from small space debris, and the design decreases the chance of these impacts creating a measurable effect on the IPV's mission success is highly unlikely.
Assembly Vehicle	Handles the construction of the IPV in Low Earth Orbit and integrates each launch into the final assembly.	Arm Failure: Power Loss, Stress Failure.	Active use during the assembly phase before the IPV begins its transit to Mars.	2	Failures in the mechanical or propulsion components leading to innelectiveness.	Subsystems may be misaligned with each other during assembly.	Subsystems are not able to interact with one another properly, causing failures in systems like propulsion or power generation.	The mission timeline may be delayed and launch windows become suboptimal.	The assembly vehicle, along with the manned crew have the task of assembling the IPV in Low Earth Orbit, which must be completed in an efficient manner, which can be impacted by these potential failures.
Tele-Operated Mars Assets (TMSA)	Conducts scientific investigations on the surface of Mars.	Communication Failure: Power Loss, Signal Loss	Active during the IPV stay at Mars with extended life beyond the mision timeline possible.	1	Inability to conduct experiments and procure mission data.	Asset becomes unable to be operated properly or at full function capacity.	Reduced scientific output and resource and data collection.	Mission goal of gathering data for future Mars missions may become increasingly difficult to achieve.	The potential for failure in the TMSA technology is very low risk due to the proven technology that is already in use and the design choices implemented to mirror those of past successful missions.
		Entry Failure: Inadequate landing zone, propulsion/trajectory failure	Active during the IPV stay at Mars with extended life beyond the mision timeline possible.	1	Inability to conduct experiments and procure mission data.	Asset becomes unable to be operated properly or at full function capacity.	Reduced scientific output and resource and data collection.	Mission goal of gathering data for future Mars missions may become increasingly difficult to achieve.	The potential for failure in the TMSA technology is very low risk due to the proven technologies that have placed technology onto the surface of Mars.
Radiation Shielding	Protects the crew in the habitable volume from potentially harmful dosages of radiation.	Material Degradation: Polyethylene breakdown, Water Leakage	Operational during all phases of the mission as a passive component of the IPV and DeV.	2	Reduced radiation protection.	Increased radiation exposure to internal compartments.	Electronics and health of crew members may become compromised.	Long term mission degradation as the increased radiation dosages effects continue.	The radiation shielding solution is modular in its water wall and polyethylene bag solution; a failure in a singular bag would have a small overall impact on mission success.

Figure 13.4: Failure Modes and Criticality Effects Analysis (FMECA) Continued

From this analysis, time was allocated to ensure that all potential failures of each subsystem or component was evaluated and found to be in a satisfactory state.

14 Mars Assets

14.1 Ballistic Entry

14.1.1 Entry CONOPS

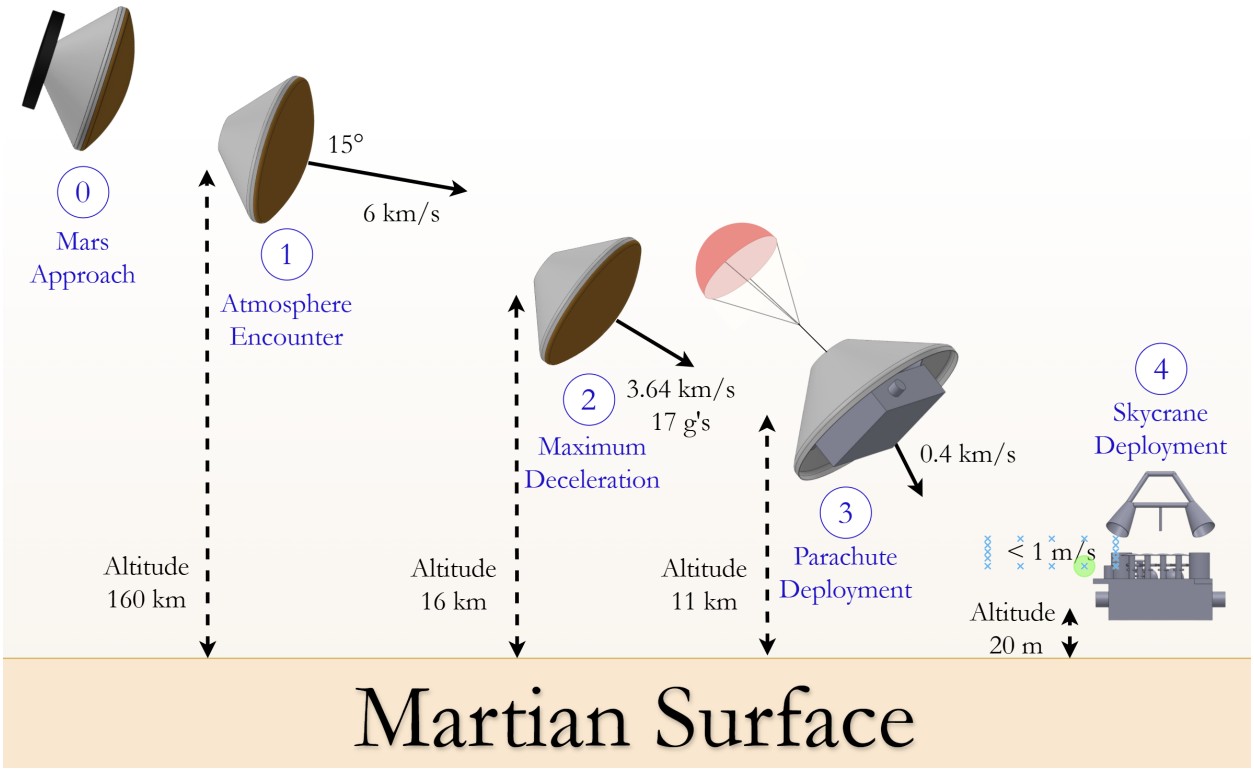

Figure 14.1: Martian Entry CONOPS

The Martian entry CONOPS is shown in Figure 14.1. The TMSA entry vehicle uses a cruise stage to perform mid-course corrections while on the Earth-Mars Hohmann transfer. The cruise stage is detached shortly before entry into the Martian atmosphere at a flight angle of 15 ° and at an entry velocity of 6 km/s. The entry capsule experiences its maximum deceleration of 17Gs at an altitude of 16 km. Shortly thereafter, a parachute is deployed at 11 km to prepare for the skycrane landing procedure, which is performed at 20m above the Martian surface [112].

14.1.2 Entry Vehicle Geometry

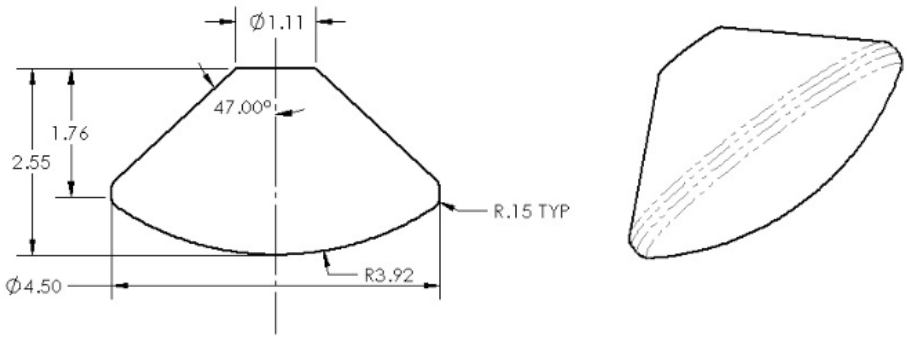

Figure 14.2: Entry Vehicle Dimensions

The geometry of the TMSA entry vehicle is shown in Figure 14.2. The capsule dimensions are similar to those of the Mars Science Laboratory (MSL) missions [113]. The capsule features a diameter of 4.5 m with a 70 ° sphere cone aero shell. These dimensions allow for ample clearance to stow the Mars assets and help to minimize aerodynamic heating upon entry into the Martian atmosphere.

14.1.3 Effective Nose Radius

Aerodynamic heating calculations are based on stagnation-point heating of hemispherical bodies. As such, an effective nose radius must be calculated. Figure 14.3 details the geometry of an asymmetrical entry capsule and its multiple radii [11].

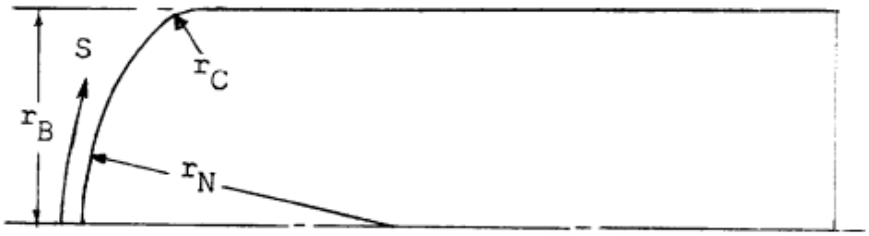

Figure 14.3: Sketch of Typical Blunt Body [11]

The radii for the TMSA entry capsule as presented in Section 14.1.2 are displayed in

Table 14.1:

Radius	(m)
R_c	2.25
R_B	0.15
R_N	2.92

Table 14.1: Entry Vehicle Radii

Figure 14.4 displays a ratio between effective nose radius, and actual nose radius for varying corner radii.

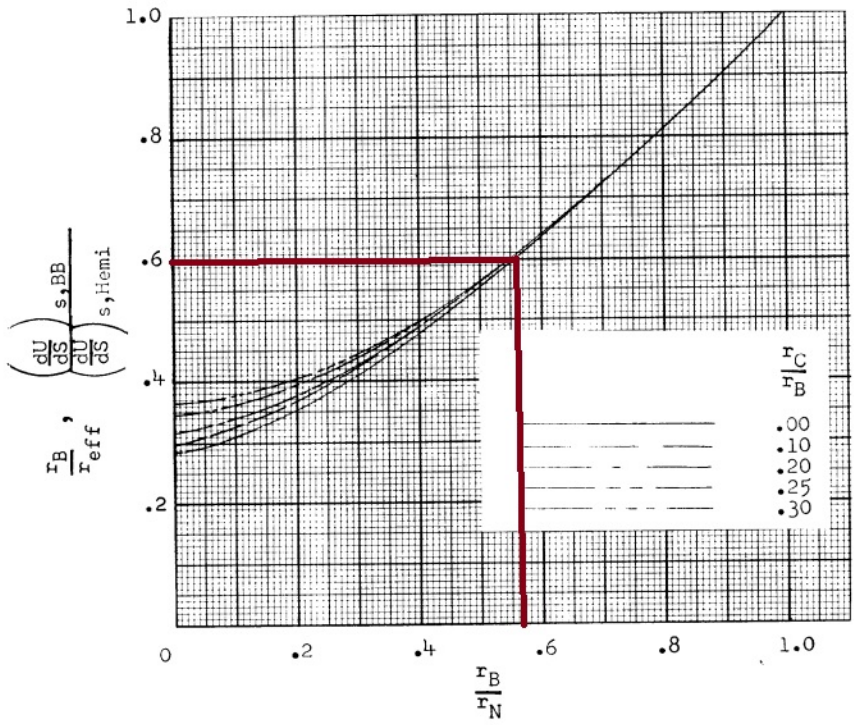

Figure 14.4: Variation of Effective Radius for Varying Corner Radius Ratios [11]

Using Figure 14.4 and the values from Table 14.1 the effective nose radius is found to be 3.75 m.

14.1.4 Entry Velocity Profile

The ballistic entry profile is derived from Allen and Eggers based on the following assumptions [114][115]:

1. Gravity is negligible compared to deceleration
2. Drag coefficient is constant
3. Lift is negligible
4. Density if an exponential function of altitude (the Martian atmosphere is modeled using a density scale height of 11.1×10^3 and a reference density of 0.02 kg/m^3 [116])

The Martian entry flight path is displayed below in Figure 14.5:

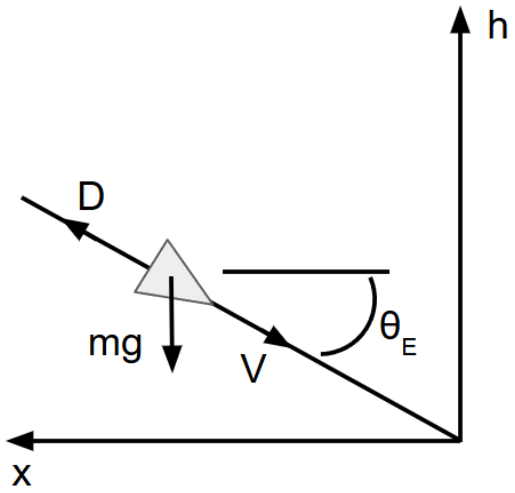

Figure 14.5: Ballistic Entry Diagram

The ballistic entry profile can then be used to calculate the velocity as a function of altitude (h)[114][115]:

$$V(h) = V_e \exp[\frac{C_D A}{2m \sin \theta_E} \frac{\rho_0}{\beta} e^{-\beta h}] \tag{14.1}$$

Additionally, the properties associated with the maximum deceleration can be calculated [114] [115]:

$$-\frac{dV/dt}{g}|_{max} = \frac{1}{g}(\frac{\beta V_e^2 \sin\theta_E}{2e}) \tag{14.2}$$

$$h_{max_g} = \frac{1}{\beta} ln(\frac{C_D A \rho_0}{\beta m \sin(\theta_e)}) \tag{14.3}$$

$$V_{max_g} = V_E e^{-1/2} \tag{14.4}$$

The entry vehicle detailed in Section 14.1.2 along with typical Martian entry conditions found in Table 14.2 produce the velocity profile found in Figure 14.6 using MATLAB in Appendix G.2 [117].

Key Entry Parameters	
$\frac{m}{C_D A}$	145 $\frac{kg}{m^2}$
V_E	6 km/s
θ_E	15°

Table 14.2: Ballistic Entry Parameters

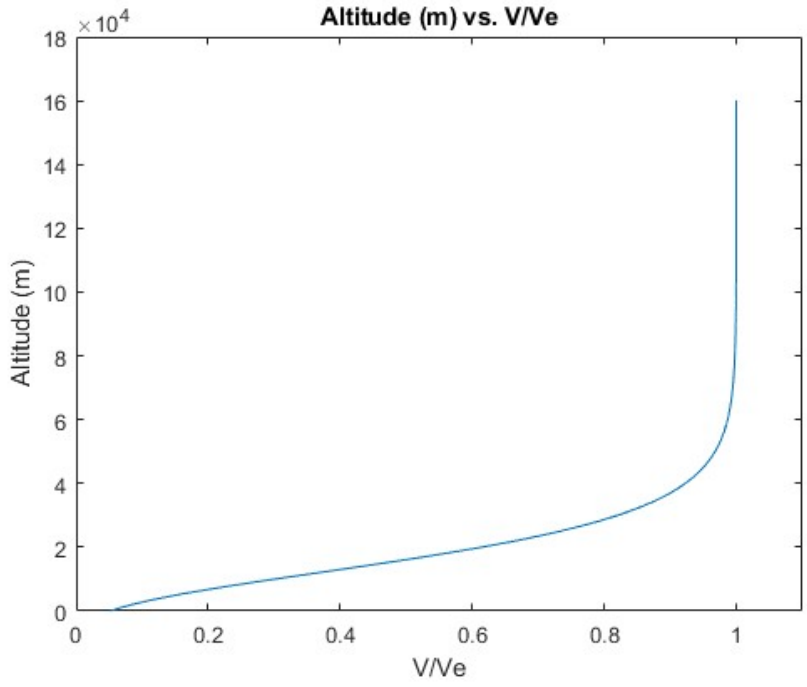

Figure 14.6: Entry Velocity Profile

Furthermore, using Equations 14.2 , 14.3, and 14.4, Table 14.3 is obtained.

Max Deceleration	
$max_g(g)$	17
$V_{max_g}(km/s)$	3.64
$h_{max_g}(km)$	19.7

Table 14.3: Max Deceleration Characteristics

Stagnation-Point Heating In order to adequately size the heat shield on the TMSA entry capsule, both convective and radiative stagnation-point heating are considered. The convective heat rate is calculated using the Sutton-Graves Equation [118] for stagnation-point convective heating:

$$\dot{q}_{conv} = k\sqrt{\frac{\rho}{R_{eff}}}V^3 \tag{14.5}$$

The following values in Table 14.4 are for the Martian atmosphere and the TMSA entry vehicle are provided:

Key Parameters	
k	$1.9027E-4$
R_{eff}	3.75 m

Table 14.4: Convective Heating Values

Additionally, the radiative stagnation-point heating is calculated using the following relation [119]:

$$\dot{q_{rad}} = 2.35 \times 10^4 R_{eff}^{0.526} \rho^{1.19} f(V) \tag{14.6}$$

However, radiative heating is only a concern with high entry velocities. This is demonstrated as the tabulated f(V) values only contains tabulated values of 9 km/s to 16 km/s [119]. As such, radiative heating is not considered. The convective heat flux of the entry vehicle along its flight path is calculated using Equation 14.5 using values from Table14.4. Next, the equilibrium wall temperature is calculated by Equation 14.7 [120].

$$T_w = (\frac{\dot{q_{conv}}}{\epsilon\sigma} + T_{surr}^4)^{(1/4)} \tag{14.7}$$

Both the convective heat flux and equilibrium wall temperature are plotted in Figure 14.7 using MATLAB code from Appendix G.2.

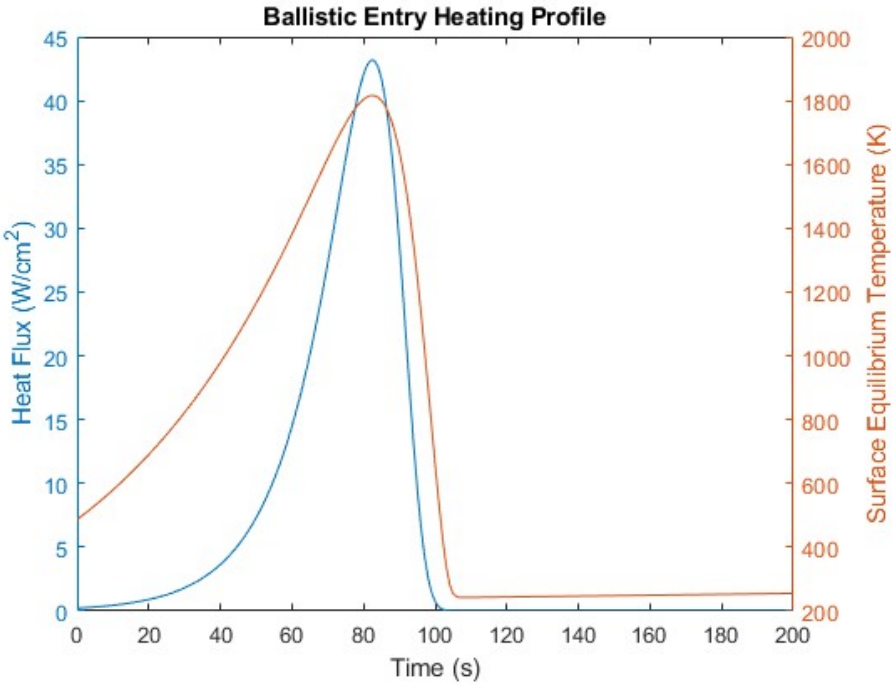

Figure 14.7: Ballistic Entry Heating Profile

14.1.5 Heat-shield Sizing

A Phenolic Impregnated Carbon Ablator material is used for the heat shield. PICA is commonly used on re-entry vehicles due to its low density and thermal conductivity. Its material properties are shown in Table 14.5[120] [113]:

Property	Value
$\rho\ (kg/m^3)$	265
Q^*W/cm^2	1500
$k\ (W/mK)$	1.6
$C_p(J/kgK)$	1592.0

Table 14.5: PICA Material Properties

A simplified approach uses 1D-transient conduction for an infinite plate with a constant surface temperature as a preliminary calculation to determine the appropriate thick-

ness of the heat shield. The approach is shown in Equation 14.8 [120].

$$T(x,t) = erf(\frac{x}{2\sqrt{\alpha}t})(T_i - T_s) + T_s \tag{14.8}$$

The surface temp (T_s) was taken as the average equilibrium temperature and T_i as the initial temperature upon entry into the Martian atmosphere. Results for multiple heat-shield thicknesses are shown below based on the MATLAB code from Appendix G.2:

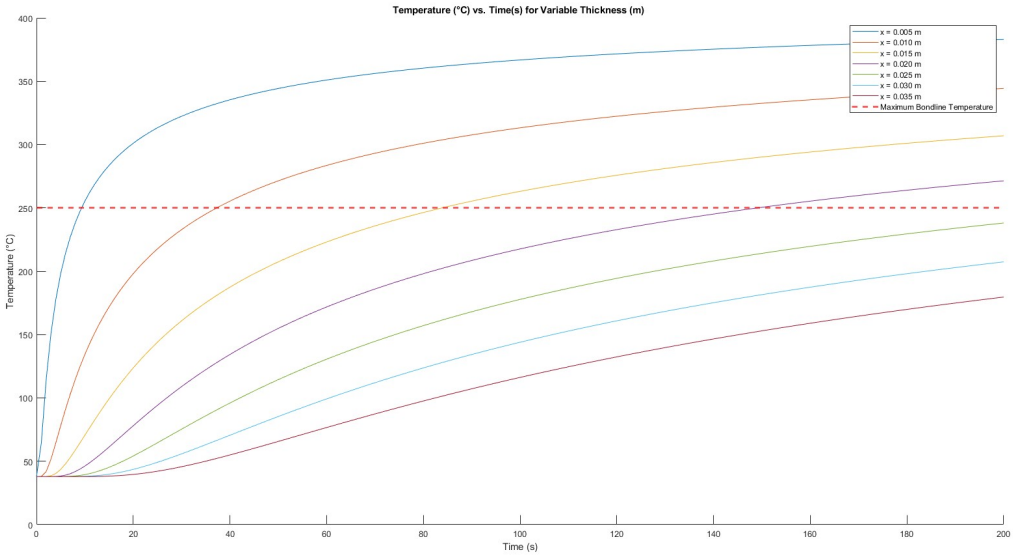

Figure 14.8: Heat-shield Thickness

Examining Figure 14.8 a heat shield thickness of 2.5 cm yields a maximum temperature, which is lower than the maximum bondline temperature of PICA. In addition, the results shown in Figure 14.8 only account for the maximum bondline temperature of the material [113]. As a result, the recession due to ablation must be calculated separately. Recession rate of the heat-shield is calculated using Equations 14.10 and 14.9 [121]:

$$\dot{Q_{hw}} = \dot{Q_{cw}}(1 - \frac{H_w}{H_r}) \tag{14.9}$$

$$\dot{s} = \frac{\dot{Q_{hw}}}{\rho Q^*} \tag{14.10}$$

H_r and H_w are approximated as $\frac{V^2}{2}$ and $C_{p_{CO_2}}T$ respectively. Recession rate calculated using MATLAB code from Appendix G.2 is then plotted against time since entry into the Martian atmosphere in Figure 14.9.

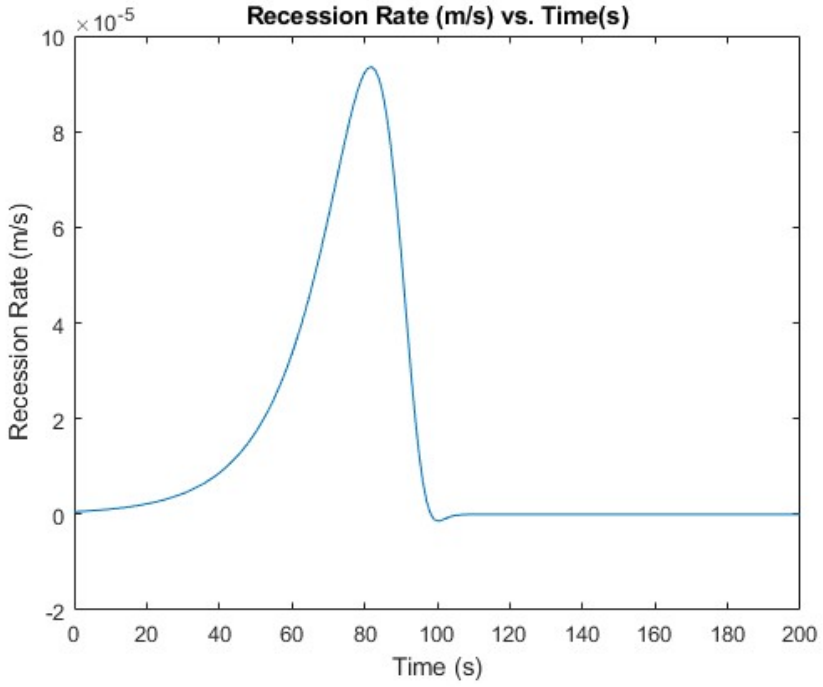

Figure 14.9: Recession Rate

The recession rate from Figure 14.9 is then numerically integrated to provide the total recession of the heat shield $s = 0.28$ cm. As a result, the total thickness is **2.78 cm** accounting for the bondline temperature and recession rate. The final heat shield properties are displayed in Table 14.6:

Heatshield Properties	
Mass (kg)	133
Thickness (cm)	2.78

Table 14.6: Heatshield Properties

14.1.6 Landing

Landing Site In October 2015, NASA held the first *Landing Site/Exploration Zone Workshop for Human Missions to the Surface of Mars*. During this workshop the participants and presenters rated a wide variety of potential landing sites based on a range of criteria. The completed rubric, tallying all participants results, can be found in figure G.1. The overwhelming winner of the vote is the endeavor crater, the locale of which is shown below in figure 14.10.

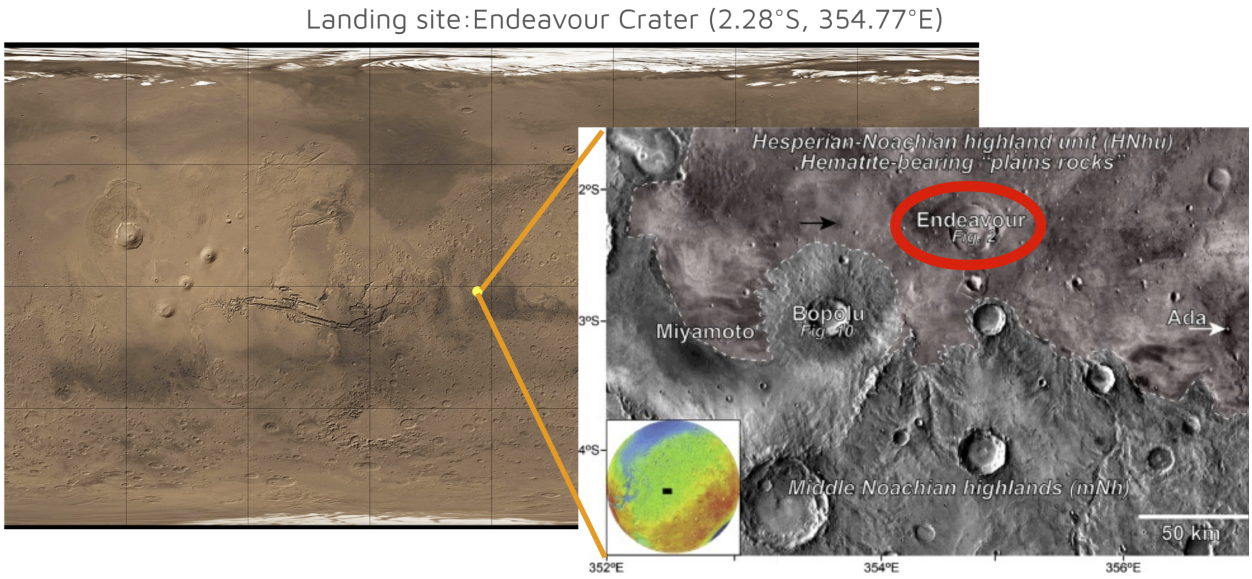

Figure 14.10: Landing site: Endeavor crater on mars surface

It should be noted that the current mission's landing method, a Skycrane has a landing accuracy within a 12-by-4 mile ellipse[122]. Due to the size of the landing zone, the TSMA will be aimed at the outside rim of the crater to ensure the landing does not occur in the crater depression (see figure 14.11) Additional, this landing site is almost directly on the equator (only 2.28°S) which decreases the necessary propellant by not having to do a plane change maneuver due to Deimos's circular orbit being aligned with Mars' equator.

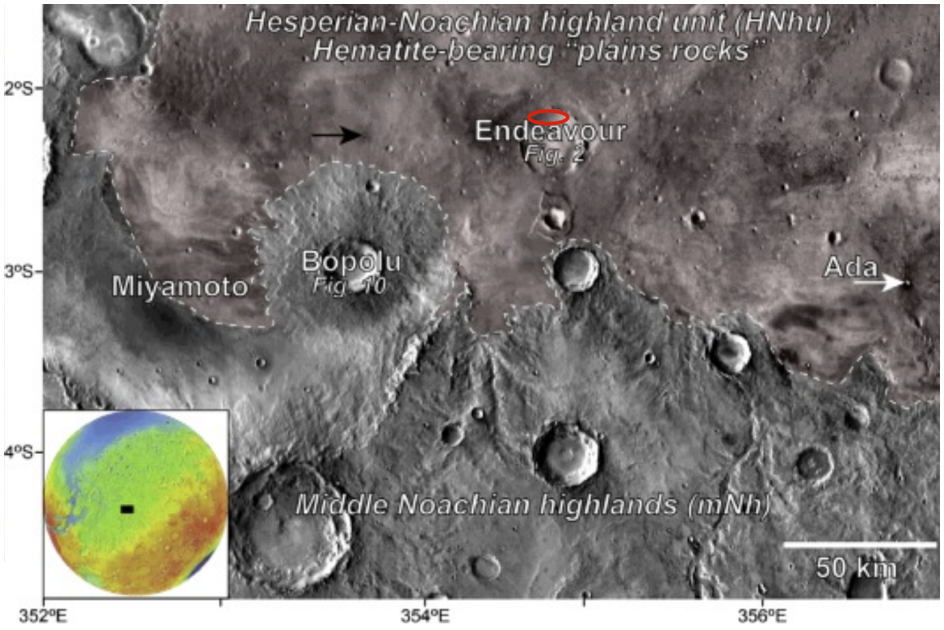

Figure 14.11: Landing site: Endeavor crater on mars surface

14.1.7 Rover

Mass and Dimensions The mass of the rover is estimated to be 700 kg. The rover can fit into the following rectangular profile in table 14.7 and can be seen in figure 14.12. Figure 14.12 also displays the stake compartments.

Length	Width	Height
2.5m	2m	.8m

Table 14.7: Minerva Dimensions

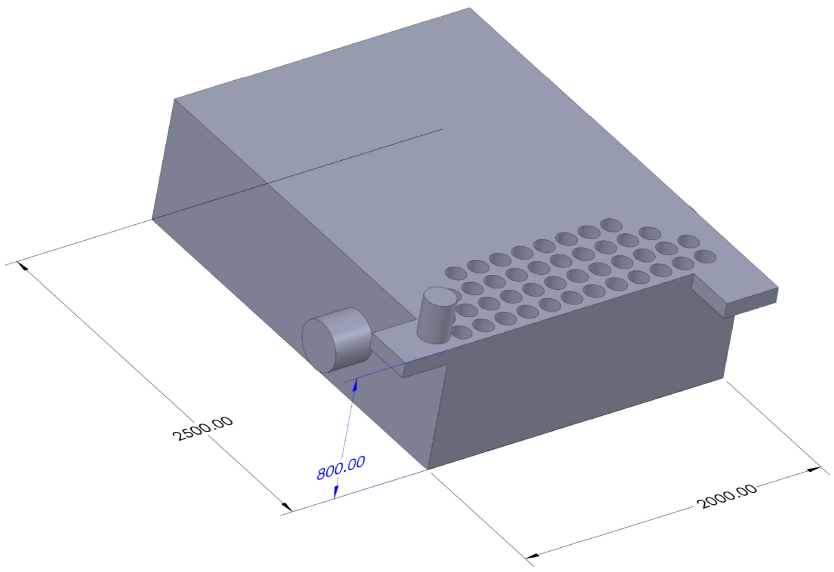

Figure 14.12: The dimensions of Minerva's main body

Power Power to the Minerva rover is provided by a set of 7 retractable solar panels, seen in Figure 14.13. The total area of the panel design is 8 m^2, providing a total power of 1.44 kWe assuming 30% efficiency. This is far greater than the power production of compatible rovers such as Curiosity and Perseverance, which both produce a steady stream of 110 watts using MMRTG. [123] Solar panel technology has the disadvantage of being both weather and environment dependent. This is offset by adding additional batteries with 100 kg of mass that is saved by removing the reactor. While the solar panels will produce more than enough power to run the rover and charge the batteries to full capacity during the day, the battery charge should be conserved during the night by not performing experiments. Performing experiments without solar contact has the potential to shut down locomotion capabilities. The reason for this is twofold, the first being the need to keep the rovers internals and instrument warm by powering additional heaters, as many rover components break below certain temperatures. The second is as a contingency in the event

that dust inhibits the solar panel's efficiency. The rover is responsible for the well being and maintenance of the stakes and is equipped to remove dust from the stake's solar panels. Hence, should the rover's own solar panels be inhibited by particulate, it is possible to remove enough dust to continue operation.

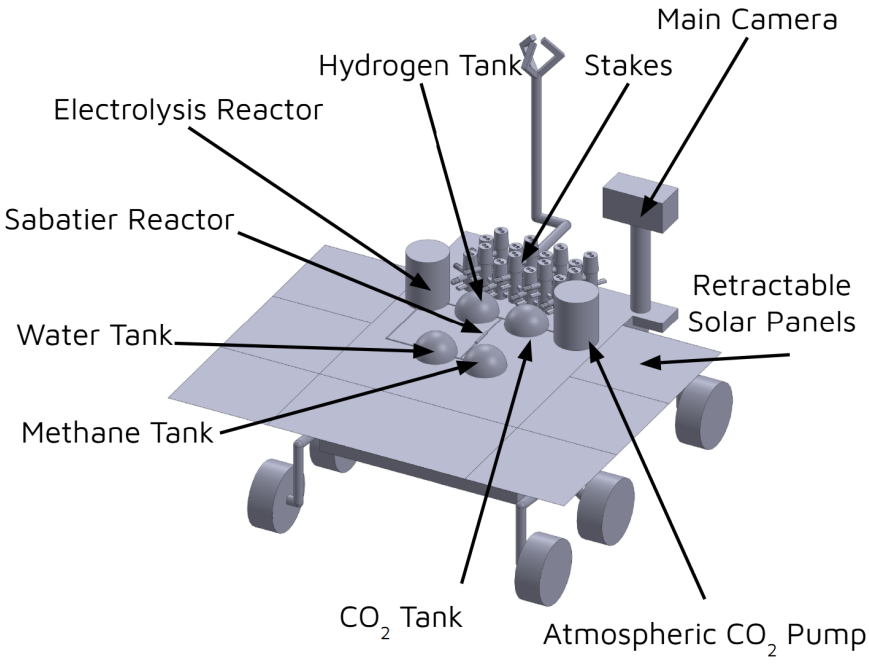

Figure 14.13: Minerva Rover: A possible layout of the rover components, leave extra room for additional instruments

Science Goals The science goals for this mission are obtained from a report that NASA's MEPAG published in 2018 [20]. Filtering the science requirements down by both priority and common instrumentation, a set of goals is obtained. These goals focus on long-term measurement of various atmospheric properties, aerosols, and behaviors over a wide-spread area. Included in the goals is the testing of the Sabatier process using CO2 harvested from the Martian atmosphere and water harvested from potential ice deposits; and measuring the composition of the local regolith. The full list of the goals is in the Table 14.8 below. The numerical codes refer to the Goal, Objective, Sub-objective, and Investigation of the goal in the source paper.

Science Goal	Investigation Codes
Atmospheric	II.A1.1, II.A1.2, II.A1.3, IV.A1.1 IV.A1.2, IV.B1.2, IV.B1.3
Sabatier	IV.B4.1, IV.D1.1, IV.D1.2, IV.D1.3
Composition	IV.B5.2, IV.B6.3., IV.B6.5

Table 14.8: Science Goal Investigation Codes [20]

Science Instruments The proposed Minerva rover carries multiple innovative and experimental technologies to meet its science goals. Focusing first on the atmospheric instruments, the proposed stakes are the main method of measurement. Each stake contains the following suite of TRL 8 and 9 instruments:

Measurables	Instruments	Power(Watts)	Size	Mass	Quantity
Surface pressure	MEDA PS	0.015	62×50×17 mm (without pipe)	40	x2
Wind speed and direction	MEDA WS	negligable	Length: 170 mm Diameter: 50 mm	305	x2
Temperature	MEDA ATS Thermocouples	negligable	0.075 diameter	negligable	x2
Humidity	MEDA HS	0.021	55 × 25 × 95 mm	45	x2
Dust and other aerosol, water vapor, carbon dioxide	EXOMARS Lidar	4	170 × 80 × 48 mm	450	x1

Table 14.9: Power Requirements, Mass, and Quantity of Technologies on Minerva Rover [21] [22]

All of the MEDA instruments already have flight heritage with the Perserverance Rover and the Phoenix Lidar was built for the ExoMars-2022 mission. All of these instruments are contained or attached to an aluminum stake, which contains solar panels and batteries for power. Additionally the MEDA PS, Lidar, and batteries require temperature control, so the design includes heaters. Table 14.10 contains the expected characteristics of these components. See Figure 14.14 below for the proposed layout of the stake assembly.

Component	Power(W)	Size	Mass(g)	Quantity
Estimated Heater	≈3.5	N/A	N/A	N/A
Estimated Battery	64 Wh	90.5x84.1x77	1400	x2
Solar Panels	15.8	30cm^2	135.21	x1
Aluminum Shell	N/A	Diameter 120 mm Height: 720 mm	1450	x1

Table 14.10: Expected Characteristics of Rover Components[21]

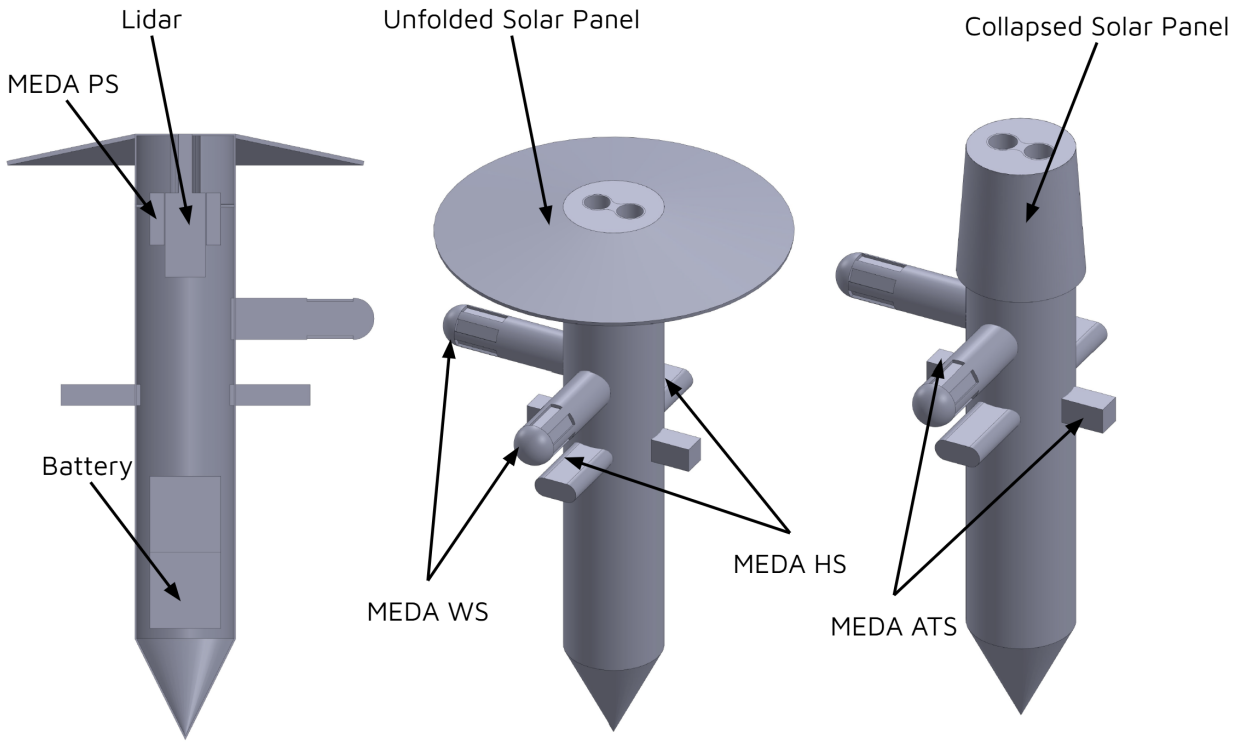

Figure 14.14: Minerva's Spears: A possible layout of the atmospheric science instruments and components

The goal of this design is that Minerva will carry 16 spears in its current configuration and place them in locations of interest, though depending on available mass the quantity can be increased. The goal of the Sabatier process is to harvest the Martian atmosphere and potential Martian water sources to create methane and water using a Sabatier reactor. The Minerva rover will navigate around the Endeavor Crater while harvesting the CO_2 from

the atmosphere using the pump in Figure 14.13. The rover is equipped with sufficient hydrogen in the hydrogen tanks in the event that Minerva does not find water sources on the surface of Mars. Additionally, Minerva will analyze the composition of the regolith surrounding the Endeavor Crater in greater depth than the operations completed by the Opportunity Rover. This assessment aims to prepare for a future human landing mission, as was discussed in Section 14.1.7

Operations The following figure 14.15 illustrates the operations the rover will perform on the Martian surface. The following image depicts a notional map of the locations where the crew can place the spears. Along the path, frequent measurements will be taken to evaluate the soil for volatiles and ice deposits. Minerva will also maintain constant contact with the spears to monitor for any complications that may arise with their operations. It is proposed to maintain the connection between the rover and the spears using Nokia cell chips recently used in the Intuitive Machines mission to the moon. The cell chips will treat the rover as their cell tower, transmitting all data and status updates to it for storage and transmission. The rover will transmit these readings to the IPV at its earliest capability.

Crew members can steer the rover from the IPV, allowing it to travel faster with greater accuracy than if it were autonomous. Humans are able to perform active avoidance, as opposed to the predictive avoidance necessary in previous rovers. Predictive avoidance is where the rover must fully scan, model, analyze, and pathfind its surroundings before performing movements, greatly slowing its progression. Humans can perform these maneuvers in real time using the onboard camera, though the rover is able to perform predictive avoidance when not operated by a crew member.

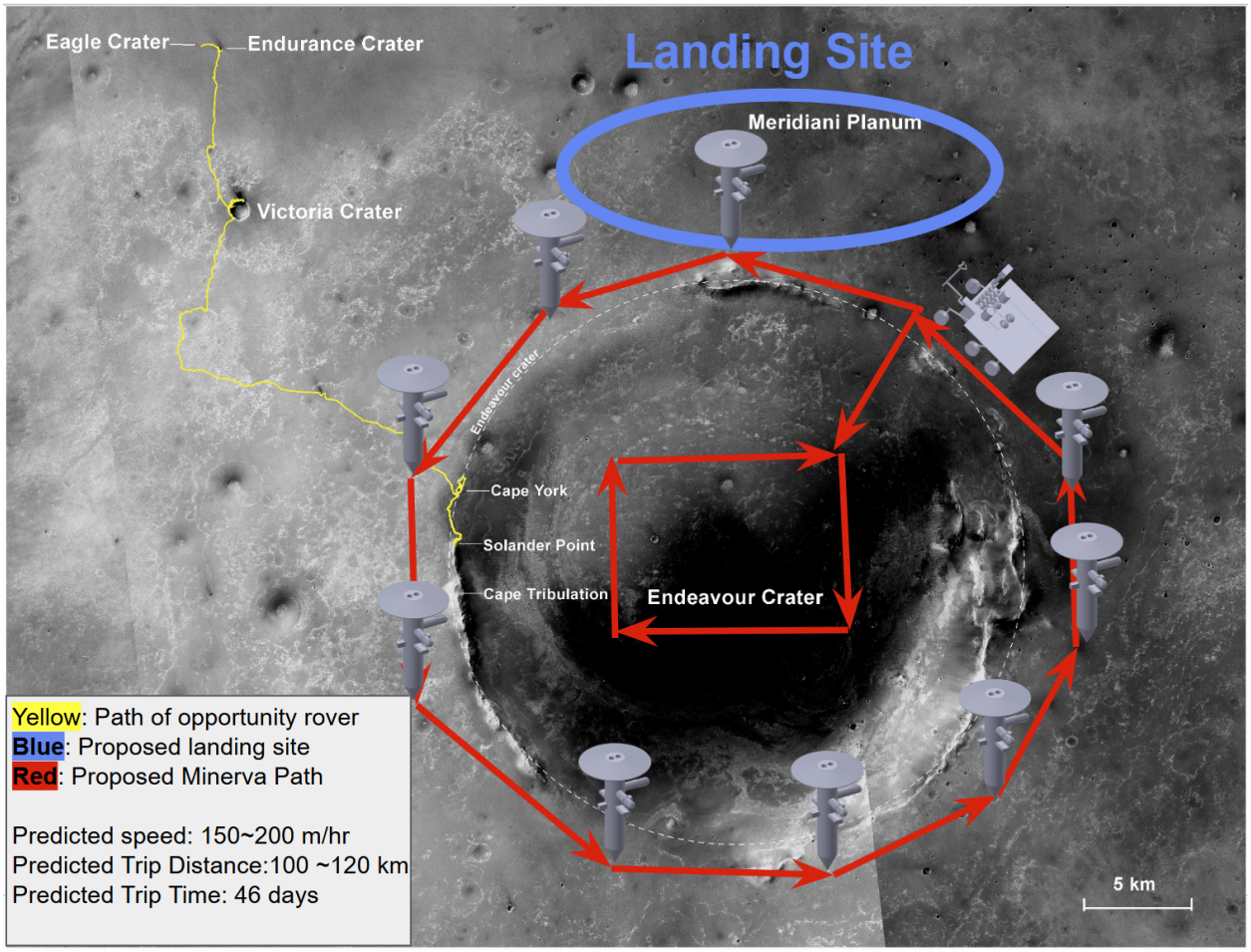

Figure 14.15: Minerva Rover: A possible layout of the rover components, leaving extra room for additional instruments

15 Deimos Science Plan

15.1 Block Diagram

Figure 15.1 outlines the purposes for which each of the science technologies being utilized while on Deimos serve.

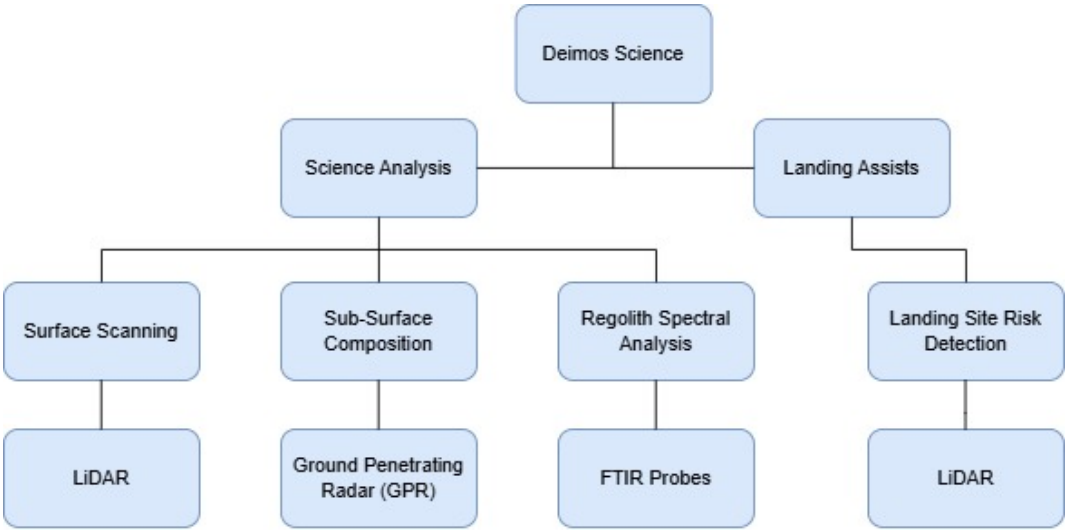

Figure 15.1: Deimos Science Functional Block Diagram

15.2 Deimos Science Goals

The primary goal of the DEV is to carry out scientific operations on Deimos to determine its origin: specifically, whether Deimos is a captured asteroid or a fragment of Mars. This objective guides the design of the science equipment and the on-surface operations of the DEV, which employ the use of advanced instrumentation and reliable maneuvering systems to support in-depth analysis of Deimos' surface and subsurface materials.

To accomplish these goals, a host of technologies will be used to ensure full analysis of each of the landing sites on Deimos incorporated in the mission. LiDAR scanning of the surface will determine the surface composition of the landing sites to ensure low risk surface impacts. Additionally, the landing sites contain craters which will allow for analysis on the age and force of impact of the craters. GPR will be used to explore the subsurface

of the regolith layer, shedding insight on its depth and composition. The composition of this layer is important for determining whether or not Deimos has the composition of an asteroid, or similar to the surface of Mars. Finally, FTIR spectroscopy will be implemented to ensure that a chemical composition analysis of the regolith can be taken. This composition can be compared to the samples taken on the surface of Mars, which will allow for identification of possible similarities. With the information taken through each of these technologies, a full picture of the origin of Deimos will be able to be put together. By determining whether or not the subsurface composition, chemical composition of the regolith, and surface composition are consistent with information from data compiled about Mars, a conclusion will be able to be drawn in regard to Deimos' relation to Mars.

15.3 Science Equipment and Capabilities

The first technology that will be implemented to conduct experiments on the surface of Deimos is LiDAR technology. LiDAR is a technology that implements light focused in a laser to measure distances to surfaces, gaining knowledge of the surface.[124] This knowledge is used to produce precise three dimensional information about the shape and contours of the composition of the surface that it is scanning. The rapid pulsing of the laser measures the time it takes for each pulse to return to the system, deriving the position of the surface from that information. The housing for the LiDAR system can be seen in Figure 15.2:

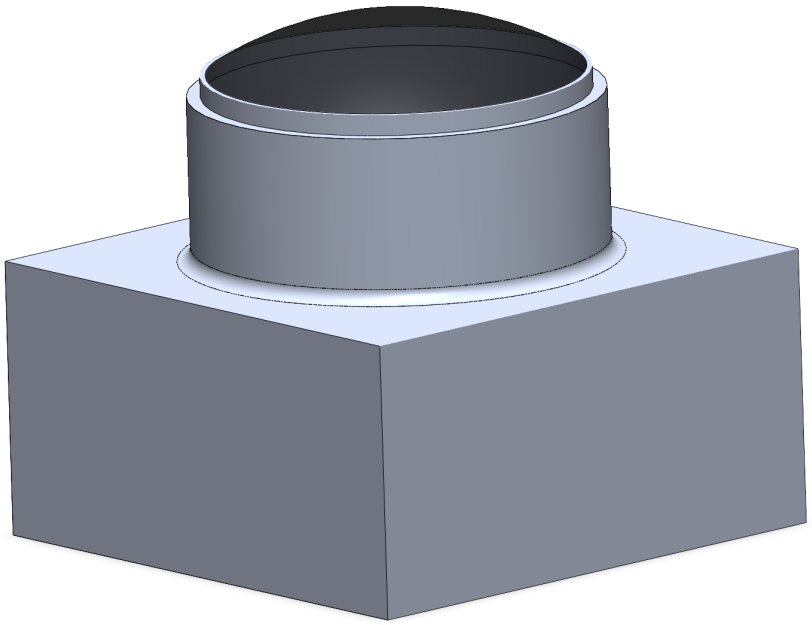

Figure 15.2: LiDAR Housing[12]

This housing will contain the LiDAR technology, which will aid in not just the gain in knowledge of Deimos' origin, but will also allow the DEV to have increased knowledge about the landing sites that will be used during the mission. The LiDAR system has a mass of 14 kg and a size of 20cm by 20cm by 15cm. This increased knowledge about the landing sites will be paramount in ensuring safe landing operations, decreasing the risk about potential damages caused by impact forces at landing. The LiDAR is mounted on the bottom of the DEV to ensure that it has the greatest range of operation in relation to the surface of Deimos, maximizing its efficiency and efficacy. The LiDAR system also has the capability of identifying potential risks with landing sites as it creates a detailed map of the surface, leading to a decrease in risk during landing operations.

The second technology that will be implemented to conduct experiments on the surface of Deimos is GPR. GPR is a geophysical method that uses radar pulses to image the subsurface, allowing the crew members to investigate the internal structure of Deimos's regolith layer by measuring the reflection of electromagnetic waves from different mate-

rials beneath the surface.[125] This data enables the identification of subsurface layers, buried objects, and changes in material composition, which are crucial for determining whether Deimos is a captured asteroid or originated from Mars. The housing for the GPR can be seen in Figure 15.3:

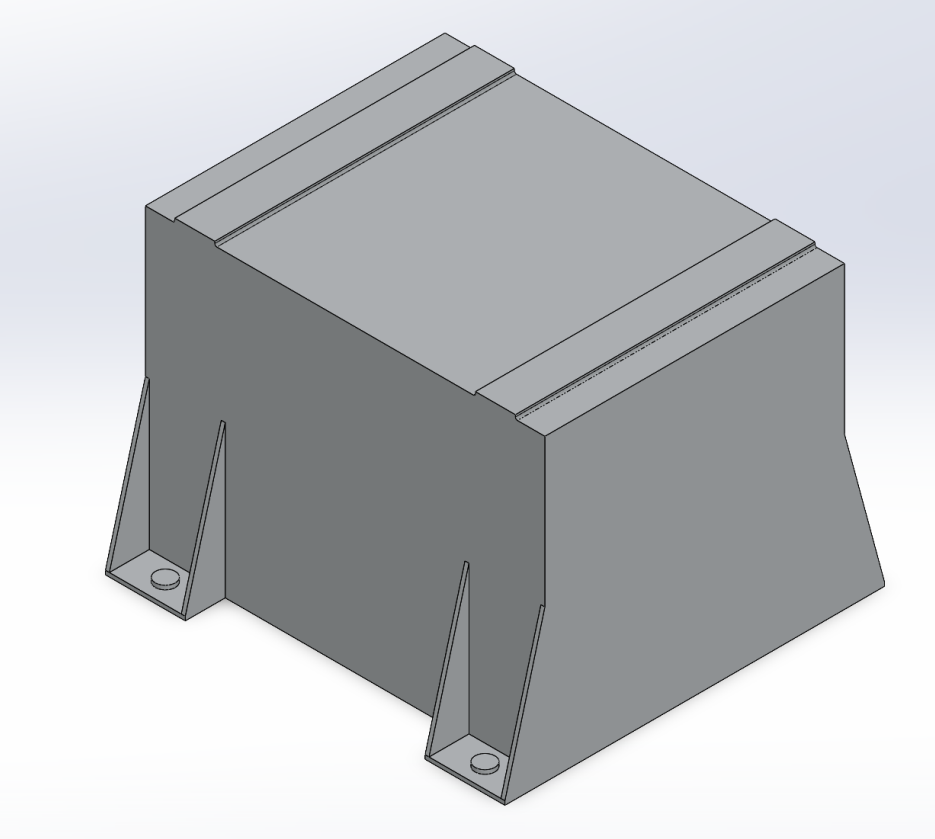

Figure 15.3: Ground Penetrating Radar[12]

The GPR system will be integrated into the DEV chassis to ensure stable contact with the surface and optimal signal penetration. The GPR has a mass of 10kg and a size of 20cm by 19cm by 8cm. It will work in tandem with LiDAR to provide a comprehensive understanding of Deimos' geological makeup, enhancing mission safety and science information collection. The GPR is mounted on the bottom of the DEV, to maximize its effective use time while operating near and on the surface of Deimos. The information gained by the GPR will be instrumental in determining the composition and depth of the regolith layer on Deimos, which is currently unknown and only speculative at this mo-

ment in time. Understanding the depth of the regolith layer and its overall composition across the multiple landing sites and trips will help to form a picture of how the regolith layer was formed and the origin of Deimos can be derived.

The third technology implemented to conduct scientific experiments on Deimos is FTIR. FTIR probes detect the infrared absorption spectra of materials, allowing for identification of molecular compositions.[126] This spectral data provides insights into the mineralogical makeup of the surface and near-surface materials on Deimos. The FTIR probes are integrated into each of the leg assemblies on the DEV, allowing for instantaneous composition analysis at each landing site. It will be especially useful in identifying hydrated minerals, organic compounds, or signatures of Martian crustal materials, which are the key indicators in identifying whether Deimos originated from Mars or is a captured asteroid. The FTIR probes can be seen in Figure 15.4:

Figure 15.4: FTIR Probe[12]

The FTIR probe will have wiring from the probe itself to the science station on the interior of the DEV via fiber optic cables to ensure the integrity of the data is not compromised during data transfer. The FTIR probe has a mass of 0.24kg and a size of 3cm by 3cm by

15cm. There is one probe per landing leg on the DEV, which yields a total of 4 FTIR probes. Total integration of FTIR data with LiDAR and GPR findings will yield a comprehensive understanding of Deimos' composition and history.

The DEV is designed to perform scientific operations on Deimos, with the primary goal of determining whether the moon is a captured asteroid or a fragment of Mars. To achieve this, the DEV is equipped with three advanced technologies: LiDAR, GPR, FTIR spectroscopy. The sum of the information gathered from these technologies offer a robust and integrated approach to characterizing Deimos' origin through the interpretation of the data gathered. This approach allows for complete spectral, surface, and subsurface analysis of Deimos without the need for physical samples, which would greatly increase the risk and likelihood of catastrophic failure during the mission. The implementation of these technologies on the DEV gathers all necessary information needed to determine the origin of Deimos without having to complete any complex and mission endangering maneuvers.

16 Trajectory Analysis

16.1 Hohmann Trajectory Analysis

To define the mission's orbital trajectories, a Hohmann Transfer analysis is performed. Following Reference [127], a series of calculations are used to obtain preliminary values for ΔV, I_{sp}, and propellant masses.

Using the distances between Earth and Mars and the Sun, as well as their orbital velocities about the Sun, the ΔV Requirements for each leg of the Hohmann transfer are defined.

$$V_{Earth} = \sqrt{\frac{\mu_{Sun}}{a_{Earth}}} \tag{16.1}$$

$$V_{Mars} = \sqrt{\frac{\mu_{Sun}}{a_{Mars}}} \tag{16.2}$$

$$\Delta V_1 = V_{Earth}(\sqrt{\frac{2a_{Mars}}{a_{Earth} + a_{Mars}}} - 1) \tag{16.3}$$

$$\Delta V_2 = V_{Mars}(1 - \sqrt{\frac{2a_{Earth}}{a_{Mars} + a_{Earth}}}) \tag{16.4}$$

$$\Delta V_{Hohmann} = \Delta V_1 + \Delta V_2 \tag{16.5}$$

$$t_{transfer} = \pi\sqrt{\frac{a_T^3}{\mu_{sun}}} \tag{16.6}$$

$$a_T = \frac{a_{Earth} + a_{Mars}}{2} \tag{16.7}$$

In addition to the transfer time and the waiting time, or the required time between Mars capture and departure burns, is calculated for the Hohmann transfer using Equations 16.6 and 16.8.

$$t_w = \frac{\alpha}{\pi} S \tag{16.8}$$

$$\frac{\alpha}{\pi} = (\frac{a_{Earth} + a_{Mars}}{2a_{Earth}})^{3/2} - 1 \tag{16.9}$$

$$S = \frac{T_{Earth} T_{Mars}}{T_{Mars} - T_{Earth}} \tag{16.10}$$

However, these ΔV values do not take into account the fact that the spacecraft will first need to exit Earth's sphere of influence before entering the first Hohmann transfer orbit, and similarly will need to exit Mars' sphere of influence before entering the second transfer.

To better define the ΔV requirements, the method of patched conics is used: hyperbolic trajectories are used to enter and exit Earth and Mars spheres of influence.

$$V_{LEO} = \sqrt{\frac{\mu_{Earth}}{R_{LEO}}} \tag{16.11}$$

$$V_{MPO} = \sqrt{\frac{\mu_{Mars}}{R_{MPO}}} \tag{16.12}$$

After the velocities at the starting and final orbit are defined, the V_∞ values for the hyperbolic trajectories are defined as the Hohmann transfer $\Delta V's$.

$$V_{\infty_{Earth}} = \Delta V_1 \tag{16.13}$$

$$V_{\infty_{M}ars} = \Delta V_2 \tag{16.14}$$

Using these values, the dimensions and eccentricities of both the hyperbolic departure and capture trajectories are calculated.

$$a_{hyp_{Earth}} = \sqrt{\frac{\mu_{Earth}}{\Delta V_1^2}} \tag{16.15}$$

$$a_{hyp_{Mars}} = \sqrt{\frac{\mu_{Mars}}{\Delta V_2^2}} \tag{16.16}$$

$$e_{hyp_{Earth}} = \frac{R_{LEO}}{a_{hyp_{Earth}}} \tag{16.17}$$

$$e_{hyp_{Mars}} = \frac{R_{MPO}}{a_{hyp_{Mars}}} \tag{16.18}$$

Finally, the hyperbolic velocities, and the total ΔV values for both departure and capture are calculated.

$$V_{hyp_{Earth}} = \sqrt{\frac{e_{hyp_{Earth}} + 1}{e_{hyp_{Earth}} - 1}} \Delta V_1 \tag{16.19}$$

$$V_{hyp_{Mars}} = \sqrt{\frac{e_{hyp_{Mars}} + 1}{e_{hyp_{Mars}} - 1}} \Delta V_2 \tag{16.20}$$

$$\Delta V_{Departure} = V_{hyp_{Earth}} - V_{LEO} \tag{16.21}$$

$$\Delta V_{Capture} = V_{hyp_{Mars}} - V_{MPO} \tag{16.22}$$

A simultaneous plane change with escape and departure is considered for all burns which involve an inclination change. Equation (16.23) expresses how the simultaneous plane change ΔV is solved for.

$$\Delta V_{simul} = \sqrt{V_{LEO}^2 + V_{hyp_{Earth}}^2 + 2V_{LEO}V_{hyp_{Earth}} \cos(\phi)} \tag{16.23}$$

Table 16.1 shows the angles of the launch orbit and angles relative to the ecliptic. The angles denote the angle of one plane relative to the other.

Plane Rel Plane	Angles (°)
Earth tilt rel Ecliptic	23.4
KSC Launch rel Equator	28.6
Mars tilt rel Ecliptic	25.2
Mars orbit rel Ecliptic	1.85
KSC launch rel Ecliptic	5.2
KSC launch rel Mars orbit, ϕ	3.35

Table 16.1: Simultaneous Plane Change Angles

A plane change is required for Earth departure, Mars capture, and Mars departure.

For an impulsive burn the ΔV with plane change for Mars departure and capture are equal, and can be labeled as simply ΔV_{Mars}. Therefore, the total ΔV for impulsive burns is calculated.

$$\Delta V_{Total} = \Delta V_{EarthDeparture} + \Delta V_{EarthCapture} + 2\Delta V_{Mars} \tag{16.24}$$

Variable	Value	Units
Total Hohmann ΔV	11.22	km/s
Single Leg Transfer Time	259	days
Waiting Time	454	days
Total Mission Duration	972	days
Earth DepartureΔV with Plane Change	3.61	km/s
Earth Capture ΔV without Plane Change	3.57	km/s
Mars ΔV with Plane Change	2.13	km/s
Total ΔV with Plane Changes	11.44	km/s

Table 16.2: Impulsive Orbital Trajectory Values.

As seen in Table 16.2, the Hohmann transfer ΔV requirement is lower than the requirement when taking into account plane changes and patched conics. However, this analysis still assumes impulsive, or instantaneous, burns, and can be refined further with a finite burn analysis.

16.2 IPV Finite Burn Analysis

A finite burn model is considered in order to improve the accuracy of the ΔV estimate for the mission. The relatively low thrust of the nuclear engine leads to the consideration of non-impulsive burns. Following Reference [128], the first-order vector equations of the motion are integrated over the thrusting period of the IPV.

The dimensionless parameters below are introduced:

$$r(\tau) = \frac{R(t)}{R_{ref}} \tag{16.25}$$

$$v(\tau) = \frac{R(t)}{V_{c,ref}} \tag{16.26}$$

$$\tau = \frac{V_{c,ref}}{\mu/R_{ref}^2} t \tag{16.27}$$

$$g = \frac{1}{r^2} \tag{16.28}$$

$$v_j = \frac{g_0 I}{V_{c,ref}} \tag{16.29}$$

$$v_\infty^2 = (\frac{v_\infty}{V_{c,ref}})^2 \tag{16.30}$$

The dimensionless equations of motion are then written as Equations 16.31 to 16.34.

$$r(\tau) = v \sin\alpha \tag{16.31}$$

$$v(\tau) = a\cos u - \frac{\sin\alpha}{r^2} \tag{16.32}$$

$$\alpha(\tau) = \frac{a\sin u}{v} + (v^2 - \frac{1}{r})\frac{\cos\alpha}{rv} \tag{16.33}$$

$$\theta(\tau) = \frac{v}{r}\cos\alpha \tag{16.34}$$

It is assumed that the vehicle operates with constant thrust and jet velocity, v_j, thus the acceleration $a(\tau)$ is given by Equation (16.35) for an escape maneuver during the burning

period, where

$$a(\tau)_{esc} = \frac{a_{po}}{1 - a_{po}\tau/v_j} \tag{16.35}$$

a_{po} is the initial acceleration at the power on point. For capture burns, Equation (16.36) gives the acceleration during the burning period. The equations of motion are integrated backwards in time during the capture burns.

$$a(\tau)_{capture} = \frac{a_{bo}}{1 + a_{bo}\tau/v_j} \tag{16.36}$$

a_{bo} is the acceleration of the vehicle at the burn out point.

Four boundary conditions are specified in order to numerically integrate the equations of motion. In the analysis, $\tau = 0$ is considered to be the power on point. The vehicle starts its escape burns in a circular orbit. Thus, the initial conditions are simply

$$r(0) = 1 \tag{16.37}$$

$$v(0) = 1 \tag{16.38}$$

$$\alpha(0) = 0 \tag{16.39}$$

$$\theta(0) = 0 \tag{16.40}$$

With known initial conditions and a known form for the steering of the vehicle, the equations of motion can be integrated. For the analysis, MATLAB's ode45 function is used to numerically integrate with the specified set of initial conditions above. After numerical integration, r, v, α, and θ are obtained as functions of τ, dimensionless time. The analysis steps through dimensionless time values until the desired characteristic energy is reached. The dimensionless characteristic energy is written as

$$v_\infty^2(\tau_{bo}) = v^2(\tau_{bo}) - \frac{2}{r(\tau_{bo})} \tag{16.41}$$

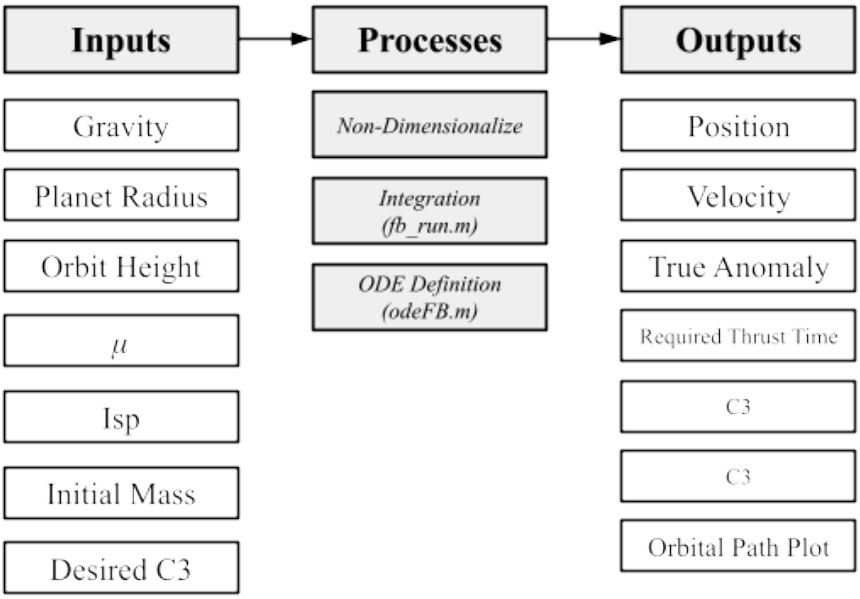

Figure 16.1: Finite Burn MATLAB Program Flow Diagram

The analysis makes several key assumptions to simplify the procedure. First, the IPV burns for Mars capture and escape are considered to be impulsive due to the high orbital period of 30 hours relative to the burn time of minutes. The Earth capture and escape burns cannot be considered impulsive due to the low orbital period of approximately 90 minutes compared to the burn time. Second, tangential steering was considered ($u = 0$). Third, the Earth capture burn analysis is performed with circular orbit initial conditions and is considered to have an identical desired characteristic energy requirement, v_∞^2.

The MATLAB code is attached in Appendix C.1 and outputs orbital trajectory plots, escape energy, and required burning time.

Figure 16.1 shows the inputs, outputs, and process flow of the MATLAB program.

Figures 16.2 and 16.3 show the orbital trajectory plots and dimensional burn time of the Earth Capture and Earth Departure Burns.

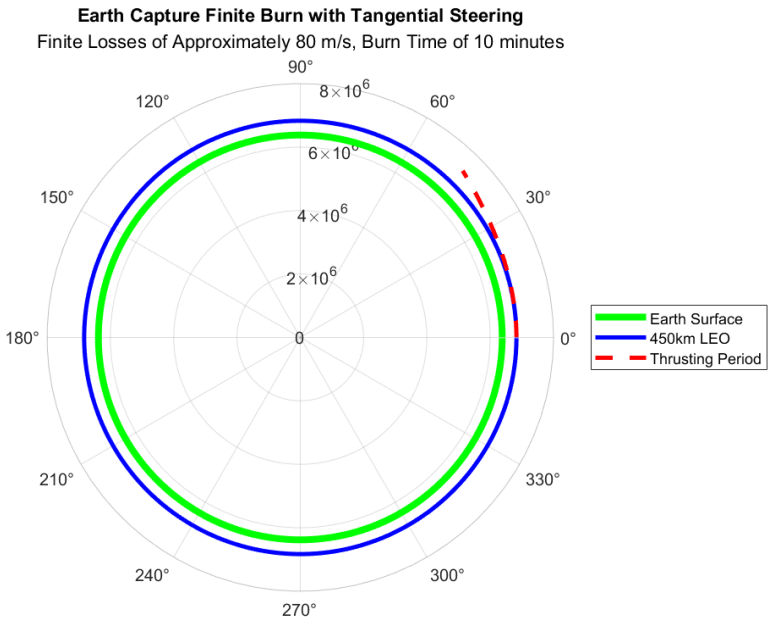

Figure 16.2: Finite Burn Orbital Trajectory Plot, Earth Capture

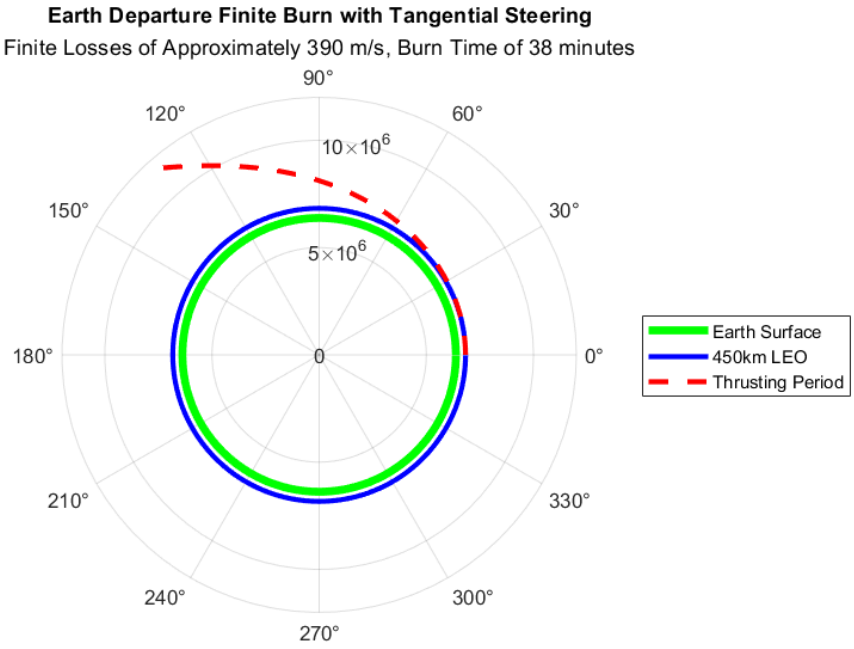

Figure 16.3: Finite Burn Orbital Trajectory Plot, Earth Departure

16.3 Total ΔV Budget

Using the finite loss numbers from the previous section and adding them to the impulsive burn ΔV budget, the final ΔV budget for the mission is obtained.

Burn	Value	Units
Earth Departure ΔV	3.82	km/s
Mars Capture ΔV	2.13	km/s
Mars Departure ΔV	2.13	km/s
Earth Capture ΔV	3.78	km/s
Total Finite ΔV	11.86	km/s

Table 16.3: Total Finite ΔV Budget.

16.4 Total Mission Mass Ratio Calculations

Using the calculated ΔV values, a total mission mass ratio is calculated.

$$V_{eq} = g_0 Isp \tag{16.42}$$

For this analysis, it is assumed that $V_e = V_{eq}$.

$$\Delta V = V_e ln(\frac{m_0}{m_f}) \tag{16.43}$$

The values for I_{sp} and initial mass are varied until the desired final mass, or dry mass on return, is obtained. The rationale behind the selections for each of these values can be found in Section 7.1.

16.5 DEV Maneuvering Analysis

16.5.1 Overview

The DEV must maneuver between the IPV and Deimos twice, back and forth. The DEV will need to rotate and maneuver through space as well as maneuvering around on

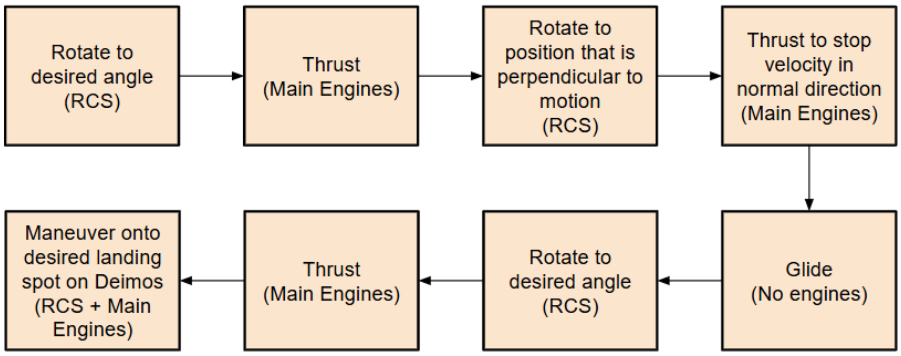

Figure 16.4: DEV Deimos Maneuvering Simple Flow Chart

the surface of Deimos. In order to do so, the DEV uses two engine systems: two MDEs and 16 RCS thrusters. The MDE's responsibility is to transport the DEV between the IPV and Deimos. The RCS thrusters are for smaller maneuvers that either require rotation or quick adjustments. Due to their larger thrust, the RCS thrusters will also be relied on for maneuver around the surface of Deimos.

16.5.2 Transport between IPV and Deimos

In order for the DEV to reach Deimos, it must increase its velocity by changing its orbit radius about Mars. The orbit radius that the IPV remains in while parked in Mar's orbit is the same as Deimos's: 23460km. Since the IPV is parked 100km away from Deimos, the orbit radius change is minimal. The orbit radius change was determined by optimizing both time and ΔV during the transfer. A small angular rotation was also considered, between about 5° to 15° which is typical according to CWRU's Dr. Paul Barnhart.

Before beginning the analysis, the path and rotations in which the DEV follows must be determined. A flow chart is seen in Figure 16.4 to lay out the transfer between the IPV and Deimos. The progress shown in the chart occurs after detaching from the IPV and before landing on Mars. It provides a better understanding of what calculations will be needed in order for a successful execution of the flight.

A visual of the desired flight path is seen in Figure 16.5.

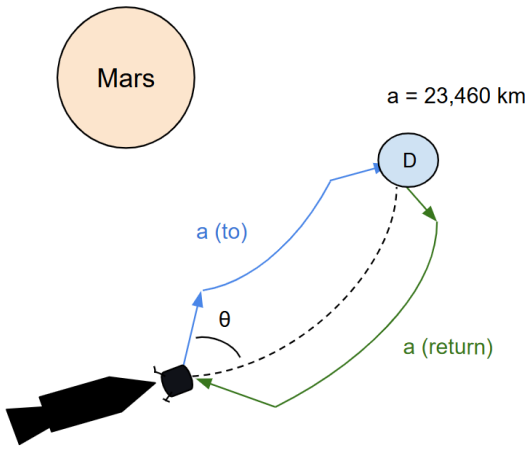

Figure 16.5: DEV Maneuvering (Not to Scale)

Since the IPV is parked about 100km away from Deimos, the maximum change in orbit radius should be less than that value. Otherwise, it would be excessive and require more ΔV than needed. The orbits that resulted in the most optimal travel included 23410km and 23510km, one to speed up the DEV and one to slow down the DEV, respectively. For consistency in velocity and time, orbits are both 50km away from Deimos's, one closer to mars and one further. This was determined by calculating the orbital velocity.

$$v = \sqrt{\frac{\mu_{mars}}{a}} \tag{16.44}$$

$$\mu_{mars} = GM_{mars} \tag{16.45}$$

Where a is the orbit radius. Using Equations 16.44 and 16.45 as well as the chosen values for the orbit radius, the orbital velocities are $1.353\frac{m}{s}$ and $1.350\frac{m}{s}$, respectively. Since Deimos has an orbit velocity of $1.351\frac{m}{s}$, the relative velocities for these orbits in reference to Deimos's are $1.442\frac{m}{s}$ and $-1.438\frac{m}{s}$.

In order to get to the lower or higher orbit about Mars, the DEV must have a normal velocity included in its propulsion maneuvering. This value is changed to optimize the

ΔV and so that the DEV can spend a significant amount of time in faster or slower orbit. The resulting value for this variable is $0.40\frac{m}{s}$ for both transfers with only difference being in which direction the DEV is moving making the value positive or negative. In order to get the total ΔV for the first burn, the magnitude of the burns must be found.

$$V_{magnitude} = \sqrt{V_{normal}^2 + V_{tangent}^2} \tag{16.46}$$

This value is found using Equation 16.46 where V_{normal} is the normal velocity and $V_{tangent}$ is the tangent velocity with respect to the orbit, also referred to as the relative velocity. The values for this are seen in Table 16.4.

Variable	IPV to Deimos	Deimos to IPV	Units
$V_{tangent}$	1.442	-1.438	$\frac{m}{s}$
V_{normal}	0.400	0.400	$\frac{m}{s}$
$V_{magnitude}$	1.497	1.492	$\frac{m}{s}$

Table 16.4: Velocity triangle for first burn in orbit transfer

Once the DEV has reached its travel orbit, it must burn again to stop its velocity in the normal direction. This ΔV is equal but opposite in magnitude to the first burn's normal ΔV $0.400\frac{m}{s}$. By the time the DEV has reached the new orbit, it will spend about 3.638 km in the lower orbit or 3.660 km in the upper orbit. Most of the time it will be spend making its way to the new orbit or returning to Deimos/IPV's orbit. The travel distance for the DEV is broken down in Table 16.5.

Variable	IPV to Deimos	Deimos to IPV	Units
Tangential distance traveled before getting to new orbit	48.181	48.170	km
Distance traveled in new orbit	3.638	3.660	km
Tangential distance traveled before getting to original orbit	48.181	48.170	km

Table 16.5: Transfer distance broken down

Due to the small angle and the desire to increase the speed to minimize the total transfer time, the DEV spends less than 4km in the new orbit and the rest of the time moving between orbits. The total time break down is seen in Table 16.6

Variable	IPV to Deimos	Deimos to IPV	Units
Time to new orbit	9.28	9.30	hours
Time spent traveling in new orbit	0.71	0.70	hours
Time to original orbit	9.28	9.30	hours
Total travel time	19.26	19.32	hours

Table 16.6: Transfer time broken down

These values were determined using simple physics relations between velocity, distance, and time. This relationship can be determined using Equation 16.47.

$$d = \frac{1}{2}a_0t^2 + v_0t + d_0 \tag{16.47}$$

Where d is the distance traveled, a_0 is the initial acceleration, v_0 is the initial velocity, and d_0 is the initial distance. Since these calculations assume an impulse burn, at $d_0 = 0$ the DEV has already accelerated and is maintaining a steady velocity of v_0. This simplifies Equation 16.47 to Equation 16.48.

$$d = V_0t \tag{16.48}$$

In order to solve for t, Equation 16.48 is rearranged so that t is in terms of d and v_0. The relative velocities from Table 16.4 are plugged into Equation 16.48 for v_0 as well as the total distance of 100 km for both cases. This resulted in the total transfer time being 19.26 hours from the IPV to Deimos, and the returning trip, from Deimos to IPV, being 19.32 hours. Since the crew will be there 135 days at a time, spending almost a full day in transit is small enough that it will count towards the total required time spent on Deimos. The total propellant needed for these transfers are is listed in Table 16.7.

Variable	Value	Units
$m_{N_2O_4}$	5.80	kg
m_{mmh}	3.62	kg
m_{total}	9.42	kg

Table 16.7: Transfer time broken down

The total propellant mass needed for a single transfer between Deimos and the IPV for all trips is 39.55kg, with a 5% margin.

The rotations must also be determined when transporting from the IPV to Deimos and back. As seen in the flow chart in Figure 16.4, in order to get into the correction position for firing the MDEs, the RCS must fire to rotate the DEV. Table 16.8 displays the values for these rotations.

Variable	Angle (°)	time (s)	mass (kg)
$Rotation\#1$ (to Deimos)	15.50	6.96	0.87
$Rotation\#2$ (to Deimos)	105.50	18.16	2.26
$Rotation\#3$ (to Deimos)	15.50	6.96	0.87
$Rotation\#1$ (to IPV)	15.50	6.97	0.87
$Rotation\#2$ (to IPV)	105.5	18.16	2.26
$Rotation\#3$ (to IPV)	15.5	6.97	0.87

Table 16.8: Transfer time broken down

The resulting total propellant mass for all trips with a 5% margin is 29.88kg. In order for these values to be calculated, Equations 16.49 to 16.52 are implemented.

$$I_{zz} = \frac{1}{2}MR^2 \tag{16.49}$$

$$I_{yy} = I_{xx} = \frac{1}{4}MR^2 + \frac{1}{12}ML^2 \tag{16.50}$$

$$\tau = I\alpha \tag{16.51}$$

$$\tau = r \times F_{thrust} \tag{16.52}$$

The moments of inertia of the DEV and other values can be found in Table 16.9

The resulting angular accelerations are used to find determine the timing in Table 16.8 using the following equation:

Variable	Value	Unites
I_{xx}	9.31×10^4	kgm^2
I_{yy}	9.31×10^4	kgm^2
I_{zz}	9.61×10^4	kgm^2
α (x and y)	0.011	$\frac{rad}{s^2}$
α (z)	0.006	$\frac{rad}{s^2}$
a	0.010	$\frac{m}{s^2}$

Table 16.9: Rotation variables for DEV

$$\theta = \frac{1}{2}\alpha_0 t^2 + \omega_0 t + \theta_0 \tag{16.53}$$

16.5.3 Deimos Surface Maneuvering

In order to acquire a large range of data for science collection, the DEV will be moving around the surface of Deimos. The movements will range from moving from flat spot to flat spot to moving from a flat spot to inside of a deep crater. For these maneuvers, a system is developed to determine the amount of propellant needed. Due to wanting to minimize risks, only a few surface maneuvers will involve craters. Since most maneuvers will be done on flatter patches of ground, a simple process is developed. Figure 16.6 presents a visual for a simple surface maneuver between two spots across flat ground.

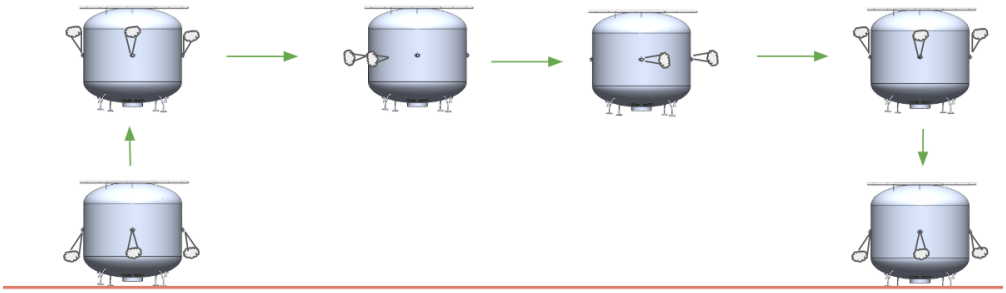

Figure 16.6: Deimos surface simple maneuver (Not to Scale)

For the DEV to move sideways, it must thrust upward, thrust again to stop moving, then it can thrust to move linearly. All maneuvers will use the RCS thruster since these movements require more accurate thrusts than the main engines can provide. Assuming

a mass flow rate of 53.42g/s and only two RCS thrusting at a time, a total thrust of 400N, Table 16.10 shows an average maneuver on the surface of Deimos.

Variable	Distance (m)	Burn time (s)	Δv (m/s)
Up	20	20	0.2
Stop	20	20	0.2
Move	20	30	0.2
Stop	20	30	0.2
Down	20	20	0.2
Stop	20	20	0.2

Table 16.10: Deimos Surface Maneuvering Transfer Times

A total of 17.41kg of propellant is used for this maneuver. For a total of 10 maneuvers, one about every two weeks, and a margin of 5%, the total mass needed is 731.19kg. This shows that the majority of the propellant will result from activities on the surface on Deimos and not from the transit between Deimos and the IPV.

16.6 TMSA Trajectory

The TMSA will be ejected shortly after the Earth departure burn. The sooner the ejection of the TMSA from the IPV, the less ΔV is required. Calculations of a Hohmann transfer from Deimos orbit to the martian calculations produce a Δ V of 0.67km/s while a course correction closer to Earth significantly reduces this value. The ΔV requirements are exceptionally low for a large window of time after Earth departure. The geometry of the Martian entry from a Hohmann transfer is provided in Figure 16.7. The entry altitude is 160km with an entry angle of 15°.

Preliminary trajectory calculations for the ΔV for the TMSA capsule were performed using Hohmann transfer Equation 16.54.

$$\Delta V_{TMSA} = V_{Earth}(\sqrt{\frac{2a_{mars_{intercept}}}{a_{mars_{intercept}}} + a_1} - 1) \tag{16.54}$$

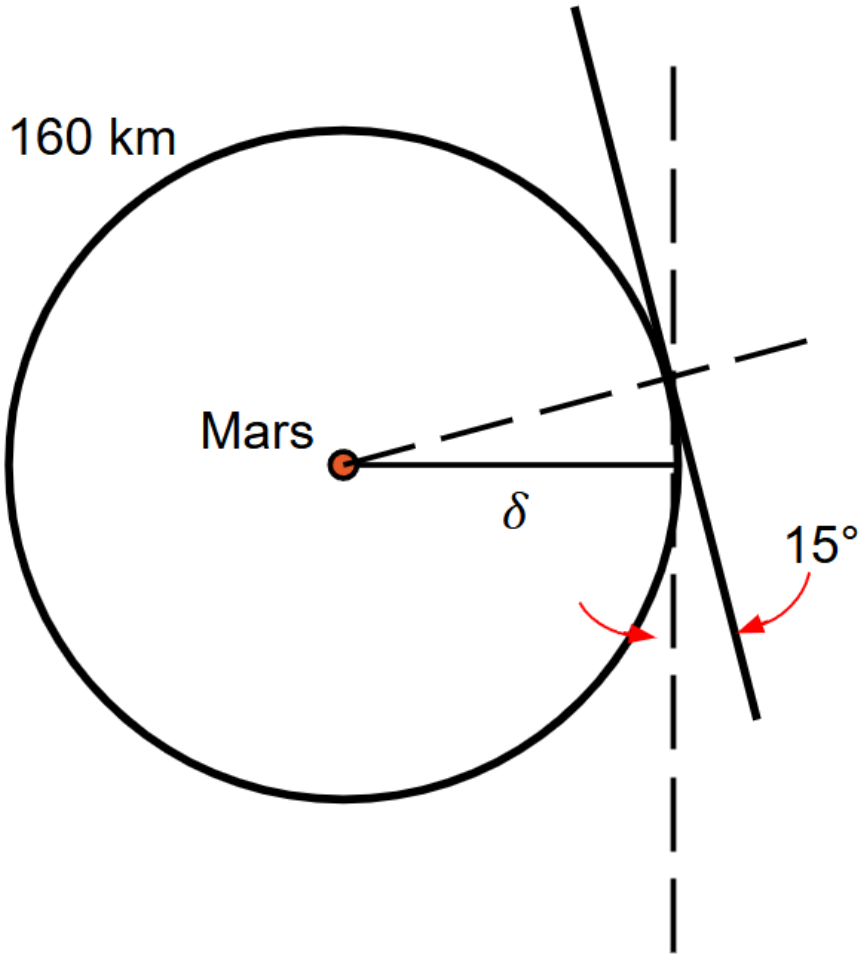

Figure 16.7: Martian Entry

where:

$$a_{mars_{intercept}} = 1.52 + \delta \tag{16.55}$$

$$\delta = h_{entry} \sin(90 - \theta_E) \tag{16.56}$$

Since the TMSA will be ejected shortly after the Earth Departure burn, the ΔV that the TMSA's own propulsive elements will need to provide can be calculated by taking the difference of the ΔV of the Hohmann burns.

$$\Delta V_{TMSA_{Burn}} = \Delta V_{TMSA} - \Delta V_{IPV} \tag{16.57}$$

The resultant burn needs to produce a Δ V = 1m/s. This value is easily manageable from RCS thrusters and requires the minimum amount of propellant. Deviations from this preliminary analysis and orbital corrections for precision are within margins.

17 Conclusion

17.1 Requirements Compliance

X.	X.X	Req Short	Requirement(s)	Final Value	Compliance (Exceed, Meets, Fails)
I-0	0	Dry Mass	The assembled vehicle shall have a maximum dry mass of 241 mT before LEO departure	212.2mT	Exceeds *changed to comply with 6 SLS launches
0	0.1	Launch Date	The mission shall launch no later than October 2041. The optimal launch window is October 19 2041. The mission shall return no later than December 31, 2044	Depart on October 19 Return on June 17	Meets
0	0.2	Mission Duration	The total mission duration shall be maximum 972 days.	972 days	Meets
0	0.3	Max Diameter	The payload shall fit within a 12-meter diameter shroud.	Compliant with 12m shroud. Max payload diameter of 11m.	Meets
0	0.3	Wet Mass	The assembled interplanetary vehicle shall have a maximum fully fueled mass of 750mT	720.5mT (margin not included)	Exceeds
0	0.3	SLS Payload Capacity	For each payload launch, the payload shall launch to Low Earth Orbit (LEO) using a 150-mT payload launch vehicle	Max payload mass 148.3mT	Meets
I-1	1.1	IPV Habitation	The IPV habitation will have a minimum 170 m of net habitable volume.	172m^3	Meets
D-1	1.1	DEV Volume	The Deimos habitat shall have a minimum of 60 m^3 of net habitable volume (30m3/CM).	62.05 m^3	Meets
I-2	2.1	O2 / N2	The interplanetary vehicle must carry 1.77mT of N2, 6.92mT of O2.	1.77mT N2, 6.92mT O2	Meets
I-2	2.2	Water Mass	The interplanetary vehicle must carry 9.23 mT of consumable water.	9.23mT consumable water	Meets
I-2	2.3	Food	The interplanetary vehicle must carry 6.22mT of food.	6.22mT food	Meets
I-3	3.1	IPV Power Peak	The interplanetary vehicle must have a power supply capable of producing a minimum peak of 25.1 kWe	25.2	Exceeds
D-3	3.1	DEV Power Peak	The DEV must have a power supply capapable of producing a minimum of 20.8 kWe (peak)	21 kW	Exceeds
I-3	3.2	IPV Power Nominal	The interplanetary vehicle must have a power supply capable of producing a minimum nominal power of 16.1 kWe	25.2 kWe	Exceeds
D-3	3.2	DEV Power Nominal	The DEV must have a power supply capable of producing a minimum of 15.8 kWe (nominal)	21 kW	Exceeds

X.	X.X	Req Short	Requirement(s)	Final Value	Compliance (Exceed, Meets, Fails)
I-6	6.1	Mission Total	The interplanetary vehicle should have a minimum total deltaV of 11.84 km/s	11.84km/s	Meets
I-4	4.2.1	Career Radiation Dose	An individual astronaut's total effective radiation dose due to space flight radiation exposure shall be less than 1.3mSv/day across the entire mission	1.3mSv/day (with shielding)	Meets
I-4	4.3.1	Micrometeoroid Impacts	Spacecraft shall be able to withstand all potential unavoidable obsticals during space travel, including micrometeorites traveling up to 10 km/s.	Up to 10.5 km/s normal to shield	Exceeds
I-5	5.2.2	Factor of Safety	All structures shall have a minimum factor of safety of 1.5.	1.5	Meets
I-6	6.3.3	IPV Engine Thrust	The IPV Engines shall have a thrust level of 351kN per Nuclear Thermal engine.	354kN	Exceeds
I-6	6.3.4	IPV Engine Isp	The interplanetary vehicle shall use a propulsion system with minimum 850s and maximum 950s	951s	Exceeds
D	D-0	Lander Mass	The Deimos lander (without systems or supplies) shall be a maximum of 15 mT.	20.5mT	Fails *still compliant with overall mass budget, non mission critical
M-1	M-1.1	Mass Budget for TMSA's	The total mass of all Tele-operating Mars Surface Assets (TMSAs) shall not exceed a maximum of 4 MT	4mT	Meets
M-2	M-2.1	Power Budget for TMSA's	The total continous power usage of all Tele-operating Mars Surface Assets (TMSAs) shall not exceed 3 kWe	1.7kWe	Exceeds

17.2 Project Conclusion

Given a 20-year period beginning in 2025, a crewed mission to Deimos, one of Mars' moons, is designed for the purpose of tele-operating Mars surface assets and studying the origins of Deimos. The mission, departing no later than October 21, 2041 carries four crew members to Deimos' orbit. In two rotations lasting 135 days, two crew members descend to the surface of Deimos while the other two crew trail Deimos in orbit around Mars. The estimated cost for this mission is $329 Billion, which includes the infrastructure update cost, technology research and development, and design and testing funding. The entire mission will take 972 days: approximately 258 days of travel to Mars, 454 days in Mars orbit, and 258 days of travel back to Earth for return on July 17, 2044. The mission utilizes 6 launches of an extended, 150-mT class of SLS heavy lift vehicle to launch all payloads into a 400km LEO staging orbit. The mission architecture utilizes a high performance solid core nuclear thermal propulsion system, bimodal power generation, next generation lightweight hybrid composite LH_2 tanks, as well as compact fission micro-reactors in order to maximize the mass efficiency of the architecture. Through development of these next generation technology, this crewed mission to Deimos allows for the possibility of future crewed Mars exploration missions.

17.3 Future Work

Moving forward with the design process, work will be done in the detailed design phase. This entails extensive data acquisition through the means of more in-depth research. The orbital trajectory analysis can be further refined. In its current state, the mission analysis assumes perfectly circular Earth and Mars orbits about the Sun, when in reality both are slightly elliptical in nature. Lambert's method can be used to further refine the orbital analysis and obtain a more accurate value for total ΔV. Furthermore, component specifications must be finalized. This includes finalizing the materials and dimensions of each subsystem. The subsystems will have more thorough technical cal-

culations to ensure the mission requirements are met. A more detailed CAD model will be created, along with using finite element analysis to obtain more information about the behavior of components within the overall system, and how the system reacts to different environments before experimental tests are performed. Once all technical details are established, the team will then create physical prototypes of the systems to collect empirical data from testing.

18 Project Management Plan

18.1 Team Organization

SRR Phase Team Structure Over the course of the project, the team utilized three main different organizational structures to effectively leverage personnel. In the Systems Requirement Phase, the team employed a very flat organizational structure with an emphasis on collaboration and group problem solving. The majority of the work was completed in a group setting as the initial mission had to become more defined. The systems engineer outlined the path forward by creating a loose weekly agenda based on the guide of the instructor, Professor Barnhart, in order to emphasize priorities for the coming week.

CoDR Phase Team Structure The team's main objective of the CoDR phase was to rapidly generate concepts and iterate concepts until the best concept was converged upon that met all engineering requirements. To accomplish this, personnel were split into 3 different subteams (Figure 18.1). The Habitable Team was tasked with concept generation and selection for IPV propellant tank configurations, on-orbit assembly concepts, and overall architecture design choices. The Habitable team was responsible for concept generation and selection of concepts for the DEV and IPV Habitat, and the Mars Asset team led concept selection and architecture decisions for the TMSA.

Habitable Team	Non-Habitable Team	Mars Assets
Ethan Cogdill (TL)	Nathan Kralik (TL)	Owen Braun (TL)
Abigail Burianek	Nathaniel Berntson	Joseph Schlager
Alexander Dudowski	Alexander Schreiter	
Tyler Griffith	Preston Yen	
Jocelyn Schechter	Katelyn Lamm	
Paul Racanelli	Joshua Berman	

Table 18.1: CoDR Phase Team Structure

PDR Phase Team Structure During the PDR phase, the team formed into a more conventional yet agile organizational structure that employed subteams and respective subteam leads. The Systems Engineer created a draft of a Gantt Chart at the beginning of the PDR phase to provide initial guidance and deadlines for the subteams to work towards. As the semester progressed, the Gantt chart was continuously updated as priorities changed in importance and as the team understood where the roadblocks were. The final Gantt Chart and schedule is detailed in Appendix F.1. Figure 18.2 displays all the subteams during the PDR phase. Team member names are listed below the subteam if they contributed a major task to that subteam. Hence, multiple team members are listed more than once in the table.

Structures	Power	Propulsion & Trajectory	Heat Rejection	Solid Modeling	Budget	Assembly
Preston Yen	Owen Braun	Joshua Berman	Nathaniel Berntson	Abigail Burianek, *IPV Hab CAD Lead*	Katelyn Lamm	Katelyn Lamm
Ethan Cogdill	Joseph Schlager	Tyler Griffith	Alexander Schreiter	Nathaniel Berntson, *Assembly Lead*		Alexander Dudowski
		Jocelyn Schechter		Jocelyn Schechter, *DEV CAD Lead*		Nathan Kralik
		Ethan Cogdill				

Table 18.2: PDR Team Structure

18.2 WBS

Tasks were delineated by subsystem, start and end date, and ordered by the critical path of the necessary analyses. Tables 18.3,18.4,18.5,18.6 show the abbreviated WBS for each subsystem. The full Gantt Chart with dates is located in the Appendix F.1. Other miscellaneous tasks not shown in the major subsystem WBS below are shown in the Gantt Chart with integrated WBS in the Appendix F.1.

Subsystem	WBS #	Task	Primary	Secondary	Plan Start	Plan Finish	Days
Pressure Vessel	SHPV1.0	Design Standards Research & Mat'l Options	Nate	Preston	3/18/2025	3/23/2025	5
Pressure Vessel	SPT1.0	Design Standards Research & Mat'l Options	Alex	Ethan	3/18/2025	3/23/2025	5
Pressure Vessel	SHPV2.0	Analysis Write-Up	Nate	Preston	3/18/2025	3/25/2025	7
Pressure Vessel	SPT2.0	Analysis Write-Up	Alex	Ethan	3/18/2025	3/25/2025	7
Pressure Vessel	SHPV0	Micrometeoroid Analysis Progress Slide	Abby	Ethan	3/20/2025	3/30/2025	10
Pressure Vessel	SPT0	Updated Boil Off Model	Alex	Ethan	3/18/2025	4/1/2025	14
Pressure Vessel	SHPV3.0	Isogrid Selection for Dev and Hab	Ethan		3/23/2025	3/27/2025	4
Pressure Vessel	n/a	SLS Launch Loading	Ethan	Preston	3/25/2025	3/30/2025	5
Pressure Vessel	SPT3.0	Composite and Hab End Caps	Ethan		3/27/2025	4/3/2025	7
Pressure Vessel	MMOD	Micrometeoroid Shielding Mass/Construction	Ethan	Nathan	3/30/2025	4/5/2025	6
Pressure Vessel	VIB1	Vibrations for Structures: Natural Freqs	Ethan	Preston	3/30/2025	4/14/2025	15
Pressure Vessel	SPT3.1	Composite Tank Compressive Loading	Nathan	Ethan	4/3/2025	4/7/2025	4
Pressure Vessel	SPT3.2	Propellant Tanks: Link to mass budget	Ethan	Nathan	4/1/2025	4/6/2025	5
Pressure Vessel	SPT5	Vibration Analysis Tanks and Pressure Vessels	Ethan		4/8/2025	4/13/2025	5
Pressure Vessel	SPT3.3	Water / O2 Tank Sizing	AJ		4/8/2025	4/13/2025	5
Pressure Vessel	SHPV2.1	Isogrid Mars Asset	Owen	Ethan	4/8/2025	4/10/2025	2
Pressure Vessel	SPT4.0	Plumbing	Nathan	Josh	4/15/2025	4/21/2025	6
Pressure Vessel	SPT	Tank / Liner Thermal Expansion	Ethan		4/15/2025	4/19/2025	4

Table 18.3: Habitat and Propellant Tank Structure Subsystem WBS

Subsystem	WBS #	Task	Primary	Secondary	Plan Start	Plan Finish
Truss	STRS1.0	Design Process Research (Talk to Ali)	Preston	Nate	3/18/2025	3/23/2025
Truss	STRS2.0	Initial Analysis Framework Write-Up	Preston	Nate	3/20/2025	3/23/2025
Truss	STRS2.0	Design Goals/Drivers, Allowable Loads, FoS	Preston	Nate	3/23/2025	4/1/2025
Truss	STRS3.0	Thrust Structure	Preston	Ethan	4/17/2025	4/20/2025
Truss	STRS2.0	Main Truss	Preston		4/10/2025	4/17
Truss	STRS3.1	Saddle Truss	Preston		4/12/2025	4/20/2025
Truss	STRS3.2	Payload Adapters	Preston		4/12/2025	4/17/2025

Table 18.5: Truss Structure Subsystem WBS

Subsystem	WBS #	Task	Primary	Secondary	Plan Start	Plan Finish
Power	PG1.0	DeV Nuclear Reactor Analysis Framework	Joseph	Owen	3/18/2025	3/23/2025
Power	PHJ1.0	Spacecraft Radiator Design Research	Katelyn		3/18/2025	3/23/2025
Power	PHJ2.0	Radiator Design: Materials	Nate		3/23/2025	3/30/2025
Power	PG2	Brayton Cycle Analysis: Mass Flow	Owen		3/23/2025	3/28/2025
Power	PHJ3.0	Bimodal Power: Cycle Analysis	Owen	Nathan	3/27/2025	4/15/2025
Power	PHJ3.0	DeV and IPV Heat Transfer	Nate	Alex	3/30/2025	4/6/2025
Power	PG3	DeV Reactor P&ID	Owen	Joseph	3/30/2025	4/4/2025
Power	PG4	Bimodal P&ID	Owen	Joseph	3/30/2025	4/4/2025
Power	PG5	Pressure drop across tie tubes	Owen		4/8/2025	4/10/2025
Power	PG6	Turbomachinery for Bimodal and DeV	Owen		4/8/2025	4/13/2025
Power	PHJ4	Fix Bimodal Radiator Design	Nate		4/8/2025	4/13/2025
Power	PHJ5	DeV and IPV Heat Rejection	Alex		4/8/2025	4/13/2025
Power	PHJ6	Heat Rejection Heat Exchangers	Alex		4/15/2025	4/17/2025
Power	PHJ7	Radiator Analysis & Materials	Nate		4/8/2025	4/20/2025
Power	PHJ8	DEV & Hab Loop Pressure Losses	Ethan		4/15/2025	4/20/2025
Power	PHJ9	Combine Heat Rej Analyses	Alex	Nate	4/20/2025	4/21/2025
Power	PHJ10	MLI for Habs	Alex		4/21/2025	4/21/2025

Table 18.4: Power Subsystem WBS

A Structural Design Appendix

A.1 Vibrational Analysis

A.1.1 Individual Payload Element Vibrational Parameters

A table of each component and their respective parameters that is used for the vibrational analysis is below:

Component Parameters									Lateral Vibrational Analysis		Axial Stiffness	
Item (per unit)	Length (m)	Shell Thickness (m)	Approximate Mass (kg)	Outer Diameter (m)	Inner Diameter (m)	Outer Width (m)	Material	Mass/Unit Length (kg/m)	I_area Moment (m^4)	Elastic Modulus (Pa)	Cross Sectional Area (m^2)	Axial Stiffness
ED Tank	12.3	0.0035	73500	11	10.993	N/A	Carbon Fiber	5975.6	1.828	2.00E+11	0.1209	1.97E+09
MC Tank	10.4	0.0035	55300	11	10.993	N/A	Carbon Fiber	5317.3	1.828	2.00E+11	0.1209	2.33E+09
MD Tank	8.3	0.0035	41000	11	10.993	N/A	Carbon Fiber	4939.8	1.828	2.00E+11	0.1209	2.91E+09
EC Tank	15.3	0.0035	101700	11	10.993	N/A	Carbon Fiber	6647.1	1.828	2.00E+11	0.1209	1.58E+09
Truss Box	3.5	0.025	5202	N/A	N/A	3.5	Graphite-Epoxy	1486.3	0.353	1.07E+11	0.1744	5.33E+09
Truss Triangular	2	0.019	9100	N/A	N/A	2	Graphite-Epoxy	4550.0	0.050	1.07E+11	0.0756	4.05E+09
Engines	8.31	0.1	18000	11	10.8	N/A	Aluminum 2219	2166.1	50.860	7.30E+10	3.4243	3.01E+10
DEV	3.2	0.006	20000	5.4	5.388	N/A	Aluminum 2219	6250.0	0.370	7.30E+10	0.1017	2.32E+09
Hab	6	0.006	43000	5.5	5.488	N/A	Aluminum 2219	7166.7	0.391	7.30E+10	0.1036	1.26E+09
Orion Cap	15	0.1	33000	5	4.8	N/A	Al-Li 2195	2200.0	4.622	6.90E+10	1.5394	7.08E+09
Payload Adapter	1.5	0.01	1300	12	11.98	N/A	T800S	866.7	6.769	2.94E+11	0.3767	7.38E+10
Assembly Vehicle	10	0.1	940	5	4.8	N/A	Al-Li 2195	94	4.621989652	6.90E+10	1.5393804	1.06E+10

Subsystem	WBS #	Task	Primary	Secondary	Plan Start	Plan Finish
Engine Design	PNT1.1	Nuclear Engine Performance Analysis Write-Up	Tyler	Josh	3/16/2025	3/20/2025
Engine Design	PNT1.1	Nuclear Engine Notional Diagram	Tyler	Josh	3/16/2025	3/20/2025
Engine Design	PNT1.2	Nuclear Engine Design Process Description	Tyler	Josh	3/20/2025	3/23/2025
Engine Design	PMAN1.0	Orbital Maneuvering System Analysis	AJ	Ethan	3/18/2025	4/8/2025
Trajectory	PTRJ1.1	Lambert Method MATLAB Code for Transfer	Paul		3/16/2025	3/27/2025
Trajectory	PTRJ1.2	Real dV for transfers with actual planet orbits	Paul	Jocelyn	3/18/2025	3/30/2025
Trajectory	PTRJ1.3	Launch window porkchop plots	Jocelyn	Paul	3/18/2025	3/30/2025
Engine Design	PNT1.3	Engine cycle, states	Josh	Tyler	3/23/2025	3/27/2025
Engine Design		Engine nozzle	Josh	Tyler	3/23/2025	3/27/2025
Trajectory	PTRJ1.4	Transfer Trajectory Course Corrections dV Margin	Jocelyn	Paul	3/23/2025	3/30/2025
Engine Design	PMAN2.0	Orbital Maneuvering System Detail Design	AJ	Abby	3/25/2025	3/30/2025
Engine Design		DeV Engine Cycle Analysis	Jocelyn		3/25/2025	4/7/2025
Engine Design	PNT1.4	Nuclear Reactor Design	Tyler	Josh	3/27/2025	4/6/2025
Engine Design		RCS Design: P&ID and Design Decisions	Jocelyn	Paul	3/30/2025	4/3/2025
Engine Design	PNT1.5	NTP Engine Nozzle Sizing Analysis	Josh	Tyler	3/27/2025	3/30/2025
Engine Design	PNT1.6	NTP Engine Nozzle Cooling	Josh		3/30/2025	4/1/2025
Trajectory	PTRJ1.2	Finite Burn MATLAB Losses and Burn Times	Ethan	Paul	4/8/2025	4/13/2025
Engine Design	PNT1.7	Finish Nozzle	Josh	Tyler	3/30/2025	4/8/2025
Engine Design	PNT1.8	Cool Down Period	Tyler	Josh	4/1/2025	4/8/2025
Engine Design	PNT1.9	Ullage + Piping	Nathan	Josh	4/3/2025	4/8/2025
Engine Design	PNT1.10	P&ID	Josh	Tyler	4/1/2025	4/8/2025
Engine Design	PNT1.11	Turbomachinery	Josh	Tyler	4/1/2025	4/8/2025
Trajectory		Mars Assets Cruise Stage Maneuvers	Nathan	Owen	4/8/2025	4/10/2025
Trajectory		DeV RCS and Maneuvering	Jocelyn		4/8/2025	4/10/2025
Trajectory		Finite Burn MATLAB Visuals	Ethan		4/20/2025	4/22/2025
Engine Design		NTP Nozzle Mass Fix	Josh	Tyler	4/17/2025	4/19/2025

Table 18.6: Propulsion and Trajectory Subsystem WBS

A.1.2 Vibrational Analysis MATLAB Codes

```
function f = lateral_vibs(N,m,k)
%N is number of DOF in system

%uses a basic spring damper model to approximate the natural
   frequency of
%each launch

%m is a vector that represents the masses. the first mass is the
   payload
%adpter. see the diagram in the drive for more details.

%Adapter, ED, AV, Orion

%w represents for whole system
```

```
Mw = diag(m);


a = length(N); b = length(N);


for i = 1:N
   if i ~= N
       a(i) = k(i) + k(i+1);
       b(i) = -k(i+1);
   else
       a(i) = k(i);
   end
end


Kw = zeros(N,N) + diag(a.*ones(1,N)) + diag(b.*ones(1,N-1),1) +
   diag(b.*ones(1,N-1),-1);


[eigenvec, eigenval] = eig(Kw, Mw);


f = sqrt(diag(eigenval)) / (2*pi);
format shortG;
sort(f);


end


clc
clear


mL1 = [9.43e2 7.35e4 5.97e3 9.4e2 3.30E+04];
kL1 = [6.11e12 9.43E+09 4.23E+10 1.53E+10 4.54E+09];
```

```
L1lat = lateral_vibs(length(kL1),mL1,kL1);
disp(['Launch 1 Lateral NF (Hz):',num2str(L1lat(1))])

mL2 = [9.43e2 7.20E+04 7.20E+04];
kL2 = [6.11e12 9.43E+09 9.43E+09];
L2lat = lateral_vibs(length(kL2), mL2, kL2);
disp(['Launch 2 Lateral NF (Hz):',num2str(L2lat(1))])

mL3 = [9.43e2 5.53E+04 7.35E+04 4.30E+04];
kL3 = [6.11E+12 1.56E+10 9.43E+09 6.34E+09];
L3lat = lateral_vibs(length(kL3), mL3, kL3);
disp(['Launch 3 Lateral NF (Hz):',num2str(L3lat(1))])

mL4 = [9.43e2 4.10E+04 5.53E+04 2.00E+04 4.00E+03];
kL4 = [6.11E+12 3.07E+10 1.56E+10 6.12E+10 2.00E+09];
L4lat = lateral_vibs(length(kL4), mL4, kL4);
disp(['Launch 4 Lateral NF (Hz):',num2str(L4lat(1))])

mL5 = [9.43e2 9.40E+04 1.50E+04];
kL5 = [6.11E+12 4.90E+09 3.21E+10];
L5lat = lateral_vibs(length(kL5), mL5, kL5);
disp(['Launch 5 Lateral NF (Hz):',num2str(L5lat(1))])

mL6 = [9.43e2 1.80E+04 4.10E+04 3.30E+04];
kL6 = [6.11E+12 3.11E+11 3.07E+10 4.54E+09];
L6lat = lateral_vibs(length(kL6), mL6, kL6);
disp(['Launch 6 Lateral NF (Hz):',num2str(L6lat(1))])
NF_lateral = [L1lat(1) L2lat(1) L3lat(1) L4lat(1) L5lat(1) L6lat
   (1)]';
```

```
disp(num2str(NF_lateral))



%% Launch 1
clc
clear

%uses a basic spring damper model to approximate the natural
   frequency of
%each launch

%m is a vector that represents the masses. the first mass is the
   payload
%adpter. see the diagram in the drive for more details.

%Adapter, ED, AV, Orion
m = [1460 72000 10000 33000];

k = [4.43e10 1.97e9 1.06e10 7.08e9];

%w represents for whole system

Mw = [m(1) 0 0 0; 0 m(2) 0 0; 0 0 m(3) 0; 0 0 0 m(4)];

Kw = [ sum(k) -k(2) -k(3) -k(4); -k(2) k(2) 0 0; -k(3) 0 k(3) 0;
   -k(4) 0 0 k(4)];

[eigenvec, eigenval] = eig(Kw, Mw);
```

```
f = sqrt(diag(eigenval)) / (2*pi);
format shortG
sort(f)

%% Launch 2
clc
clear

m = [1460 72000 72000 0];
k = [4.43e10 1.97e9 1.97e9 0];

%w represents for whole system

Mw = [m(1) 0 0 0; 0 m(2) 0 0; 0 0 m(3) 0; 0 0 0 m(4)];

Kw = [ sum(k) -k(2) -k(3) -k(4); -k(2) k(2) 0 0; -k(3) 0 k(3) 0;
   -k(4) 0 0 k(4)];

[eigenvec, eigenval] = eig(Kw, Mw);

f = sqrt(diag(eigenval)) / (2*pi);
format shortG
sort(f)

%% Launch 3
clc
clear

m = [1460 72000 57000 42000];
```

```
k = [4.43e10 1.97e9 2.33e9 1.26e9];

%w represents for whole system

Mw = [m(1) 0 0 0; 0 m(2) 0 0; 0 0 m(3) 0; 0 0 0 m(4)];

Kw = [ sum(k) -k(2) -k(3) -k(4); -k(2) k(2) 0 0; -k(3) 0 k(3) 0;
   -k(4) 0 0 k(4)];

[eigenvec, eigenval] = eig(Kw, Mw);

f = sqrt(diag(eigenval)) / (2*pi);
format shortG
disp(['Launch 3 NF: ',num2str( sort(f(1) ))]);

%% Launch 4
clc
clear
%PA, MD, MC, DeV
m = [1460 41000 57000 20000];

k = [4.43e10 2.91e9 2.33e9 2.68e9];

%w represents for whole system

Mw = [m(1) 0 0 0; 0 m(2) 0 0; 0 0 m(3) 0; 0 0 0 m(4)];

Kw = [ sum(k) -k(2) -k(3) -k(4); -k(2) k(2) 0 0; -k(3) 0 k(3) 0;
```

```
    -k(4) 0 0 k(4)];

[eigenvec, eigenval] = eig(Kw, Mw);

f = sqrt(diag(eigenval)) / (2*pi);
format shortG
disp(['Launch 4 NF: ',num2str( sort(f(1) ))]);
%% Launch 5
clc
clear

m = [1460 94000 0 0];

k = [4.43e10 1.58e9 0 0];

%w represents for whole system

Mw = [m(1) 0; 0 m(2)];

Kw = [ sum(k) -k(2); -k(2) k(2)];

[eigenvec, eigenval] = eig(Kw, Mw);

f = sqrt(diag(eigenval)) / (2*pi);
format shortG
sort(f)

%% Launch 6
clc
```

```
clear

m = [1460 18000 41000 33000];

k = [4.43e10 3.01e10 2.33e9 1.26E09];

%w represents for whole system

Mw = [m(1) 0 0 0; 0 m(2) 0 0; 0 0 m(3) 0; 0 0 0 m(4)];

Kw = [ sum(k) -k(2) -k(3) -k(4); -k(2) k(2) 0 0; -k(3) 0 k(3) 0;
   -k(4) 0 0 k(4)];

[eigenvec, eigenval] = eig(Kw, Mw)

f = sqrt(diag(eigenval)) / (2*pi);
format shortG
sort(f)
```

A.2 Habitable Structures

```
%v3 iterative design approach for isogrids
%Ethan Cogdill 3/27

%for mass calculations, assuming monocoque endcap sized for pressure,
    not
%loading

%INPUTS
id = 2.5; %Inner Diameter, meters
length = 5; %Length, meters

%factor of safety
fs = 1.5;

%TANK GEOMETRY



%SKIN THICKNESS INPUT
t = 1.7; %mm
%RIB THICKNESS INPUT
b = 1; %mm
%WALL THICKNESS INPUT
wall_t = 5; %mm
%NUMBER OF TRIANGLE CELLS INPUT
cells = 150;
%LOADING INPUTS
```

```
W = 2.2*2000; % lbs (kg*2.2)
F_a = W*4.1*fs; %axial // lbs
M_b = 3*fs*W*length*.5*39.37; %bending moment



id = id*39.37; %in
%convert from mm to in
t= t/25.4;
b = b/25.4;
wall_t = wall_t/25.4;

od = id + 2*wall_t;
R = od/2;

%MATERIAL PROPERTIES - Aluminum 2219-t62
E = 10600000; %psi
Ftu = 60000; %psi // Tensile Ultimate
Fty = 42000; %psi // Tensile Yield
v = 0.33; %poisson
%isogrid geometry from Handbook Section 2

%assuming unflanged isogrid

%RIB DEPTH
d = wall_t - t;




h = (od*pi)/cells;
```

```
alpha = (b*d)/(t*h);

t_eff = t*(1+alpha);

delta = (d/t);

beta = sqrt( 3*alpha*(1+delta)^2 + (1+alpha)*(1+alpha*delta^2));

t_star = t*(beta/(1+alpha)); %equivalent thickness

E_star = E*(1+alpha)^2/beta; %equivalent young's modulus



%LOAD CALCULATIONS - BUCKLING AND BURST

%constants

c0 = 0.397;

c1 = 10.2;

c2 = 0.616;


N_b = (M_b/(pi*R^2));

N_a = (F_a / (2*pi*R));

Ncr =  N_a + N_b;


Ncr1 = c0*E*(t^2)*beta/R;

Ncr1m = Ncr1*2*pi*R;

Ncr2 = c1*E*t*(1+alpha)*(t^2/h^2);

Ncr2m = Ncr2*2*pi*R;

Ncr3 = c2*E*t*(1+alpha)*(b^2/d^2);

Ncr3m = Ncr3*2*pi*R;


p_burst = Ftu*t*(1+alpha)/R;


p_allow = p_burst/fs;
```

```
%MEMBRANE RIB STRESS CALCS // x is hoop, y is longitudinal
Nx = p_allow*R;
Ny = p_allow*R/2;
Nxy = 0;

sigma_x = Nx/t_eff;
sigma_y = Ny/t_eff;

sigma_1 = 1/(3*t_eff)*(3*Nx-Ny);
sigma_2 = 2/(3*t_eff)*(Ny+3^0.5*Nxy);
sigma_3 = 2/(3*t_eff)*(Ny-3^0.5*Nxy);

%weight
t_equiv = t*(1+3*alpha);
mass = 2840*pi*length*( ( (id/(2*39.37)) + t_equiv/39.27)^2 - (id
   /(2*39.37))^2);

%PRINT RESULTS
disp('INPUTS: IPV Hab')
disp(['Chosen Skin Thickness (t): ', num2str(t*25.4),'mm']);
disp(['Chosen Rib Thickness (b): ', num2str(b*25.4),'mm']);
disp(['Chosen Rib Depth (d): ', num2str(d*25.4),'mm']);
disp(['Number Cells: ', num2str(cells)]);
disp(['N cr allow (Loading): ',num2str(Ncr*0.1751268),'kN/m'])
disp('RESULTS:')
% disp(['General Instability: ', num2str(Ncr1m),'lbf']);
% disp(['Skin Buckling: ', num2str(Ncr2m),'lbf']);
% disp(['Rib Crippling: ', num2str(Ncr3m),'lbf']);
```

```
% disp(['Allowable Pressure: ', num2str(p_allow),'psi']);

disp(['General Instability: ', num2str(Ncr1*0.1751268),'kN/m']);
disp(['Skin Buckling: ', num2str(Ncr2*0.1751268),'kN/m']);
disp(['Rib Crippling: ', num2str(Ncr3*0.1751268),'kN/m']);
disp(['Allowable Pressure: ', num2str(p_allow*6.89476),'kPa']);
disp(['Burst Pressure: ', num2str(p_burst*6.89476),'kPa']);
disp(['t_star: ', num2str(t_star*25.4),'mm']);
disp(['Equivalent Weight Thickness: ', num2str(t_equiv*25.4),'mm']);

%
% disp(['sigma_x: ', num2str(sigma_x),'psi']);
% disp(['sigma_y: ', num2str(sigma_y),'psi']);
% disp(['sigma_1: ', num2str(sigma_1),'psi']);
% disp(['sigma_2: ', num2str(sigma_2),'psi']);
% disp(['sigma_3: ', num2str(sigma_3),'psi']);

disp(['mass: ', num2str(mass),'kg']);
```

A.3 Propellant Tanks

A.3.1 Propellant Tank Netting Theory Trade Study Print Out

Below is the trade study print out for the Earth Departure Tank Trade Study. Inputs, outputs, and intermediate parameters are displayed.

Ethan Cogdill 3/23

NETTING THEORY ANALYSIS

Inputs	
Helical Angle (deg)	30
Prop Pressure (MPa)	0.234
Factor of Safety	1.5
Ult Ten Strength (MPa) (IM7-977-3)	1200
Volume Factor	0.7
Yield Strength (Aluminum) (MPa)	290
Liner pressure (kpa)	0.0117
Liner pressure (kpa)	0.234
Assuming metallic liner supports 5% of internal pressure load Using netting theory to calculate the thickness of carbon fiber needed	
Tank Geometry Inputs	
Tank Radius (m)	4.75
Diameter to height coeff for ellipse	0.455
Ellipse Height	4.3225
Tank Barrel Length (m)	6.955
tank length	15.6
Est. Mass (kg)	73000

Intermediate	
Tank Radius (mm)	4750
Hoop Loading (N/mm)	1111.5
Axial Loading (N/mm)	555.75
Stress allow	800
radians of helical	0.5235987756
K	0.5345972709
V_cyl	492.9855914
V_ellipsoid	408.5176552
Axial Thrust Loading	95.9
Bending Moment	236.3

Output	
Thickness helical wind (mm)	1.09
Thickness 90-deg wind (mm)	1.45
total thickness (mm)	3.63
liner thickness (mm)	0.29
Mass	
CF Barrel Mass (kg)	2634.53
Aluminum Barrel Mass (kg)	338.90
Total Barrel Mass (kg)	2973.43
Endcaps	
t (mm) CF	0.74
Liner Mass (kg)	217.49
Endcap Mass (kg) (for 1 side)	346.38
TOTAL TANK MASS (kg)	**3901.4**
PROP VOLUME m^3	**901.5**

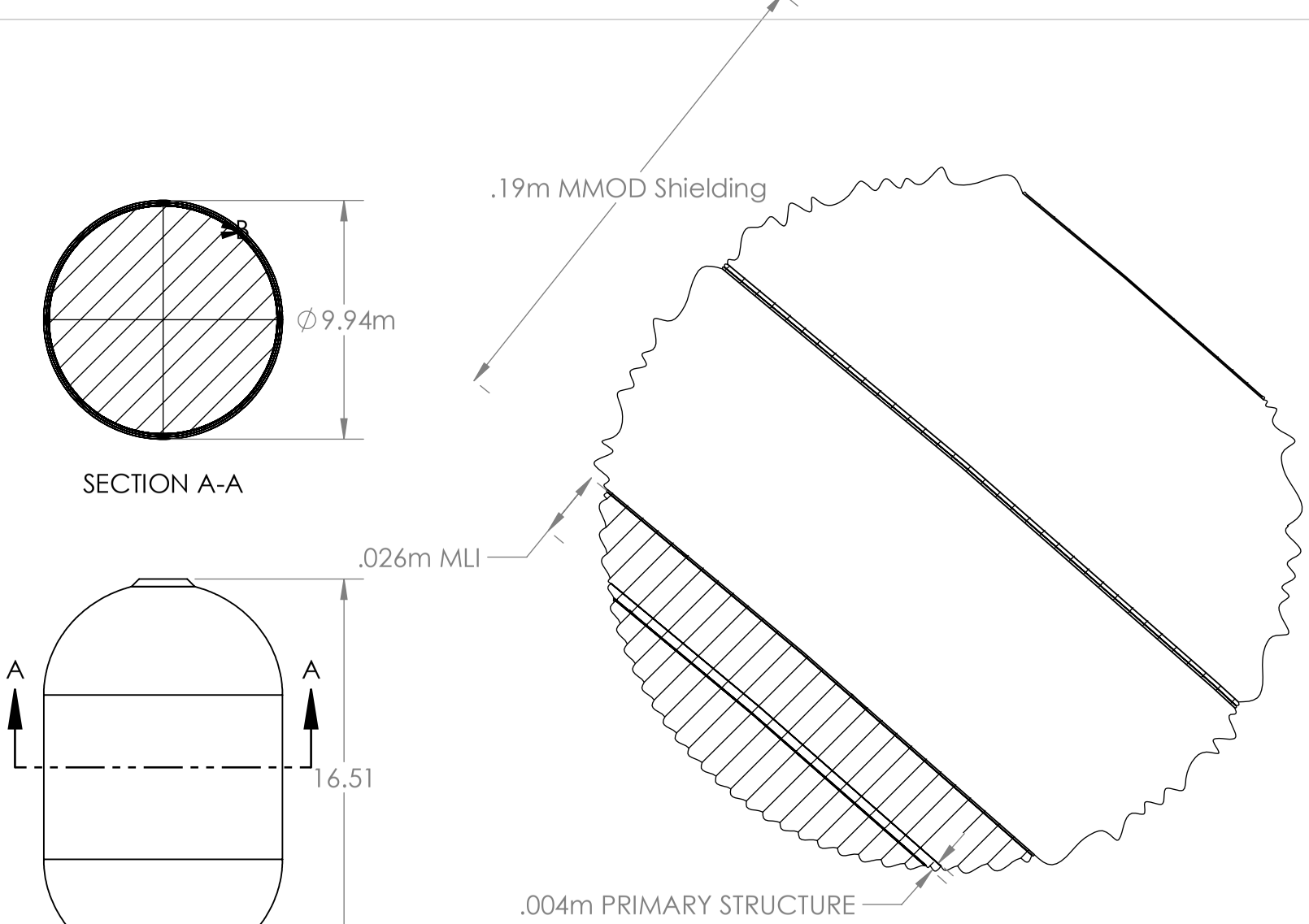

UNLESS OTHERWISE SPECIFIED:
DIMENSIONS IN INCHES

TOLERANCES:
.XX ±.01 .XXX ±.005
FRACTIONS ±1/64
ANGULAR MACHINED ±.5°
ANGULAR BEND ±1°
SURFACE FINISH 125
BREAK ALL EDGES .030

DO NOT SCALE

SHEET 1 OF 1

CASE SCHOOL OF ENGINEERING
CASE WESTERN RESERVE UNIVERSITY

TITLE: EARTH DEPARTURE TANK

SIZE:	DATE:	DRAWN BY:	
A	5/6/2025	EHC	
MATERIAL:		PART #:	REV:
VARIOUS		25A01005	B

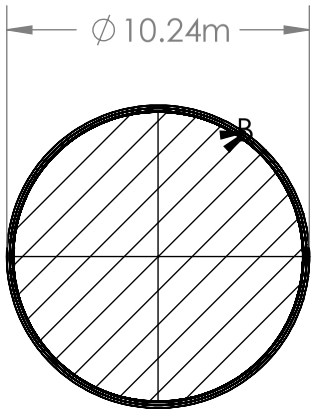

SECTION A-A

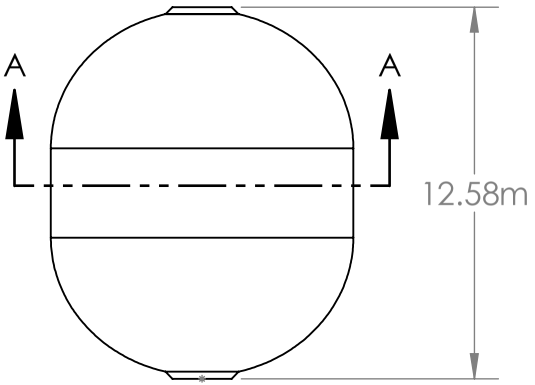

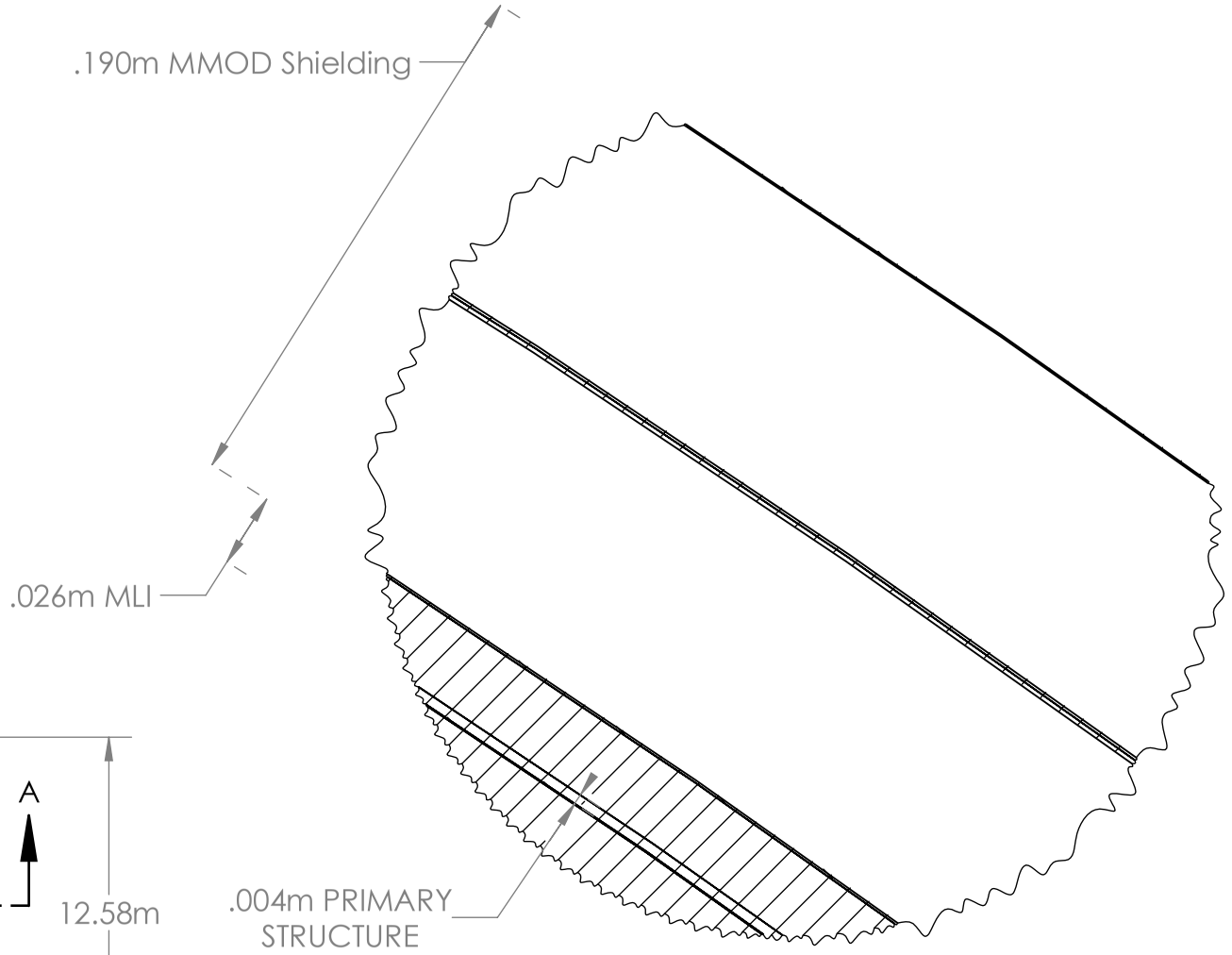

UNLESS OTHERWISE SPECIFIED:
DIMENSIONS IN INCHES

TOLERANCES:
.XX ±.01 .XXX ±.005
FRACTIONS ±1/64
ANGULAR MACHINED ±.5°
ANGULAR BEND ±1°
SURFACE FINISH 125
BREAK ALL EDGES .030

DO NOT SCALE

SHEET 1 OF 1

CASE SCHOOL OF ENGINEERING
CASE WESTERN RESERVE UNIVERSITY

TITLE: MARS CAPTURE TANK

SIZE:	DATE:	DRAWN BY:	
A	5/6/2025	EHC	
MATERIAL:		PART #:	REV:
VARIOUS		25A01006	B

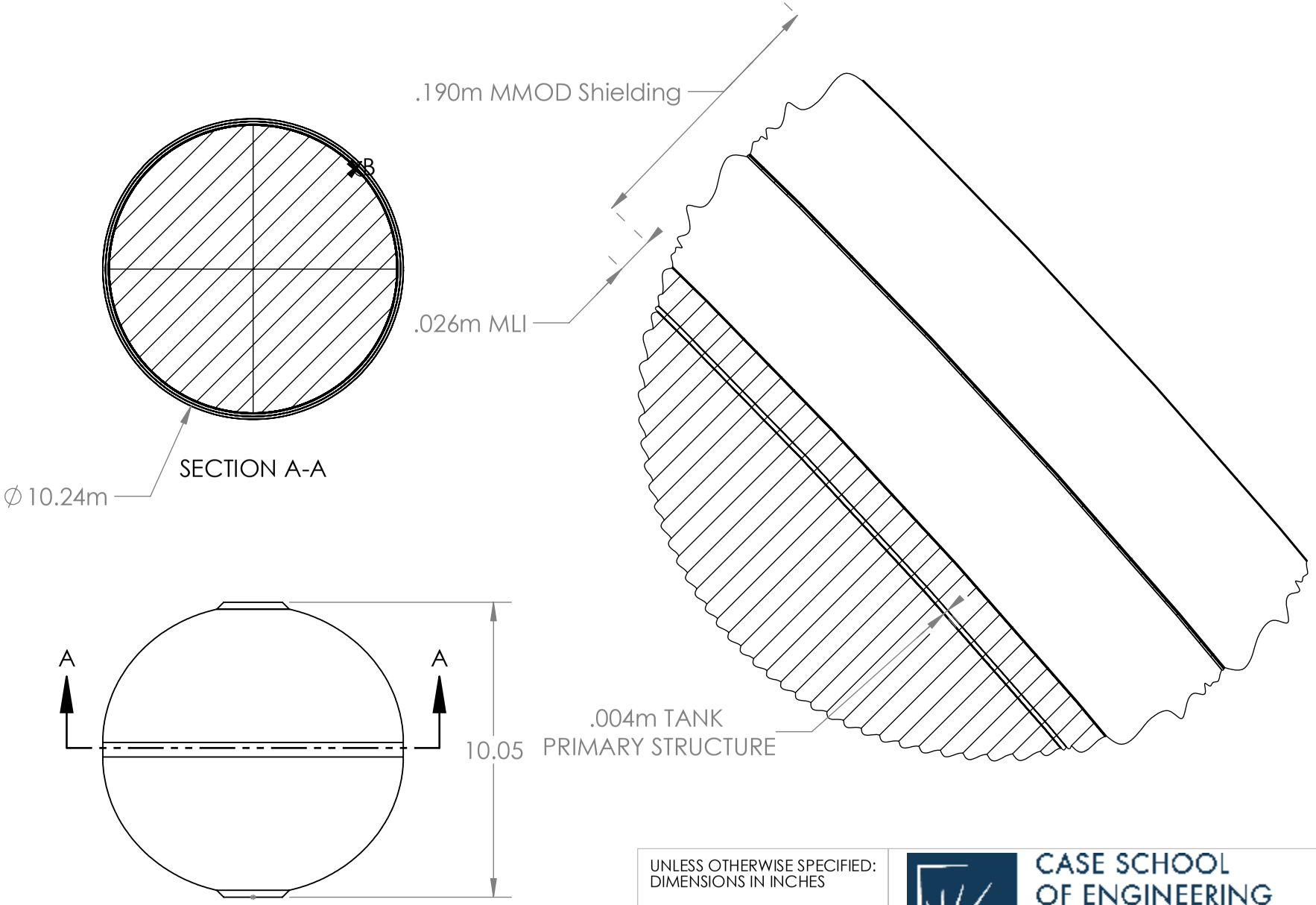

UNLESS OTHERWISE SPECIFIED:
DIMENSIONS IN INCHES

TOLERANCES:
.XX ±.01 .XXX ±.005
FRACTIONS ±1/64
ANGULAR MACHINED ±.5°
ANGULAR BEND ±1°
SURFACE FINISH 125
BREAK ALL EDGES .030

DO NOT SCALE

SHEET 1 OF 1

CASE SCHOOL OF ENGINEERING
CASE WESTERN RESERVE UNIVERSITY

TITLE:
MARS DEPARTURE TANK

SIZE:	DATE:	DRAWN BY:	
A	5/6/2025	EHC	
MATERIAL:		PART #:	REV:
VARIOUS		25A01007	A

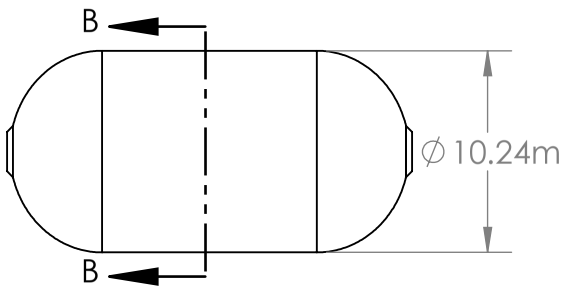

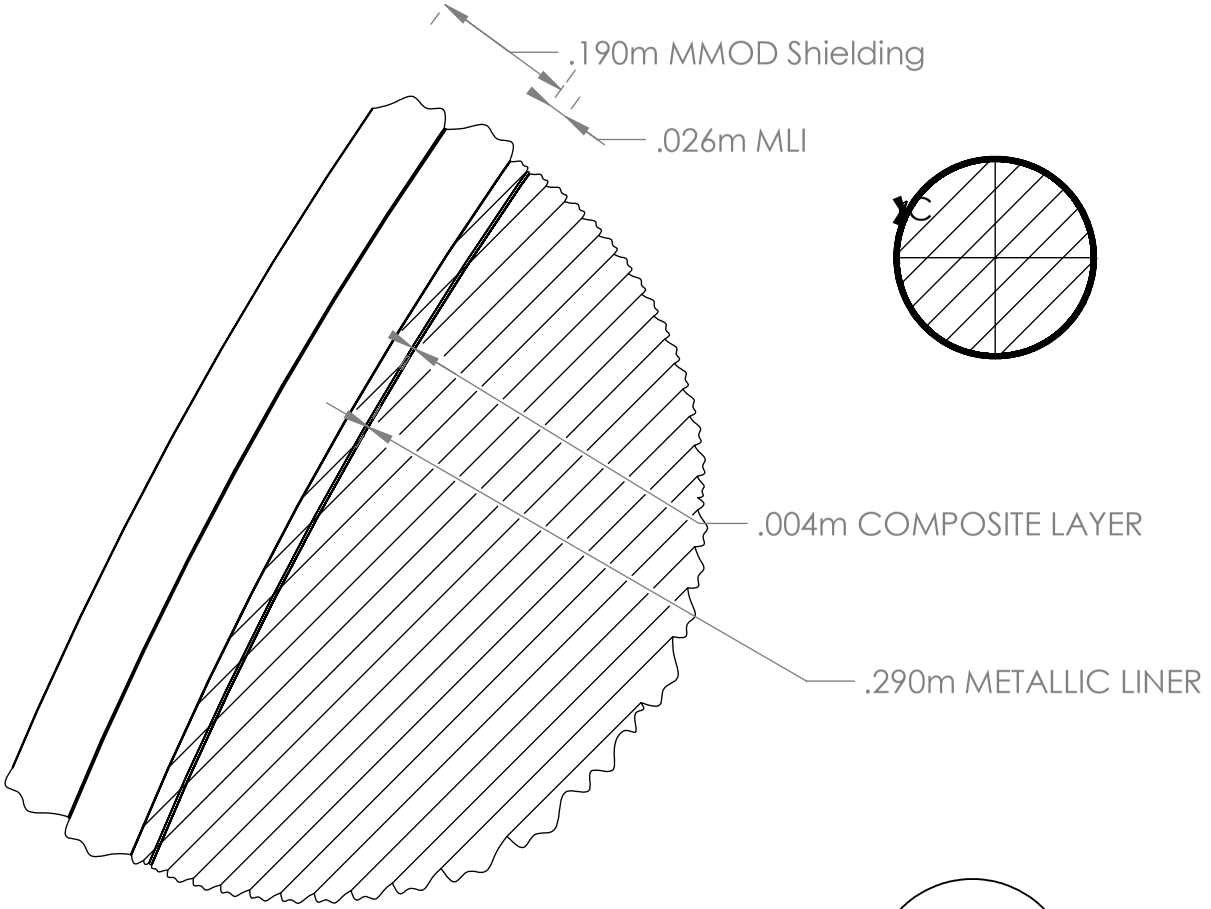

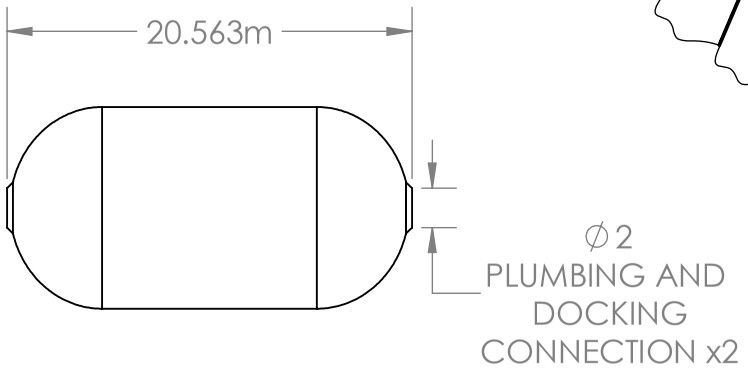

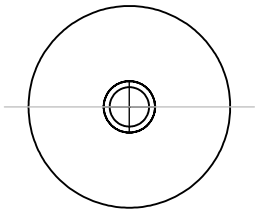

UNLESS OTHERWISE SPECIFIED:
DIMENSIONS IN INCHES

TOLERANCES:
.XX ±.01 .XXX ±.005
FRACTIONS ±1/64
ANGULAR MACHINED ±.5°
ANGULAR BEND ±1°
SURFACE FINISH 125
BREAK ALL EDGES .030

DO NOT SCALE

SHEET 1 OF 1

CASE SCHOOL OF ENGINEERING
CASE WESTERN RESERVE UNIVERSITY

TITLE:			
EHC			
SIZE: A	DATE: 5/6/2025	DRAWN BY: EHC	
MATERIAL: VARIOUS		PART #: 25A01008	REV: B

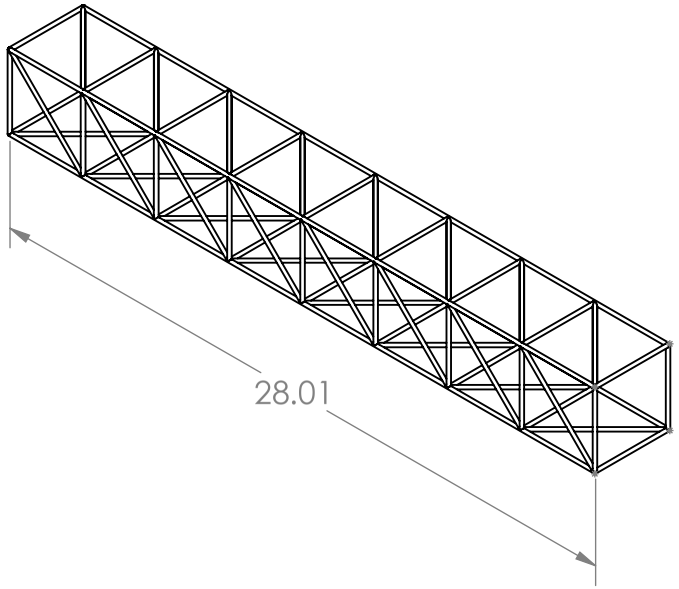

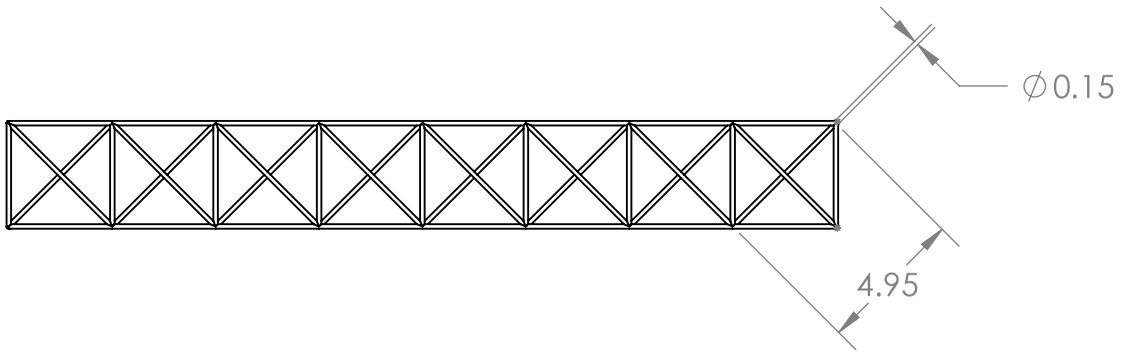

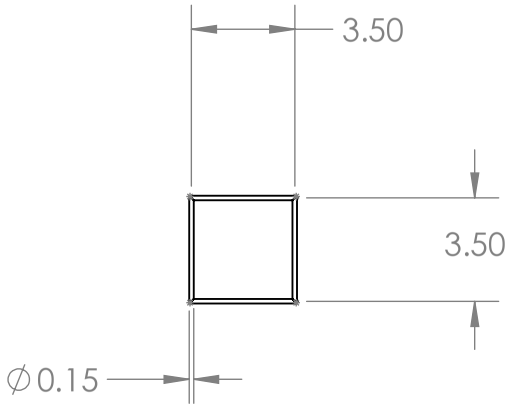

UNLESS OTHERWISE SPECIFIED:
DIMENSIONS IN INCHES

TOLERANCES:
.XX ±.01 .XXX ±.005
FRACTIONS ±1/64
ANGULAR MACHINED ±.5°
ANGULAR BEND ±1°
SURFACE FINISH
BREAK ALL EDGES .030

DO NOT SCALE

SHEET 1 OF 1

CASE SCHOOL OF ENGINEERING
CASE WESTERN RESERVE UNIVERSITY

TITLE: MAIN TRUSS

SIZE:	DATE:	DRAWN BY:
A	5/6/2025	PMY

MATERIAL:	PART #:	REV:
IM7/5555	25A02002	A

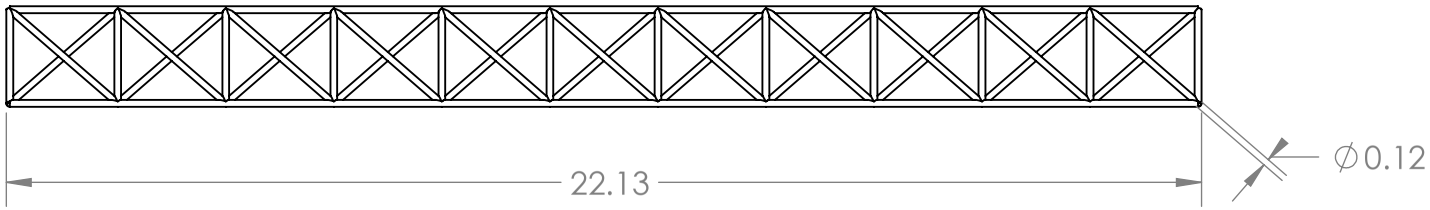

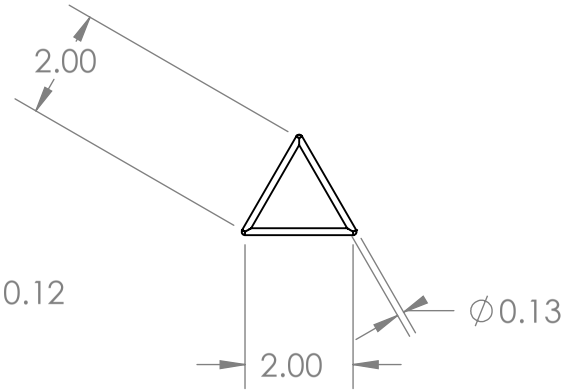

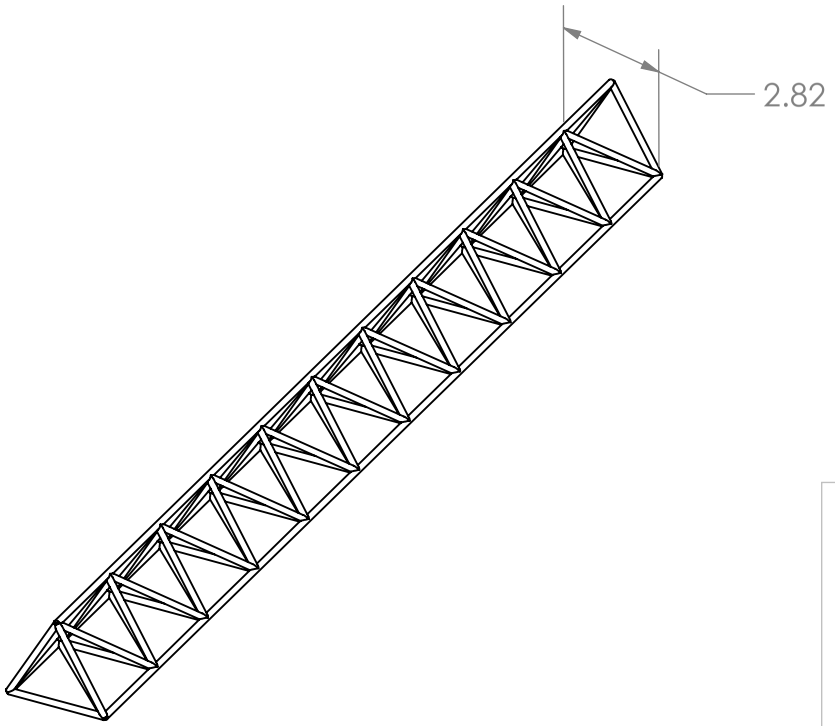

UNLESS OTHERWISE SPECIFIED:
DIMENSIONS IN INCHES

TOLERANCES:
.XX ±.01 .XXX ±.005
FRACTIONS ±1/64
ANGULAR MACHINED ±.5°
ANGULAR BEND ±1°
SURFACE FINISH
BREAK ALL EDGES .030

DO NOT SCALE

SHEET 1 OF 1

CASE SCHOOL OF ENGINEERING
CASE WESTERN RESERVE UNIVERSITY

TITLE: TRIANGULAR TRUSS

SIZE:	DATE:	DRAWN BY:	
A	5/6/2025	PMY	
MATERIAL:		PART #:	REV:
IM7/5555		25A02003	A

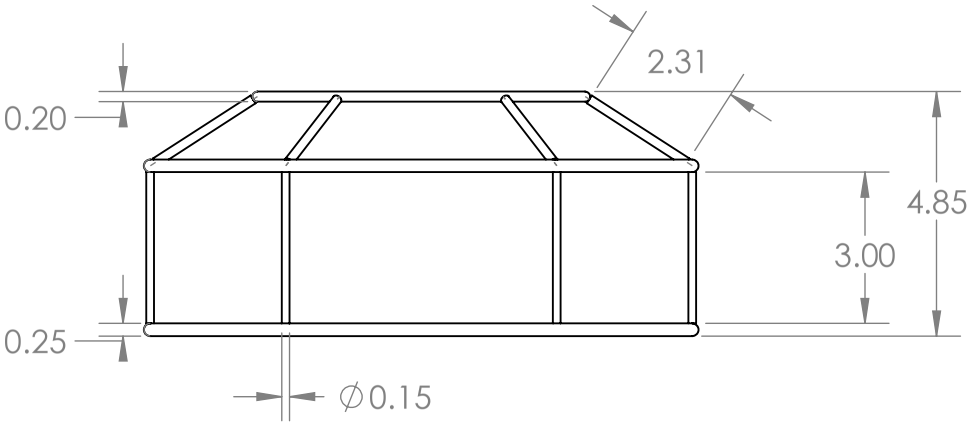

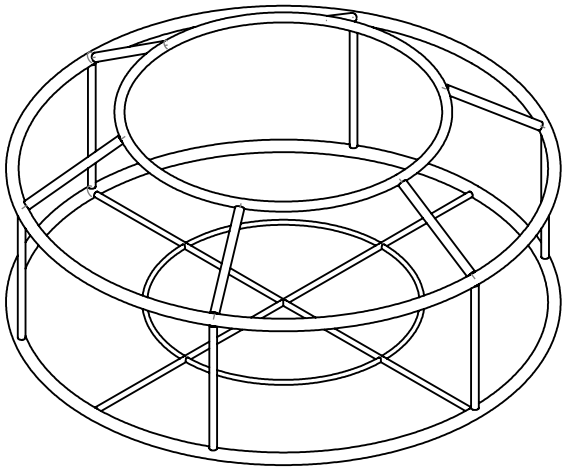

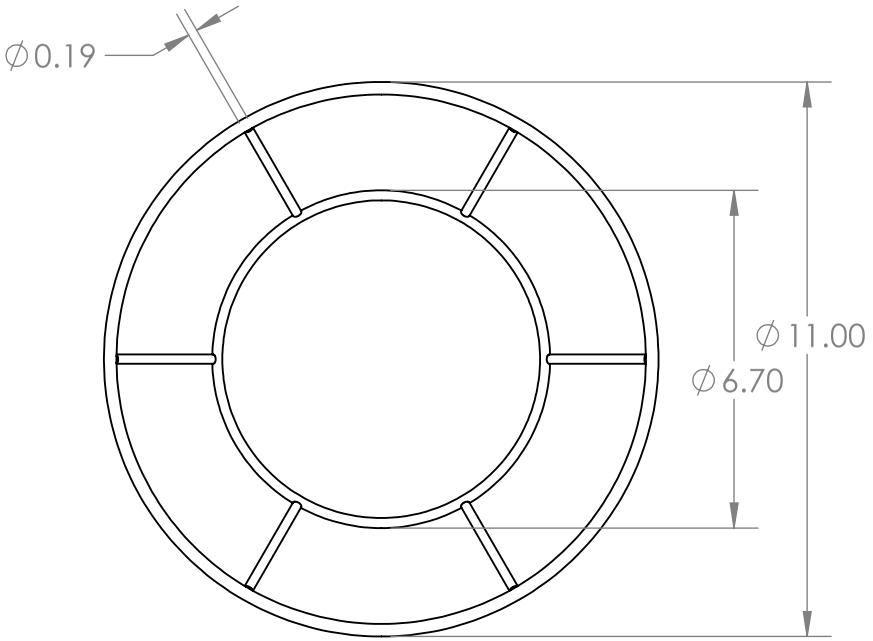

UNLESS OTHERWISE SPECIFIED:
DIMENSIONS IN INCHES

TOLERANCES:
.XX ±.01 .XXX ±.005
FRACTIONS ±1/64
ANGULAR MACHINED ±.5°
ANGULAR BEND ±1°
SURFACE FINISH
BREAK ALL EDGES .030

DO NOT SCALE

SHEET 1 OF 1

CASE SCHOOL OF ENGINEERING
CASE WESTERN RESERVE UNIVERSITY

TITLE: THRUST STRUCTURE

SIZE:	DATE:	DRAWN BY:
A	5/6/2025	PMY

MATERIAL:	PART #:	REV:
VARIOUS	25A02012	A

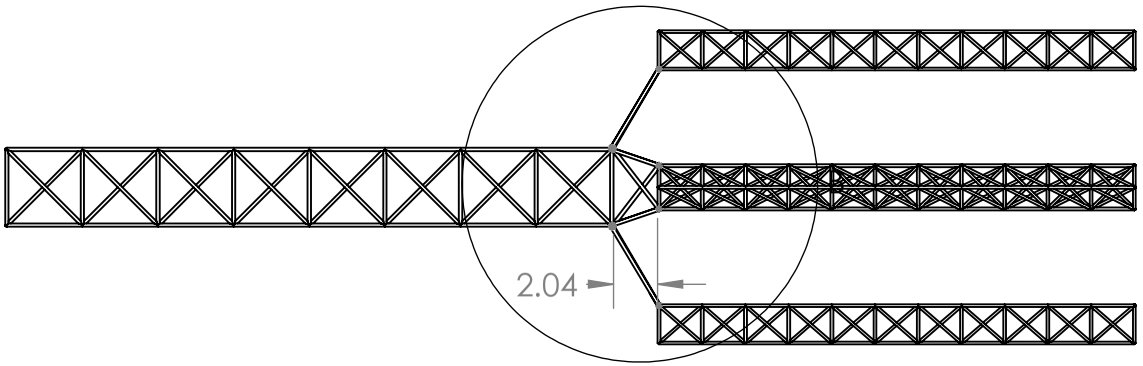

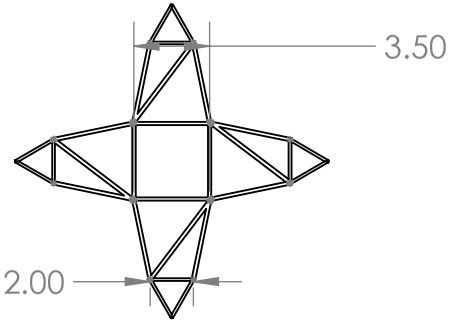

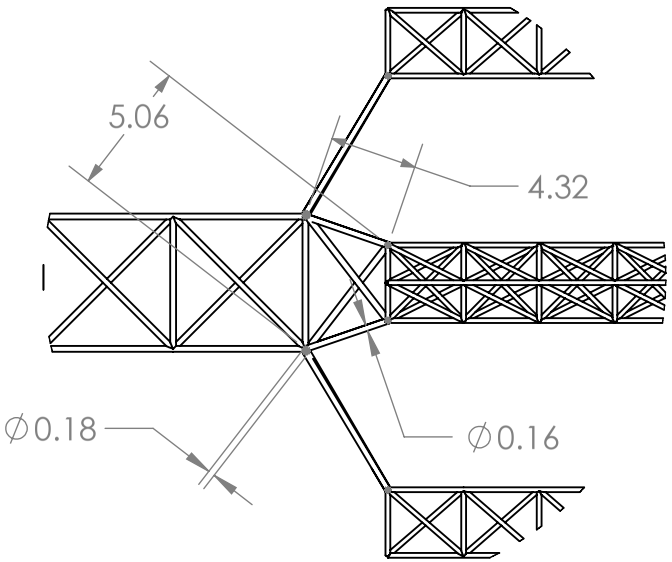

DETAIL B
SCALE 1 : 200

UNLESS OTHERWISE SPECIFIED:
DIMENSIONS IN INCHES

TOLERANCES:
.XX ±.01 .XXX ±.005
FRACTIONS ±1/64
ANGULAR MACHINED ±.5°
ANGULAR BEND ±1°
SURFACE FINISH
BREAK ALL EDGES .030

DO NOT SCALE

SHEET 1 OF 1

CASE SCHOOL OF ENGINEERING
CASE WESTERN RESERVE UNIVERSITY

TITLE: CONNECTION TRUSS			
SIZE: A	DATE: 5/6/2025	DRAWN BY: PMY	
MATERIAL: IM7/5555		PART #: 25A02032	REV: A

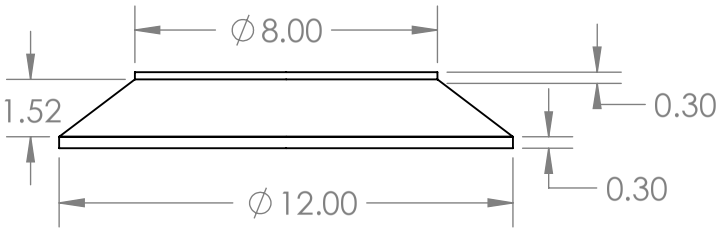

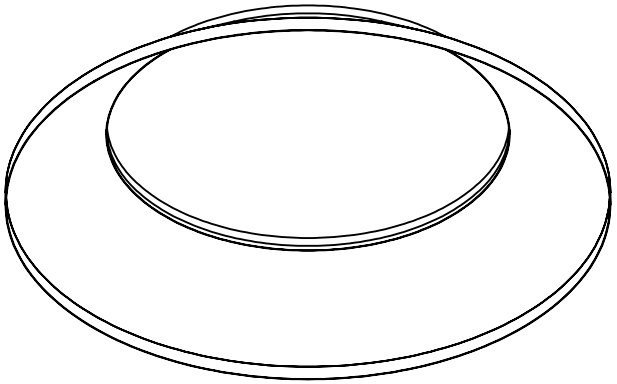

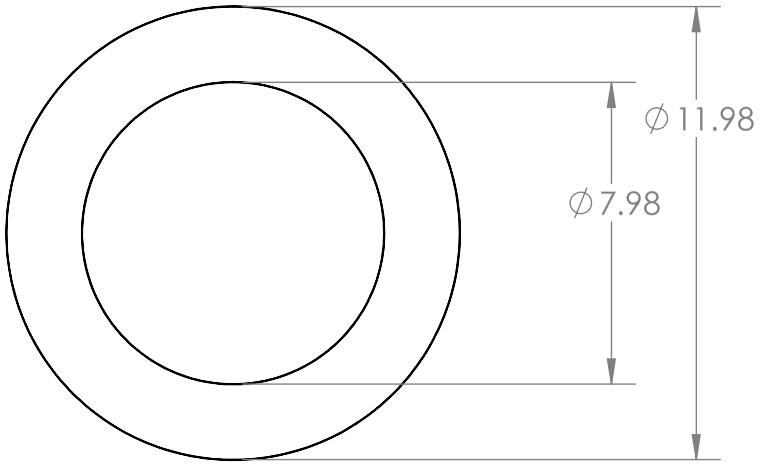

UNLESS OTHERWISE SPECIFIED:
DIMENSIONS IN INCHES

TOLERANCES:
.XX ±.01 .XXX ±.005
FRACTIONS ±1/64
ANGULAR MACHINED ±.5°
ANGULAR BEND ±1°
SURFACE FINISH
BREAK ALL EDGES .030

DO NOT SCALE

SHEET 1 OF 1

CASE SCHOOL OF ENGINEERING
CASE WESTERN RESERVE UNIVERSITY

TITLE:
PAYLOAD ADAPTER FOR LAUNCHES 1- 5

SIZE:	DATE:	DRAWN BY:	
A	5/6/2025	PMY	
MATERIAL:		PART #:	REV:
VARIOUS		25A02030	A

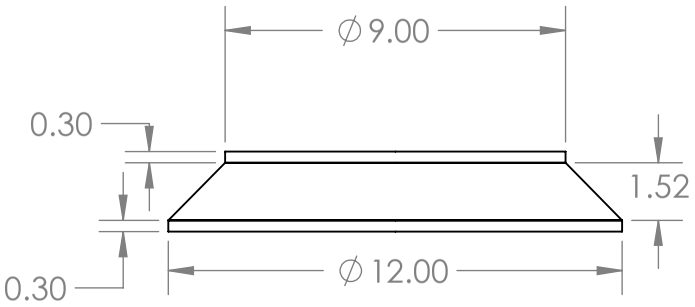

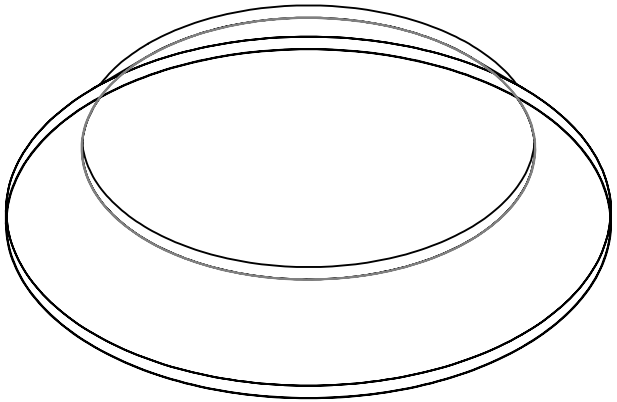

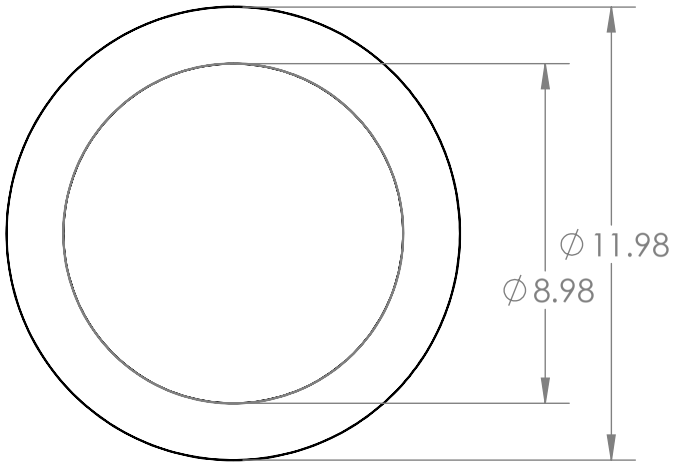

UNLESS OTHERWISE SPECIFIED:
DIMENSIONS IN INCHES

TOLERANCES:
.XX ±.01 .XXX ±.005
FRACTIONS ±1/64
ANGULAR MACHINED ±.5°
ANGULAR BEND ±1°
SURFACE FINISH
BREAK ALL EDGES .030

DO NOT SCALE

SHEET 1 OF 1

CASE SCHOOL OF ENGINEERING
CASE WESTERN RESERVE UNIVERSITY

TITLE:
PAYLOAD ADAPTER FOR LAUNCH 6

SIZE:	DATE:	DRAWN BY:	
A	5/6/2025	PMY	
MATERIAL:		PART #:	REV:
VARIOUS		25A02031	A

A.4 MMOD Cross Section View

Below is a drawing of the cross section of the IPV Hab shielding layers, including radiation shielding, MLI, and MMOD Shielding.

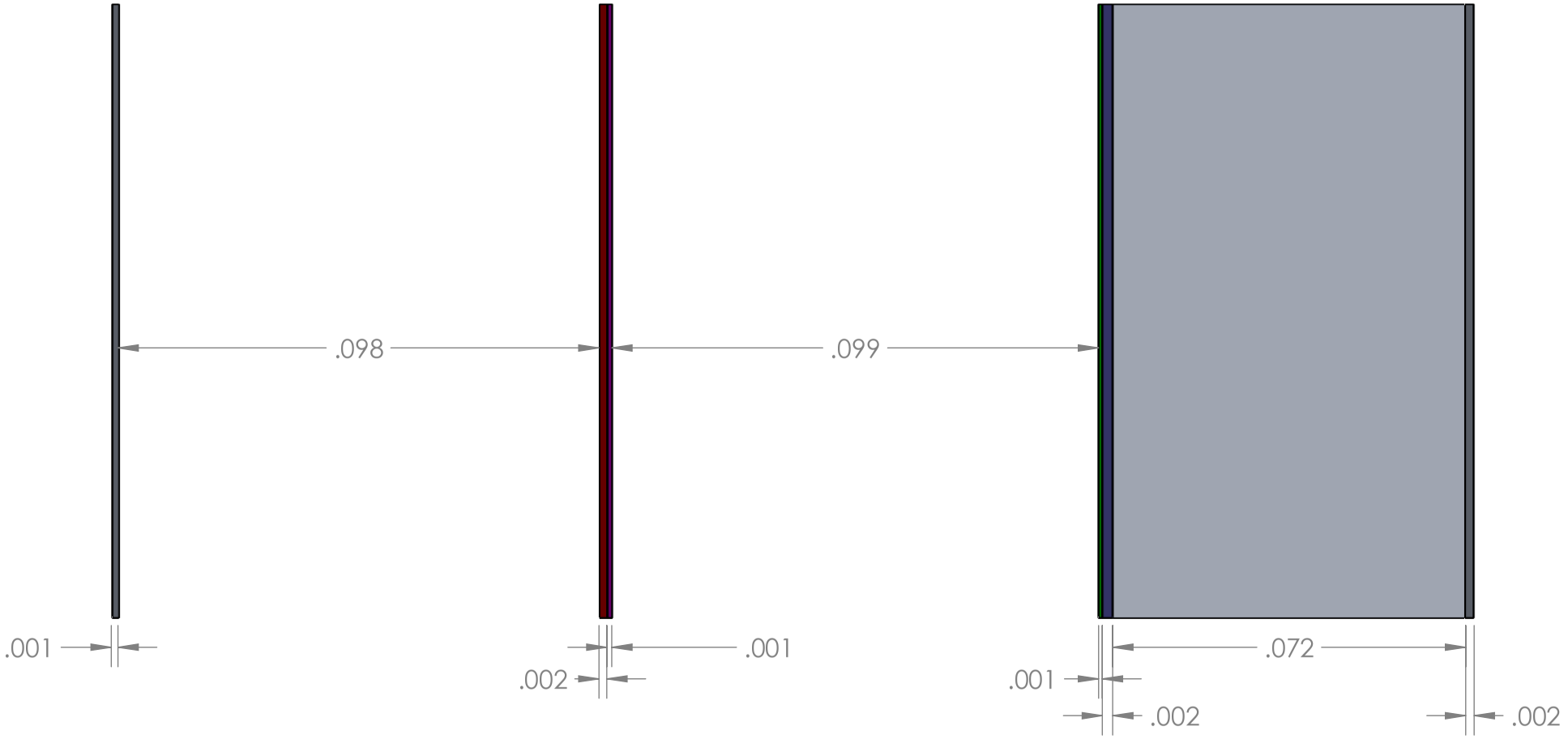

RIGHT TO LEFT (INSIDE TO OUTSIDE):

1. PRESSURE WALL (Al 2219-T37)
2. WATER RADIATION SHIELDING
3. INSULATION (ALUMINIZED MYLAR & DACRON)
4. MMOD REAR WALL (Al 2219-T87)
5. VACUUM
6. KEVLAR KM2 705
7. NEXTEL AF-52
8. VACUUM
9. MMOD BUMPER (Al 6061-T6)

UNLESS OTHERWISE SPECIFIED:
DIMENSIONS IN INCHES

TOLERANCES:
.XX ±.01 .XXX ±.005
FRACTIONS ±1/64
ANGULAR MACHINED ±.5°
ANGULAR BEND ±1°
SURFACE FINISH 125
BREAK ALL EDGES .030

DO NOT SCALE

SHEET 1 OF 1

CASE SCHOOL OF ENGINEERING
CASE WESTERN RESERVE UNIVERSITY

TITLE:
IPV HAB SHIELDING CROSS SECTION

SIZE:	DATE:	DRAWN BY:	
A	4/23/2025	A. BURIANEK	
MATERIAL:		PART #: 25A04000	REV:

B Propulsion Appendix

B.1 Nuclear Thermal propulsion

Constants	
Pressure (MPa)	0.225
Gas Density (kg/m3)	0.18
Liquid Density (kg/m3)	71.442

ASME B31.3 Process Piping

Total Ullage Mass (mT)	1.278627097
Material	Al 6061-T6 B210

Constants	
Allowable Stress (MPa)	96.5266
Quality Factor	0.8
Propellant Internal Pressure (MPa)	0.225
Ullage Internal Pressure (MPa)	1.2
Weld Joint Strength Reduction Factor	1
Propellant Piping Diameter	16.45887138
Ullage Piping Diameter	1.358190773
Materal Density (kg/m3)	2700
Coefficient	0.4

Earth Capture Tank	
Mass Flow Rate Out (kg/s)	38
Tank Volume (m3)	1215.213
# of Tanks	1
Volumetric Flow Rate (m3/s)	0.5319000028
Mass Flow Rate In (kg/s)	0.0957420005
Total Ullage Mass (mT)	0.2187384076

Earth Departure Tank	
Mass Flow Rate Out (kg/s)	38
Tank Volume (m3)	3566.039971
# of Tanks	4
Volumetric Flow Rate (m3/s)	0.5319000028
Mass Flow Rate In (kg/s)	0.0957420005
Total Ullage Mass (mT)	0.6418871948

Internal Pressure Sizing	
Propellent Flow Velocity (m/s)	25
Propellent Pipe Diameter (cm)	16.45887138
Ullage Max Speed (m/s)	800
Ullage Density in Pipe (kg/m3)	0.82604
Ullage Pipe Diameter (cm)	1.358190773
Propellent Pipe Thickness (mm)	0.2694401009
Ullage Propellant Pipe Thickness (mm)	0.1179876022
Total Piping Mass (kg)	20.16742912

Mars Capture Tank	
Mass Flow Rate Out (kg/s)	38
Tank Volume (m3)	1360.793506
# of Tanks	2
Volumetric Flow Rate (m3/s)	0.5319000028
Mass Flow Rate In (kg/s)	0.0957420005
Total Ullage Mass (mT)	0.2449428311

Launch Load Sizing	
Max Launch Load (g)	10
Thickness Guess (mm)	4
Area Guess (m^2)	0.002018017294
Mass of Propellant Piping (kg)	279.2181748
Mass of Ullage Piping (kg)	46.08232726
Total Piping Mass (kg)	325.300502
Propellant Pipng Axial Force (N)	27380.13422
Ullage Pipng Axial Force (N)	4518.833012
Material Allowable Stress (MPa)	289.58
Safety Factor	2
Allowable Stress w FoS (MPa)	144.79
Prop. Pipe Actual Stress (MPa)	13.56783924
Ullage Pipe Actual Stress (MPa)	2.239243948

Mars Departure Tank	
Mass Flow Rate Out (kg/s)	38
Tank Volume (m3)	961.4370221
# of Tanks	2
Volumetric Flow Rate (m3/s)	0.5319000028
Mass Flow Rate In (kg/s)	0.0957420005
Total Ullage Mass (mT)	0.173058664

Harmonia Engine Assembly Drawing

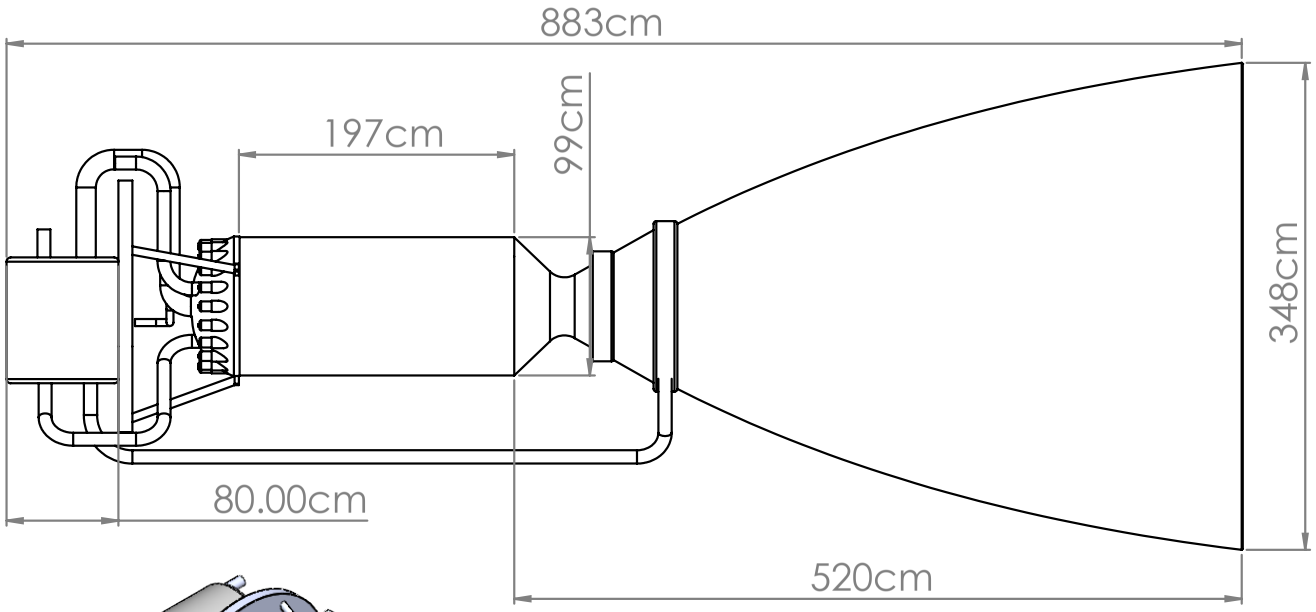

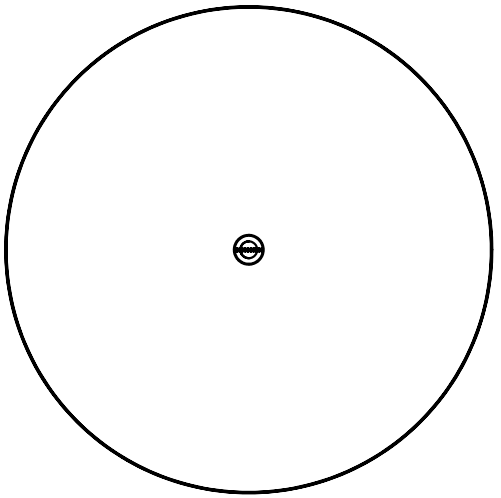

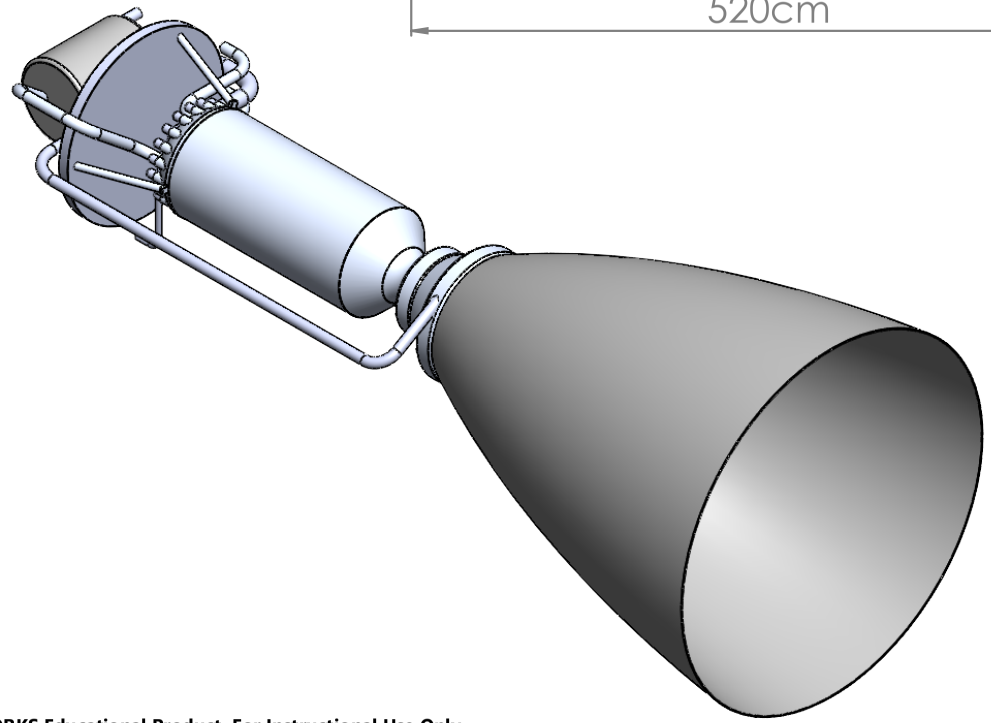

UNLESS OTHERWISE SPECIFIED:
DIMENSIONS IN INCHES

TOLERANCES:
.XX .01 .XXX .005
FRACTIONS 1/64
ANGULAR MACHINED .5
ANGULAR BEND 1
SURFACE FINISH
BREAK ALL EDGES .030

DO NOT SCALE

SHEET 1 OF 1

CASE SCHOOL OF ENGINEERING
CASE WESTERN RESERVE UNIVERSITY

TITLE:			
NTP Assembly			
SIZE: B	DATE: 4/23/2025	DRAWN BY: JMB548	
MATERIAL: N/A		PART #: PART NO.	REV: A

B.2 OMS

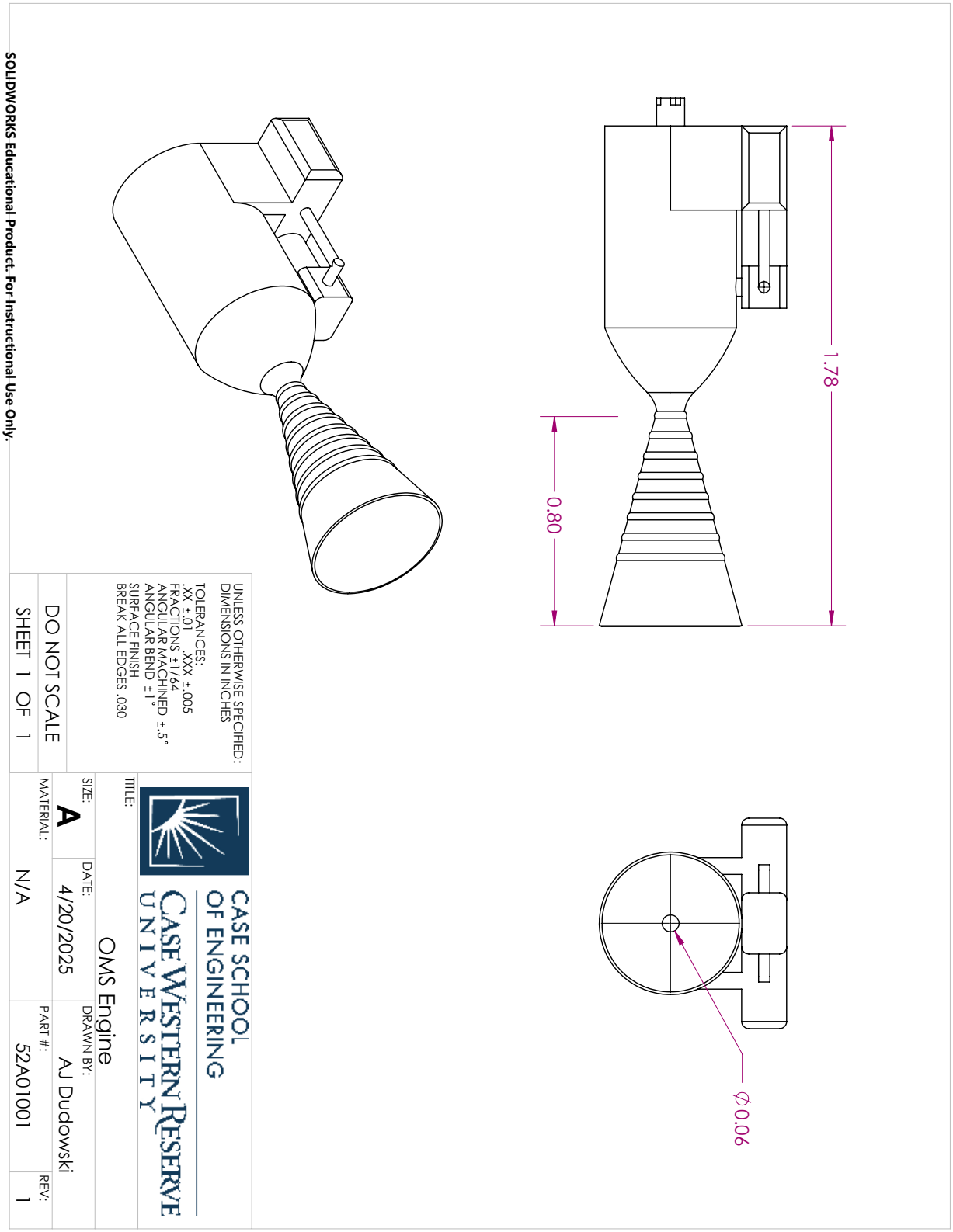

Figure B.1: OMS Engine Sketch

B.3 MDE

B.3.1 MDE Nozzle Contour MATLAB code

```
clc;clear; close all


E = 100;
R_t = 0.018 / 2; % (m)
R_e = 0.178 / 2; % (m)
Perc_bell = 0.8; % (%)
L_Ncone = (sqrt(E) - 1) * R_t / tand(15) * Perc_bell; % (m)



%% Entrant and exit section of throat
theta_entrant = -135:3:-90; % (degrees)
x_entrant = 1.5 * R_t * cosd(theta_entrant); % (m)
y_entrant = 1.5 * R_t * sind(theta_entrant) + 1.5 * R_t + R_t; % (m)

theta_n = 32; % (degrees)
theta_exit = -90:3:(theta_n - 90); % (degrees)
x_exit = 0.382 * R_t * cosd(theta_exit); % (m)
y_exit = 0.382 * R_t * sind(theta_exit) + 0.382 * R_t + R_t; % (m)



%% The Bell
t = 0:0.1:1;
Nx = x_exit(end);
Ny = y_exit(end);
Ex = L_Ncone;
Ey = R_e;
```

```
Calculate Qx

theta_e = 7.5; % (degrees)

m1 = tand(theta_n);

m2 = tand(theta_e);

C1 = Ny - m1 * Nx;

C2 = Ey - m2 * Ex;

Qx = (C2 - C1) / (m1 - m2);

Qy = (m1 * C2 - m2 * C1) / (m1 - m2);


%% Calculate bell curve

x_bell = (1 - t).^2 * Nx + 2 * (1 - t) .* t * Qx + t.^2 * Ex;

y_bell = (1 - t).^2 * Ny + 2 * (1 - t) .* t * Qy + t.^2 * Ey;


x = round([x_entrant x_exit x_bell], 5);

y = round([y_entrant y_exit y_bell], 5);


plot(x,y)

title('Maine Engine Nozzle Contour')

xlabel('(m)')

ylabel('(m)')

xlim([-0.05 0.3]);

ylim([-0.05 0.3]);


z = [];

for c = 1:length(x)

    z(c) = 0;

end


grid on
```

```
T = table(x',y',z')

writetable(T,'MainEngineNozzleContout.txt')


Nozzle material thickness

t = 0.1 * R_t * 2; % (m)
```

B.3.2 MDE CAD drawing

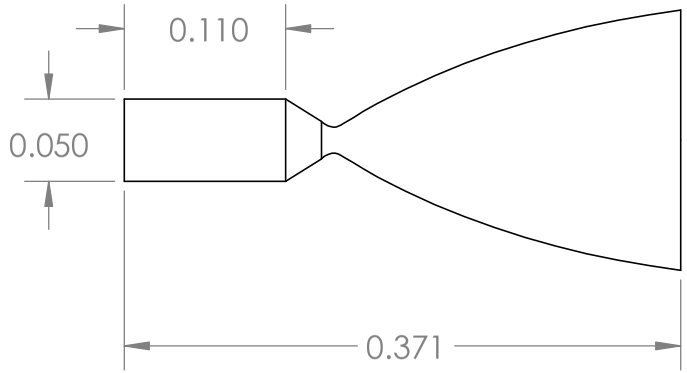

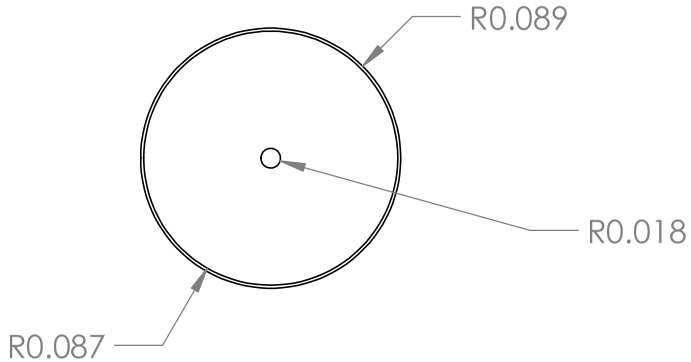

UNLESS OTHERWISE SPECIFIED:
DIMENSIONS IN INCHES

TOLERANCES:
.XX .01 .XXX .005
FRACTIONS 1/64
ANGULAR MACHINED .5
ANGULAR BEND 1
SURFACE FINISH
BREAK ALL EDGES .030

DO NOT SCALE

SHEET 1 OF 1

CASE SCHOOL OF ENGINEERING
CASE WESTERN RESERVE UNIVERSITY

TITLE:			
MDE ENGINE			
SIZE: A	DATE: 5/6/2025	DRAWN BY: JRS	
MATERIAL: PTAL3		PART #: 25A05004	REV: 1

B.4 RCS

B.4.1 RCS Nozzle MATLAB

```
clc;clear; close all


E = 60;
R_t = 0.0080 / 2; % (m)
R_e = 0.0625 / 2; % (m)
Perc_bell = 0.65; % (%)
L_Ncone = (sqrt(E) - 1) * R_t / tand(15) * Perc_bell; % (m)



%% Entrant and exit section of throat
theta_entrant = -135:3:-90; % (degrees)
x_entrant = 1.5 * R_t * cosd(theta_entrant); % (m)
y_entrant = 1.5 * R_t * sind(theta_entrant) + 1.5 * R_t + R_t; % (m)

theta_n = 37; % (degrees)
theta_exit = -90:3:(theta_n - 90); % (degrees)
x_exit = 0.382 * R_t * cosd(theta_exit); % (m)
y_exit = 0.382 * R_t * sind(theta_exit) + 0.382 * R_t + R_t; % (m)



%% The Bell
t = 0:0.05:1;
Nx = x_exit(end);
Ny = y_exit(end);
Ex = L_Ncone;
```

```
Ey = R_e;

%% Calculate Qx
theta_e = 12.5; % (degrees)
m1 = tand(theta_n);
m2 = tand(theta_e);
C1 = Ny - m1 * Nx;
C2 = Ey - m2 * Ex;
Qx = (C2 - C1) / (m1 - m2);
Qy = (m1 * C2 - m2 * C1) / (m1 - m2);

%% Calculate bell curve
x_bell = (1 - t).^2 * Nx + 2 * (1 - t) .* t * Qx + t.^2 * Ex;
y_bell = (1 - t).^2 * Ny + 2 * (1 - t) .* t * Qy + t.^2 * Ey;

x = round([x_entrant x_exit x_bell], 5);
y = round([y_entrant y_exit y_bell], 5);

plot(x,y)
title('RCS Nozzle Contour')
xlabel('(m)')
ylabel('(m)')
xlim([-0.01 0.08]);
ylim([-0.01 0.08]);

z = [];
for c = 1:length(x)
    z(c) = 0;
end
```

```
grid on


T = table(x',y',z')
writetable(T,'RCSEngineNozzleContout.txt')


Nozzle material thickness
t = 0.1 * R_t * 2; % (m)
```

B.4.2 RCS CAD drawing

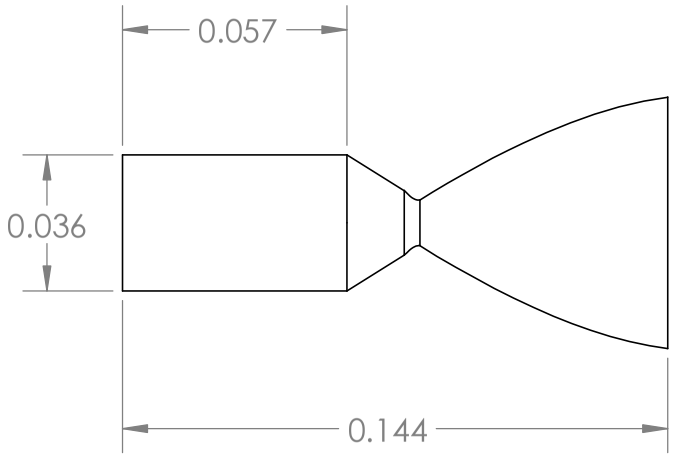

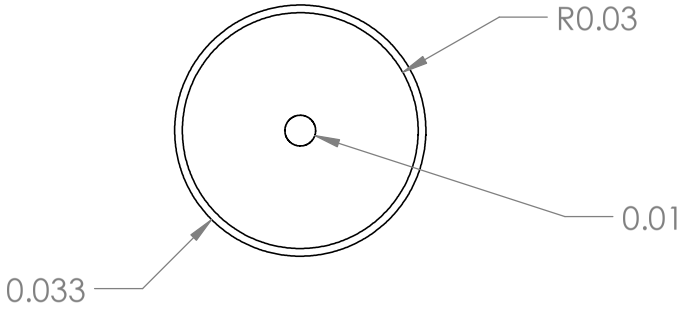

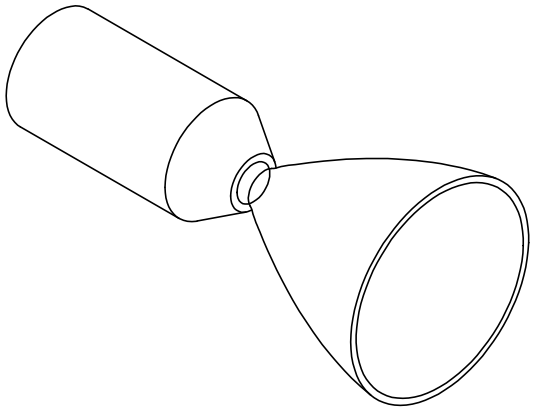

UNLESS OTHERWISE SPECIFIED:
DIMENSIONS IN INCHES

TOLERANCES:
.XX .01 .XXX .005
FRACTIONS 1/64
ANGULAR MACHINED .5
ANGULAR BEND 1
SURFACE FINISH
BREAK ALL EDGES .030

DO NOT SCALE

SHEET 1 OF 1

CASE SCHOOL OF ENGINEERING
CASE WESTERN RESERVE UNIVERSITY

TITLE: RCS ENGINE			
SIZE: A	DATE: 5/6/2025	DRAWN BY: JRS	
MATERIAL: PTAL3		PART #: PART NO.	REV: 1

C Trajectory Analysis Appendix

C.1 Finite Burns

Finite Burn MATLAB Code Parent Function (finiteburnv2.m)

```
i = 7; %minutes (i is starting time in minutes)


%INPUT ALL DIMENSIONAL PARAMETERS
g = 9.80665;
h = 450e3; %orbit height in meters
Rp = 6378e3; %radius of the planet in m
R_ref = Rp+h; %m radius of earth + orbit altitude (m)
mu = 3.986e14; %m3s-2
V_c = sqrt(mu/R_ref); %m/s
Isp = 950;
T = 351*3*1000; %thrust in N
Mi = 215e3; %initial mass before thrusting in kg
c3dep = 8.688; %km2/s2


%     1  2    3  4   5   6 7
DP = [g R_ref mu V_c Isp T Mi];


u = 0; %u is steering approach (0 is tangential)
converged = 0;
n = 1;
while converged == 0
    [y, t, NDOut(n,:),DOut(n,:)] = fb_run(i, DP,u);


    error = abs(DOut(n,1) - c3dep);
```

```
    if  error < 0.08
        converged = 1;
    else
        converged = 0;
    end
    i = i+0.02; % increment time by 0.0x minutes
    n = n+1;
end


%RESULTS

%Losses vs. C3 and Burn Time Table
Losses = DOut(n-1,2)-DOut(n-1,3);
DOut(n-1,1)
%T=table(DOut(:,1),Losses,i',DOut(:,2), DOut(:,3),'VariableNames',{'
   C3', 'Finite Loss (m/s)', 'Burn Time (mins)','Finite dV','Impulse
   dV'});
disp(['Burn Time is:  ',num2str(i),' minutes']);
disp(['Finite Losses:  ',num2str(Losses),' m/s']);
disp(['Achieved C3:  ',num2str(DOut(n-1,1)),' km2/s2']);

%coasting phase math for r vs theta
th_c_end = NDOut(n-1,4);

th_c = y(end,4):0.001:2.34;
for i = 1:length(th_c)
r_c(i) = (NDOut(n-1,2)*R_ref) ./ (1 + NDOut(n-1,3)*cos(th_c(i)));
end
```

```
figure(1)
whole = 0:0.01:2*pi;
Rp_orb = ones(length(whole))*Rp;
R_ref_orb = ones(length(whole))*R_ref;

pp1 = polarplot(whole, Rp_orb,'g','LineWidth',4); %Earth
hold on
pp2 = polarplot(whole, R_ref_orb,'b','LineWidth',2.5); %
pp3 = polarplot(y(:,4), y(:,1)*R_ref,'r--','LineWidth',2.5);

% polarplot(th_c,r_c,'r')
title('Earth Capture Finite Burn with Tangential Steering')
subtitle('Finite Losses of Approximately 80 m/s, Burn Time of 10
   minutes')
legend([pp1(1), pp2(1), pp3(1)],'Earth Surface','450km LEO','
   Thrusting Period')
hold off
```

Finite Burn MATLAB Code Child Function (fbrun.m)

```
%V2: clear nondim/dimensional outputs, more user friendly
function [y,t, NDOut, DOut] = fb_run(time, DP, u)

%y(1) = r, dAdt(1) = r'
%y(2) = v, dAdt(2) = v'
%y(3) = alpha
%y(4) = theta

%INPUT (dimensional inputs)
time = time*60; %time turned into seconds

% dimensionless parameters
vj = DP(1)*DP(5)/DP(4);
a_po = (DP(6))/(DP(7)*(DP(3)/(DP(2)^2)));
tau = (DP(4)/DP(2))*time;

%time span (non dimensional time)
tspan = [0.01 tau];

%Initial conditions for circular orbit // work on getting IC's for
%elliptical orbit
y0 = [1; 1; 0; 0];

%Solve
[t, y] = ode45(@(t,y) odeFB(a_po, vj,u, t,y), tspan, y0);

%vinfsq is non dimensional velocity parameter
vinfsq = y(end,2)^2 - (2/(y(end,1)));
```

```
%COASTING PHASE
p_bo = (y(end,1)^2) * (y(end,2)^2) * (cos(y(end,3))^2 );
e_bo = (1 + p_bo*vinfsq)^(0.5);
th_ch = y(end,4) + acos(-1/e_bo) - acos( ((p_bo/y(end,1))-1)/e_bo );

%finite burn delta v
NDdvfb = vj * log( 1 / ( 1 - ((a_po*tau)/vj)) );
Ddvfb = NDdvfb*DP(4);

%impulse burn delta v
NDdvimp = sqrt(vinfsq + 2) - sqrt(1);
Ddvimp = NDdvimp*DP(4);

%c3
c3 = (vinfsq*DP(4)^2)/(1e6);

%Packaging Non Dimensional Parameters for Output
%          1      2   3    4       5      6
NDOut = [vinfsq p_bo e_bo th_ch NDdvfb NDdvimp];

%Packing Dimensional Parameters for Output
DOut = [c3 Ddvfb Ddvimp];

end
```

Finite Burn MATLAB Code Child-Child Function (odeFB.m)

```
%(Non-Dim Params) a_po is init accel, vj jet vel, u steering, t -
%tau

function dydt = odeFB(a_po,vj,u, t, y)
    r = y(1);
    v = y(2);
    al = y(3);
    th = y(4);

    a = a_po / (1 - (a_po*t)/(vj));

    drdt = v*sin(al);
    dvdt = a*cos(u) - sin(al)/(r^2);
    daldt = ((a*sin(u))/v) + (v^2 - (1/r))*(cos(al)/(r*v));
    dthdt = (v/r)*cos(al);

    dydt = [drdt; dvdt;  daldt; dthdt];

end
```

C.2 Deimos Maneuver

To Deimos					From Deimos to IPV				
Deimos orbit					Deimos orbit				
a	23460	km			a	23460	km		
mu	42828	km^3/s^2			mu	42828	km^3/s^2		
v	1.351	km/s			v	1.351	km/s		
New Orbit					New Orbit				
a	23410	km			a	23510	km		
mu	42828	km^3/s^2			mu	42828	km^3/s^2		
v	1.353	km/s			v	1.350	km/s		
Relative Velocity and Time					Relative Velocity and Time				
DeltaV	0.001497	km/s	1.497	m/s	DeltaV	0.001492	km/s	1.492	m/s
Rel Velocity (tangent)	0.001442	km/s	1.442	m/s	Rel Velocity (tangent)	0.001438	km/s	1.438	m/s
Rel Velocity (normal)	0.0004	km/s	0.40	m/s	Rel Velocity (normal)	0.0004	km/s	0.40	m/s
Acceleration	0.00005	km/s^2	0.05	m/s^2	Acc	0.0001	km/s^2	0.05	m/s^2
Distance between orbits	50.00	km	θ	15.50	Distance between orbits	50.00	km	θ	15.55
Acceleration distance (total)	0.0224	km	22.39	m	Acceleration distance	0.02	km		
Acceleration distance (tangent)	0.0216	km	21.57	m	Acceleration distance (tangent)	0.02	km		
Acceleration distance (normal)	0.0060	km	5.98	m	Acceleration distance (normal)	0.01	km		
Glide distance (total)	49.98	km			Glide distance (total)	49.98			
Glide distance (tangent)	48.16	km			Glide distance (tangent)	48.15			
Glide distance (normal)	13.36	km			Glide distance (normal)	13.40			
Time to new orbit	33394.47	s	9.28	hr	Time to new orbit	33493.84	s	9.30	hr
Distance left to move in lower orbit	3.68	km			Distance left to move in lower orbit	3.70			
Time in lower orbit	2552.55	s	0.71	hr	Time in lower orbit	2575.86	s	0.72	hr
Travel time	69341.50	s	19.26	hours	Travel time	69563.53	s	19.32	hours
Total delta V	0.004	km/s	3.79	m/s	Total delta V	0.004	km/s	3.78	m/s
Force Calculations (to Deimos) X 2					Force Calculations (to IPV) X 2				
Thrust	500	N			Thrust	500	N		
mdot	0.16	kg/s			mdot	0.16	kg/s		
Veff	3177.122058	m/s			Veff	3177.122058	m/s		
Isp	323.964725	s			Isp	323.964725	s		
mo/mf	1.000471161				mo/mf	1.000469764			
mo	10000	kg			mo	9995.290609	kg		
mf	9995.290609	kg			mf	9990.597383	kg		
mfuel	4.70939062	kg			mfuel	4.69322645			
Burn time	29.92461764				Burn time	29.82190655			

KEY	input	ouput	yikes	holy shit

INPUTS		OUTPUTS		
Mission Information				
# of Launches	5	Total Delta V	11.8569	
Mass Left in LEO	0			
Isp	951			
Engine Information				
Thrust/Engine	333616.6211	*# Engines Required for:*		
Mass/Engine	9	Earth Dep.	2	
Earth Dep. BT	2400	Mars Cap.	2	
Mars Cap. BT	2000	Mars Dep.	1	
Mars Dep. BT	2000	Earth Cap.	2	
Earth Cap. BT	2000	# of Engines Required	2	
		Mass of Engines	18	
Tank Information				
Number of Tanks For:		*Propellant w/ BO Required for:*		
Earth Dep.	4	Earth Dep.	256.54	
Mars Cap.	2	Mars Cap.	96.41	
Mars Dep.	2	Mars Dep.	68.12	
Earth Cap.	1	Earth Cap.	86.1	
Tank Radius	4.9	Ullage Propellant	1.278627097	
Propellant Margin	0.03	Total	508.45	
Mass Used During:		*Tank Lengths for EACH TANK:*		
Earth Dep.	6.4324	Earth Dep. Tanks	14.828	
Mars Cap.	31.742162	Mars Cap. Tanks	12.03	
Mars Dep.	6.4324	Mars Dep. Tanks	9.382	
		Earth Cap. Tanks	19.119	
		Tank Masses for ALL TANKS (including insulation and MMOD):		
		Earth Dep. Tanks	41.17	
		Mars Cap. Tanks	15.47	

		Mars Dep. Tanks	11.054
		Earch Cap. Tanks	14.512
		Total Tank Mass	82.21
DeV and Hab Information			
		Mass Required for:	
		Food	6.22
		Oxygen	6.92
		Nitrogen	1.77
		Water	9.23
		Water Recycling Sys.	1.39
		Total DeV Mass (no supplies)	20.466862
		Total Hab Mass (no supplies)	16.73638754
Center of Mass			
		Center of Mass (X Direction)	17.63527271
		Center of Mass (Y Direction)	0
		Center of Mass (Z Direction)	0
Structural Mass Information			
Total Launch A Mass	120	Total Truss Structure Mass	18.303
Total Launch B Mass	128	Total Structure Connection Mass	0
Axial Launch Loading (g's)	4.1	Total Structural Mass	18.303
Lateral Launch Loading (g's)	3		
Payload Adapters Information			
Mass of Full Payload	138	Mass of 1 Payload Adapter	1.248
		Total Payload Adapter	7.550

Units in (Kg Km s) Unless Specified As Days/Yrs

FB = .417

Earth Departure	
μ_Earth	3.99E+05
R_LEO	6,780
V_circ	7.667
V_∞	2.948
a	4.59E+04
e	1.148
b	2.58E+04
ψ	29.40
V_Hyp,P	11.24
ΔV_D	**3.778**
ΔV_D_simul	3.819
C3	8.688

Mars Capture	
μ_Mars	4.28E+04
V_∞	2.66
R_MPO	23,458
V_circ	1.351
a	6,062
e	4.870
b	2.89E+04
ψ	78.15
V_Hyp,P	3.27
ΔV_C	**1.922**
ΔV_C_simul	2.130

9.81

Inputs	
Number of SLS	5
Isp	951
Mass Loss	0

Launches to LEO	
#	Mass Achievable
1	150,000
2	300,000
3	450,000
4	600,000
5	750,000
6	900,000

Isp Requirements	
M_0 1 -> 2	**750,000**
Isp	951
M_i / M_f	1.50605
M_D	497,992
M_i / M_f	1.25658
M_C	396,308
M_Jettisoned	0
M_0 2 -> 1	396,308
M_i / M_f	1.25658
M_D	315,386
M_i / M_f	1.49943
M_C (Final Mass)	**210,337**
LEO Assembled Dry Mass	**242,832**

ΔV Requirements	
ΔV E -> M	5.95
ΔV M -> E	5.91
ΔV_tot w/	**11.8569**

Fuel Masses	
Departure	**256,540**
Mars Cap	**96,412**
Mars Dep	**68,118**
Earth Cap	**86,098**
Total Fuel	**507,168**

242,832

Timing		
Period	(Days)	(Yrs)
T1	365	1.00
T2	687	1.88
S	780	2.14
α / π	0.42	-
t_w	**454**	1.24
t_tot	**972**	**2.66**

Hohmann Transfer	
μ_Sun	1.33E+11
a_E	1.496E+08
V_A	29.8
a_M	2.28E+08
V_B	24.20
ΔV_A	2.95
ΔV_B	2.66
ΔV_Total	**5.61**
e_T	0.21
a_T	1.89E+08
t_T (s)	2.24E+07
t_T (days)	**259**

Faster Ellipse Tranfer	
μ_Sun	1.33E+11
a_E	1.50E+08
V_A	29.8
a_M	2.28E+08
V_B	24.20
ΔV_A	
ΔV_B	
ΔV_Total	**0.00**
e_T	0.21
a_T	1.89E+08
t_T (s)	2.24E+07
t_T (days)	**259**

ANGLES		
Plane rel Plane	(rad)	(deg)
Earth tilt rel ecliptic	0.408	23.40
KSC launch rel equator	0.499	28.60
Mars tilt rel ecliptic	0.440	25.19
Mars orbit inclination relative to ecliptic	0.032	1.85
KSC launch rel ecliptic	0.091	5.20
KSC launch rel Mars orbit	0.059	3.35

Useful Constants	
1 AU	1.496E+08
R_E	6,378.00
R_M	3,389.50
h_D	20,068.00
g_0	9.81

Useful Formulas
ΔV = g_o * Isp * ln(Mi/Mf)
Mi/Mf = exp[ΔV / (g_o * Isp)]
Plane Change: ΔV = V sin θ/2

Assumptions:

Tank Dimensions and mass only include tank and boil off itself, Values will change when takeoff insulation is added

Inputs

Per Burn

Burn 1 - Earth Depature		Units
Tank #	4	
Tank Radius	4.9	m
Tank Jettison (Y/N)	Y	
Other Mass Jettisoned	6.4324	mT

Burn 2 - Mars Capture		
Tank #	2	
Tank Radius	4.9	m
Tank Jettison (Y/N)	Y	
Other Mass Jettisoned	31.74216	mT

Burn 3 - Mars Departure		
Tank #	2	
Tank Radius	4.9	m
Tank Jettison (Y/N)	Y	
Other Mass Jettisoned	6.4324	mT

Burn 4 - Earth Capture		
Tank #	1	
Tank Radius	4.9	m
Tank Jettison (Y/N)	Y	
Other Mass Jettisoned	0	mT

Note:

Boil Off has been added. In order to adjust Boil off values change inputs in "MLI Clacs" sheet

Outputs

Per Burn

Burn 1 - Earth Depature		Units
LH2 Mass	256.54	mT
Tank Vol.	891.510	m^3
Tank Length	14.828	m
Mass of Empty Tank	6.392	mT
Total Mass of All Empty Tanks	25.57	mT
Depart Mass	465.99	mT
Total Mass Per Tank	70.53	mT

Burn 2 - Mars Capture		
LH2 Mass	96.41	mT
Tank Vol.	680.40	m^3
Tank Length	12.03	m
Mass per tank	5.21	mT
Total Mass	10.41	mT
Capture Mass	327.67	mT
Total Mass Per Tank	53.41	

Burn 3 - Mars Departure		
LH2 Mass	68.12	mT
Tank Vol.	480.719	m^3
Tank Length	9.382	m
Mass per tank	4.085	mT
Total Mass	8.170	mT
M Depart Mass	245.126	mT
Total Mass Per Tank	38.14	mT

Burn 4 - Earth Capture		
LH2 Mass	86.1	mT
Tank Vol.	1215.213	m^3
Tank Length	19.119	m
Mass per tank	8.209	mT
Total Mass	8.209	mT
E Capture Mass/ Final Mass	151.043	mT
Total Mass Per Tank	94.31	mT

Overall Totals

Item		Units
LH2 Mass	507.2	mT
Tank Mass	52.36	mT
Total Tank/LH2 Mass	559.5	mT
Remaining Mass	**151.0**	mT

AVG BOR	
Tank 1	0.007
Tank 2	0.007
Tank 3	0.007
Tank 4	0.007
Tank 5	0.005
Tank 6	0.000
Tank 7	0.004
Tank 8	0.000
Tank 9	0.004
Total Avg BOR	0.00

Tanks 1-4 occurs Boil off for t_assm time till exit burn

D Thermal Control Appendix

D.1 Additional Equations Used for NaK Analysis

Below are a list equations taken from "SODIUM-NaK Engineering Handbook" that give thermal properties of Eutectic NaK as a function of temperature [88]. Scaling values for these equations into SI units has been provided at the end of the equation. Additionally, units have been provided next to the following equations for easy reference. Note that some equations require inputs with a specific set of units, which has been specified in corresponding footnotes.

$$c_p = \left[0.2320 - 8.82 \times 10^{-5}(T_m) + 8.2 \times 10^{-8}(T_m)^2\right] \cdot 4200 \qquad \left[\mathrm{J/kg \cdot K}\right]^{2} \tag{D.1}$$

$$\rho = \left[-2.4545 \times 10^{-4}(T_m) + 0.85\right] \cdot 1000 \qquad \left[\mathrm{kg/m^3}\right]^{3} \tag{D.2}$$

$$k = \left[0.214 + 2.07 \times 10^{-4}(T_m) - 2.2 \times 10^{-7}(T_m)^2\right] \cdot 100 \qquad \left[\mathrm{W/m \cdot K}\right]^{4} \tag{D.3}$$

$$\mu = \left[0.082\ \rho^{1/3}\ \exp\left(\frac{979\ \rho}{T_m}\right)\right] \cdot 10^{-3} \qquad \left[\mathrm{Pa \cdot s}\right]^{5} \tag{D.4}$$

Note that μ is the absolute viscosity of the fluid, and that this can be used to calculate the kinematic viscosity, ν, of the fluid using the following equation:

[2] T_m must be in °C
[3] T_m must be in °C
[4] T_m must be in °C
[5] T_m must be in K, ρ must be in g/cm^3

$$\nu = \frac{\mu}{\rho} \tag{D.5}$$

D.2 Additional Radiator Figures

The following list of figures shows how temperature changes for various parameters for radiators in the x and y-directions shown in Fig. D.1. The bimodal radiator plots are not shown here, as they are already listed in Section 10.4.3.

Plots for DEV Power Cycle Radiators

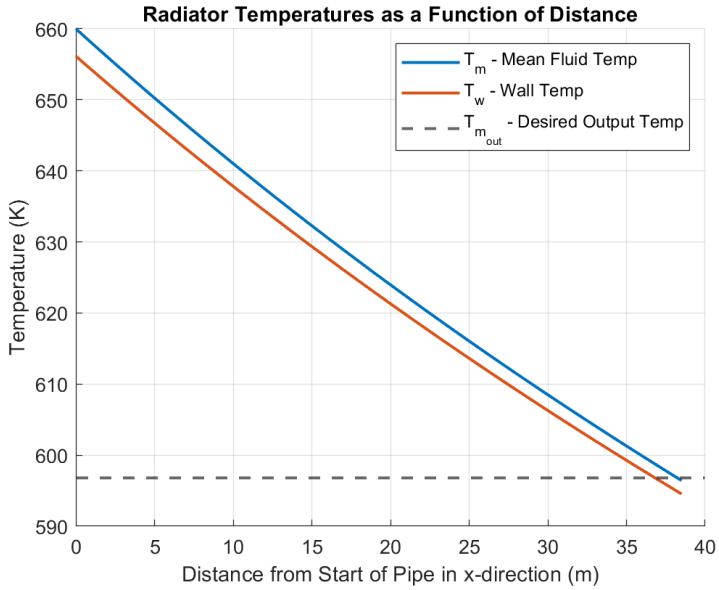

Figure D.1: DEV Power Radiator Temperatures in x-direction

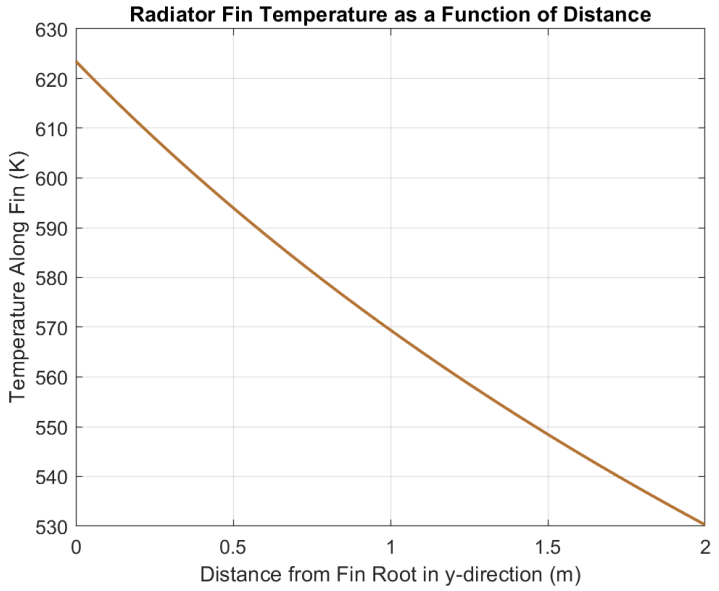

Figure D.2: DEV Power Radiator Temperature in y-direction

Plots for IPV Habitat Solar Heat Rejection Radiators

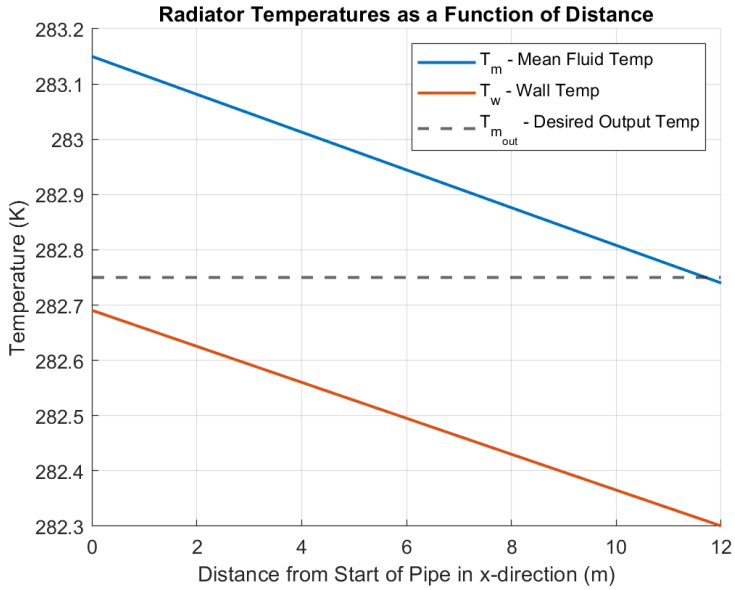

Figure D.3: IPV Hab Solar Heat Rejection Temperatures in x-direction

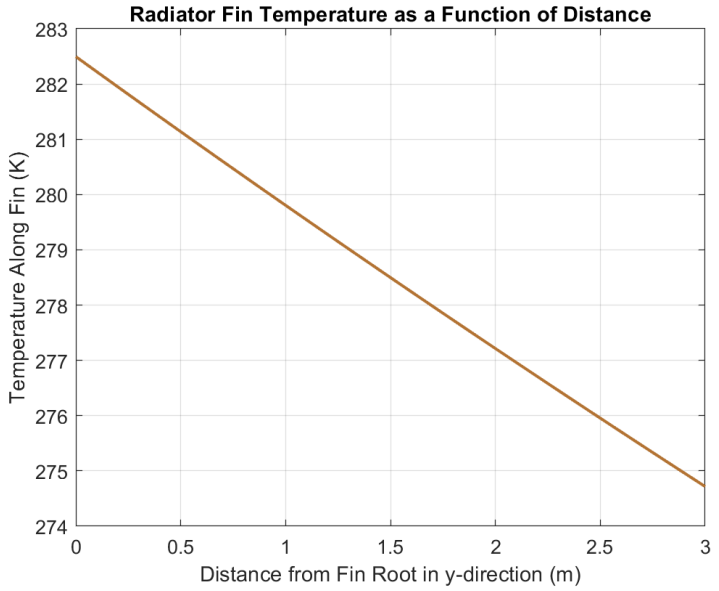

Figure D.4: IPV Hab Solar Heat Rejection Temperatures in y-direction

Plots for DEV Solar Heat Rejection Radiators

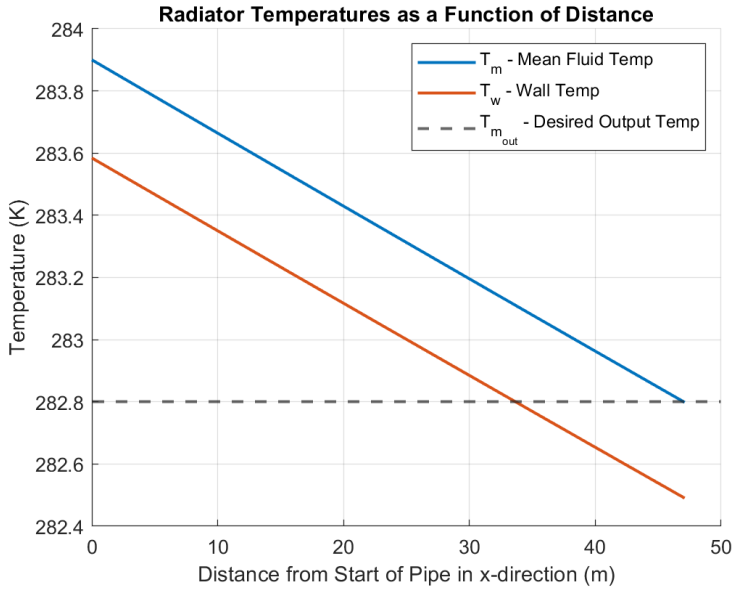

Figure D.5: DEV Solar Heat Rejection Temperatures in x-direction

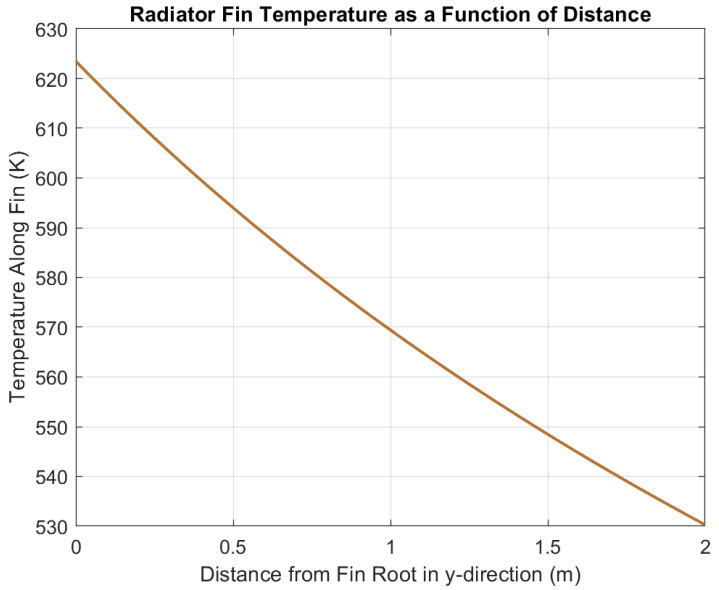

Figure D.6: DEV Solar Heat Rejection Temperatures in y-direction

D.3 MatLab Code Listing for Radiator Analysis

The following lists the code used to calculate parameters for the radiator analysis. The specific code listed below was used for the bimodal radiator analysis. The only difference between this code and other analyses is the fact that the heat transfer coefficient equation is different for ammonia (as NaK is used for bimodal analysis), and general inputs such as the mean input and output temperatures vary per radiator analysis.

```
% Radiator Sizing | EMAE 356 - Aerospace Design
% Created by Nate Berntson on 4/7/2025



%% Case 1: Simple Tube
clc; clear; close all

%%% Inputs
% Lengths
delta_x = 0.5; %m - "Differential" Element length
D_i = 0.05; %m - Interior Diameter of Tube
t_wall = 0.005; %m - Thickness of Tube Wall
D_o = D_i + 2*t_wall; %m - Calc for Outer Tube Diameter
w = 0.65; %m - Length of Radiator

% Mass Flow Rate
m_dot = 3; %kg/s - Mass Flow Rate

% Temperature
T_m_in = 283.15; %K - Input Mean Temperature of Fluid
T_m_out = 282.75; %K - Desired Outpet Mean Temperature of Fluid
```

```
% Material Properties at a Given Temperature
epsilon_r = 0.9; % Emmisivity of Radiator


%%% Constants
sigma = 5.670374419e-8; - Stefan-Boltzmann Constant
T_s = 3; %K - Temperature of Space


%%% Calculation While Loop for Fluid and Radiation
T_m = T_m_in;
n = 1;
while T_m > T_m_out
    % Determine Thermodynamic States
    P_set = 500; %kPa
    c_p_f(n) = refpropm('C', 'T', T_m(n), 'P', P_set, 'ammonia'); %J/
       kg*K - Specific Heat Capacity of Fluid
    k_f(n) = refpropm('L', 'T', T_m(n), 'P', P_set, 'ammonia'); %W/m*
       K - Thermal Conductivity of Fluid
    mu_f(n) = refpropm('V', 'T', T_m(n), 'P', P_set, 'ammonia'); %Pa*
       s - Absolute (Dynamic) Viscosity of Fluid
    rho_f(n) = refpropm('D', 'T', T_m(n), 'P', P_set, 'ammonia'); %kg
       /m^3 - Density of Fluid
    alpha_f(n) = k_f(n)/(rho_f(n)*c_p_f(n)); %m^2/s - Thermal
       Diffusivity of Fluid
    nu_f(n) = mu_f(n)/rho_f(n); %m^2/s - Kinematic Viscocity of Fluid

    % Calculate h_f - Heat Transfer Coefficient of Fluid
    V_f(n) = m_dot/(rho_f(n)*1/4*pi*D_i^2); %m/s - Fluid Velocity
```

```
    Re(n) = (V_f(n)*D_i)/nu_f(n); % Reynolds Number
    Pr(n) = nu_f(n)/alpha_f(n); % Prandtl Number
    Pe(n) = Re(n)*Pr(n); % Peclet Number
    h_f(n) = 0.023*(k_f(n)/D_i)*(Re(n))^(4/5)*(Pr(n))^0.3; %W/(m2K) -
        Heat Transfer Coeff for Ammonia

    % Solve for T_w Numerically
    syms T_w_sym
    T_m_num = T_m(n);
    h_f_num = h_f(n);
    func_T_w = delta_x*pi*D_i*h_f_num*(T_m_num - T_w_sym) == delta_x
       *(pi*D_o + w)*epsilon_r*sigma*(T_w_sym^4 - T_s^4); %Q_dot_conv
        = Q_dot_rad, Assuming Radiating only on 1 side
    T_w_sol = double(solve(func_T_w));
    T_w(n) = min(abs(real(T_w_sol)));

    % Solve for Next T_m
    Q_dot(n) = delta_x*pi*D_i*h_f(n)*(T_m(n) - T_w(n));
    T_m(n+1) = -Q_dot(n)/(m_dot*c_p_f(n)) + T_m(n);

    % Iterate n
    n = n + 1;

end


%%% Calculate Totals
L = delta_x*(n-1) %m - Tube Total Length
A = L*w %m^2 - Total Area
```

```
%%% Plot Results for T_m and T_w
x_w = linspace(0, L, n-1);
x_m = linspace(0, L, n);

hold on
lwid = 1.5;
figure(1)
plot(x_m, T_m, 'LineWidth', lwid)
plot(x_w, T_w, 'LineWidth', lwid)
yline(T_m_out, '--', 'LineWidth', lwid)
hold off

grid on
title('Radiator Temperatures as a Function of Distance')
xlabel('Distance from Start of Pipe in x-direction (m)')
ylabel('Temperature (K)')
legend('T_m - Mean Fluid Temp', 'T_w - Wall Temp', 'T_{m_{out}} -
   Desired Output Temp')




%% Case 2: Consider Conduction

%%% New Inputs
t = 0.005; %m - Thickness of Fin
T_fin_set = 281; %K - End of Fin Temperature
```

```
w_set = 3; %m - Fin Length Set
delta_x = 0.01; %m - Smaller delta_x Increment
k = 237; %W/mK - Thermal Conductivity of Fin Material


%%% Find Log Mean Temp
% Find Average T_w Temperature
T_wbar = mean(T_w);


%%% Calculation While Loop for Conduction and Radiation of Fin
T_x = T_wbar;
w = 0; % Reset w from Case 1
n = 1;
while w < w_set
    % Solve for T_x Numerically
    syms T_x_sym
    T_x_num = T_x(n);
    func_T_x = -k*t*T_x_sym - epsilon_r*sigma*delta_x^2*T_x_sym^4 ==
       -epsilon_r*sigma*delta_x^2*T_s^4 - k*t*T_x_num; %Q_dot_cond =
       Q_dot_rad
    T_x_sol = double(solve(func_T_x));
    T_x(n+1) = min(abs(real(T_x_sol)));

    % Pick Distance at Which T_fin_set found
    if T_x(n+1) > 0.999*T_fin_set && T_x(n+1) < 1.001*T_fin_set
        w_sel = delta_x*n
    end
```

```
    % Iterate n
    w = delta_x*n;
    n = n + 1;

end


%%% Determine Overall Dimensions from This Analysis
A_sel = w_sel*L
N = A/A_sel %Ratio should be 1 if analyses match


%%% Plot Results
lwid = 1.5;
figure(2)
x_x = linspace(0, w_set, n);
plot(x_x, T_x, 'LineWidth', lwid, 'Color', [0.7 0.45 0.2])

grid on
title('Radiator Fin Temperature as a Function of Distance')
xlabel('Distance from Fin Root in y-direction (m)')
ylabel('Temperature Along Fin (K)')



%% Choose Overall Radiator Dimensions
%%% NOTE: ONLY works if N=1

%%% Inputs
```

```
L_tot_sel = 7.5;



%%% Output Lengths
% Find Area per Section & Numer of Sections
A_section = L_tot_sel*D_o + L_tot_sel*2*w_sel;
N_sections = A/A_section

% Find Overall Dimensions
w_tot = 2*w_sel*N_sections + D_o*N_sections
w_section = w_tot/N_sections
```

E Power Appendix

E.1 Matlab Code: Bimodal Brayton Cycle

```
%Owen Braun: 5/7/25
function bimodalAnalysis()
    %Set Parameters
    mdot = 1.1;
    startTemp = 450;
    p2_p1 = 2.2;
    isentropicEfficiencies = [0.9,0.9]
    regenEffectiveness = 0.9;

    %Close All Figures
    close all
    %Retreieve Inputs
    nc = isentropicEfficiencies(1);
    nt = isentropicEfficiencies(2);
    compressorPressureRatio = p2_p1;
    effectiveness = regenEffectiveness;
    %Mixture Molar Mass (kg/mol)
    mixture_molar_mass = 40;
    %Element Molar Mass
    He_molar_mass = 4.002602;
    Xe_molar_mass = 131.293;
    %Set Up Matrices to Solve for Molar Mass Fractions
    A = [1 1;
    Xe_molar_mass He_molar_mass];
    B = [1; mixture_molar_mass];
```

```
%Solve for Molar Fractons
C = A\B;
Xe_molar_fraction = C(1);
He_molar_fraction  = C(2);
%Calculate Mass Fractions
Xe_mass_fraction = Xe_molar_fraction*Xe_molar_mass/
   mixture_molar_mass;
He_mass_fraction = He_molar_fraction*He_molar_mass/
   mixture_molar_mass;
%Specific Heats (kJ/kgK)
Cp_Xe = 0.16;
Cv_Xe = 0.097;
Cp_He = 5.19;
Cv_He = 3.12;
%Calculate Cp Of Mixture
Cp = Xe_mass_fraction * Cp_Xe + He_mass_fraction * Cp_He;
%Calculate Cv of Mixture
Cv = Xe_mass_fraction * Cv_Xe + He_mass_fraction * Cv_He;
%Calculate Gamma of Mixture
gamma = Cp/Cv;
%Calculate Specific Gas Constant
R = Cp - Cv;

%Define State 1: Compressor Inlet
T1 = startTemp;
p1 = 2.5;

%Calculate State 2: Compressor Outlet
p2_p1 = compressorPressureRatio;
```

```
T2_T1 = (p2_p1)^((gamma-1)/gamma);
T2s = T1*T2_T1;
T2 = (T2s-T1)/nc + T1;
p2 = p1 * p2_p1;

%Define State 4: Turbine Inlet
T4 = 1000;
p4 = p2*0.99*0.98;

%Calculate State 5: Turbine Outlet
p5 = p1/(0.99)^2;
T5s_T4 = (p5/p4)^((gamma-1)/gamma);
T5s = T5s_T4 * T4;
T5 = T4 - nt*(T4-T5s);

%Calculate States 3 and 6: Regenerator
T3 = effectiveness * (T5-T2) + T2;
p3 = p2*0.99;
T6 = T5 - (T3-T2);
p6 = p1/0.99;

%Store Results:
T = [T1 T2 T3 T4 T5 T6]
p = [p1 p2 p3 p4 p5 p6]
specificVolume = (R*1e3 * T) ./ (p*1e6)

%Plot Results
plotStates(p,specificVolume,T)
```

```
%Calculate Thermodynamic Performance
Wnet = 0.98*(mdot)*Cp*((T4-T5)-(T2-T1))
Qin = mdot * Cp * (T4-T3)
Qout = mdot * Cp * (T6-T1)
thermalEfficiency = Wnet/Qin

%Size The Turbomachinery
g = 9.807;
%Turbine Sizing
omegaS = 1.1553;
Ds = 3.1;

deltaHead = (-p5*specificVolume(5)/g + p4*specificVolume(4)/g)*1
    e6;
W = deltaHead * g;
V = mdot*(specificVolume(4)+specificVolume(5))/2;
turbineDiameter = Ds / (W^(1/4)/V^(1/2));
turbineSpeedRPM = omegaS * W^(3/4) / V^(1/2) * 60 / (2*pi)

%Compressor Sizing
omegaS = 1.0564;
Ds = 3.5;
deltaHead = (p2*specificVolume(2)/g - p1*specificVolume(1)/g)*1e6
    ;
W = deltaHead * g;
V = mdot*(specificVolume(2)+specificVolume(1))/2;
compressorDiameter = Ds / (W^(1/4)/V^(1/2))
compressorSpeedRPM = omegaS * W^(3/4) / V^(1/2) * 60 / (2*pi)
```

```
    %Size The Regenerator
    NTU = 5;
    UA = NTU*Cp*1e3

end

function plotStates(p,specificVolume,T)
    %Extract Pressures
    p1 = p(1);
    p2 = p(2);
    p3 = p(3);
    p4 = p(4);
    p5 = p(5);
    p6 = p(6);
    %Create Figure
    figure();
    %Scatter Plot
    scatter(specificVolume,p)
    %Create Labels
    labels = {sprintf('State 1\nT = %.1f K',T(1)),
        sprintf('State 2\nT = %.1f K',T(2)),
        sprintf('State 3\nT = %.1f K',T(3)),
        sprintf('State 4\nT = %.1f K',T(4)),
        sprintf('State 5\nT = %.1f K',T(5)),
        sprintf('State 6\nT = %.1f K',T(6)),
    };
    %Location of Labels
    xOffset = 0;
    yOffset = 0;
```

```
%Add Labels to Plot
for i = 1:length(p)
    if(i==3)
        yOffset = -0.2;
    else
        yOffset = 0.3;
    end
    text(specificVolume(i) + xOffset, p(i) + yOffset, labels{i},
       ...
        'FontSize', 10, ...
        'HorizontalAlignment', 'left');
end
%Plot Lines For Pressure Drop Through Regenerator and Reactor
hold on
plot([specificVolume(2), specificVolume(4)], [p(2), p(4)],'b')
plot([specificVolume(1), specificVolume(5)], [p(1), p(5)],'b')
%Plot Polytropic Process
%States 1-2: Compression
V1 = specificVolume(1);
V2 = specificVolume(2);
n = log(p2/p1) / log(V1/ V2);
V_actual = linspace(V2, V1, 100);
P_actual = p1 * (V1 ./ V_actual).^n;
plot(V_actual, P_actual, 'r--', 'LineWidth', 2);
%States 4-5: Expansion
V4 = specificVolume(4);
V5 = specificVolume(5);
n = log(p5/p4) / log(V4/ V5);
V_actual = linspace(V4, V5, 100);
```

```
    P_actual = p4 * (V4 ./ V_actual).^n;
    plot(V_actual, P_actual, 'r--', 'LineWidth', 2);

    %Label Graph
    ylabel('Pressure (Mpa)')
    xlabel('Specific Volume (m^3/kg)')
    title('P-v Diagram')
    xlim([specificVolume(2)-0.01 specificVolume(5)+0.01])
    ylim([2 2.5*2.5])
end
```

E.2 Matlab Code: DEV Brayton Cycle

```
%Owen Braun: 5/7/25
function devCycleAnalysis()
    %Set Parameters
    mdot = 0.8;
    startTemp = 500;
    p2_p1 = 2.1;
    isentropicEfficiencies = [0.9,0.9]
    regenEffectiveness = 0.9;

    %Close All Figures
    close all
    %Retreieve Inputs
    nc = isentropicEfficiencies(1);
    nt = isentropicEfficiencies(2);
    compressorPressureRatio = p2_p1;
    effectiveness = regenEffectiveness;
```

```
%Mixture Molar Mass (kg/mol)
mixture_molar_mass = 40;
%Element Molar Mass
He_molar_mass = 4.002602;
Xe_molar_mass = 131.293;
%Set Up Matrices to Solve for Molar Mass Fractions
A = [1 1;
Xe_molar_mass He_molar_mass];
B = [1; mixture_molar_mass];
%Solve for Molar Fractons
C = A\B;
Xe_molar_fraction = C(1);
He_molar_fraction  = C(2);
%Calculate Mass Fractions
Xe_mass_fraction = Xe_molar_fraction*Xe_molar_mass/
   mixture_molar_mass;
He_mass_fraction = He_molar_fraction*He_molar_mass/
   mixture_molar_mass;
%Specific Heats (kJ/kgK)
Cp_Xe = 0.16;
Cv_Xe = 0.097;
Cp_He = 5.19;
Cv_He = 3.12;
%Calculate Cp Of Mixture
Cp = Xe_mass_fraction * Cp_Xe + He_mass_fraction * Cp_He;
%Calculate Cv of Mixture
Cv = Xe_mass_fraction * Cv_Xe + He_mass_fraction * Cv_He;
%Calculate Gamma of Mixture
gamma = Cp/Cv;
```

```
%Calculate Specific Gas Constant
R = Cp - Cv;

%Define State 1: Compressor Inlet
T1 = startTemp;
p1 = 2.5;

%Calculate State 2: Compressor Outlet
p2_p1 = compressorPressureRatio;
T2_T1 = (p2_p1)^((gamma-1)/gamma);
T2s = T1*T2_T1;
T2 = (T2s-T1)/nc + T1;
p2 = p1 * p2_p1;

%Define State 4: Turbine Inlet
T4 = 1000;
p4 = p2*0.99*0.98;

%Calculate State 5: Turbine Outlet
p5 = p1/(0.99)^2;
T5s_T4 = (p5/p4)^((gamma-1)/gamma);
T5s = T5s_T4 * T4;
T5 = T4 - nt*(T4-T5s);

%Calculate States 3 and 6: Regenerator
T3 = effectiveness * (T5-T2) + T2;
p3 = p2*0.99;
T6 = T5 - (T3-T2);
p6 = p1/0.99;
```

```
%Store Results:
T = [T1 T2 T3 T4 T5 T6]
p = [p1 p2 p3 p4 p5 p6]
specificVolume = (R*1e3 * T) ./ (p*1e6)

%Plot Results
plotStates(p,specificVolume,T)

%Calculate Thermodynamic Performance
Wnet = 0.98*(mdot)*Cp*((T4-T5)-(T2-T1))
Qin = mdot * Cp * (T4-T3)
Qout = mdot * Cp * (T6-T1)
thermalEfficiency = Wnet/Qin

%Size The Turbomachinery
g = 9.807;
%Turbine Sizing
omegaS = 1.0421;
Ds = 3;

deltaHead = (-p5*specificVolume(5)/g + p4*specificVolume(4)/g)*1
   e6;
W = deltaHead * g;
V = mdot*(specificVolume(4)+specificVolume(5))/2;
turbineDiameter = Ds / (W^(1/4)/V^(1/2));
turbineSpeedRPM = omegaS * W^(3/4) / V^(1/2) * 60 / (2*pi)

%Compressor Sizing
```

```
    omegaS = 0.93;
    Ds = 3.5;
    deltaHead = (p2*specificVolume(2)/g - p1*specificVolume(1)/g)*1e6
       ;
    W = deltaHead * g;
    V = mdot*(specificVolume(2)+specificVolume(1))/2;
    compressorDiameter = Ds / (W^(1/4)/V^(1/2))
    compressorSpeedRPM = omegaS * W^(3/4) / V^(1/2) * 60 / (2*pi)

    %Size The Regenerator
    NTU = 5;
    UA = NTU*Cp*1e3

end

function plotStates(p,specificVolume,T)
    %Extract Pressures
    p1 = p(1);
    p2 = p(2);
    p3 = p(3);
    p4 = p(4);
    p5 = p(5);
    p6 = p(6);
    %Create Figure
    figure();
    %Scatter Plot
    scatter(specificVolume,p)
    %Create Labels
    labels = {sprintf('State 1\nT = %.1f K',T(1)),
```

```
        sprintf('State 2\nT = %.1f K',T(2)),
        sprintf('State 3\nT = %.1f K',T(3)),
        sprintf('State 4\nT = %.1f K',T(4)),
        sprintf('State 5\nT = %.1f K',T(5)),
        sprintf('State 6\nT = %.1f K',T(6)),
    };
    %Location of Labels
    xOffset = 0.00;
    yOffset = 0;
    %Add Labels to Plot
    for i = 1:length(p)
        if(i==3 || i==6)
            yOffset = -0.2;
        else
            yOffset = 0.3;
        end
        text(specificVolume(i) + xOffset, p(i) + yOffset, labels{i},
           ...
            'FontSize', 10, ...
            'HorizontalAlignment', 'left');
    end
    %Plot Lines For Pressure Drop Through Regenerator and Reactor
    hold on
    plot([specificVolume(2), specificVolume(4)], [p(2), p(4)],'b')
    plot([specificVolume(1), specificVolume(5)], [p(1), p(5)],'b')
    %Plot Polytropic Process
    %States 1-2: Compression
    V1 = specificVolume(1);
    V2 = specificVolume(2);
```

```
    n = log(p2/p1) / log(V1/ V2);
    V_actual = linspace(V2, V1, 100);
    P_actual = p1 * (V1 ./ V_actual).^n;
    plot(V_actual, P_actual, 'r--', 'LineWidth', 2);
    %States 4-5: Expansion
    V4 = specificVolume(4);
    V5 = specificVolume(5);
    n = log(p5/p4) / log(V4/ V5);
    V_actual = linspace(V4, V5, 100);
    P_actual = p4 * (V4 ./ V_actual).^n;
    plot(V_actual, P_actual, 'r--', 'LineWidth', 2);

    %Label Graph
    ylabel('Pressure (Mpa)')
    xlabel('Specific Volume (m^3/kg)')
    title('P-v Diagram')
    xlim([specificVolume(2)-0.01 specificVolume(5)+0.01])
    ylim([2 2.5*2.5])
end
```

E.3 Matlab Code: Tie Tube Pressure Drop

```
%Owen Braun: 5/7/25
%Clear Workspace
clc
clear
close all

%Solve for Mixture Properties
```

```
%Mixture Molar Mass (kg/mol)
mixture_molar_mass = 40;
%Element Molar Mass
He_molar_mass = 4.002602;
Xe_molar_mass = 131.293;
%Set Up Matrices to Solve for Molar Mass Fractions
A = [1 1;
 Xe_molar_mass He_molar_mass];
B = [1; mixture_molar_mass];
%Solve for Molar Fractons
C = A\B;
Xe_molar_fraction = C(1);
He_molar_fraction  = C(2);
%Calculate Mass Fractions
Xe_mass_fraction = Xe_molar_fraction*Xe_molar_mass/mixture_molar_mass
   ;
He_mass_fraction = He_molar_fraction*He_molar_mass/mixture_molar_mass
   ;
%Specific Heats (kJ/kgK)
Cp_Xe = 0.16;
Cv_Xe = 0.097;
Cp_He = 5.19;
Cv_He = 3.12;
%Calculate Cp Of Mixture
Cp = Xe_mass_fraction * Cp_Xe + He_mass_fraction * Cp_He;
%Calculate Cv of Mixture
Cv = Xe_mass_fraction * Cv_Xe + He_mass_fraction * Cv_He;
%Calculate Gamma of Mixture
gamma = Cp/Cv;
```

```
%Convert to Joules
R = (Cp - Cv)*1e3;
Cp = Cp*1e3;

%Starting Conditions
T_start = 760;
p_start = 2.5 * 2.2 * 1e6;
rho_start = p_start/(R*T_start);

%Reactor Paramaters From Brayton Cycle Analysis
mdot = 1.1; %kg/s
Qdot = 138.8; %kWt

%Friction Factor
f = 0.005;

%Number of Tie Tubes
nTubes = 140;
%Length of Channels (m)
L = 2;

%Supply Channel Geometry
Dhs = 4.0e-3;
A = pi*(Dhs/2)^2;

%Return Passage Geometry
ro = 6.0e-3;
ri = 5.25e-3;
Acr = pi*(ro^2-ri^2);
```

```
Ai = 2*pi*ri * L;
Ao = 2*pi*ro * L;



%Number of Slices
numSlices = 1000;

%Slice Length
dx = L/numSlices;

%Return Passage Slice Area
dA3 = 2*pi*ri*dx;
dA4 = 2*pi*ro*dx;

%Divide Heat and Mass By Tubes
mdot = mdot/nTubes;
Qdot = Qdot/nTubes;

%Heat Per Slice
qSlice = Qdot*1e3/(numSlices*3);

%Initial Conditions
T_inlet = T_start;
p_inlet = p_start;
rho_inlet = rho_start;

%Supply Passage Pressure Drop
for i=2:numSlices
    %Calculate Outlet Temperature
```

```
    T_outlet = T_inlet + qSlice/(mdot*Cp);
    rho_outlet = p_inlet/(R*T_outlet);
    %Calculate Drop in Pressure
    dP = (mdot/A)^2*(1/rho_inlet - 1/rho_outlet - 1/(rho_inlet+
       rho_outlet)*4*f*dx/Dhs);
    %Calculate Outlet Pressure
    p_outlet = p_inlet + dP;
    %Update Values
    T_inlet = T_outlet;
    rho_inlet = rho_outlet;
    p_inlet = p_outlet;
end

%Return Passage Pressure Drop
for i=2:numSlices
    %Calculate Outlet Temperature
    T_outlet = T_inlet + qSlice/(mdot*Cp);
    rho_outlet = p_inlet/(R*T_outlet);
    %Calculate Drop in Pressure
    dP = (mdot/Acr)^2*(1/rho_outlet - 1/rho_inlet + 1/(rho_inlet+
       rho_outlet)*(1/Acr)*(f*(dA3+dA4)));
    %Calculate Outlet Pressure
    p_outlet = p_inlet - dP;
    %Update Values
    T_inlet = T_outlet;
    rho_inlet = rho_outlet;
    p_inlet = p_outlet;
end
```

```
disp(sprintf('Pressure Recovery: %.3f', p_outlet/p_start))
```

E.4 Matlab Code: DEV Reactor Pressure Drop

```
%Owen Braun: 5/7/25
%Clear Workspace
clc
clear
close all

%Solve for Mixture Properties
%Mixture Molar Mass (kg/mol)
mixture_molar_mass = 40;
%Element Molar Mass
He_molar_mass = 4.002602;
Xe_molar_mass = 131.293;
%Set Up Matrices to Solve for Molar Mass Fractions
A = [1 1;
Xe_molar_mass He_molar_mass];
B = [1; mixture_molar_mass];
%Solve for Molar Fractons
C = A\B;
Xe_molar_fraction = C(1);
He_molar_fraction  = C(2);
%Calculate Mass Fractions
Xe_mass_fraction = Xe_molar_fraction*Xe_molar_mass/mixture_molar_mass
   ;
He_mass_fraction = He_molar_fraction*He_molar_mass/mixture_molar_mass
   ;
```

```
%Specific Heats (kJ/kgK)
Cp_Xe = 0.16;
Cv_Xe = 0.097;
Cp_He = 5.19;
Cv_He = 3.12;
%Calculate Cp Of Mixture
Cp = Xe_mass_fraction * Cp_Xe + He_mass_fraction * Cp_He;
%Calculate Cv of Mixture
Cv = Xe_mass_fraction * Cv_Xe + He_mass_fraction * Cv_He;
%Calculate Gamma of Mixture
gamma = Cp/Cv;
%Convert to Joules
R = (Cp - Cv)*1e3;
Cp = Cp*1e3;

%Starting Conditions
T_start = 775;
p_start = 2 * 2.1 * 1e6;
rho_start = p_start/(R*T_start);

%Reactor Paramaters
mdot = 0.8; %kg/s
Qdot = 94; %kWt
f = 0.005; %Friction Factor

%Number of Tie Tubes
nTubes = 140;
%Length of Channels (m)
L = 0.507;
```

```
%Supply Channel Geometry
Dhs = 3e-3;
A = pi*(Dhs/2)^2;

%Number of Slices
numSlices = 1000;

%Slice Length
dx = L/numSlices;

%Divide Heat and Mass By Tubes
mdot = mdot/nTubes;
Qdot = Qdot/nTubes;

%Heat Per Slice
qSlice = Qdot*1e3/(numSlices);

%Initial Conditions
T_inlet = T_start;
p_inlet = p_start;
rho_inlet = rho_start;

%Passage Pressure Drop
for i=2:numSlices
    %Calculate Outlet Temperature
    T_outlet = T_inlet + qSlice/(mdot*Cp);
    rho_outlet = p_inlet/(R*T_outlet);
    %Calculate Drop in Pressure
```

```
    dP = (mdot/A)^2*(1/rho_inlet - 1/rho_outlet - 1/(rho_inlet+
       rho_outlet)*4*f*dx/Dhs);
    %Calculate Outlet Pressure
    p_outlet = p_inlet + dP;
    %Update Values
    T_inlet = T_outlet;
    rho_inlet = rho_outlet;
    p_inlet = p_outlet;
end
%Print Out Pressure Recovery
disp(sprintf('Pressure Recovery: %.3f', p_outlet/p_start))
```

E.5 Matlab Code: Differential Element Sensitivity Study

```
%Owen Braun: 5/7/25
%Clear Workspace
clc
clear
close all

%Solve for Mixture Properties
%Mixture Molar Mass (kg/mol)
mixture_molar_mass = 40;
%Element Molar Mass
He_molar_mass = 4.002602;
Xe_molar_mass = 131.293;
%Set Up Matrices to Solve for Molar Mass Fractions
A = [1 1;
 Xe_molar_mass He_molar_mass];
```

```
B = [1; mixture_molar_mass];
%Solve for Molar Fractons
C = A\B;
Xe_molar_fraction = C(1);
He_molar_fraction  = C(2);
%Calculate Mass Fractions
Xe_mass_fraction = Xe_molar_fraction*Xe_molar_mass/mixture_molar_mass
   ;
He_mass_fraction = He_molar_fraction*He_molar_mass/mixture_molar_mass
   ;
%Specific Heats (kJ/kgK)
Cp_Xe = 0.16;
Cv_Xe = 0.097;
Cp_He = 5.19;
Cv_He = 3.12;
%Calculate Cp Of Mixture
Cp = Xe_mass_fraction * Cp_Xe + He_mass_fraction * Cp_He;
%Calculate Cv of Mixture
Cv = Xe_mass_fraction * Cv_Xe + He_mass_fraction * Cv_He;
%Calculate Gamma of Mixture
gamma = Cp/Cv;
%Convert to Joules
R = (Cp - Cv)*1e3;
Cp = Cp*1e3;

%Starting Conditions
T_start = 760;
p_start = 2.5 * 2.2 * 1e6;
rho_start = p_start/(R*T_start);
```

```
%Reactor Paramaters
mdot = 0.9; %kg/s
Qdot = 156.75; %kWt
f = 0.005; %Friction Factor

%Number of Tie Tubes
nTubes = 140;
%Length of Channels (m)
L = 2;

%Supply Channel Geometry
Dhs = 3.5e-3;
A = pi*(Dhs/2)^2;

%Return Passage Geometry
ro = 6.0e-3;
ri = 5.25e-3;
Acr = pi*(ro^2-ri^2);
Ai = 2*pi*ri * L;
Ao = 2*pi*ro * L;

%Divide Heat and Mass By Tubes
mdot = mdot/nTubes;
Qdot = Qdot/nTubes;


%Number of Slices
numSliceArray = 2:1:1000;
```

```
%Counter Variable
j=1;

for i=numSliceArray
    %Number of Slices
    numSlices = i;

    %Slice Length
    dx = L/numSlices;

    %Return Passage Slice Area
    dA3 = 2*pi*ri*dx;
    dA4 = 2*pi*ro*dx;



    %Heat Per Slice
    qSlice = Qdot*1e3/(numSlices*3);

    %Initial Conditions
    T_inlet = T_start;
    p_inlet = p_start;
    rho_inlet = rho_start;

    %Supply Passage Pressure Drop
    for i=2:numSlices
        %Calculate Outlet Temperature
        T_outlet = T_inlet + qSlice/(mdot*Cp);
        rho_outlet = p_inlet/(R*T_outlet);
```

```
        %Calculate Drop in Pressure
        dP = (mdot/A)^2*(1/rho_inlet - 1/rho_outlet - 1/(rho_inlet+
           rho_outlet)*4*f*dx/Dhs);
        %Calculate Outlet Pressure
        p_outlet = p_inlet + dP;
        %Update Values
        T_inlet = T_outlet;
        rho_inlet = rho_outlet;
        p_inlet = p_outlet;
    end

    %Return Passage Pressure Drop
    for i=2:numSlices
        %Calculate Outlet Temperature
        T_outlet = T_inlet + qSlice/(mdot*Cp);
        rho_outlet = p_inlet/(R*T_outlet);
        %Calculate Drop in Pressure
        dP = (mdot/Acr)^2*(1/rho_outlet - 1/rho_inlet + 1/(rho_inlet+
           rho_outlet)*(1/Acr)*(f*(dA3+dA4)));
        %Calculate Outlet Pressure
        p_outlet = p_inlet - dP;
        %Update Values
        T_inlet = T_outlet;
        rho_inlet = rho_outlet;
        p_inlet = p_outlet;
    end
    pressureRecovery(j) = (p_outlet/p_start);
    j = j + 1;
end
```

```
plot(numSliceArray,pressureRecovery,'LineWidth',2)
xlabel('Number of Slices')
ylabel('Pressure Recovery')
title('Pressure Recovery vs. Number of Slices')
```

E.6 Matlab: Brayton Cycle Optimization

```
 %Owen Braun: 5/7/25
function results = BraytonCycleOptimization(efficiencies, startTemp)
    %Retrieve Inputs
    nc = efficiencies(1);
    nt = efficiencies(2);
    %Mixture Molar Mass (kg/mol)
    mixture_molar_mass = 40;
    %Element Molar Mass
    He_molar_mass = 4.002602;
    Xe_molar_mass = 131.293;
    %Set Up Matrices to Solve for Molar Mass Fractions
    A = [1 1;
    Xe_molar_mass He_molar_mass];
    B = [1; mixture_molar_mass];
    %Solve for Molar Fractons
    C = A\B;
    Xe_molar_fraction = C(1);
    He_molar_fraction  = C(2);
    %Calculate Mass Fractions
    Xe_mass_fraction = Xe_molar_fraction*Xe_molar_mass/
       mixture_molar_mass;
```

```
He_mass_fraction = He_molar_fraction*He_molar_mass/
   mixture_molar_mass;
%Specific Heats (kJ/kgK)
Cp_Xe = 0.16;
Cv_Xe = 0.097;
Cp_He = 5.19;
Cv_He = 3.12;
%Calculate Cp Of Mixture
Cp = Xe_mass_fraction * Cp_Xe + He_mass_fraction * Cp_He
%Calculate Cv of Mixture
Cv = Xe_mass_fraction * Cv_Xe + He_mass_fraction * Cv_He;
%Calculate Gamma of Mixture
gamma = Cp/Cv
R = Cp - Cv;
i = 1;
for compressorPressureRatio = 1.1:.1:5
    j = 1;
    for massFlowRate = 0.1:0.1:5
        %Define State 1: Compressor Inlet
        T1 = startTemp;
        p1 = 2.5;

        %Calculate State 2: Compressor Outlet
        p2_p1 = compressorPressureRatio;
        T2_T1 = (p2_p1)^((gamma-1)/gamma);
        T2s = T1*T2_T1;
        T2 = (T2s-T1)/nc + T1;
        p2 = p1 * p2_p1;
```

```
%Define State 4: Turbine Inlet
T4 = 1000;
p4 = p2*0.99*0.98;

%Calculate State 5: Turbine Outlet
p5 = p1/(0.99)^2;
T5s_T4 = (p5/p4)^((gamma-1)/gamma);
T5s = T5s_T4 * T4;
T5 = T4 - nt*(T4-T5s);

%Calculate States 3 and 6: Regenerator
effectiveness = 0.9;
T3 = effectiveness * (T5-T2) + T2;
p3 = p2*0.99;
T6 = T5 - (T3-T2);
p6 = p1/0.99;
%Store State Points
T = [T1 T2 T3 T4 T5 T6];
p = [p1 p2 p3 p4 p5 p6];
%Create Data Structure to Store All Results
results{i,j}.T = T;
results{i,j}.p = p;
results{i,j}.PR = compressorPressureRatio;
results{i,j}.mdot = massFlowRate;
results{i,j}.Wnet = 0.98 * massFlowRate * Cp *((T4-T5)-(
   T2-T1));
results{i,j}.Qin = massFlowRate * Cp * (T4-T3);
results{i,j}.Qout = massFlowRate * Cp * (T6-T1);
```

```
            j = j +1;
        end
        i = i + 1;
    end
    createPlots(results)
end

function createPlots(data)
    %Create Graph
    rows = size(data,1);
    cols = size(data,2);

    PR_grid    = zeros(rows, cols);
    mdot_grid  = zeros(rows, cols);
    Wnet_grid  = NaN(rows, cols);

    for i = 1:rows
        for j = 1:cols
            if isfield(data{i,j}, 'Wnet')
                PR_grid(i,j)   = data{i,j}.PR;
                mdot_grid(i,j) = data{i,j}.mdot;
                Wnet_grid(i,j) = data{i,j}.Wnet;  % in kWe or kW
                Qin_grid(i,j) = data{i,j}.Qin;
                Qout_grid(i,j) = data{i,j}.Qout;
                Thermal_efficiency(i,j) = data{i,j}.Wnet/data{i,j}.
                   Qin*100;
            end
        end
    end
```

```
%Plot Relevant Results
%Net Work
subplot(2,2,1)
contourf(mdot_grid, PR_grid, Wnet_grid, 20);
colorbar;
xlabel('Mass Flow Rate (kg/s)');
ylabel('Compressor Pressure Ratio');
title('Net Power Output (W_{net}) [kW]');
%Heat Rejection
subplot(2,2,2)
contourf(mdot_grid, PR_grid, Qout_grid, 20);
colorbar;
xlabel('Mass Flow Rate (kg/s)');
ylabel('Compressor Pressure Ratio');
title('Heat Output (Q_{out}) [kW]');
%Heat Input
subplot(2,2,3)
contourf(mdot_grid, PR_grid, Qin_grid, 20);
colorbar;
xlabel('Mass Flow Rate (kg/s)');
ylabel('Compressor Pressure Ratio');
title('Heat Input (Q_{in}) [kW]');
%Thermal Efficiency
subplot(2,2,4)
contourf(mdot_grid, PR_grid, Thermal_efficiency, 20);
colorbar;
xlabel('Mass Flow Rate (kg/s)');
ylabel('Compressor Pressure Ratio');
title('Thermal Efficiency (%)');
```

```
end
```

E.7 Power Requirement Derivations

Table 3.1.3 Independent Exploration Mission: Mars Transit Vehicle using ISS ECLSS Technologies

Subsystem / Interface	Mass [kg]	Volume [m^3]	Power [kW_e]	Cooling [kW_{th}]	Crewtime [CM-h]	ESM [kg]
Air	2,217	3.37	4.35	2.79	12.78	3,401
Biomass	761	17.03	12.03	12.03	0.00	4,249
Food	4,158	15.12	2.40	2.40	0.00	4,961
Thermal	369	1.09	1.07	1.07	2.00	677
Waste	393	10.03	0.01	0.01	0.00	488
Water	2,587	4.18	1.00	1.00	0.00	2,902
Extravehicular Activity Support	0	0.00	0.00	0.00	0.00	0
Human Accommodations	1,763	6.87	0.00	0.00	0.00	1,826
Totals	**12,248**	**57.69**	**20.86**	**19.30**	**14.78**	

Figure E.1: ISS ECLSS Values [13]

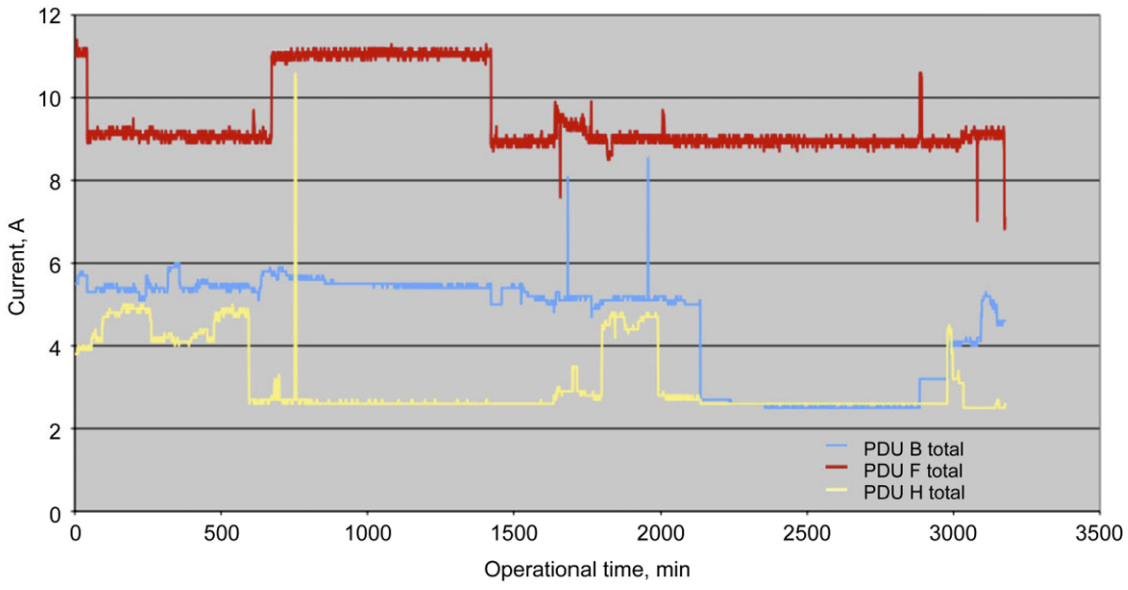

Figure 25.—Total output current for PDUs B, F, and H.

Figure E.2: Current Draw For Desert RATS [14]

F Project Management Appendix

The complete Gantt Chart for all tasks is shown below.

F.1 Gantt Chart

									Sun	Mon	Tue	Wed	Thu	Fri	Sat	Sun	Mon	Tue	Wed	Thu	Fri	Sat	Sun	Mon	Tue	Wed	Thu	Fri	Sat	Sun	Mon
	WBS #	**Task**	**Primary**	**Secondary**	**Plan Start**	**Plan Finish**	**Days**	**Done**	3/16	3/17	3/18	3/19	3/20	3/21	3/22	3/23	3/24	3/25	3/26	3/27	3/28	3/29	3/30	3/31	4/1	4/2	4/3	4/4	4/5	4/6	4/7
Schedule		Concept Assembly Refinement	Katelyn	Ethan	3/16/2025	3/23/2025	7	TRUE																							
Engine Design	PNT1.1	Nuclear Engine Performance Analysis Write-Up	Tyler	Josh	3/16/2025	3/20/2025	4	TRUE																							
Engine Design	PNT1.1	Nuclear Engine Notional Diagram	Tyler	Josh	3/16/2025	3/20/2025	4	TRUE																							
Schedule	PR1	**PDR Progress Review 1 / Delta CoDR**			3/18/2025	3/18/2025	0	TRUE																							
Pressure Vessel	SHPV1.0	Design Standards Research & Mat'l Options	Nate	Preston	3/18/2025	3/23/2025	5	TRUE																							
Pressure Vessel	SPT1.0	Design Standards Research & Mat'l Options	Alex	Ethan	3/18/2025	3/23/2025	5	TRUE																							
Pressure Vessel	SHPV2.0	Analysis Write-Up	Nate	Preston	3/18/2025	3/25/2025	7	TRUE																							
Pressure Vessel	SPT2.0	Analysis Write-Up	Alex	Ethan	3/18/2025	3/25/2025	7	TRUE																							
Truss	STRS1.0	Design Process Research	Preston	Nate	3/18/2025	3/23/2025	5	TRUE																							
Truss	STRS2.0	Initial Analysis Framework Write-Up	Preston	Nate	3/20/2025	3/23/2025	3	TRUE																							
Power	PG1.0	DeV Nuclear Reactor Analysis Framework	Joseph	Owen	3/18/2025	3/23/2025	5	TRUE																							
Power	PHJ1.0	Spacecraft Radiator Design Research	Katelyn		3/18/2025	3/23/2025	5	TRUE																							
Engine Design	PNT1.2	Nuclear Engine Design Process Description	Tyler	Josh	3/20/2025	3/23/2025	3	TRUE																							
Engine Design	PMAN1.0	Orbital Maneuvering System Analysis	AJ	Ethan	3/18/2025	4/8/2025	21	TRUE																							
Models	M1	Updated DeV 3 View	Jocelyn		3/20/2025	3/23/2025	3	TRUE																							
Models	M1	Updated IPV 3 View	Nate		3/20/2025	3/23/2025	3	TRUE																							
Schedule	PR2	**PDR Progress Review 9**			3/25/2025	3/25/2025	0	TRUE																							
Trajectory	PTRJ1.1	Lambert Method MATLAB Code for Transfer	Paul		3/16/2025	3/27/2025	11	TRUE																							
Pressure Vessel	SHPV0	Micrometeoroid Analysis Progress Slide	Abby	Ethan	3/20/2025	3/30/2025	10	TRUE																							
Pressure Vessel	SPT0	Updated Boil Off Model	Alex	Ethan	3/18/2025	4/1/2025	14	TRUE																							
Engine Design	PNT1.3	Engine cycle, states	Josh	Tyler	3/23/2025	3/27/2025	4	TRUE																							
Engine Design		Engine nozzle	Josh	Tyler	3/23/2025	3/27/2025	4	TRUE																							
Power	PHJ2.0	Radiator Design: Materials	Nate		3/23/2025	3/30/2025	7	TRUE																							
Power	PG2	Brayton Cycle Analysis: Mass Flow	Owen		3/23/2025	3/28/2025	5	TRUE																							
Schedule	T1.0	Assembly Vehicle Concept	Katelyn		3/23/2025	3/30/2025	7	TRUE																							
Trajectory	PTRJ1.4	Transfer Trajectory Course Corrections dV Margin	Jocelyn	Paul	3/23/2025	3/30/2025	7	TRUE																							
Pressure Vessel	SHPV3.0	Isogrid Selection for Dev and Hab	Ethan		3/23/2025	3/27/2025	4	TRUE																							
Truss	STRS2.0	Design Goals/Drivers, Allowable Loads, FoS	Preston	Nate	3/23/2025	4/1/2025	9	TRUE																							
Engine Design	PMAN2.0	Orbital Maneuvering System Detail Design	AJ	Abby	3/25/2025	3/30/2025	5	TRUE																							
Engine Design		DeV Engine Cycle Analysis	Jocelyn		3/25/2025	4/7/2025	13	TRUE																							
Models		Mars Asset Refined Concept	Joe	Owen	3/25/2025	4/1/2025	7	TRUE																							
Models	M2	Updated DeV 3 View	Jocelyn		3/25/2025	4/1/2025	7	TRUE																							
Models	M2	Updated IPV 3 View	Nate		3/25/2025	3/30/2025	5	TRUE																							
Power	PHJ3.0	Bimodal Power: Cycle Analysis	Owen	Nathan	3/27/2025	4/15/2025	19	TRUE																							
Pressure Vessel	n/a	SLS Launch Loading	Ethan	Preston	3/25/2025	3/30/2025	5	TRUE																							
Schedule	PR3	**PDR Progress Review 10**			4/1/2025	4/1/2025	0	TRUE																							
Pressure Vessel	SPT3.0	Composite and Hab End Caps	Ethan		3/27/2025	4/3/2025	7	TRUE																							
Pressure Vessel	MMOD	Micrometeoroid Shielding Mass/Construction	Ethan	Nathan	3/30/2025	4/5/2025	6	TRUE																							
Power	PHJ3.0	DeV and IPV Heat Transfer	Nate	Alex	3/30/2025	4/6/2025	7	TRUE																							
Power	PG3	DeV Reactor P&ID	Owen	Joseph	3/30/2025	4/4/2025	5	TRUE																							
Power	PG4	Bimodal P&ID	Owen	Joseph	3/30/2025	4/4/2025	5	TRUE																							
Engine Design	PNT1.4	Nuclear Reactor Design	Tyler	Josh	3/27/2025	4/6/2025	10	TRUE																							
Engine Design		RCS Design: P&ID and Design Decisions	Jocelyn	Paul	3/30/2025	4/3/2025	4	TRUE																							
Engine Design	PNT1.5	NTP Engine Nozzle Sizing Analysis	Josh	Tyler	3/27/2025	3/30/2025	3	TRUE																							
Engine Design	PNT1.6	NTP Engine Nozzle Cooling	Josh		3/30/2025	4/1/2025	2	TRUE																							
Models	M2	Center of Mass	Nathan		4/1/2025	4/7/2025	6	TRUE																							
Pressure Vessel	VIB1	Vibrations for Structures: Natural Freqs	Ethan	Preston	3/30/2025	4/14/2025	15	TRUE																							
Pressure Vessel	SPT3.1	Composite Tank Compressive Loading	Nathan	Ethan	4/3/2025	4/7/2025	4	TRUE																							
Pressure Vessel	SPT3.2	Propellant Tanks: Link to mass budget	Ethan	Nathan	4/1/2025	4/6/2025	5	TRUE																							
Models	M3	CAD: DeV	Jocelyn		4/1/2025	4/6/2025	5	TRUE																							
Models	M3	Updated IPV 3 View	Nate		4/1/2025	4/6/2025	5	TRUE																							

									Sat	Sun	Mon	Tue	Wed	Thu	Fri	Sat	Sun	Mon	Tue	Wed	Thu	Fri	Sat	Sun	Mon	Tue	Wed	Thu	Fri	Sat	Sun	Mon	Tue	Wed	Thu	Fri	Sat	Sun	Mon	Tue	Wed	Thu	Fri	Sat	Sun	Mon	Tue	Wed	Thu
	WBS #	Task	Primary	Secondary	Plan Start	Plan Finish	Days	Done	4/5	4/6	4/7	4/8	4/9	4/10	4/11	4/12	4/13	4/14	4/15	4/16	4/17	4/18	4/19	4/20	4/21	4/22	4/23	4/24	4/25	4/26	4/27	4/28	4/29	4/30	5/1	5/2	5/3	5/4	5/5	5/6	5/7	5/8
Models	M3	Updated IPV 3 View	Nate		4/1/2025	4/6/2025	5	TRUE																																							
Schedule	T1.0	Timeline: Launches, Cost, Mission Ops	Katelyn		3/23/2025	3/30/2025	7	TRUE																																							
Schedule	B1	Budget	Katelyn		4/3/2025	4/6/2025	3	TRUE																																							
Schedule	S1	Human Systems Integration Adherence	Ethan	Abby	4/3/2025	4/5/2025	2	TRUE																																							
Schedule	DSO1	Deimos Surface Ops	Joseph	Jocelyn			0	TRUE																																							
Schedule	S2	Reliability and Human Safety	Abby	Ethan	4/3/2025	4/6/2025	3	TRUE																																							
Schedule	PR4	**PDR Progress Review 11**			4/8/2025	4/8/2025	0	TRUE																																							
ECLSS	S3	Robotic Resupply: Boil off, total mass, etc	Abby		4/8/2025	4/10/2025	2	TRUE																																							
Models	CAD1	CAD: IPV Hab	Abby		4/8/2025	4/13/2025	5	TRUE																																							
Models	CAD1	CAD: Propellant Tanks	Nathan	Ethan	4/8/2025	4/13/2025	5	TRUE																																							
Models	CAD2	CAD: Trusses and Payload Adapters	Preston		4/8/2025	4/13/2025	5	TRUE																																							
Models	CAD3	CAD: Docking and Assembly Operations	Katelyn		4/8/2025	4/13	5	TRUE																																							
Models	CAD3	CAD: Thrust Structures	Preston		4/8/2025	4/13	5	TRUE																																							
Models	CAD3	CAD: Secondary Engine CAD	AJ		4/8/2025	4/13	5	TRUE																																							
Models	CAD3	CAD: Nuclear Engine CAD	Josh	Tyler	4/8/2025	4/13	5	TRUE																																							
Pressure Vessel	SPT5	Vibration Analysis Tanks and Pressure Vessels	Ethan		4/8/2025	4/13/2025	5	TRUE																																							
Trajectory	PTRJ1.2	Finite Burn MATLAB Losses and Burn Times	Ethan	Paul	4/8/2025	4/13/2025	5	TRUE																																							
Engine Design	PNT1.7	Finish Nozzle	Josh	Tyler	3/30/2025	4/8/2025	9	TRUE																																							
Engine Design	PNT1.8	Cool Down Period	Tyler	Josh	4/1/2025	4/8/2025	7	TRUE																																							
Engine Design	PNT1.9	Ullage + Piping	Nathan	Josh	4/3/2025	4/8/2025	5	TRUE																																							
Engine Design	PNT1.10	P&ID	Josh	Tyler	4/1/2025	4/8/2025	7	TRUE																																							
Engine Design	PNT1.11	Turbomachinery	Josh	Tyler	4/1/2025	4/8/2025	7	TRUE																																							
Models	AV1	Detailed Assembly Vehicle	Katelyn		4/7/2025	4/13/2025	6	TRUE																																							
Models	CAD2	Full Assembly CAD Draft	Nate		4/7/2025	4/13/2025	6	TRUE																																							
Pressure Vessel	SPT3.3	Water / O2 Tank Sizing	AJ		4/8/2025	4/13/2025	5	TRUE																																							
Power	PG5	Pressure drop across tie tubes	Owen		4/8/2025	4/10/2025	2	TRUE																																							
Pressure Vessel	SHPV2.1	Isogrid Mars Asset	Owen	Ethan	4/8/2025	4/10/2025	2	TRUE																																							
Truss	STRS3.0	Thrust Structure	Preston	Ethan	4/17/2025	4/20/2025	3	TRUE																																							
Truss	STRS2.0	Main Truss	Preston		4/10/2025	4/17	7	TRUE																																							
Trajectory		Mars Assets Cruise Stage Maneuvers	Nathan	Owen	4/8/2025	4/10/2025	2	TRUE																																							
Power	PG6	Turbomachinery for Bimodal and DeV	Owen		4/8/2025	4/13/2025	5	TRUE																																							
Trajectory		DeV RCS and Maneuvering	Jocelyn		4/8/2025	4/10/2025	2	TRUE																																							
Trajectory		Finite Burn MATLAB Visuals	Ethan		4/20/2025	4/22/2025	2	TRUE																																							
Truss	STRS3.1	Saddle Truss	Preston		4/12/2025	4/20/2025	8	TRUE																																							
Truss	STRS3.2	Payload Adapters	Preston		4/12/2025	4/17/2025	5	TRUE																																							
Power	PHJ4	Fix Bimodal Radiator Design	Nate		4/8/2025	4/13/2025	5	TRUE																																							
Power	PHJ5	DeV and IPV Heat Rejection	Alex		4/8/2025	4/13/2025	5	TRUE																																							
Schedule	PR5	**PDR Progress Review 12**			4/15/2025	4/15/2025	0	TRUE																																							
Schedule		**Tuesday Meeting**			4/15/2025	4/15/2025	0	TRUE																																							
Pressure Vessel	SPT4.0	Plumbing	Nathan	Josh	4/15/2025	4/21/2025	6	TRUE																																							
Models		Mars Asset Assembly CAD	Joe		4/15/2025	4/16/2025		TRUE																																							
Pressure Vessel	SPT	Tank / Liner Thermal Expansion	Ethan		4/15/2025	4/19/2025	4	TRUE																																							
Power	PHJ6	Heat Rejection Heat Exchangers	Alex		4/15/2025	4/17/2025	2	TRUE																																							
Power	PHJ7	Radiator Analysis & Materials	Nate		4/8/2025	4/20/2025	12	TRUE																																							
Power	PHJ8	DEV & Hab Loop Pressure Losses	Ethan		4/15/2025	4/20/2025	5	TRUE																																							
Power	PHJ9	Combine Heat Rej Analyses	Alex	Nate	4/20/2025	4/21/2025	1	TRUE																																							
Power	PHJ10	MLI for Habs	Alex		4/21/2025	4/21/2025	0	TRUE																																							
Models		DEV CAD	Jocelyn		4/15/2025	4/21/2025	6	TRUE																																							
Models		Launch Packaging in CAD	AJ	Katelyn	4/15/2025	4/17/2025	2	TRUE																																							
Schedule		Structures Slides Outline	Ethan, Pr	Alex	4/15/2025	4/17/2025	2	TRUE																																							
Schedule		Propulsion Slides Outline	Josh		4/15/2025	4/17/2025	2	TRUE																																							
Schedule		Power Slides Outline	Owen	Joe	4/15/2025	4/17/2025	2	TRUE																																							
Schedule		Deimos Operations Slides Outline	Paul		4/15/2025	4/17/2025	2	TRUE																																							
Schedule		Mars Asset Slides Outline	Owen	Joe	4/15/2025	4/17/2025	2	TRUE																																							
Schedule		**Thursday Meeting**			4/17/2025	4/17/2025	0	TRUE																																							
Engine Design		NTP Nozzle Mass Fix	Josh	Tyler	4/17/2025	4/19/2025	2	TRUE																																							
Models		Assembly CAD Improvement	Nate		4/15/2025	4/19/2025	4	TRUE																																							
Schedule		***Sunday Meeting: PDR Slides Done***			4/20/2025	4/20/2025	0	TRUE																																							
Models		Mars Ops Diagrams	Joe		4/20/2025	4/22/2025	2	TRUE																																							
Models		Deimos Ops Diagrams	Paul		4/21/2025	4/22/2025	1	TRUE																																							
Models		Tank Docking Mechanism	Katelyn	AJ	4/21/2025	4/22/2025	1	TRUE																																							
Models		Assembly CAD Done	Nate		4/21/2025	4/22/2025	1	TRUE																																							
Schedule		***Tuesday Meeting: PDR Slide Review***			4/22/2025	4/22/2025	0	TRUE																																							
Schedule		***Wednesday Meeting: PDR Slides Review 2***			4/23/2025	4/23/2025	0	TRUE																																							
	PDR	**PDR Presentation**			4/24/2025	4/24/2025	0	TRUE																																							
Schedule		FMECA	Paul		4/27/2025	4/29/2025	2	TRUE																																							
Schedule		**Proofreading Day 1 from 12PM Onwards**			5/6/2025	5/6/2025	0	TRUE																																							
Schedule		**Proofreading Day 2 ALL DAY**			5/7/2025	5/7/2025	0	TRUE																																							
Schedule		**Final Report Due AT 5PM // PRINT AT 9AM**	**Ethan**		5/8/2025	5/6/2025	-2	TRUE																																							

G Tele-Operated Appendix

G.1 Teleoperated Mars Surface Assets

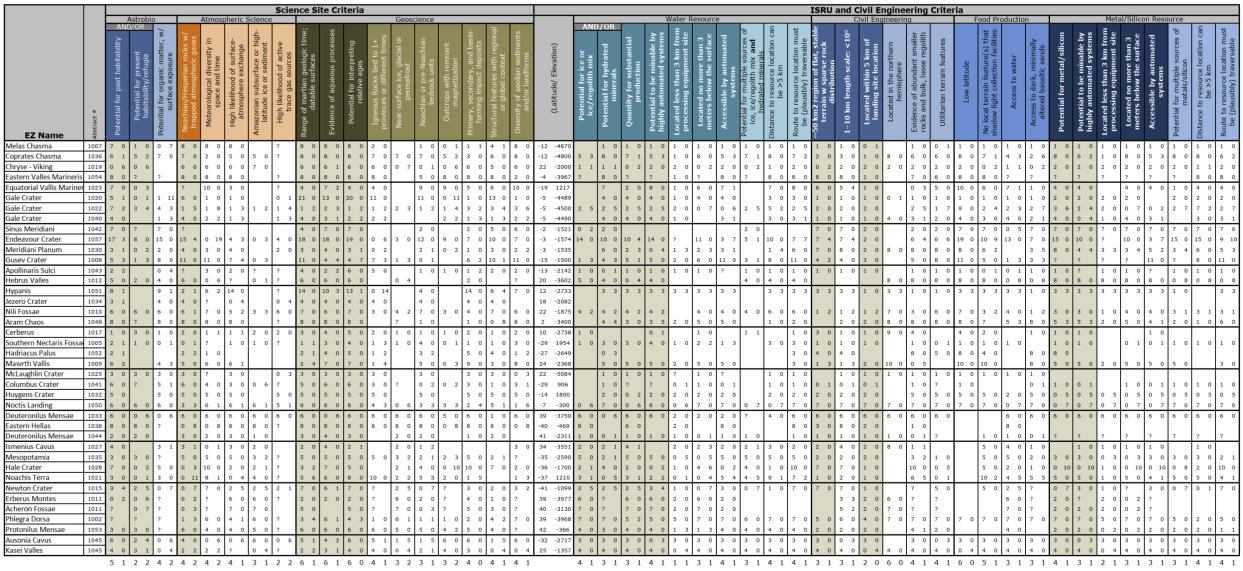

Figure G.1: Landing site: Endeavour crater on mars surface

G.2 MATLAB: Ballistic Entry Calculations

```
%Owen Braun: 5/7/25

clc

clear

close all


%Entry Parameters

ballistic_coeff = 145; %kg/m^2

entry_angle = 15; %Degress

Ve = 6e3; %m/s

entry_altitude = 160e3 %m


%Exponential Model of the Atmosphere
```

```
rho_ref = 0.02; %kg/m^3
density_scale_height = 11.1e3; %m
beta = 1/density_scale_height;

%Calculate Location of Max Decceleration
Vmax_g = exp(-1/2)*Ve
y_maxg = 1/beta * log(rho_ref/(ballistic_coeff*beta*sind(entry_angle)
   ))
max_g = 1/9.081 * (beta*Ve^2*sind(entry_angle))/(2*exp(1))

%Sutton Graves Stagnation Point Heating
k = 1.9027e-4;
Rn = 3.75;

%Calculate Velocity Profile and Convective Heating
%Altitude Array
altitude_values = 0:100:160100;
V = zeros(1,length(altitude_values));
i=1;
for altitude = altitude_values
    V_alt = Ve * exp(-1/(ballistic_coeff*2*sind(entry_angle)) *
       rho_ref/beta * exp(-beta*altitude));
    V(i) = V_alt/Ve;
    density = rho_ref * exp(-beta*altitude);
    convHeating(i) = (k * sqrt(density/Rn)*V_alt^3)/(100^2);
    i=i+1;
end

%Plot Altitude (m) vs. V/Ve
```

```
figure();
plot(V,altitude_values)
xlim([0 1.1])
xlabel('V/Ve')
ylabel('Altitude (m)')
title('Altitude (m) vs. V/Ve')

%Plot gconv (W/cm^2) vs. Altitude (m)
figure();
plot(altitude_values,convHeating)
xlabel('Altitude (m)')
ylabel('Heat Flux (W/cm^2)')
title('Heat Flux (W/cm^2) vs. Altitutde (m)')



%Heating Calculations
%Sutton-Graves Stagnation Point Convective Heating
heat_flux = zeros(1,length(altitude_values));

%Allen Edgars Trajector Equations
dh_dt = Ve*sind(entry_angle);

%Convert to Time Domain
time = 0:1:200;

%Intialize Convective Heat Flux Array
convenction_flux = zeros(size(time));
```

```
%Pica Material Properties
rho = 265;
Qstar = 1500*100^2;
Cp = 1.0075e3;

i=1;
Tsurr = 170;
epsilon = 1e-10;
for t = time
    %Solve for Altitude
    altitude = entry_altitude - Ve*sind(entry_angle)*t;
    %Calculate Surrounding Temperature Based on Atmospherical Model
    if (altitude>7000)
        Tsurr = (-23.4-0.00222*altitude)+273;
    else
        Tsurr = (-31.4-beta*altitude)+273;
    end
    %Calculate Velocity at Altitude
    V_alt = Ve * exp(-1/(ballistic_coeff*2*sind(entry_angle)) *
       rho_ref/beta * exp(-beta*altitude));
    %Calculate Density
    density = rho_ref * exp(-beta*altitude);
    %Calculate Heat Flux
    heat_flux_at_altitude = (k * sqrt(density/Rn)*V_alt^3)/(100^2);
    %Store Heat Flux In Array
    convenction_flux(i) = heat_flux_at_altitude;
    %Solve for Radiative Equilibrium Temperature
    Tw = (heat_flux_at_altitude*100^2/(0.7*5.67e-8)+Tsurr^4)^(1/4);
    Tw_array(i) = Tw;
```

```
    %Recession Calculations
    Hr = V_alt^2/2;
    Hw = Cp*Tw;
    qDothw = heat_flux_at_altitude*100^2*(1-Hw/(Hr+epsilon));
    sdot(i) = qDothw/(rho*Qstar);
    %sdot(i) = (heat_flux_at_altitude * 100^2 * (Hr - Hw) / (Hr +
       epsilon) - (0.7 * 5.67e-8) * Tw^4) / (rho * Qstar + epsilon);
    i=i+1;
end
%Numerically Integrate to Find Total Recession
sTot = trapz(time, sdot);
disp(['Total recession (cm) = ', num2str(sTot*100)]);

%Plot Heat Flux and Eq. Wall Time as Function of Time
figure();
yyaxis left
plot(time,convenction_flux)
xlabel('Time (s)')
ylabel('Heat Flux (W/cm^2)')
yyaxis right
plot(time,Tw_array)
xlabel('Time (s)')
ylabel('Surface Equilibrium Temperature (K)')
title('Ballistic Entry Heating Profile')


%Plot Recession Rate
figure();
plot(time,sdot)
```

```
xlabel('Time (s)')
ylabel('Recession Rate (m/s)')
title('Recession Rate (m/s) vs. Time(s)')


%Size the Heat Shield;
%Initial Temp on Entry
Ti= (-23.4-0.00222*altitude);
alpha = 1.6/(265.0*1592.0);
%Average Equilibrium Temperature
Ts = mean(Tw_array);


%Conditions
thickness = 0.005:0.005:0.035;
time = 0:1:200;


%Loop Through Multiple Thicknesses for Bondline Temperature
   Calculations
figure();
hold on
for x = thickness
    Temp = zeros(1, length(time));
    i = 1;
    for t = time
        Temp(i) = (erf(x/(2*sqrt(alpha*t))) *(Ti-Ts)+Ts)-273;
        i = i + 1;
    end
```

```
    plot(time, Temp, 'DisplayName', sprintf('x = %.3f m', x))
end

%Plot Data
yline(250, '--r','LineWidth',2 ,'DisplayName','Maximum Bondline
   Temperature');
xlabel(Time (s));
ylabel(Temperature (C));
title(Temperature (C) vs. Time(s) for Variable Thickness (m) );
legend show;
```

H Mission Overview Appendix

H.1 All Requirements

Using preliminary versions of the trade studies described in all of the subsystems of the report, requirements were generated for each subsystem during the SRR phases. These requirements were used to guide the design throughout the CoDR and PDR phases, and subsequently used to evaluate the success of the final design produced at the end of the PDR phase. All requirements match back to their respective number on the Functional Block Diagram in Figures 3.1 3.2, 3.3, 3.4.

		Category Name	Req Short	Requirement(s)	Rationale
0	0.1	Mission Trajectory	Launch Date	The mission shall launch no later than October 2041. The optimal launch window is October 19 2041.	Interplanetary Mission Design Handbook: Earth-to-Mars Mission Opportunities 2026 to 2045: NASA Glenn
0	0.3	Size Envelope Requirements	Max Diameter	The payload shall fit within a 12-meter diameter shroud.	Mission Requirements
0	0.3	Total Vehicle Mass	Wet Mass	The assembled IPV shall have a maximum fully fueled mass of 750mT	Trade Study
0	0.3	Size Envelope Requirements	SLS Payload Capacity	For each payload launch, the payload shall launch to Low Earth Orbit (LEO) using a	Mission Requirements
I-1	1.1	Habitation	IPV Habitation	The IPV habitation will have a minimum 170 m^3 of net habitable volume.	NASA-STD-3001 Vol 1
I-1	1.1	Habitation	IPV Habitation	Vehicle shall support at least 4 crewmembers throughout a mission of minimum 972 days	Mission Requirements
I-1	1.2	Temperature Regulation	IPV Habitation	IPV Hab: The atmosphere of spacecraft shall operate between 20°C and 23°C and be adjustable for human comfort	NASA-STD-3001 Vol 1
I-1	1.2	Temperature Regulation	IPV HAbitation	IPV Hab: The atmosphere of spacecraft shall operate between 20°C and 23°C and be adjustable for human comfort	NASA-STD-3001 Vol 1
I-1	1.3	Environmental Cntrol	Cabin Pressure	The IPV Hab spacecraft shall maintain an internal pressure of 101.325 kPa (1 atm)	NASA-STD-3001 Vol 1
I-1	1.3	Environmental Cntrol	Cabin Pressure	The IPV Hab spacecraft shall not exceed an internal pressure change of 93.1 kPa/min	NASA-STD-3001 Vol 1
I-1	1.3	Environmental Cntrol	Cabin Pressure	The IPV Hab spacecraft shall maintain an internal pressure of 101.325 kPa (1 atm)	NASA-STD-3001 Vol 1
I-2	2.3	Food Supplies	Water Mass	The spacecraft must be able to carry 9.23 mT of water for drinking and the rehydration of food.	75% recycling efficiency, Trade Study
I-3	3.1	IPV Power Usage	IPV Power Peak	The IPV must have a power supply capable of producing a minimum peak of 25.07 kWe	Power Trade Study
I-3	3.2	IPV Power Usage	IPV Power Nominal	The IPV must have a power supply capable of producing a minimum nominal power of 16.49 kWe	Power Trade Study
I-5	5.1	IPV Non-Hab Structural Mass	IPV Struct Mass	The IPV shall have a maximum structural mass of 20mT.	Trade Study
I-6	6.1	Total dV Budget	Mission Total	The IPV should have a minimum total deltaV of 11.84 km/s	Trade Study
0	0.1.1	Total Vehicle Mass	SLS Launches	The IPV shall be assembled with maximum 6 SLS launches.	Trade Study

		Category Name	Req Short	Requirement(s)	Rationale
I-2	2.1.1	Atmosphere	OGS Primary Mass	The IPV shall have a primary oxygen generation system with a minimum mass of 675 kg	"Would Current International Space Station Recycling Life Support Systems Save Mass on a Mars Transit?", Jones, NASA Ames, 2017
I-2	2.1.3	Atmosphere	Co2 Max Limit	The IPV shall maintain a ppCO2 level of no higher than 2.8mmHg on a 24-hour average	ISS US Segment allowable max
I-4	4.1.1	Radiator Area	Rad Area	The radiators from bimodal power shall have a maximum area of 200m2.	Preliminary radiator trade study
i-4	4.2.1	Allowable Astronaut Radiation	Career Radiation Dose	An individual astronaut's total effective radiation dose due to space flight radiation exposure shall be less than 1.3mSv/day across the entire mission	NASA Human System Standards All crew radiation exposures shall be minimized using the ALARA (as little as reasonably allowable) principle. The total career dose limit is based on ensuring all astronauts (inclusive of all ages and sexes) remain below 3% mean risk of
I-4	4.2.1	Radiation Shielding Rate (Nuclear Technologies)	Rad Shielding	Crewmembers will be exposed to a maximum of 0.05 mSv/day (48.85 mSv/Mission Total) from nuclear technologies.	NASA-STD-3001 4.8.5 [V1 4032], David Francisco, 2023-09-15
I-4	4.2.1	Radiation Shielding Rate (Solar Particle Events)	Rad Shielding	Crewmembers will be exposed to a maximum of 250 mSv from a singular Solar Particle Event (SPE).	NASA-STD-3001 4.8.5 [V1 4031], David Francisco, 2023-09-15
I-4	4.3.1	Environmental Control	Micrometeoroid Impacts	IPV shall be able to withstand all potential unavoidable obsticals during space travel, including micrometeorites traveling up to 10 km/s.	Article: Riley, Heather F. "NASA's Mars Mission Shields Up for Tests." Oct. 12 2022
I-5	5.1.1	IPV Hab Structural Mass		The IPV Hab shall have a maximum mass of 20mT, not including supplies	Trade Study / Mass Budget
I-5	5.2.1	Launch Loading	Launch Loading SLS	Payloads shall be constructed to withstand an axial load factor of 4.1G, and a lateral load factor of 3G.	SLS Mission Planner's Guide, ESD 2019 (ESD-3000)
I-5	5.2.2	Factor of Safety	FoS	All structures shall have a minimum factor of safety of 1.5.	NASA-STD-5001, NASA-STD-5002
I-5	5.2.3	Vibrational Loading	Vib	Stacked payloads shall have a cantilever fundamental frequency of greater than 8Hz in the lateral direction and 15Hz in the axial direction.	SLS Mission Planner's Guide, ESD 2019 (ESD-3000)
I-6	6.1.2	Delta V	Earth Departure dV	The IPV shall use minimum 4.00 km/s during Earth escape burn	Trajectory Trade Study, Finite Burn Trade Study
I-6	6.1.3	Delta V	Mars Capture dV	The IPV shall use minimum 2.13 km/s during Mars capture burn	Trajectory Trade Study
I-6	6.1.4	Delta V	Mars Depart dV	The IPV shall use minimum 2.13 km/s during Mars escape burn	Trajectory Trade Study
I-6	6.1.5	Delta V	Earth Capture dV	The IPV shall use minimum 3.61 km/s during Earth capture burn	Trajectory Trade Study
I-6	6.2.1	Propellant Storage	Total Propellant Mass	The IPV shall have a total fuel mass of minimum 509mT	Trajectory Trade Study
I-6	6.2.3	Propellant Storage	Earth Depart Tank Mass	The IPV Earth Depart Tank shall have a fuel mass of minimum 97mT	Trajectory Trade Study

		Category Name	Req Short	Requirement(s)	Rationale
I-6	6.2.4	Propellant Storage	Mars Capture Tank Mass	The IPV Mars Capture Tank shall have a fuel mass of minimum 97mT	Trajectory Trade Study
I-6	6.2.5	Propellant Storage	Mars Depart Tank Mass	The IPV Mars Depart Tank shall have a fuel mass of minimum 97mT	Trajectory Trade Study
I-6	6.2.6	Propellant Storage	Earth Capture Tank Mass	The IPV Earth Capture Tank shall have a fuel mass of minimum 87mT	Trajectory Trade Study
I-6	6.2.7	Propellant Pressure and Temp	Prop P and T	The LH2 shall be stored at minimum 234kPa and a temperature of maximum 20K.	Trajectory Trade Study
I-6	6.3.3	Engines	Thrust Level	The IPV Engines shall have a thrust level of 351kN per Nuclear Thermal engine.	Trade Study
I-6	6.3.4	IPV Propulsion	IPV Engine Isp	The IPV shall use a propulsion system with minimum 850s and maximum 950s	Trade Study
I-6	6.3.5	Engine and Reactor Mass	IPV Engines Mass	The IPV Engine and Reactors shall have a mass of 18mT total.	Mass Budget
I-7	7.1.1	Auxillary: Docking	n/a	Space craft and on planet habitation shall support 32 GHz Ka-Band communication systems.	Ka-band is superior over X- and S- band communication networks. It has a higher data rate, greater reliability and requires a smaller antena size. Nasa's Evolving Ka-band Network Capabilities to Meet
7	7.2.1	Docking	Docking Adapter Size	Docking and LEO assembly will utilize the International Docking System Standard which utilizes a two stage docking approach. The docking passagway has a diameter of 800 mm.	IDSS is the current standard for the ISS.
D-1	1.1	Deimos Lander/Hab	Lander Capabilities	Deimos lander shall support at least 4 crewmembers descending to Deimos' surface	Mission Requirements
D-1	1.1	DEV	Volume	The Deimos habitat shall have a minimum of 60 m3 of net habitable volume (30m3/CM).	NASA-STD-3001 Vol 1
D-1	1.2	DEV Internal Temperature	DEV Crew Habitat	DEV Hab: The atmosphere of spacecraft shall operate between 20°C and 23°C and be adjustable for human comfort	NASA-STD-3001 Vol 1
D-1	1.3	DEV Internal Pressure	DEV Crew Habitat	DEV Hab: The atmosphere of spacecraft shall operate between 20°C and 23°C and be adjustable for human comfort	NASA-STD-3001 Vol 1
D-3	3.1	DEV Power	DEV Power Peak	The DEV must have a power supply capapable of producing a minimum of 20.3 kWe (Peak)	The IPV habitation will have a minimum 120 m^3 of net habitable volume.
D-3	3.2	DEV Power	DEV Power Nominal	The habitat for the mission period near deimos must have a power supply capapable of producing a minimum of 15 kWe	Anthony J. Colozza, 2020, "Small Lunar Base Camp and In Situ Resource Utilization Oxygen Production Facility Power System Comparison," https://ntrs.nasa.
D-5	5.2	DEV Propulsion	DEV Engine Isp	The DEV engines shall have a minimum Isp of 300s	Trade Study
I-0	0	Total Vehicle Mass	Dry Mass	The assembled vehicle shall have a maximum dry mass of 241 mT before LEO departure	Trade Study
		Total Vehicle Mass	Fuel Tank Mass	The IPV fuel tanks shall have a maximum mass of 100 mT for all tanks	Trade Study

		Category Name	Req Short	Requirement(s)	Rationale
D	D-0	Deimos Lander/Hab	Lander Mass	The Deimos lander (without systems or supplies) shall be a maximum of 15 mT.	Trade Study
M-0	M-0	Tele-operating Mars Surface Asset (TMSA)	Number of TMSA's	The architecture of the mission shall include a minmum of 2 distinct Tele-operating Mars Surface Assets (TMSAs)	Trade Study
M-1	2.2	Tele-operating Mars Surface Asset (TMSA)	Mass Budget for TMSA's	The total mass of all Tele-operating Mars Surface Assets (TMSAs) shall not exceed a maximum of 4 MT	
M-2	2.1	Tele-operating Mars Surface Asset (TMSA)	Power Budget for TMSA's	The total continous power usage of all Tele-operating Mars Surface Assets (TMSAs) shall not exceed 3 kWe	
I-2	I-2.3.1	Water Processing Assem	WPA Mass	The spacecraft shall have a water recovery system with a minimum mass of 1385kg	
I-4.2.1	4.2.1	Radiation Shielding Rate (Galactic Cosmic Radiation)	Rad Allowable Amount	Crewmembers will be exposed to a maximum of 1.3 mSv/day from galactic cosmic radiation (GCR).	NASA-STD-3001 4.8.5 [V1 4033], David Francisco, 2023-09-15

I Alternative Concepts Appendix

I.1 Alternate Interplanetary Vehicle Concepts

Two alternate designs are made for the CoDR phase. These concepts are considered along with the Starfish Design, and are ultimately much more detrimental in particular aspects of their design. The radiator panels for both of these alternative designs are the same. The view of the radiators are included in Figure I.1

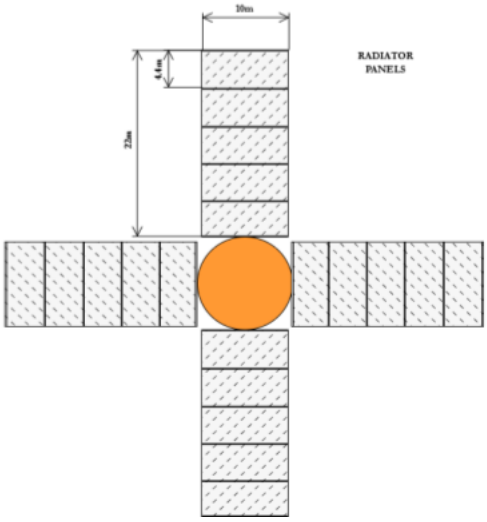

Figure I.1: Conceptual Design for Radiator Panels

Comparing Figure I.1 to the Starfish Design, the panel orientation remains the same, but the final design has a much smaller panel area. So the final design has saved on radiator mass.

The first alternative concept is the Vending Machine Design. This vehicle design has the propellant tanks stored inline with the Habitat and the Engines, with each tank connecting to two truss structures and the fuel piping connecting to another truss structure. The tanks will be jettisoned by ejecting from the fuel pipe truss. Figure I.2 shows the conceptual design of the Vending Machine, as well as the top-down view showing how the tanks are attached and jettisoned:

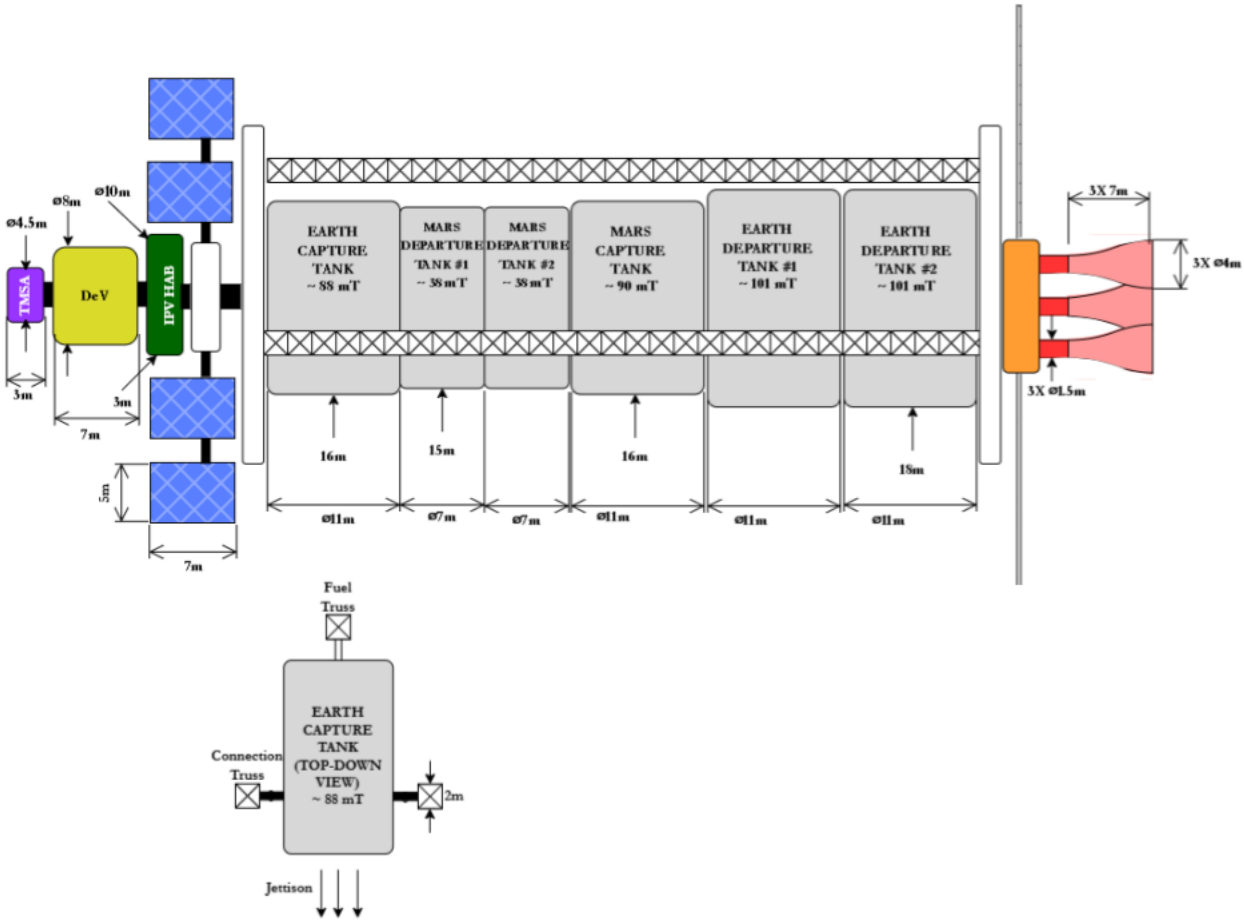

Figure I.2: Interplanetary Vehicle Alternative Design 1

The reason why this alternate design is not the chosen design is because this concept has too much truss mass, which will make the launch packaging configurations and the overall IPV mass increase, making the masses heavier than the Starfish Design. The second alternative concept is the Albatross Design. This vehicle design has the propellant tanks stored adjacent to each other, with the Earth Capture Tank stored inline with the Habitat and the Engines. All of the tanks are connected to a giant truss structure. Figure I.3 shows the conceptual design of the Albatross:

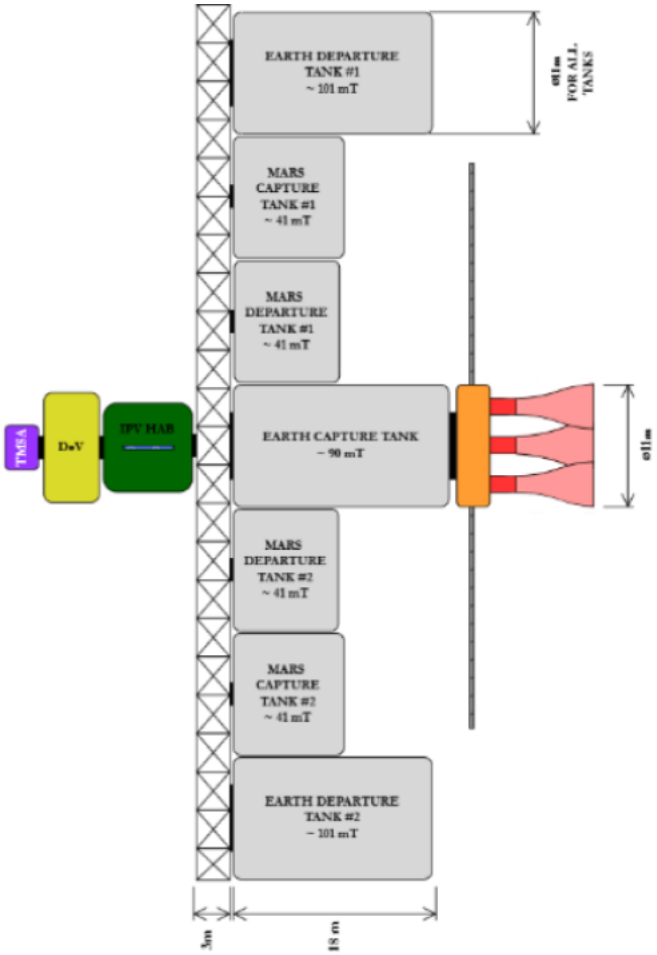

Figure I.3: Interplanetary Vehicle Alternative Design 2

The reason why this alternate design is not the selected design is because this concept has the engines thrusting into the Earth Capture tank, which will not be structurally sound. Additionally, the Habitat is in the radiation zone of the reactors from the Engines. These consequences to both of the alternate designs are part of the reason why the Starfish Design is chosen.

J Assembly Appendix

J.1 Assembly

Figure J.1 represents the International Docking System Standard Docking System for pressurized connections, which features an androgynous peripheral docking system. This is the docking system for the DEV and IPV Hab.

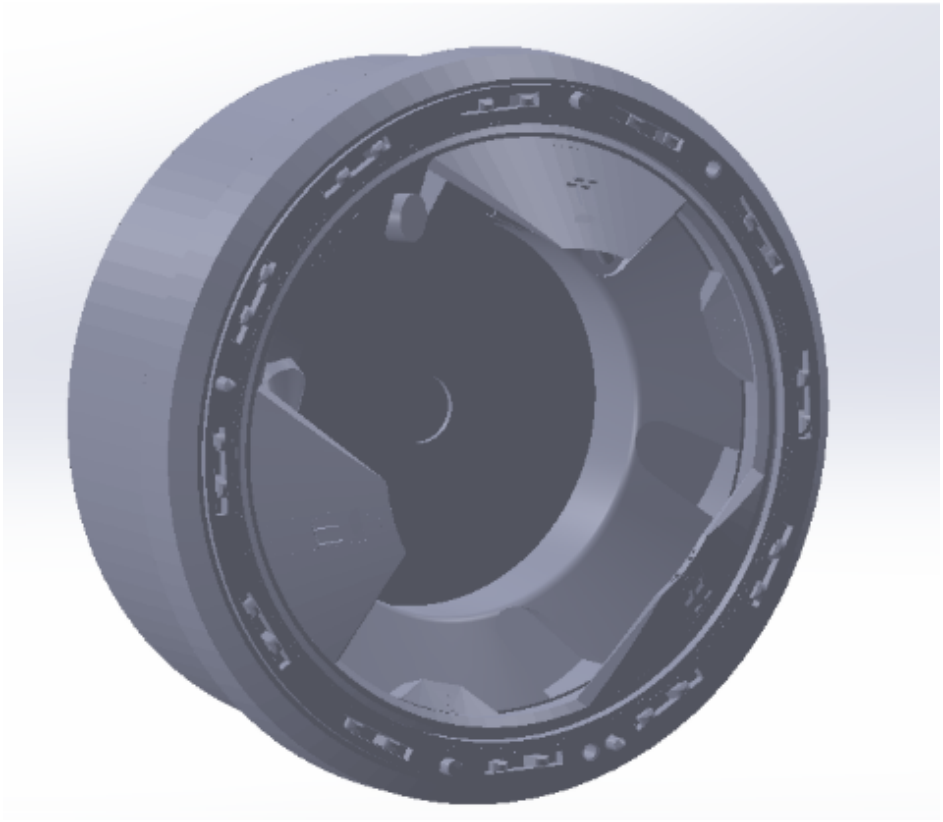

Figure J.1: Pressurized Docking

Figure J.2 represents the probe and drogue docking system for unpressurized connections. This is the docking system for the tanks and assembly vehicle.

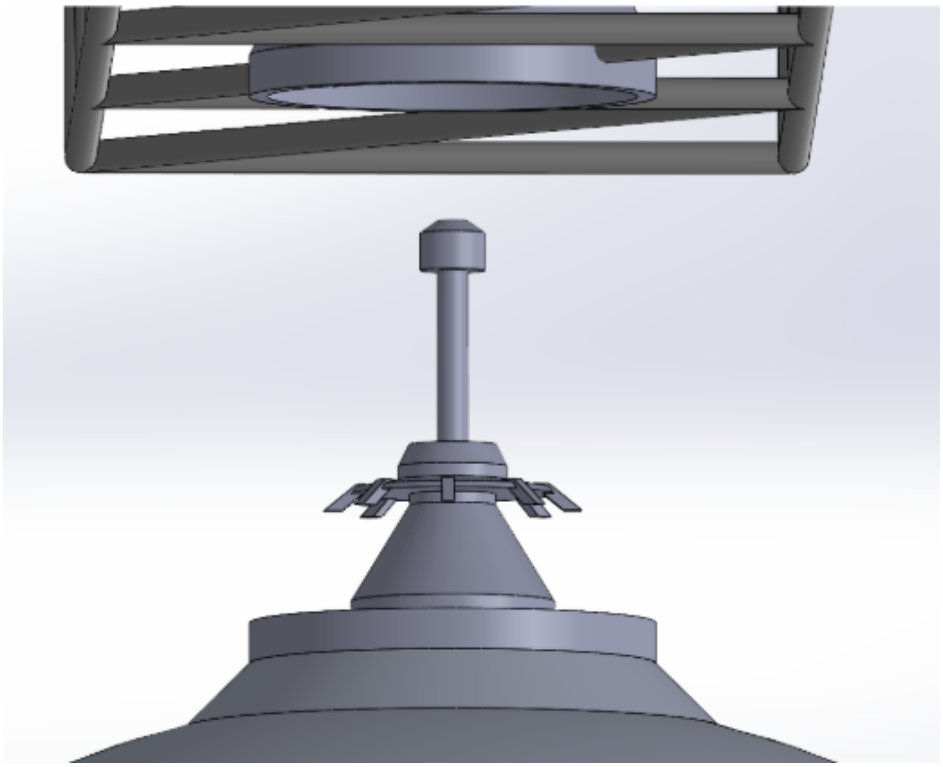

Figure J.2: Unpressurized Docking

References

[1] et al, P. L., 2022, "Design and Mechanical Characterisation of a Large Truss Structure for Continuous Manufacturing in Space," MDPI.

[2] Hopkins, J. B., 2011, "Comparison of Deimos and Phobos as Destinations for Human Exploration and Identification of Preferred Landing Sites," Lockheed Martin Space Systems.

[3] Nikitaev, D., 1966, "Nuclear Thermal Propulsion Turbomachinery Modeling," NASA, NASA Technical Note 20220002087.

[4] Newlands, R., 2017, "The Thrust Optimised Parabolic Nozzle," .

[5] Theodore L. Bergman, e. a., 2011, *Fundamentals of Heat and Mass Transfer*, 7th ed., John Wiley and Sons.

[6] Gambini and Vellini, 2020, *Turbomachinery: Fundamentals, Selection and Preliminary Design*, Springer.

[7] Clough, J., Starkey, R., Lewis, M., and Lavelle, T., 2006, *Reactor Modeling for Bimodal Nuclear Thermal Rockets*.

[8] Ewert, M. K., 2019, "Astronaut Mass Balance for Long Duration Missions," NASA, Tech. Rep. 20190027563, NASA Technical Reports Server.

[9] Rais-Rohan, M., 2005, "On Structural Design of a Mobile Lunar Habitat With Multi-Layered Environmental Shielding," NASA Marshall Flight Center.

[10] Center, R. A., 1993, "Failure Mode, Effects and Criticality Analysis (FMECA)," DoD Information Analysis Center.

[11] Zoby and Sullivan, 1965, "Effects Of Corner Radius on Stagnation-Point Velocity Gradients on Blunt Axisymetric Bodies," NASA, NASA Report 19660017753.

[12] Elphic, R., 2016, "Neutron Spectroscopy Can Constrain The Composition and Provenance of Phobos and Deimos," NASA Ames Research Center.

[13] Hanford, A. J., 2004, "Advanced Life Support Research and Technology Development Metric – Fiscal Year 2004," NASA, NASA Report CR-208944.

[14] Colozza, A., 2010, "Overview of the Habitat Demonstration Unit Power System Integration and Operation at Desert RATS 2010," NASA, NASA Report CR-217861.

[15] Kasturi, K., 2006, "Microcracking Fracture Toughness for Graphite Epoxy Composite Laminates Using Finite Fracture Mechanics," University of New Orleans.

[16] MatWeb, 2011, "Materion AlBeMet AM 162 Properties," MatWeb.

[17] Toray, 2018, "T800S INTERMEDIATE MODULUS CARBON FIBER," Toray Composite Materials America, Inc.

[18] NASA, 2018, "Space Flight System Design and Environmental Test," Tech. Rep. ARC-STD-8070.1.

[19] Benton, S., 2017, "S3001: Guidelines for Risk Management," NASA.

[20] Mars Exploration Program Analysis Group (MEPAG), 2018, "Mars Scientific Goals, Objectives, Investigations, and Priorities: 2018," White paper, 81 pages, posted October 2018, `https://mepag.jpl.nasa.gov/reports.cfm`

[21] Rodriguez-Manfredi, J. A., 2021, "The Mars Environmental Dynamics Analyzer, MEDA. A Suite of Environmental Sensors for the Mars 2020 Mission," Space Science Reviews, **217**(3), p. 48.

[22] Kudryashov, I. L. and Kudryashov, A. A., 2023, "Assessment of the Possibility of Using a Nuclear Power Plant for the Power Supply of a Martian Base," Solar System Research, **57**(4), pp. 287–293.

[23] NASA, "The Apollo Program," .

[24] NASA, "Mars Missions," .

[25] NASA, 2025, "Station Record Holders," .

[26] Barnhart, P., "Crewed Mars Moon Mission Requirements," .

[27] NASA, 2021, "Human Systems Integration Handbook," NASA Handbook SP-20210010952.

[28] et al., L. M. B., 2010, "Interplanetary Mission Design Handbook: Earth-to-Mars Mission Opportunities 2026 to 2045," NASA Glenn Research Center, Tech. Rep. NASA/TM-2010-216764.

[29] Christiansen, D. E. L., 2009, "Handbook for Designing MMOD Protection," NASA, NASA Handbook JSC-64399.

[30] NASA, 2023, "NASA Spaceflight Human-System, Standards Volume 1: Crew Health," NASA Standard NASA-STD-3001.

[31] NASA, 2022, "Structural Design and Test Factors of Safety for Spaceflight Hardware," NASA Standard NASA-STD-5001.

[32] Wilkerson, R., 2019, "Nuclear Thermal Propulsion: An Overview of NASA Development Efforts," NASA.

[33] FINSETH, J., 1991, "RnVFR NUCLEAR ROCKET ENGINE PRROGRA": OVERVIEW OF ROVER ENGINE," NASA.

[34] Halchak, J. A., *Materials for Liquid Propulsion Systems*, NASA Marshall Space Flight Center.

[35] McCarville, D. A., 2017, "Design, Manufacture and Test of Cryotank Components," Boeing, NASA Marshall Flight Center.

[36] Proctor, C. L., 2003, "Internal Combustion Engines," *Encyclopedia of Physical Science and Technology (Third Edition)*, Third edition ed., R. A. Meyers, ed., Academic Press, New York, pp. 33–44.

[37] Johnson, G. A. and Mason, L. S., 2008, "Initial Test Results of a Dual Closed-Brayton-Cycle Power Conversion System," NASA Glenn Research Center, Tech. Rep. NASA/TM-2008-215080, Accessed: 2025-05-06.

[38] Hervol, D., Mason, L., and Birchenough, A., 2003, "Experimental Results from a 2kW Brayton Power Conversion Unit," NASA Glenn Research Center, Tech. Rep. NASA/TM-2003-211999, Accessed: 2025-05-06.

[39] Hervol, 2003, "Experimental Results From a 2kW Brayton Power Conversion Unit," NASA, Tech. Rep. E-13671.

[40] Stromgren, C., Burke, C., Cho, J., Calderon, R., and Rucker, M., 2023, "Defining the Required Net Habitable Volume for Long-Duration Exploration Missions," Binera, Inc. and NASA Johnson Space Center, 77 S. Washington St., Rockville, MD 20850 and 2101 NASA Parkway, Houston, TX 77058.

[41] Gernhardt, M., Chappell, S., Beaton, K., Litaker, H., Bekdash, O., Newton, C., and Stoffel, J., 2019, "Deep Space Habitability Design Guidelines Based on the NASA NextSTEP Phase 2 Ground Test Program," NASA Johnson Space Center, Houston, TX, Tech. Rep. NASA/TP-2020-220505.

[42] Cawley, J., 2019, "Orion Window Testing Brings Artemis I Closer into View," Accessed: 2025-05-07, https://www.nasa.gov/missions/artemis/orion/orion-window-testing-brings-artemis-1-closer-into-view/

[43] Powell, D., 1978, "Space Fabrication and Assembly of Graphite Composite Trusses," NASA.

[44] Prince, A., Alford, B., Boswell, B., Pitlyk, M., and Pedigo, M., 2014, "Development of a Project Cost Estimating Capability," NASA Marshall Space Flight Center, https://www.nasa.gov/wp-content/uploads/2023/06/pcec-carpediem-may2014.pdf

[45] Friz, P. D., 2020, "Parametric Cost Estimates of Four 20 Ton Payload Mars EDL Vehicle Concepts," NASA Langley Research Center, Conference Paper AIAA 2020-1514.

[46] Board, N. I. R., 2024, "Final Report of the OSAM-1 Independent Review Board," NASA, https://www.nasa.gov/wp-content/uploads/2023/02/osam-1-irb-final-report-022729-cleared-redacted-20mar2024.pdf

[47] Dreier, C., 2012, "Cost of MSL Curiosity," https://www.planetary.org/space-policy/cost-of-msl-curiosity

[48] NASA Office of Inspector General, 2023, "NASA's Transition of the Space Launch System to a Commercial Services Contract," NASA Office of Inspector General, Audit Report IG-24-001.

[49] NASA Office of Inspector General, 2024, "NASA's Management of the Mobile Launcher 2 Project," NASA Office of Inspector General, Audit Report IG-24-016.

[50] 2021, "NASA's Construction of Facilities," NASA Office of Inspector General, Audit NASA-IG-21-027.

[51] Jones, H. W., 2016, "Humans to Mars Will Cost About "Half a Trillion Dollars" and Life Support Roughly Two Billion Dollars," NASA Ames Research Center, Conference Paper ARC-E-DAA-TN33332.

[52] NASA Cost Analysis Division, 2015, *NASA Cost Estimating Handbook Version 4.0*, National Aeronautics and Space Administration, `https://www.nasa.gov/ocfo/ppc-corner/nasa-cost-estimating-handbook-ceh/`

[53] Dreier, C., 2021, "How much does the James Webb Space Telescope cost?" The Planetary Society, `https://www.planetary.org/articles/cost-of-the-jwst`

[54] NASA, 2018, "SLS Mission Planner's Guide," Tech. Rep. ESD-30000.

[55] DoD, 1998, "Metallic Materials and Elements for Aerospace Vehicle Structures," Handbook MIL-HDBK-5H.

[56] Solvay, 2017, "Cycom 5250-4 Datasheet," .

[57] Company, M. D. A., 1973, "Isogrid Design Handbook," NASA Contractor Report CR-124075.

[58] ASME, 2023, "ASME Boiler and Pressure Vessel Code," Tech. Rep. ASME-BPV-VIII.

[59] Gates, T. S., 2005, "Hydrogen Permeability of Polymer Matrix Composites at Cryogenic Temperatures," American Institute of Aeronautics and Astronautics.

[60] Tew, B. W., 1995, "Preliminary Design of Tubular Composite Structures Using Netting Theory and Composite Degradation Factors," Journal of Pressure Vessel Technology, **117**(4), pp. 390–394.

[61] T.P. Sarafin, W. L., 1995, *Spacecraft Structures and Mechanisms: From Concept to Launch*, Springer.

[62] Purdue, "Axial and Hoop Stresses in in Thin-Walled Pressure Vessels," Purdue University.

[63] D.A.Smith, 2018, "SLS Payload Delivery Capability Overview," NASA.

[64] Wijker, J., 2008, *Spacecraft Structures*, Springer.

[65] NASA, 2019, "Load Analyses of Spacecraft and Payloads," NASA Standard NASA-STD-5002a.

[66] Division, M. A. M., "3M^{TM} Nextel^{TM} Ceramic Fabrics 312 and 440 Data Sheet," `https://multimedia.3m.com/mws/media/1242135O/3m-nextel-ceramic-fabrics-312-and-440.pdf?&fn=FINAL_063016_Celum.pdf`

[67] of Energy, D., 1992, *Thermodynamics, Heat Transfer, and Fluid Flow*, Department of Energy.

[68] cheng S. Chen, S., 2006, "Turbopump Design and Analysis Approach for Nuclear Thermal Rocket," NASA, NASA Technical Note 20060051740.

[69] Pelaccio, D. G., 1993, "Nuclear engine simulation (NESS)," NASA, NASA Technical Note NAS3-25809.

[70] Borowski, S. K., 2012, "Small Fast Spectrum Reactor Designs Suitable for Direct Nuclear Thermal Propulsion," NASA, NASA Technical Note NAS3-25809.

[71] Oates, G. C., 1997, *Aerothermodynamics of Gas Turbine and Rocket Propulsion*, American Institute of Aeronautics and Astronautics, Inc.

[72] Tomberlin, T. A., 2004, "BERYLLIUM – A UNIQUE MATERIAL IN NUCLEAR APPLICATIONS," Idaho National Engineering and Environmental Laboratory.

[73] Caffrey, J. A., 2015, "Shielding Development for Nuclear Thermal Propulsion," NASA Marshal.

[74] Gruneisen, S., 1991, "SHIELDING REQUIREMENTS FOR PARTICLE BED PROPULSION SYSTEMS," Phillips Lab.

[75] D, H., 2022, "Development Trend of Liquid Hydrogen-Fueled Rocket Engines," International Journal of Aeronautical and Space Sciences.

[76] Farokhi, S., 2021, *Aircraft Propulsion: Cleaner, Leaner, and Greener*, 3rd ed., Wiley, Hoboken, NJ.

[77] White, F. M., 2016, *Fluid Mechanics*, McGraw Hill.

[78] ASME, 2020, "Process Piping: ASME Code for Pressure Piping," ASME Code ASME-B31.3-2020.

[79] Hostler, P., 2025, "In Person Conference for Pump Analysis," .

[80] Zukowski, E. and Miller, D. W., 2005, "Lecture 25: Rocket Nozzle Performance," Accessed: 2025-05-06, `https://ocw.mit.edu/courses/16-512-rocket-propulsion-fall-2005/8b2220397190eb677d156c4b486dd069_lecture_25.pdf`

[81] Team, C.-R., 2023, "5.2 Nozzle Geometry," Accessed: 2025-05-06, https://www.cryo-rocket.com/flow-model/5.2-nozzle-geometry/

[82] Sutton, G. P. and Biblarz, O., 2010, *Rocket Propulsion Elements*, 8th ed., John Wiley & Sons, Accessed 2025-05-06.

[83] Ward, B. and Connolly, J. W., 2023, "LOX and LCH4 Propulsion Architecture Design for Lunar Ascent and Descent Vehicles," AIAA.

[84] Huzel, D. K. and Huang, D. H., 1970, "Design of Liquid Propellant Rocket Engines," NASA, Washington, DC, Tech. Rep. NASA-TN-D-5992, NASA Technical Note D-5992.

[85] Dieter K. Huzel, D. H. H., 1967, *Design of Liquid Propellant Rocket Engines*, American Institute of Aeronautics and Astronautics.

[86] NASA, 2006, "Active Thermal Control System (ATCS) Overview," NASA, St, Louis, MO, Available at https://www.nasa.gov/wp-content/uploads/2021/02/473486main_iss_atcs_overview.pdf,.

[87] P.E, K. E. N., 2009, *How to Select Turbomachinery For Your Application*, Barber Nichols, Arvada, CO, Available at https://barber-nichols.com/wp-content/uploads/2019/11/how_to_select_turbomachinery_for_your_application.pdf.

[88] Foust, O., 1972, "SODIUM-NaK Engineering Handbook," Division of Reactor Development and Technology, United States Atomic Energy Commission.

[89] Kamran Daryabeigi, e. a., "Heat Transfer in High Temperature Multilayer Insulation," NASA.

[90] 2004, "A Coating That Cools and Cuts Costs," https://spinoff.nasa.gov/Spinoff2004/ip_7.html

[91] C. W. Keller, e. a., 1974, "FINAL REPORT: THERMAL PERFORMANCE OF MULTILAYER INSULATIONS," NASA, Cleveland , OH.

[92] Finckenor, M., 1999, "Multilayered Insulation Material Guidelines," NASA, Huntsville , AL.

[93] Ryan Honour, e. a., 2011, "Thermal Optimization and Assessment of a Long Duration Cryogenic Propellant Depot," NASA.

[94] Johnson, W., 2019, "Thermal, Avionics, and Power Considerations for Designing a Nuclear Thermal Propulsion Flight Demonstrator," NASA, NASA Report M19-7775.

[95] Green, C., 2023, "MUSTANG: A Workhorse for NASA Spaceflight Avionics," Goddard Space Flight Center, NASA Report 20230003757.

[96] Engler, S., Binsted, K., and Leung, H., 2016, "HI-SEAS habitat energy requirements and forecasting," Acta Astronautica," Acta Astronautica, **162**.

[97] Wikipedia, 2025, "Electrical system of the International Space Station," `https://en.wikipedia.org/wiki/Electrical_system_of_the_International_Space_Station`

[98] REDWIRE, 2021, "SOLAR ARRAYS – ROLL OUT SOLAR ARRAY (ROSA)," .

[99] ASTM, 2018, "Standard Extraterrestrial Spectrum Reference," Tech. Rep. ASTM E-490.

[100] Wagner, H. A., 1972, "Space-shuttle fuel cell," NASA, NASA Report CR-127057.

[101] Fuller, R. L., 2010, "Closed Brayton Cycle Power Conversion Unit for Fission Surface Power Phase I Final Report," Barber-Nichols Engineering Co., NASA Report CR-215673.

[102] Juhasz, A., 2018, "A Mass Computation Model for Lightweight Brayton Cycle Regenerator Heat Exchangers," NASA, Tech. Rep. 216799.

[103] Oeftering, R. C. and Gardner, B. G., 2016, "A 20 kiloHertz space station power system," NASA, NASA Report TM-88801.

[104] Flinn, C., 2025, *Trigonometry and Single Phase AC Generation for Electricians*, LibreTexts Workforce.

[105] Schwenk, H. C. and Shannon, R. H., 1957, *Nuclear Power Engineering*, McGraw-Hill, New York.

[106] World Nuclear Association, 2025, "Nuclear Power Reactors," Accessed: 2025-05-07, `https://world-nuclear.org/information-library/nuclear-fuel-cycle/nuclear-power-reactors/nuclear-power-reactors`

[107] Gietl, E., 2000, "The Electric Power System of the International Space Station: A Platform for Power Technology Development," NASA, NASA Report TM-210209.

[108] Carter, L., Brown, C., and Orozco, N., 2014, "Status of ISS Water Management and Recovery," *International Conference on Environmental Systems* (*ICES*), American Institute of Aeronautics and Astronautics, `https://ntrs.nasa.gov/api/citations/20140002687/downloads/20140002687.pdf`

[109] Jones, H. W., 2016, "Using the International Space Station (ISS) Oxygen Generation Assembly (OGA) Is Not Feasible for Mars Transit," *46th International Conference on Environmental Systems* (*ICES*), Vienna, Austria, ICES-2016-103, `https://ntrs.nasa.gov/api/citations/20160014553/downloads/20160014553.pdf`

[110] Cucinotta, F. A., 2013, "How Safe is Safe Enough? Radiation Risk for a Human Mission to Mars," NASA Lyndon B. Johnson Space Center.

[111] NASA, 2023, "NASA Spaceflight Human-System, Standards Volume 2: Human Factors, Habitability, and Environmental Health," NASA Standard NASA-STD-3001.

[112] Wikipedia, 2025, "Sky crane (landing system)," .

[113] et. al, M., 2022, "Development and Sizing of the Mars 2020 Thermal Protection System," NASA, NASA Report 20100021401.

[114] Allen and Eggers, 1957, "Coupled Fluids-Radiation Analysis of a High-Mass Mars Entry Vehicle," NASA, NASA Report Report 1381.

[115] Barnhart, P., 2024, "Orbital Dynamics," .

[116] NASA, 2021, "Mars Atmosphere Model Glenn Research Center," .

[117] et. al, W., 2009, "A Review of Aerothermal Modeling for Mars Entry Missions," Ames Research Center, NASA Report 20100021401.

[118] Sutton and Graves, 1971, "A General Stagnation-Point Convective-Heating Equation for Arbitrary Gas Mixtures," NASA Langley, NASA Report TR R-376.

[119] Tauber, M. E. and Sutton, K., 1991, "Stagnation-point radiative heating relations for earth and Mars entries," Journal of Spacecraft and Rockets, **28**(1), pp. 40–42.

[120] Akin, D., 2016, "Entry Aerothermodynamics," ENAE 791 - Launch and Entry Vehicle Design.

[121] Anderson, T. R., Putnam, Z. R., and Braun, R. D., 2016, *Strategies for Landing Large Ballistic Coefficient Vehicles on Mars*.

[122] NASA/JPL-Caltech/ESA, 2012, "Landing Accuracy on Mars: A Historical Perspective," `https://doi.org/10.2514/3.26206, https://www.jpl.nasa.gov/images/pia16039-landing-accuracy-on-mars-a-historical-perspective/`

[123] NASA Jet Propulsion Laboratory, 2020, "Mars 2020 Perseverance Launch Press Kit|Power," Accessed: 2025-05-08, https://www.jpl.nasa.gov/news/press_kits/mars_2020/launch/mission/spacecraft/power/

[124] Spiers, G. D., 1994, "Lidar Performance Analysis," NASA.

[125] Grimm, R., 2003, "Comparison of Ground-Penetrating Radar and Low-Frequency Electromagnetic Sounding for Detection and Characterization of Groundwater on Mars," Blackhawk Geoservices.

[126] Mullen, M., 2016, "Fourier Transform Infrared Spectroscopy: Unknown Aerospace Contaminant Analysis," Nasa Kennedy Space Center.

[127] Curtis, H. D., 2005, *Orbital Mechanics for Engineering Students*, Elsevier Butterworth-Heinemann.

[128] Willis, E. A., 1966, "Finite-Thrust Escape from and Capture into Circular and Elliptic Orbits," NASA, NASA Technical Note NASA TN D-3606.